

# **Local FEM Analysis of Composite Beams and Plates: Free-Edge effect and Incompatible Kinematics Coupling**

Doctoral thesis  
in structural mechanics  
by  
Dipl. Ing. Christian Wenzel

October 2014

Université Paris Ouest Nanterre La Défense  
Ecole doctorale 139 : Connaissance, langage, modélisation  
Laboratoire Energétique Mécanique Electromagnétisme

Politecnico di Torino  
Scuola di Dottorato  
Dipartimento di Ingegneria Meccanica e Aerospaziale

A. Milazzo	Rapporteur
A. Beakou	Rapporteur
S. Di Rosa	
H. Dumontet	
M. D'Ottavio	
P. Vidal	
O. Polit	Advisor
E. Carrera	Co-Advisor

# Abstract

The use of composite laminated structures helped in the last two decades to reduce overall weight of transportation structures. As a consequence the energy needed to power those transportation means is reduced and hence fuel and monetary resources are economized and emissions are reduced. Especially the aerospace sector has a high need of a favourable weight to power ratio. Orthotropic laminated structures are able to provide a higher stiffness combined with a lower density compared to monolithic isotropic materials used in the past. It seems hence, that they are perfect for the use in even a wider spectrum of applications. However through the assembly of differently layers, it is more difficult to model and predict the structures mechanical response to outer loadings. In the recent past different computational methods were developed. Most of them under the scope of being capable to deliver very detailed results of the global behaviour of the structure but also of the interaction between the different layers of the laminate. As a major drawback, a detailed result comes with high computational costs. Hence a need for a good compromise between costs and accuracy has to be found. This benefits especially from the fact that stress concentrations in composites occur mainly in local domains of the structure. The use of detailed models only in those local domains of interest seems therefore straightforward.

Examples for such local domains with stress concentrations are laminates with free edges. At the interface between two layers with different elastic properties the stresses have singular behaviour in the immediate vicinity of the free edge, assuming linear elastic material behaviour. This is due to the material discontinuity and the resulting mismatch of the elastic properties at the interface of the layers, the condition of traction-free edges and the equilibrium between the layers. Therefore they are critical to promote delamination.

An adequate analysis method for this would be the use of a full three-dimensional analysis model. However it's computational cost is significant. Composites are often rather thin planar structures, allowing the use of reduced dimensional models, which are also more attractive through their reduced computational cost. Therefore different reduced models with their appropriate hypotheses in the thickness direction are under consideration in this work. Via different thickness expansion functions suitable kinematical theories, are expressed. The Carrera's Unified Formulation (CUF) is used to have a common base to build the models with the different kinematical theories. The CUF allowing not only purely displacement based models using the

Principle of Virtual Displacements (PVD), but also mixed stress and displacement based models with the Reissner's Mixed Variational Theorem (RMVT).

In the first part of this work, the reduced dimensional modelling approaches are compared. Two main class are presented: Equivalent Single Layer (ESL) models treating the layered structure like one homogenous plate of equal mechanical properties, and the Layer Wise approach, treating each layer independently. Subsequently their capabilities to capture the appearing singularities are compared. In order to have a comparable measurement of those singularities, the obtained stress distributions will be expressed via a power law function, which has a priori a singular behaviour. Only two parameters fully describe therefore the singular stress components in the vicinity of the free edge. With the help of these two parameters not only the different models capabilities will be compared, but also the free edge effect itself will be measured and compared for different symmetrical laminates and the case of extensional and uniform bending load. The results for all laminates under both load cases confirm the before stated need for rather complex models in the vicinity of the free edge. However far from the free edges, in the composite plates centre, no significant difference can be noted for rather simple models.

The second part of this work is therefore dedicated to the coupling of kinematically incompatible models. The use of costly expensive complex models is restricted to local domains of interest, while economic simple models will model the global domain. The Extended Variational Formulation (XVF) is identified as the most suitable way to couple the kinematically heterogenous but dimensional homogenous models. As it uses a configuration with one common interface without domain overlap, the additional efforts for establishing the coupling are limited. Further the XVF offers the possibility to adapt the conditions imposed at the interface using a single scalar parameter. It will be shown that for the homogenous dimensional problem under consideration only two different conditions can be imposed by this parameter. One matching the strong conditions imposed by the classical Multi Point Constraints (MPC) and a second one providing a weak condition. The last one is shown to provide the possibility to reduce further the domain using the complex kinematical model, without the loss of local precision. As this is the first application of the XVF towards composite structures, the need for a new coupling operator was identified. A new form is proposed, tested and its robustness will be evaluated.

# Résumé

L'utilisation de structures stratifiées composites a permis de réduire le poids d'ensemble de structures de transport au cours des deux dernières décennies. En conséquence, l'énergie nécessaire pour alimenter ces moyens de transport est réduite et donc les ressources monétaires et en combustibles sont économisées et les émissions sont réduites. En particulier, le secteur de l'aérospatiale a grand besoin d'un poids favorable au rapport de puissance. Des structures stratifiées orthotropes sont capables de fournir une rigidité plus élevée au cas où elles sont combinées avec une plus faible densité par rapport aux matériaux isotropes monolithiques utilisés dans le passé. Ainsi semble-t-il qu'elles soient parfaites pour l'utilisation même dans un plus large éventail d'applications. Toutefois, grâce à l'assemblage de couches différentes, il est plus difficile à modéliser et prédire la réponse mécanique des structures à des charges externes. Dans les dernières années, différentes méthodes de calcul ont été développées. La plupart d'entre elles ont été déterminées sous la prémissse d'être capable de fournir des résultats très détaillés du comportement global de la structure, mais aussi de l'interaction entre les différentes couches du stratifié. Comme inconvénient majeur, un résultat détaillé est automatiquement lié aux coûts informatiques élevés. Par conséquent, un bon compromis entre les coûts et la précision doit être trouvé. Ce compromis profite surtout du fait que les concentrations de contraintes dans les matériaux composites se produisent principalement dans les domaines locaux de la structure. L'utilisation de modèles détaillés seulement pour les domaines d'intérêt locaux semble donc simple.

Des exemples de ces domaines locaux possédant des concentrations de contraintes sont stratifiés avec des bords libres. A l'interface entre deux couches ayant des propriétés élastiques différentes contraintes, ces dernières ont un comportement singulier à proximité immédiate du bord libre en supposant que le comportement du matériau élastique soit linéaire. Cela est dû à la discontinuité de la matière et la non-concordance qui résulte des propriétés élastiques à l'interface entre les couches, la condition de bords libres sans traction et de l'équilibre entre les couches. Par conséquent, ils sont essentiels pour le délaminate. Une méthode d'analyse appropriée serait l'utilisation d'un modèle complet d'analyse tridimensionnelle. Toutefois, le temps de calcul est important. Les composites sont souvent des structures planes et plutôt minces, permettant l'utilisation de modèles réduits tridimensionnels, qui sont eux aussi beaucoup plus attrayant grâce à leur coût de calcul minimisé. Par conséquent, différents modèles réduits avec leurs hypothèses appropriées dans

le sens de l'épaisseur sont étudiés dans ce travail. Ils sont données par différentes fonctions d'extension de l'épaisseur théories cinématiques appropriées . La *Formulation unifiée de Carrera (CUF)* est utilisée pour avoir une base commune permettant de construire des modèles avec les différentes théories cinématiques. La CUF rend non seulement possible le développement des modèles avec seulement des inconnus de déplacement en utilisant le principe des déplacements virtuels (PVD), mais aussi des modèles mixtes avec des inconnus de contrainte et de déplacement sur la base de théorème variationnelle mixte de Reissner (dit RMVT).

Dans la première partie de ce travail, les approches de modélisation dimensionnelle réduites sont comparées. Deux classes principales sont présentées : des modèles à couche équivalente (ESL) qui traitent le stratifié comme une plaque homogène de propriétés mécaniques égales, et l'approche de la couche explicite (LW) qui traite chaque couche indépendamment. Par la suite, leurs capacités à saisir les singularités apparentes sont comparées. Afin d'avoir une mesure comparable de ces singularités, les distributions de contraintes obtenues seront exprimées par une fonction de loi de puissance décroissante, qui présente a priori un comportement singulier. Seuls deux paramètres décrivent donc entièrement les composantes de contraintes singulières au voisinage du bord libre. Grâce à ces deux paramètres, les différents capacités des modèles seront comparés, mais aussi l'effet de bord libre sera mesuré et comparé pour différents stratifiés symétriques dans le cas d'une charge uniforme de flexion ou extension. Tous les résultats des stratifiés pour les deux cas de charge confirment la nécessité d'appliquer des modèles d'ordre supérieur dans le voisinage du bord libre. Cependant, aucune différence significative ne peut être notée pour les modèles plutôt simples loin des bords libres au centre des plaques composites.

La deuxième partie de ce travail est donc dédiée au couplage de modèles cinématiques incompatibles. L'utilisation de modèles complexes et coûteux est limitée aux domaines d'intérêt locaux tandis que les modèles économiques simples seront appliqués aux domaines globaux. La *Formulation variationnelle étendue (XVF)* est identifiée comme le moyen le plus approprié pour coupler les modèles de dimensionnalité homogènes mais cinématiquement hétérogènes. Comme il utilise une configuration avec une interface commune sans recouvrement des domaines, les efforts supplémentaires pour établir le couplage sont limités. En outre, le XVF offre la possibilité d'adapter les conditions imposées à l'interface en utilisant uniquement un paramètre scalaire. Il sera démontré que pour le problème de dimensionnalité homogène à l'étude, deux conditions différentes peuvent être imposées par ce paramètre dont la première aux conditions fortes est appliquée de la même façon en utilisant la méthode des *Multi Point Constraints (MPC)* et dont la seconde impose les conditions faibles à l'interface. Les conditions faibles aident à réduire la taille des domaines basés sur le modèle de la cinématique complexe tout en gardant leur précision locale. Comme il s'agit de la première application de la XVF aux structures composites, le besoin d'un nouvel opérateur de couplage a été identifié. Un nouveau formulaire est proposé et testé. Sa robustesse sera évaluée.

# Riassunto

L'utilizzo di strutture laminate fatte di composti, ha aiutato negli ultimi due decenni a ridurre la massa totale delle strutture di trasporto. La conseguenza è stata la riduzione dell'impiego dell'energia necessaria per azionare questi mezzi e quindi anche la riduzione del costo, della quantità di carburante e delle emmissioni. In particolar modo, il settore aerospaziale necessita di un rapporto favorevole di peso per potenza. Le strutture laminate ortotropiche, rispetto ai materiali monolitici isotropici utilizzati in passato, riescono a fornire un'elevata rigidità e una bassa densità. Sembra che esse possano essere utilizzate per moltissime applicazioni. Tuttavia, a causa dell'assemblaggio dei differenti strati è più difficile delineare e pronosticare la loro risposta a degli sforzi esterni. Negli ultimi tempi, differenti metodi computerizzati sono stati sviluppati. Tra questi la maggior parte riferiscono dei risultati dettagliati del comportamento globale della struttura, ma anche dell'interazione tra gli strati del laminato. Uno svantaggio considerevole di questi metodi è che hanno bisogno di costi elevati di computerizzazione. Per questo è importante trovare un buon compromesso tra costi e precisione. Il compromesso è perseguitabile perché le concentrazioni elevate nei composti si riducono a delle zone locali della struttura e quindi l'utilizzo di modelli di calcolo dettagliati è necessario solo in queste zone d'interesse locale.

Un esempio di zone locali con delle concentrazioni elevate di sforzo sono i laminati con dei bordi liberi. Nell'interfaccia di due strati con delle proprietà elastiche diverse, gli sforzi hanno un comportamento singolare nell'immediata contiguità coi bordi liberi, quando come base si utilizza un comportamento lineare elastico del materiale. Ciò è dovuto alla discontinuità del materiale dell'interfaccia e alla conseguente differenza tra le proprietà elastiche degli strati, alla condizione dei bordi liberi e all'equilibrio tra gli strati. Di conseguenza essi possono apportare delaminazione.

Un metodo adeguato per analizzare tutto questo è l'utilizzo di modelli tridimensionali, ma il loro costo di computerizzazione è comunque considerabile. Per il fatto che i composti sono nella maggior parte dei casi delle strutture sottili e piane, l'applicazione dei modelli di dimensionalità ridotta è possibile per i bassi costi di computerizzazione. Di conseguenza sono stati presi in considerazione in questo lavoro diversi modelli ridotti con le loro proprie ipotesi nella direzione trasversale. Queste ipotesi esprimono una teoria cinematica conveniente e utilizzando diverse funzioni di espansione, diverse ipotesi cinematiche posso essere adoperate. Esse sono formulate su una funzione di espansione nella direzione transversale. La Carrera's Unified Formulation (CUF) è utilizzata per avere una base unica per creare modelli attraverso le

diverse teorie cinematiche. La CUF non permette solo lo spostamento dei modelli di base che usano il principio degli spostamenti virtuali (PVD), ma anche una combinazione di sforzi e spostamenti di modelli di base, attraverso il teorema variazionale mixed di Reissner (RMVT).

Nella prima parte di questo lavoro, sono confrontati gli approcci di modellazione di dimensionalità ridotta. Sono presentate due classi principali: la prima presenta i modelli di un strato unico equivalente (ESL) che trattano la struttura come un materiale omogeneo di un singolo strato con delle proprietà elastiche equivalenti; la seconda riguarda i modelli Layer-Wise che trattano ogni strato esplicitamente con un modello di comportamento indipendente. In seguito sono messe a confronto le loro capacità di riprodurre le singolarità che appaiono sui bordi liberi: al fine di avere una misura comparabile di queste forze singolari gli sforzi nell'immediata contiguità ai bordi liberi sono espressi sotto forma di una funzione esponenziale decrescente. La funzione a priori ha un comportamento singolare. Solamente due parametri descrivono in modo completo questa curva e il comportamento degli sforzi presi in considerazione. Con l'aiuto di questi due parametri, non solo sono confrontati i diversi modelli e le loro capacità, ma anche l'effetto dei bordi liberi per sé diventa misurabile. In questo modo è anche possibile confrontare l'effetto per le diverse stratificazioni esposto ai carichi di trazione e flessione. I risultati per le stratificazioni sotto i due carichi considerati confermano il bisogno di modelli complessi ai bordi liberi. Tuttavia, lontano dai bordi liberi, nella parte centrale dei laminati, non si notano differenze tra i modelli complessi e i modelli semplici.

La seconda parte di questo lavoro è dedicata, conseguentemente ai precedenti risultati, all'accoppiamento dei modelli cinematici incompatibili. L'utilizzo di costosi modelli complessi è ridotto a delle zone locali, mentre il resto della struttura viene modellizzato con dei modelli semplici ed economici dal punto di vista dei costi di computerizzazione. La eXtended Variational Formulation (XVF) è stata identificata come l'approccio migliore per l'accoppiamento dei modelli cinematicamente eterogenei, ma dimensionalmente omogenei. Per il fatto che la XVF usa una configurazione senza sovrapposizione delle diverse zone locali e globali, gli sforzi addizionali per creare l'accoppiamento sono limitati. Inoltre la XVF offre la possibilità di addattare le condizioni imposte all'interfaccia tra le zone utilizzando un singolo parametro scalare. Si dimostrerà quindi che, per il problema di dimensionalità omogenea, solo due condizioni possono essere imposte da questo parametro. Una è in accordo con le condizioni rigorose imposte dai classici Multi Point Constraints (MPC) e la seconda è creata da condizioni deboli. È dimostrato in particolar modo che l'ultima permette di ridurre la zona usando dei modelli complessi senza perdere la precisione locale. Essendo la prima applicazione di questa formulazione per dei problemi compositi, è stato identificato il bisogno di un nuovo operatore di accoppiamento. È proposta quindi una nuova formula che viene testata e la cui robustezza sarà valutata.

# Contents

<b>Abstract</b>	<b>ii</b>
<b>Contents</b>	<b>viii</b>
<b>1 Local Effects in Composite Structures</b>	<b>1</b>
1.1 Framework of the present work . . . . .	1
1.2 Heterogenous Structures . . . . .	2
1.3 The Free Edge Problem in Bending . . . . .	5
1.4 Estimation based on the Classical Lamination Plate Theory . . . . .	9
1.5 Modelling Methods for Free-Edge Problems . . . . .	11
1.5.1 Semi-Analytical Methods . . . . .	12
1.5.2 Finite Element Methods . . . . .	13
1.5.3 Comparison of Extension and Bending . . . . .	14
1.5.4 Comparison of Methods . . . . .	15
1.6 Scope of this Work . . . . .	15
<b>2 Boundary Value Problems and their Numerical Approaches</b>	<b>18</b>
2.1 Boundary Value Problem . . . . .	18
2.2 Variational Statements . . . . .	19
2.2.1 Principle of Virtual Displacements . . . . .	19
2.2.2 Reissner's Mixed Variational Theorem . . . . .	21
2.3 Reduced Models for Composite Plates . . . . .	22
2.3.1 Unified Formulation for Two Dimensional Plate Structures .	22
2.3.1.1 Equivalent Single Layer Models . . . . .	24
2.3.1.2 Layer Wise Theories . . . . .	25
2.4 FE Approximations for CUF Plate Models . . . . .	27
2.4.1 FE Approximations for the PVD case . . . . .	27
2.4.2 FE Approximations for the RMVT case . . . . .	27
2.4.3 Assembling Strategy . . . . .	28
2.4.3.1 Equivalent Single Layer Assembly . . . . .	28
2.4.3.2 Layerwise Assembly . . . . .	28
<b>3 Free Edge Effects of Composites in Plate Structures</b>	<b>31</b>
3.1 Free Edge Effects due to Extension . . . . .	31

3.1.1	Validation of the Models . . . . .	31
3.1.1.1	Cross-Ply Laminates . . . . .	32
3.1.1.2	Angle-Ply Laminates . . . . .	38
3.1.1.3	Quasi-Isotropic Laminates . . . . .	40
3.1.2	Mesh Sensitivity . . . . .	42
3.1.3	Influence of through the thickness refinement . . . . .	46
3.1.4	Assessment of the Order of Singularity . . . . .	50
3.1.4.1	Power Law Representation . . . . .	50
3.1.4.2	Assessemnt . . . . .	56
3.2	Free Edge Effects due to Bending . . . . .	63
3.2.1	Convergence Study . . . . .	63
3.2.2	Validation of Models . . . . .	70
3.2.3	Lay-Up Sensitivity . . . . .	74
3.2.3.1	Angle-Ply Laminates . . . . .	74
3.2.3.2	Cross-Ply Laminates . . . . .	79
3.2.3.3	Quasi-Isotropic Laminates . . . . .	84
3.3	On the Difference between Bending and Extension . . . . .	92
3.4	Conclusion . . . . .	97
<b>4</b>	<b>System Reduction via Model Coupling</b>	<b>99</b>
4.1	Literature Overview . . . . .	99
4.1.1	Differentiation of Techniques . . . . .	99
4.1.1.1	Non Overlapping Techniques . . . . .	100
4.1.1.2	Partial Overlap . . . . .	103
4.1.1.3	Complete Overlap . . . . .	104
4.1.2	Comparison of methods . . . . .	105
4.2	Modeling of One Dimensional Structures . . . . .	108
4.2.1	Kinematical Models . . . . .	108
4.2.1.1	Euler-Bernoulli Theory . . . . .	109
4.2.1.2	Timoshenko Theory . . . . .	109
4.2.1.3	Touratier Sinus Kinematics . . . . .	110
4.2.1.4	Touratier Sinus Theory with Transverse Normal Effect . . . . .	110
4.2.1.5	Comparison of kinematical models . . . . .	110
4.3	eXtended Variational Formulation for One Dimensional Approaches	111
4.3.1	eXtended Variational Formulation (XVF) . . . . .	111
4.3.1.1	Problem Formulation . . . . .	111
4.3.1.2	XVF Dual Products . . . . .	113
4.3.1.3	About the Choice of $\gamma$ in XVF . . . . .	117
4.3.1.4	Finite Element Formulation of XVF . . . . .	119
4.4	Unification of Approaches using the XVF . . . . .	119
4.4.1	The Arlequin Method without Overlap . . . . .	119
4.4.2	Penalty Technique . . . . .	121
4.5	Numerical Study of One Dimensional Structures . . . . .	122

4.5.1	Assessment of Models . . . . .	123
4.5.2	Homogen Beam Test . . . . .	129
4.5.2.1	One Interface . . . . .	129
4.5.2.2	Two Interfaces . . . . .	137
4.5.3	Layered Structures . . . . .	142
4.5.3.1	Modified Coupling Operator . . . . .	142
4.5.3.2	Sandwich Structure . . . . .	145
4.6	Conclusion . . . . .	151
<b>5</b>	<b>Conclusion and Outlook</b>	<b>152</b>
5.1	Conclusion . . . . .	152
5.2	Outlook . . . . .	154
<b>A</b>	<b>Arlequin Method by Ben Dhia</b>	<b>161</b>
A.1	The Classical Arlequin Method with Overlap . . . . .	161
A.2	Arlequin System in Finite Element Method . . . . .	163
<b>B</b>	<b>Coupling of Sinus <math>z^2</math> with Timoshenko Theory</b>	<b>165</b>
B.1	Projection of Sinus $z^2$ into Tmoshenko model . . . . .	165
B.2	Dual products of Sinus $z^2$ coupled with Tmoshenko model . . . . .	166
<b>C</b>	<b>FE Approximations for One Dimensional Structures</b>	<b>169</b>
C.1	Constitutive Law for One Dimensional Structures . . . . .	169
C.2	Geometric and Mechanical Relations for One Dimensional Structures	170
C.3	Interpolation for Euler Bernoulli Theory . . . . .	171
C.4	Interpolation for Timoshenko Theory . . . . .	171
C.5	Interpolation for Sinus $z^2$ Theory . . . . .	171
<b>D</b>	<b>FE Code Implementation for One Dimensional Structures</b>	<b>175</b>
D.1	The DATA file . . . . .	175
D.2	The Geometry file NOMGEO . . . . .	179
D.3	The Material Stacking file MATEMP . . . . .	181
<b>E</b>	<b>ABAQUS Implementation of CUF Elements</b>	<b>183</b>
E.1	The Problem Statement . . . . .	183
E.2	The FE Approximation . . . . .	184
E.3	Post-Procesing . . . . .	186

# List of Figures

1.1	Layer stacking order and orientation . . . . .	3
1.2	Interface of two adjacent layers . . . . .	4
1.3	Configuration of a symmetric laminated plate . . . . .	5
1.4	Bending of a simply-supported plate under a uniform pressure load . . . . .	6
1.5	Deformation behaviour of unbounded plies of a $[0, 90]_s$ cross-ply laminate under uniform pressure load . . . . .	7
1.6	Compatibility condition at the interface between two layers . . . . .	7
1.7	Stress distribution from the plates middle towards the free edge . . . . .	8
2.1	Coordinate system of a plate structure . . . . .	23
2.2	Displacement $\mathbf{u}$ and transverse stresses $\sigma_n$ for (a) and ED2, (b) EDz2 and (c) EM2 model . . . . .	25
2.3	Displacement $\mathbf{u}$ and transverse stresses $\sigma_n$ for (a) and LD2, (b) LM2 model . . . . .	26
2.4	Assembly of the stiffness terms in Equivalent Single Layer description .	29
2.5	Assembly of Top and Bottom DOF in Layerwise Formulation . . . . .	30
3.1	Extension: $\sigma_{zz}$ at $(x = 0, y = b, z)$ for $[0, 90]_s$ using RMVT & PVD . .	34
3.2	Extension: $\sigma_{zz}$ at $(x = 0, y, z = \frac{h}{4})$ for $[0, 90]_s$ using RMVT & PVD .	35
3.3	Extension: $\sigma_{zz}$ at $(x = 0, y = b, z)$ for $[90, 0]_s$ using RMVT & PVD . .	36
3.4	Extension: $\sigma_{zz}$ at $(x = 0, y, z = \frac{h}{4})$ for $[90, 0]_s$ using RMVT & PVD .	37
3.5	Extension: $\sigma_{xz}$ at $(x = 0, y = b, z)$ for $[\pm 45]_s$ using RMVT & PVD . .	38
3.6	Extension: $\sigma_{xz}$ at $(x = -a, y, z = \frac{h}{4})$ for $[\pm 45]_s$ using RMVT & PVD .	39
3.7	Extension: $\sigma_{zz}$ at $(x = -a, y = b, z)$ for $[90, 0, \pm 45]_s$ using RMVT & PVD . .	40
3.8	Extension: $\sigma_{xz}$ at $(x = 0, y, z = \frac{3h}{8})$ for $[\pm 45, 0, 90]_s$ using RMVT & PVD . .	41
3.9	Principle of the regularly and continuously refined in-plane mesh ( <i>I</i> ) . .	42
3.10	Extension: sensitivity of regular meshes of $\sigma_{xz}$ at $(x = 0, y = b, z)$ for $[\pm 45]_s$ using LM4 & LD4 . .	43
3.11	Extension: sensitivity of regular meshes on $\sigma_{zz}$ at $(x = 0, y, z = \frac{h}{4})$ for $[0, 90]_s$ using LM4 & LD4 . .	44
3.12	Principle of partly refinement through width for mesh ( <i>II</i> ) . . . . .	44

3.13	Extension: sensitivity of refined meshes of $\sigma_{zz}$ at $(x = 0, y = b, z)$ for $[0, 90]_s$ using LM4 & LD4 . . . . .	45
3.14	Extension: sensitivity of $N_{ml}$ for $\sigma_{xz}$ at $(x = 0, y, z = \frac{h}{4})$ for $[\pm 45]_s$ using LM4 & LD4 . . . . .	47
3.15	Extension: Confrontation of regular and irregular refined meshes; $\sigma_{zz}$ at $(x = 0, y, z = \frac{h}{4})$ for $[0, 90]_s$ using LM4 & LD4 . . . . .	48
3.16	Extension: Confrontation of regular and irregular refined meshes; $\sigma_{zz}$ at $(x = 0, y = b, z)$ for $[0, 90]_s$ using LM4 & LD4 . . . . .	48
3.17	Extension: mesh sensitivity of $\sigma_{zz}$ at $(x = 0, y, z = \frac{h}{4})$ for $[0, 90]_s$ using a generalized plain strain model within Ansys . . . . .	49
3.18	The distance $r$ is measured from the free edge along the plate width and at the layers interface, $(\beta = 0)$ . . . . .	51
3.19	Stress representation using the power law; using: $\alpha_1 < \alpha_2, A_1 < A_2$ . . . . .	51
3.20	Extension: width distribution of $\sigma_{xz}$ ; application of several irregular distributed mathematical layer per physical layer using LD4 for the $[\pm 45]_s$ laminate . . . . .	53
3.21	Extension: mesh sensitivity of $\sigma_{zz}$ at $(x = 0, y, z = \frac{h}{4})$ for $[0, 90]_s$ using an Ansys Quasi three-dimensional model . . . . .	54
3.22	Quality of fit of $\sigma_{xz}$ according to power law representation for the $[\pm 45]_s$ laminate at $(x = 0, y, z = \frac{h}{4})$ . . . . .	55
3.23	Assessment of power law fitting parameters: stress $\sigma_{xz}$ for the $[\pm 45]_s$ laminate at $(x = 0, y, z = \frac{h}{4})$ . . . . .	57
3.24	Denomination of the interfaces for the quasi-isotropic laminates . . . . .	60
3.25	Bending: $\bar{\sigma}_{zz}$ at $(x = 0, y = b, z)$ for $[0, 90]_s$ using LM4 . . . . .	64
3.26	Bending: $\bar{\sigma}_{zz}$ at $(x = 0, y = b, z)$ for $[0, 90]_s$ using LD4 . . . . .	65
3.27	Bending: oscillations in $\bar{\sigma}_{zz}$ at $(x = 0, y = b, z)$ for $[0, 90]_s$ using RMVT . . . . .	65
3.28	Bending: oscillations in $\bar{\sigma}_{zz}$ at $(x = 0, y = b, z)$ for $[0, 90]_s$ using PVD . . . . .	66
3.29	Bending: $\bar{\sigma}_{yz}$ at $(x = 0, y, z = \frac{h}{4})$ for $[0, 90]_s$ using RMVT . . . . .	67
3.30	Bending: $\bar{\sigma}_{yz}$ at $(x = 0, y, z = \frac{h}{4})$ for $[0, 90]_s$ using PVD . . . . .	68
3.31	Bending: convergence for different mathematical layers of $\sigma_{zz}$ in $[0, 90]_s$ laminate using LM4 and LD4 . . . . .	69
3.32	Bending: $\bar{\sigma}_{zz}$ at $(x = 0, y = b, z)$ for $[0, 90]_s$ using RMVT & PVD . . . . .	70
3.33	Bending: $\bar{\sigma}_{xz}$ at $(x = a, y = b, z)$ for $[0, 90]_s$ using RMVT & PVD . . . . .	71
3.34	Bending: $\bar{\sigma}_{yz}$ with upper Figure at $(x = 0, y, z = 0)$ and lower Figure at $(x = 0, y, z = \frac{h}{4})$ for $[0, 90]_s$ using RMVT & PVD . . . . .	71
3.35	Bending: $\bar{\sigma}_{xz}$ at $(x = -a, y = b, z)$ for $[90_3, 0]$ using RMVT & PVD . . . . .	72
3.36	Bending: $\bar{\sigma}_{zz}$ at $(x = 0, y = b, z)$ for $[90_3, 0]$ using RMVT & PVD . . . . .	73
3.37	Bending: $\bar{\sigma}_{zz}$ with upper Figure at $(x = 0, y, z = \frac{h}{4})$ and lower Figure at $(x = 0, y, z = 0)$ for $[90_3, 0]$ using RMVT & PVD . . . . .	73
3.38	Bending: $\sigma_{xz}$ at $(x = 0, y = b, z)$ for $[\pm 45]_s$ using RMVT & PVD LW models . . . . .	75
3.39	Bending: $\sigma_{xz}$ at $(x = 0, y = b, z)$ for $[\pm 45]_s$ using RMVT & PVD ESL models . . . . .	76

3.40	Bending: $\sigma_{xz}$ at $(x = 0, y = b, z)$ for $[\pm 45]_s$ using RMVT & PVD ESL Zig-Zag models . . . . .	76
3.41	Bending: $\sigma_{xz}$ at $(x = 0, y, z = \frac{h}{4})$ for $[\pm 45]_s$ using RMVT & PVD . . .	78
3.42	Bending: $\sigma_{zz}$ at $(x = 0, y = b, z)$ for $[0, 90]_s$ using RMVT & PVD . . .	80
3.43	Bending: $\sigma_{zz}$ at $(x = 0, y, z = \frac{h}{4})$ for $[0, 90]_s$ using RMVT & PVD . .	81
3.44	Bending: $\sigma_{zz}$ at $(x = 0, y = b, z)$ for $[90, 0]_s$ using RMVT & PVD . . .	82
3.45	Bending: $\sigma_{zz}$ at $(x = 0, y, z = \frac{h}{4})$ for $[90, 0]_s$ using RMVT & PVD . .	83
3.46	Bending: $\sigma_{zz}$ at $(x = 0, y = b, z)$ for $[\pm 45, 0, 90]_s$ using RMVT & PVD	86
3.47	Bending: $\sigma_{zz}$ at $(x = 0, y = b, z)$ for $[90, 0, \pm 45]_s$ using RMVT & PVD	86
3.48	Bending: $\sigma_{xz}$ at $(x = 0, y = b, z)$ for $[\pm 45, 0, 90]_s$ using RMVT & PVD	87
3.49	Bending: $\sigma_{xz}$ at $(x = 0, y = b, z)$ for $[90, 0, \pm 45]_s$ using RMVT & PVD	87
3.50	Bending: $\sigma_{xz}$ at $(x = 0, y, z = \frac{h}{8})$ for $[\pm 45, 0, 90]_s$ using RMVT & PVD	88
3.51	Bending: $\sigma_{xz}$ at $(x = 0, y, z = \frac{3h}{8})$ for $[\pm 45, 0, 90]_s$ using RMVT & PVD	88
3.52	Bending: $\sigma_{zz}$ at $(x = 0, y, z = \frac{3h}{8})$ for $[90, 0, \pm 45]_s$ using RMVT & PVD	89
3.53	Bending: $\sigma_{zz}$ at $(x = 0, y, z = \frac{h}{4})$ for $[90, 0, \pm 45]_s$ using RMVT & PVD	89
3.54	Extension: fitted transverse stresses close to the free edge of the $[\pm 45, 0, 90]_s$ using LD4 . . . . .	94
3.55	Bending: fitted transverse stresses close to the free edge of the $[\pm 45, 0, 90]_s$ using LD4 . . . . .	95
3.56	Extension: fitted transverse stresses close to the free edge of the $[90, 0, \pm 45]_s$ using LD4 . . . . .	95
3.57	Bending: fitted transverse stresses close to the free edge of the $[90, 0, \pm 45]_s$ using LD4 . . . . .	96
4.1	Domain arrangement: no (a), partial (b) or complete overlap (c) . . . . .	100
4.2	Continuous spline formulation based on an independent discretization to pass between incompatible domain repartitions . . . . .	101
4.3	MPC enforces complex model to be compatible with simple model . . . . .	103
4.4	Principle of the scale descending Zooming Method . . . . .	105
4.5	Coordinate system of a beam structure . . . . .	108
4.6	Deformation of Euler-Bernoulli Theory (a), Timoshenko Theory (b), Si- nus Theory (c) and Sinus $z^2$ Theory (d). . . . .	111
4.7	$\Omega_c$ and $\Omega_s$ with common interface $\Gamma_a$ in a Beam Structure . . . . .	112
4.8	Arrangements of domains in the Arlequin Method . . . . .	120
4.9	Test configuration of a beam subjected to a patch load at the beams center	123
4.10	Homogeneous Material: deflection of the different Kinematics; $s = 5$ .	126
4.11	Homogeneous Material: $\bar{\sigma}_{13}$ through thickness $z$ for different kinemat- ics; $s = 5$ . . . . .	126
4.12	Sandwich Material: deflection of the different kinematics; $s = 10$ . . . .	128
4.13	Sandwich Material: $\bar{\sigma}_{13}$ through thickness $z$ for different kinematics; $s = 10$ . . . . .	128
4.14	One interface: configuration of simple and complex domains . . . . .	130
4.15	Homogeneous Material: deflection for $\gamma = 1$ ; $\Gamma_a$ at $\bar{x} = 2.5$ ; $s = 5$ . .	130
4.16	Principal of refinement zone corresponding several times the height . .	132

4.17	Homogeneous Material: (a): $\bar{\sigma}_{13}$ for $\Omega_c = 0.5 \cdot h$ ; (b): $\bar{\sigma}_{13}$ for $\Omega_c = 1 \cdot h$ ; refined at support; $s = 5$	135
4.18	Propagation of $\bar{u}_3$ over length $x$ for cancelled double conditions; $s = 5$	136
4.19	Position of refined zones in beam model	137
4.20	Homogenous Material: $\bar{\sigma}_{11}$ at $z = -\frac{h}{2}$ with the different kinematical models; $s = 10$	138
4.21	Homogeneous Material: $\bar{\sigma}_{13}$ at $z = 0$ with the different kinematical models; $s = 10$	139
4.22	Homogenous Material: $\bar{\sigma}_{11}$ and $\bar{\sigma}_{13}$ for different positions of $\Gamma_a$ ; $\gamma = 0$ ; $s = 10$	140
4.23	Homogenous Material: $\bar{\sigma}_{11}$ and $\bar{\sigma}_{13}$ for different discretisations; $\gamma = 0$ ; $s = 10$	140
4.24	Homogenous Material: $\bar{\sigma}_{11}$ and $\bar{\sigma}_{13}$ ; $\gamma = 0$ ; $s = 1000$	141
4.25	Sandwich Beam Configuration with Local Pressure Load	142
4.26	Sandwich Material: $\bar{\sigma}_{13}$ over length $x$ for $\gamma = 1$ ; $1000 \cdot C_{11_{core}} = C_{11_{face}}$ ; $s = 10$	143
4.27	Sandwich Material: $\bar{\sigma}_{11}$ at $z = -\frac{h}{2}$ with Euler combinations over $x$ ; $s = 10$	146
4.28	Sandwich Material: $\bar{\sigma}_{13}$ at $z = 0$ with Timoshenko and Euler combinations over $x$ ; $s = 10$	146
4.29	Sandwich Material: (a): $\bar{\sigma}_{11}$ with Euler; (b): $\bar{\sigma}_{13}$ with Timoshenko through thickness $z$ ; $s = 10$	147
4.30	Sandwich Material: Error rate on $\bar{\sigma}_{11}$ for increasing number of simple elements; $s = 10$	149
4.31	Sandwich Material: Error rate on $\bar{\sigma}_{13}$ for increasing number of simple elements; $s = 10$	149
4.32	Sandwich Material: $\bar{\sigma}_{13}$ over length $x$ with 16 Timoshenko elements; $s = 10$	150
A.1	Configuration with partial overlap for Arlequin Method	162
C.1	(a): Euler Bernoulli - ; (b): Timoshenko - ; (c): Sinus $z^2$ beam element	174
E.1	Creating the mechanical problem via a Plug-Inn using pre-defined cases	184
E.2	The FE mesh is defined inside ABAQUS itself	185

# List of Tables

1.1	Techniques used to calculate free-edge effects . . . . .	16
2.1	Capabilities and characteristics of the different CUF models . . . . .	27
3.1	Single Layer Material properties . . . . .	32
3.2	Extension: Convergence of $\alpha_{xz}$ and $ A_{xz} $ for the $[\pm 45]_s$ lay-up . . . . .	52
3.3	Extension: $\alpha_{xz}$ and $ A_{xz} $ towards the $[\pm 45]_s$ lay-up . . . . .	57
3.4	Extension: Sensitivity of $\alpha_{xz}$ and $ A_{xz} $ concerning $N_{ml}$ of the $[\pm 45]_s$ lay-up . . . . .	58
3.5	Extension: $\alpha_{zz}$ and $ A_{zz} $ for the $[0, 90]_s$ and $[90, 0]_s$ lay-ups . . . . .	59
3.6	Extension: $\alpha_{xz}$ and $ A_{xz} $ as well as $\alpha_{zz}$ and $ A_{zz} $ for the $[\pm 45, 0, 90]_s$ laminate . . . . .	61
3.7	Extension: $\alpha_{xz}$ and $ A_{xz} $ as well as $\alpha_{zz}$ and $ A_{zz} $ for the $[90, 0, \pm 45]_s$ laminate . . . . .	62
3.8	Bending: Convergence of $\alpha_{zz}$ and $ A_{zz} $ for the $[0, 90]_s$ lay-up in Tahani Nosier test case . . . . .	68
3.9	Bending: load magnitude $q_0$ for the different laminates . . . . .	74
3.10	Bending: $\alpha_{ij}$ and $ A_{ij} $ for the $[\pm 45]_s$ , $[0, 90]_s$ and $[90, 0]_s$ lay-ups . . . . .	80
3.11	Bending: $\alpha_{xz}$ and $ A_{xz} $ for the $[\pm 45, 0, 90]_s$ laminate . . . . .	90
3.12	Bending: $\alpha_{zz}$ and $ A_{zz} $ for the $[90, 0, \pm 45]_s$ laminate . . . . .	91
3.13	Total number of unknowns for the four layer laminates . . . . .	98
4.1	Techniques for Coupling heterogenous Kinematics . . . . .	107
4.2	Overview of variables in the two sub-domains . . . . .	113
4.3	ANSYS meshes with PLANE82 elements for homogeneous and sandwich beams . . . . .	124
4.4	Homogeneous Material: assessment of different FE approximations . . . . .	125
4.5	Sandwich Material: assessment of different FE approximations . . . . .	127
4.6	Homogeneous Material: values of $\bar{u}_3$ , $\bar{\sigma}_{11}$ and $\bar{\sigma}_{13}$ for $\Gamma_a$ at $\bar{x} = 2.5$ , $s = 5$ . . . . .	131
4.7	Homogeneous Material: sensitivity on $\bar{u}_3$ ; refined with Sin-z2 at each of beam ends separately , $s = 5$ . . . . .	133
4.8	Homogeneous Material: sensitivity on $\bar{\sigma}_{11}$ ; refined with Sin-z2 at each of beam ends separately , $s = 5$ . . . . .	133

4.9	Homogeneous Material: sensitivity on $\bar{\sigma}_{13}$ ; refined with Sin-z2 at each of beam ends separately , s = 5 . . . . .	134
4.10	Sandwich Material: Lagrange Multipliers on $\Gamma_{a_1}$ at $\bar{x}_1 = 1.25$ ; Sin-z2 & Euler; $\gamma = 1$ ; s = 10 . . . . .	144
4.11	Sandwich Material: Lagrange Multipliers on $\Gamma_{a_1}$ at $\bar{x}_1 = 1.25$ ; Sin-z2 & Euler; $\gamma = 0$ ; s = 10 . . . . .	144
4.12	Sandwich Material: Lagrange Multipliers on $\Gamma_{a_2}$ at $\bar{x}_2 = 3.75$ ; Sin-z2 & Euler; without $C_{11}$ ; $\gamma = 1$ ; s = 10 . . . . .	145
D.1	DOF availability . . . . .	180
D.2	DOF constrainement for $w_0$ in Hermite 1D . . . . .	180
D.3	Element type numbers . . . . .	181
D.4	model type numbers . . . . .	181
D.5	available models for the three Element types . . . . .	181

# Nomenclature

abbreviation	meaning
BEM	Boundary Element Method
CFRP	Carbon Fibre Reinforced Plastic
CLPT	Classical Laminate Plate Theory
CUF	Carrera Unified Formulation
DOF	Degree Of Freedom
ESL	Equivalent Single Layer
FE	Finite Element
IC	Interlaminar Continuity
LW	Layer Wise
PVD	Principle of Virtual Displacements
RMVT	Reissners Mixed Variational Theorem
XVF	Extended Variational Formulation

bold letters are vectors or matrices, plain letters are scalars

variable	unit	physical meaning
$a$	[m]	plate length
$A$	[ $m^2$ ]	plate reference section
$\alpha_{mat}$	[ $-$ ]	stiffness coefficient factor
$b$	[m]	plate width
$\mathbf{B}$	[ $\frac{N}{m^2}$ ]	XVF coupling terms
$C$	[ $\frac{N}{m^2}$ ]	stiffness matrix in local reference system
$\tilde{C}$	[ $\frac{N}{m^2}$ ]	stiffness matrix in global reference system
$\delta$	[ $-$ ]	virtual operator
$\mathcal{D}$	[ $-$ ]	differential operator
$E$	[ $\frac{N}{m^2}$ ]	Young modulus
$\epsilon$	[ $-$ ]	strain tensor
$\mathcal{E}$	[m]	generalized displacement vector
$F$	[N]	force
$G$	[ $\frac{N}{m^2}$ ]	shear modulus
$\mathbf{g}$	[ $\frac{N}{mm^2}$ ]	nodal stress vector

$\Gamma$	[ - ]	boundary of surface or volume
$\Gamma_a$	[ - ]	interface between two surfaces or volumes
$\gamma$	[ - ]	XVF parameter for partition of unity
$h$	[ m ]	beam section height / plates thickness
$h_k$	[ m ]	$k - th$ layers thickness
$\mathbf{K}$	[ - ]	stiffness matrix
$l$	[ m ]	beam length
$\mathbf{N}_i$	[ - ]	matrix containing nodal shape functions
$N_{e\ x}$	[ - ]	number of elements in $x$ -direction
$N_{e\ y}$	[ - ]	number of elements in $y$ -direction
$N_{e\ z}$	[ - ]	number of elements in $z$ -direction
$N_{ml}$	[ - ]	number of mathematical layers per physical layer
$\mathbf{n}_i$	[ - ]	outward normal of sub region i
$\mathbf{n}_{\Gamma_i}$	[ - ]	outward normal of interface from region i
$\nu$	[ - ]	Poisson's ratio
$\omega$	[ - ]	rotation
$\Omega$	[ - ]	domain
$\phi$	[ - ]	rotational degree of freedom
$\psi$	[ - ]	rotation angle between layers orientation and reference system
$\bar{\mathbf{Q}}$	[ $\frac{N}{m^2}$ ]	effective stiffness matrix for plane stress assumption in global reference system
$\mathbf{q}$	[ m ]	nodal displacement vector
$q_0$	[ $\frac{N}{m^2}$ ]	surface load
$\mathbf{q}$	[ m ]	nodal displacement vector
$s$	[ - ]	slenderness ratio $\frac{l}{h}$
$S$	[ $m^2$ ]	beam's cross section
$\boldsymbol{\sigma}$	[ $\frac{N}{m^2}$ ]	stress tensor
$\boldsymbol{\sigma}_n$	[ $\frac{N}{m^2}$ ]	normal transverse stress components
$\boldsymbol{\sigma}_p$	[ $\frac{N}{m^2}$ ]	in-plane stress components
$t$	[ - ]	traction
$\mathbf{u}$	[ m ]	displacement vector
$W$	[ $Nm$ ]	work
$z^k$	[ m ]	position in stacking height of the k-th Layer
$\zeta_k$	[ - ]	dimensionless thickness coordinate

subscript	meaning
b	bottom surface of the assigned layer
k	layer index
n	normal or transverse component
p	in-plane component
s	virtual component of expansion order index
t	top surface of the assigned layer

$\tau$  component of expansion order index

superscript	meaning
c	complex subdomain containing complex kinematical model
P	degree of freedom of the Penalty method
s	simple subdomain containing simple kinematical model

# **Chapter 1**

## **Local Effects in Composite Structures**

First in this chapter, the general interest of the use of multilayered structures will be outlined first in this chapter. It is followed by introducing the additional efforts needed for modeling these types of structures, in special regarding the effects occurring at free edges. This chapter will be concluded by providing an overview on existing semi-analytical and discrete techniques in order to predict their mechanical behaviour at those free edges due to different loads, especially bending.

### **1.1 Framework of the present work**

The objective of saving energy did affect the design of transportation means in recent years, as the main objective was to reduce the overall weight of the structure. While reducing the weight, the energy needed to move or power the structure is minimized. As a consequence less powerful motors are needed and a higher energy efficiency is possible: the energy consumption is reduced and subsequently the emissions into the environment. Two main approaches are possible to reduce the weight: the first one is simple reducing the weight of the single components, while the second approach is to include different components into one by including their assigned functions into one single component with less weight than all the different components together. Both approaches have been addressed through the use of multilayered structures in the last decades. The most common representatives are composites and sandwich structures. Through their nature as being an inhomogenous structure, different mechanical effects occur compared to monolithic homogenous materials. This derives in one part from the assembly of the different layers, but also from the nature of the materials used, which might also be inhomogenous. Especially the use of anisotropic, in many cases orthotropic materials, having a predominant characteristic (ex. stiffness, damping coefficient or thermal conductivity into one direction combined with a relatively low mass) is interesting. Though the orientation of this direction the structure can be

adapted to the outer loadings. By the adaption of several layers, each layer can be assigned a specific function.

The function integration is normally carried out at the structural part level via the use of multilayered structures. Often relatively thin planar structures are obtained. This allows to use dimensional reduced models, like two-dimensional models, in order to predict the three-dimensional behaviour. Via the use of dimensional reduced models, the time and the assigned cost needed to calculate the solution of mathematical models representing the problem is reduced, too. This is a very attractive factor in the design process.

In order to reliably introduce several function into a multilayered structure and reducing the overall weight at the same time, the state of stress introduced by the outer loadings and the inner reactions of the part have to be known. Together with the design limits of the used materials, ie. fracture limits, maximal operating temperature or admissible deformations, they provide the design envelope for the part. In most cases, these design limits are only reached in local zones through high stress concentrations for example. Hence these local zones have to be reliably predicted and the concentrations have to be quantified. According to the hypothesis imposed to reduce the dimensionality, the model might not be able to fully and reliably render those local zones. For this type of structures, one of the most critical concentrations are the interlaminar stresses.

## 1.2 Heterogenous Structures

This preliminary chapter will introduce composite structures and describe one of those additionally mechanical effects, namely the free-edge effect. This chapter will conclude with a comparison of methods available to calculate and evaluate the free-edge effect in bending. Heterogenous structures are used nowadays in a wide spectrum of applications. The most common representatives are sandwich structures and laminates. Both may consist of a stacking of different layers. Each of the layers is included into the structure to fulfill a certain function. Those layers might be made of different isotropic materials, like sheet metal. One other possibility is to use the same material with oriented properties, the orthotropic materials. In the case of the sandwich structures, these orthotropic materials are mainly used in the core, where honeycomb hexagons, foams or folded papers are used. The outer layers might be metals or other orthotropic materials. The most frequently used materials nowadays are fibre reinforced plastics, like carbon fibre reinforced plastics (CFRP) and glass fibre reinforced plastics (GFRP). Especially laminates made of the last two materials have gained an interest in the last decades. Through the stacking of the layers it is possible to include the adequate layer at the needed position or orientation in the layup to properly respond or adapt to those outer influences. Through their nature as combination of different mechanical characteristics of the single layers, additional mechanical effects occur compared with a structure made of a single homogenous material.

---

In Figure 1.1, an example of a multilayered structure is given. In general a compound consists of a number of layers  $N_L$  from  $k = 1, \dots, N_L$ . For the purpose of modelling, they are assumed here to have the same dimensions in length and in width but the thickness  $h_k$  might differ. The middle plane is used as reference to describe the stacking of the compound. The mechanical properties depend on the local orientation of the layer. Therefore they have to be transformed into the system of reference, in order to include its contribution to the assembly of the complete compound. Its orientation with respect to the reference system is given by the rotation angle  $\psi_k$ . The material axes will be described by a Cartesian coordinate system, denoted by the 1, 2 and 3-axis. As the orientation varies around the  $z$ -axis, the local 3-axis will be identical with the global  $z$ -axis.

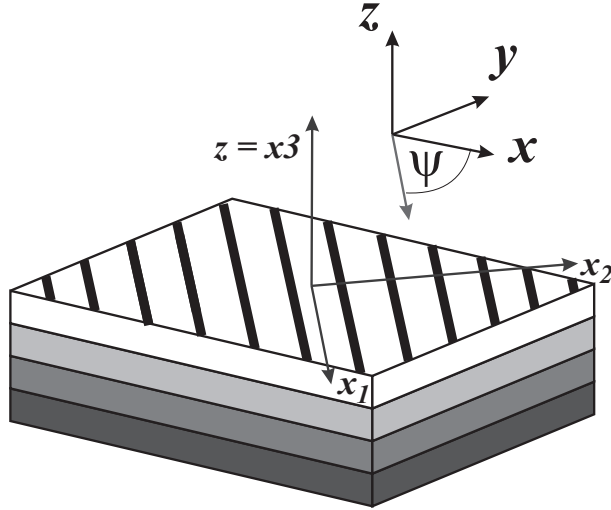


Figure 1.1: Layer stacking order and orientation

Figure 1.2 gives a reference for the notation, regarding the stacking sequence into the  $z$ -direction. In order to indicate the top surface of a layer  $k$ , it will be denoted by the subscript  $t$ , while subscript  $b$  denotes the bottom surface of the layer.

A further assumption is that all layers are perfectly bonded together. Therefore, the local displacements  $\mathbf{u}$  at the top and the bottom of two adjacent layers, have to be continuous:

$$\mathbf{u}_t^k(x, y, z_k) = \mathbf{u}_b^{k+1}(x, y, z_k) \quad \text{for } k = 1, \dots, N_L - 1 \quad (1.1)$$

The stress components can be split into two parts: the in-plane components, which will be denoted by a subscript  $p$ , and the transverse stresses, denoted by the subscript  $n$ . They are:  $\boldsymbol{\sigma}_p = (\sigma_{xx}, \sigma_{yy}, \sigma_{xy})$  and  $\boldsymbol{\sigma}_n = (\sigma_{xz}, \sigma_{yz}, \sigma_{zz})$ .

Regarding the transverse stresses, a continuity of its components has to be satisfied at the layers interface for equilibrium reason:

$$\sigma_{nt}^i = \sigma_{nb}^{i+1} \quad \text{for } i = 1, \dots, N_L - 1 \quad (1.2)$$

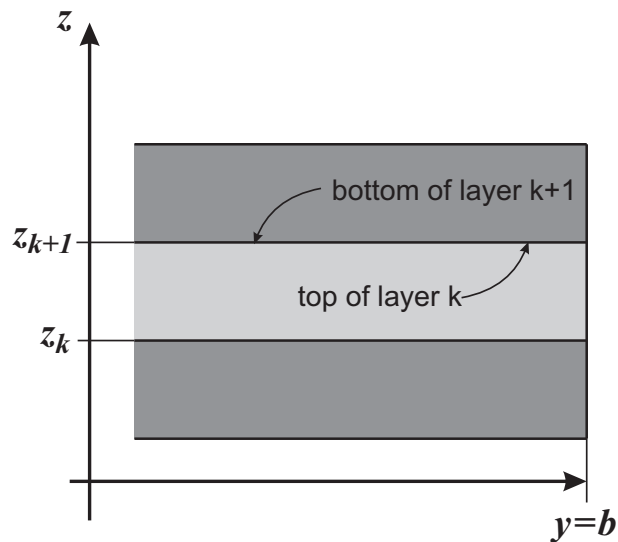


Figure 1.2: Interface of two adjacent layers

The in-plane components are not affected, they can be in fact discontinuous at the layers interface. They depend on the local in-plane elasticity of each layer, which in the global reference system is only influenced by its orientation  $\psi_k$ .

### 1.3 The Free Edge Problem in Bending

Figure 1.5 represents a cross-ply laminate consisting of four layers having the same material and the same thickness per layer  $h_k$ . Consider a  $[0/90]_s$  cross-ply laminate, where the dark grey layers represent the outer 0 degree layers, with fibres aligned in the global  $x$ -direction. In order to bend the laminate around the global  $y$ -axis, it is loaded at the top by a constant pressure load  $q_0$  and is simply supported at its short edges, as shown in Figure (1.4). Due to the uniform pressure load, a uniform curvature  $\kappa_x$  is applied along the length axis, the  $x$ -axis.

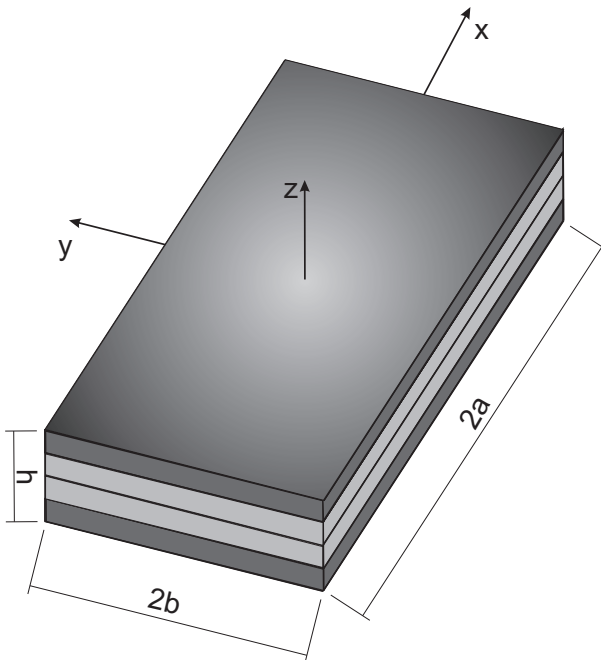


Figure 1.3: Configuration of a symmetric laminated plate

In the following, the plate is considered to be sufficiently large in length and width, in order to have stress distributions undisturbed by the boundary conditions. Through the orientation of 0 and 90 degrees, the different Poisson's ratios of each layer will provoke a different deformation behaviour in each layer. However, at the free edges of the composite plate, at any point through width and thickness, a tension free stress state is present, for which it can be stated in strong form:

$$\sigma_{yy}(x, y = \pm b, z) = \sigma_{xy}(x, y = \pm b, z) = \sigma_{yz}(x, y = \pm b, z) = 0 \quad (1.3)$$

Assuming layers which are not perfectly bounded will provoke a deformation behaviour in accordance to the orientation of the layer. This is shown in Figure 1.5, where the outermost layers, the 0 degree layers, extend more in the direction of the

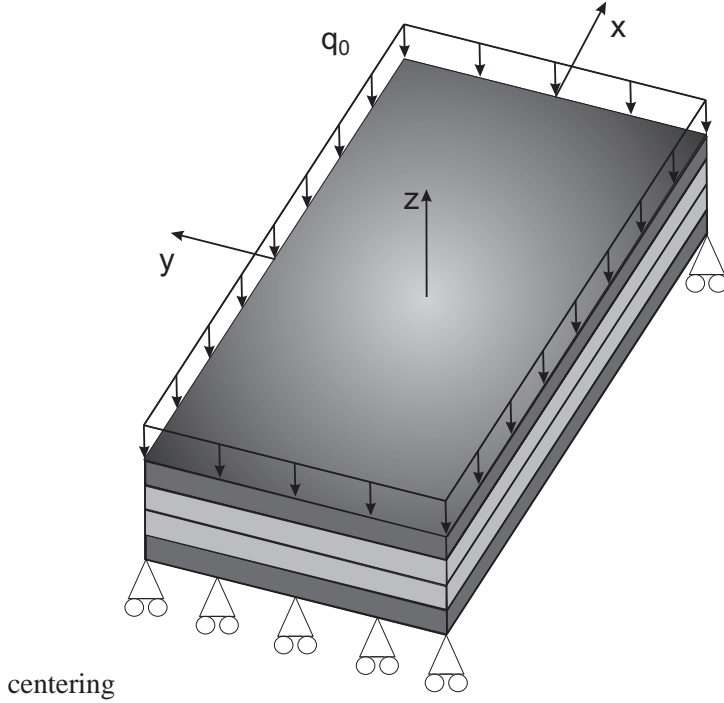


Figure 1.4: Bending of a simply-supported plate under a under uniform pressure load

$x$ -axis, while the inner 90 degree layers would extend more in the direction of the  $y$ -axis.

As stated in Equation (1.1), the displacement at the layers interfaces has to be equal due to the perfect bonding. Regarding the free edges, a normal stress  $\sigma_{yy}$  close to the edges itself is needed inside the layers to assure the continuity of the displacement component  $u_y$  at the interface between the differently orientated layers. Before it was stated that at the free edge itself, it has to vanish but also due to the symmetry of the configuration, it has to vanish at the plate's centre. Therefore the situation at the bimaterial interface has to be considered in more detail. The Poisson's ratio mismatch at the bimaterial interface influences the in-plane stress components, and the propagation of the transverse shear components. Especially the transverse shear components determine the local stress state in two adjacent layers. Figure 1.6 shows the situation for a cut through the lay-up at two adjacent layers, with the upper layer in the 0 degree orientation and the lower in the 90 degree orientation. In the Figure, both layers are shown independently. This is to highlight the role of the transverse stresses and their continuity, as given in Equation (1.2). The in-plane stress  $\sigma_{yy}$  is induced through a non vanishing interfacial transverse shear stress  $\sigma_{yz}$  which is assuring the actual connection between the two layers at the bimaterial interface. The transverse shear stress has to be present at the layers interface close to the free edge, which is pictured in the left half of Figure 1.6.

The transverse shear stress  $\sigma_{yz}$  is vanishing at the free edge and due to symmetry

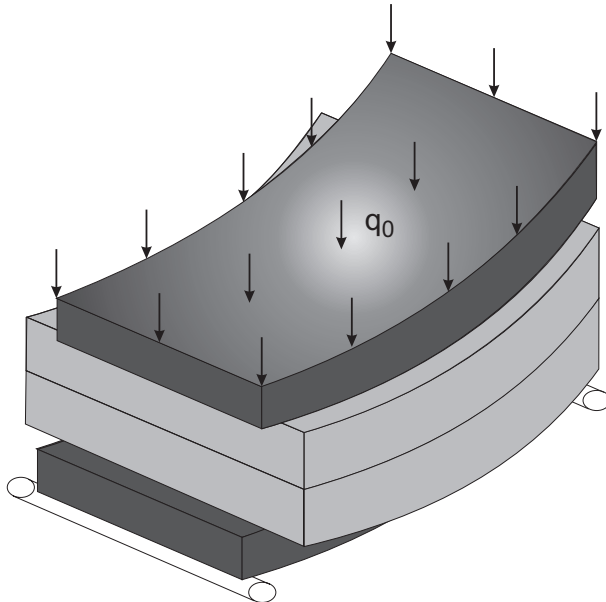


Figure 1.5: Deformation behaviour of unbounded plies of a  $[0, 90]_s$  cross-ply laminate under uniform pressure load

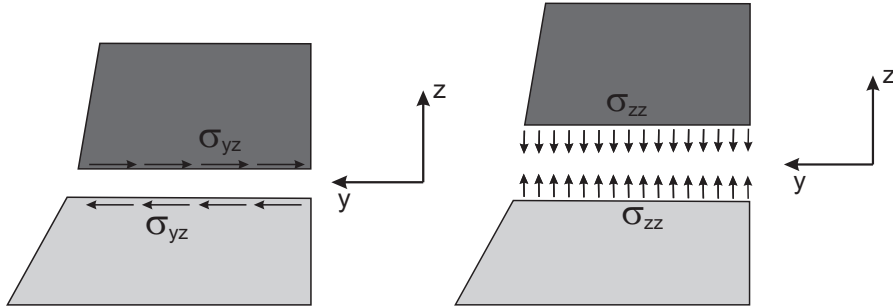


Figure 1.6: Compatibility condition at the interface between two layers

conditions it has to vanish also at the plate's middle. Therefore it has to be non-zero at some portion of the width close to the free edge. A presence of an interlaminar transverse shear stress leads to an imbalance in moments around the length-axis. Therefore the transverse normal stress  $\sigma_{zz}$  have to balance the gradients occurring in the transverse shear stress. This is shown in the right half of Figure 1.6. A typical distribution of both stresses across the width is given in Figure 1.7. A localized strong gradient can be identified in the zone close to the free edge. As described, the transverse shear stress  $\sigma_{yz}$  is bounded at the free edge. However, the transverse normal stress  $\sigma_{zz}$  is unbounded as pictured and is expected to adopt to a rather strong gradient. This rise is rather sharp with the tendency towards a peak value. With a

refinement of the mesh used for FE calculations, the maximum values of the transverse normal stress is expected to rise. If they do not converge to a finite value with the refinement of the mesh, a stress singularity is present. This is expected to be the case of the laminates under consideration.

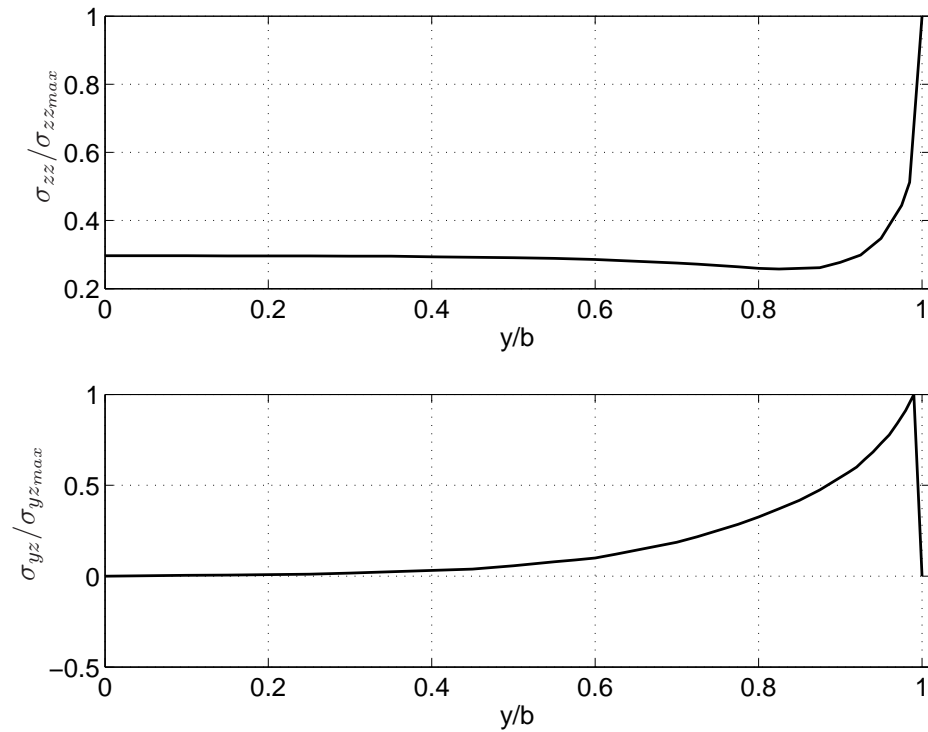


Figure 1.7: Stress distribution from the plates middle towards the free edge

## 1.4 Estimation based on the Classical Lamination Plate Theory

Herakovich [29] as well as Mittelstedt and Becker [49] gave an three steps approach to determine the mechanical effects occurring. Both assumed a planar state of stress away from the free edge, so the Classical Laminated Plate Theory (CLPT) holds true. The CLPT does predict only the in-plane components  $\sigma_{xx}$ ,  $\sigma_{yy}$  and  $\sigma_{xy}$ . The remaining three transverse components are neglected due to the simple kinematic hypothesis it is based on and have to be recovered via the equilibrium equations. Via the CLPT a first estimate can be done for the occurring inner efforts introduced by the free-edge effect.

In order to solve the system of unknowns, the stresses are linked with the deformation, ie. the strain, via Hooke's law. The stiffness moduli  $C_{ij}^k$  are used to describe the orientated stiffness components of a single layer in the local material reference system:

$$\begin{bmatrix} \sigma_{xx}^k \\ \sigma_{yy}^k \\ \sigma_{zz}^k \\ \sigma_{xz}^k \\ \sigma_{yz}^k \\ \sigma_{xy}^k \end{bmatrix} = [\mathbf{C}^k] \begin{bmatrix} \epsilon_{xx}^k \\ \epsilon_{yy}^k \\ \epsilon_{zz}^k \\ \epsilon_{xz}^k \\ \epsilon_{yz}^k \\ \epsilon_{xy}^k \end{bmatrix} \quad (1.4)$$

where the stiffness matrix reads for an arbitrarily orientated orthotropic material:

$$[\mathbf{C}^k] = \begin{bmatrix} C_{11}^k & C_{12}^k & C_{13}^k & 0 & 0 & C_{16}^k \\ C_{21}^k & C_{22}^k & C_{23}^k & 0 & 0 & C_{26}^k \\ C_{31}^k & C_{32}^k & C_{33}^k & 0 & 0 & C_{36}^k \\ 0 & 0 & 0 & C_{44}^k & C_{45}^k & 0 \\ 0 & 0 & 0 & C_{54}^k & C_{55}^k & 0 \\ C_{16}^k & C_{26}^k & C_{36}^k & 0 & 0 & C_{66}^k \end{bmatrix} \quad (1.5)$$

Note that  $C_{16}^k = C_{26}^k = C_{36}^k = C_{45}^k = C_{54}^k = 0$  for an orthotropic material in the local material reference system.

According to the orientation angle  $\psi_k$ , the stiffness coefficients of each layer can be transferred into the global reference system. They will be denoted as  $\bar{C}^k$ . Further, by the assumptions of a planar state of stress, the material stiffness coefficients are the reduced stiffness coefficients  $\bar{Q}^k$ , which are according to Herakovich [29] :

$$\bar{Q}_{ij} = \bar{C}_{ij}^k - \frac{\bar{C}_{i3}^k \bar{C}_{3j}^k}{\bar{C}_{33}^k} \quad \text{with } (i, j = 1, 2, 6) \quad (1.6)$$

The compact Hooke's law for the planar state of stress is

$$\begin{bmatrix} \sigma_{xx}^k \\ \sigma_{yy}^k \\ \sigma_{xy}^k \end{bmatrix} = \begin{bmatrix} \bar{Q}_{11}^k & \bar{Q}_{12}^k & \bar{Q}_{16}^k \\ \bar{Q}_{12}^k & \bar{Q}_{22}^k & \bar{Q}_{26}^k \\ \bar{Q}_{16}^k & \bar{Q}_{26}^k & \bar{Q}_{66}^k \end{bmatrix} \begin{bmatrix} \epsilon_{xx}^k \\ \epsilon_{yy}^k \\ \epsilon_{xy}^k \end{bmatrix} \quad (1.7)$$

Due to the planar state of stress, while using the CLPT, the transverse components have to be recovered from the in-plane components via the integration of the equilibrium equations.

In Figure 1.6 the appearance of the transverse shear stress  $\sigma_{yz}$  was introduced. The effort excerpted by this stress component can be expressed via a force per unit length, the shear force  $F_{yz}(z^*)$ . This shear force  $F_{yz}(z^*)$  has to balance the occurring inner distributions of the in-plane stress component  $\sigma_{yy}$ . It can be stated for a given position in the laminate  $z^*$ :

$$F_{yz}(z^*) = \int_{y^*}^b \sigma_{yz}(z^*) dy = - \int_{z^*}^{\frac{h}{2}} \sigma_{yy}(y^*) dz = -F_{yy}(y^*) \quad (1.8)$$

The component  $\sigma_{yz}$  is nonzero over at least some portion of  $0 < y < b$  and far from the plate's centre. Through the thickness, linear stress distributions of  $\sigma_{yy}(z)$  are defined by the CLPT per layer from Equation (1.8). This leads to a quadratic force distribution through the thickness of each layer. It can be stated for a given position at the interface  $z^* = z_k$ :

$$F_{yz}(z^*) = \int_0^b \sigma_{yz}(z^*) dy = \sum_{j=k}^{N_l} \left( \bar{Q}_{12}^j \kappa_x \frac{z_j^2 - z_{j-1}^2}{2} \right) \quad (1.9)$$

Further to the balance of the inner forces, a balance of the inner moments has to be given. The moment about the  $x$ -axis, exerted by the in-plane stress  $\sigma_{yy}$ , has to be balanced by a transverse normal stress  $\sigma_{zz}$ :

$$\int_0^b \sigma_{zz}(z^*) y dy = - \int_{z^*}^{\frac{h}{2}} \sigma_{yy}(z - z^*) dz \quad (1.10)$$

Due to the quadratic shear force distribution per layer, a cubic moment distribution is present at each layer:

$$M_z(z^*) = \sum_{j=k}^{N_l} \left[ \bar{Q}_{12}^j \kappa_x \left( \left( \frac{z_j^3 - z_{j-1}^3}{3} \right) - z^* \left( \frac{z_j^2 - z_{j-1}^2}{2} \right) \right) \right] \quad (1.11)$$

For other laminate orientations, like angle-ply [45/−45]<sub>s</sub> laminate, the effects are similar, but the magnitudes occurring are different due to the coupled behaviour in the  $x$  and  $y$ -axis. The in-plane shear  $\sigma_{xy}$  will become important and disturbs the use of symmetry conditions. The before stated equilibrium conditions from Equations (1.8) to (1.10) of the cross-ply laminates are expanded by the additional influence of the in-plane shear through their link via the transverse shear components. A more pronounced free-edge effect is hence expected. For other laminates and loads the

same phenomena will occur.

As shown, while using the CLPT, the computation of the important transverse stresses is based on the equilibrium equations. Only a planar state of stress is assumed by the CLPT directly. Through this mathematical coupling of in-plane and transverse stresses, the CLPT does generally underestimate the stresses occurring next to the free edge, as different authors showed in [18] and [49]. Therefore other methods being capable of predicting inter- and intralaminar stresses with high gradients in local areas are needed.

## 1.5 Modelling Methods for Free-Edge Problems

Two different classes of methods can be identified for describing and quantifying the free-edge effect in composites. These methods are based on continuum mechanics, which will deliver a closed form analytical solution as well as discrete solutions provided for example by the Finite Element Method. Some of the most important works will be described hereafter and a final comparison of those methods about their common aspects and differences will be given in Table 1.1.

For all methods described here, the general modelling approach is stated. The approach often depends on the specific problem treated, while not all the authors equally considered the same loading. Another very important aspect is the representation of the geometry. For a sufficiently long plate, the free-edge effects become independent from the longitudinal coordinate  $x$ . This is valid in extension, but not for all types of bending. This helps therefore to reduce the effort for modelling of only some problems. Therefore several authors reduced the three-dimensional problem to a quasi-3D dimensional, using just a representation of the axially strained cross section of the lay-up. Another common approach to reduce the dimensionality, is the type of the description of the mechanical behaviour of the compound. The mechanical behaviour can be described in a rather global way in order to ease the calculation efforts or, on the contrary, a detailed modelling of the behaviour for accurate local response. The first aspect of easing the calculation effort is covered by the so-called Equivalent Single Layer (ESL) techniques. To reduce the overall unknowns and hence the calculation efforts, the lay-up is considered as a single layer, having equivalent properties. In contrast to this technique, Layer-wise (LW) approaches model each layer independently and hence the number of unknowns increases. The increase in the demand for resources is justified by the capacity of this method to locally provide very accurate intralaminar results. The last common aspect is about the solution types. In order to ease the complexity of the solution of the three dimensional boundary value problem, different kinematical hypothesis are assumed. According to the modeling approach, they are expressed via different unknowns. They will be described, irrespectively of how the solution is achieved. The solution itself is calculated either in iterative steps, which improve the overall solution, or as a direct solution in one single step.

Pipes and Pagano [57] were the first to describe the nature and occurrence of free-

edge effects in tension. Only a two dimensional geometry was used, representing the cross section of the lay-up. The solution was gained via discrete material points in a finite difference scheme assuming bilinear approximation of the displacements. Since this pioneering work, significant scientific attention was put into the accurate calculation and prediction of the stress singularities at the free edge. A good overview about the works concerning free-edge effects in extension was given by Mittelstedt and Becker [49]. Therefore, in this overview the focus is mainly concentrated on free-edge effects in bending.

### 1.5.1 Semi-Analytical Methods

Kassapoglou [37] provided a generalized approach of some previous works done by Saeger and Lagace [46] as well as Kassapoglou and Lagace [38], [39]. His approach is capable to treat problems under in-plane loads like extension as well as problems under out-of-plane loads like symmetrical bending moments. The stress is described per layer in order to solve two coupled differential equations. The results are described independently from the composites length, which therefore provides only results in the central cross section.

M. Cho and H.S. Kim [13] were the only authors to use an iterative technique for solving the system of equations. They were considering extension, symmetrical bending, twisting and uniform thermal loadings of a composite plate. As Kassapoglou, they described the stress state in each layer through the section separately. In a first solution step, the stresses along the in-plane direction are predicted. The second step improves the transverse stresses. Successive iterations for the in-plane and the transverse stresses are computed until both are converged.

T. Kim and Atluri [41] studied the effects under shear loadings. Therefore, a full three dimensional stress field is assumed with the same description of the stresses per layer as used by Kassapoglou. For the stress unknowns in the plate's length, a linear variation is assumed. In a second article [42], higher-order stress distributions across the thickness have been introduced: this permitted to consider complex loading as thermo-mechanical problems and bending problems. Similar to the extension load case, where a constant strain is applied at both short edges of the composite, they imposed a uniform curvature  $\kappa$  to the composite plate to enable a bending state.

Problems under tension and uniform transverse load, for plates with symmetric and asymmetric lay-ups were investigated by Tahani and Nosier [72], [73]. A full three-dimensional displacement field is established per layer with a linear variation in the transverse direction per layer. Mathematical layers are introduced to increase the accuracy of the model. For the in-plane direction, a Navier-type solution is used, which is coupled with the transverse direction through a force and moment balance.

H.Y. Sarvestani and M. Y. Sarvestani [70] also used a displacement based LW modelling. They compared the classical LW theory with linear expansion in transverse direction of each layer to an improved first-order shear deformation theory. Both displacement fields were formulated as fully three dimensional. Their work considers combined bending, extension and torsion.

### 1.5.2 Finite Element Methods

The determination of the local interlaminar stress singularities is quite demanding for finite element analysis in terms of computational resources. Therefore, the first publications concerning free-edge effects were published significantly after the first paper of Pipes and Pagano.

Among the first works considering finite element analysis were Wang and Crossman [78]. Even if they investigated free-edge effects in extension, it will be stated as a reference in order to compare the modelling approaches. To reduce the computational effort, they modelled only the central lay-ups cross-section. The mesh was made up by two-dimensional triangular generalized plane strain elements. The mesh was refined towards the free edge in a stepwise rather than with a continuous spacing ratio. As the three node elements are displacement based, only a constant strain per element is recovered. Through suitable symmetry conditions, different laminates were considered.

In contrast to Wang and Crossmann, a continuous refinement of the element spacing was used by Ye [80]. He also used a two dimensional geometry representation of the central cross-section. Free-edge effects under extensional and uniform curvature bending loadings were studied. A displacement based quadratic quadrilateral elements was used together with a non-linear constitutive law.

Yi [81] investigated the free-edge effect under bending, based on a geometrical description of the cross-section of the lay-up. While Ye accounted for non-linear material elasto-plastic behaviour, Yi enabled his formulation to account for non-linear viscoelastic behaviour, including thermal and hygroscopic effects. In contrast to Ye, not a continuous refinement of the element spacing was used, but rather a stepwise refined mesh, which was comparatively more refined than that used by Wang and Crossmann. The mesh was made of quadratic quadrilateral elements with displacements as unknowns. Yi used only two elements through the thickness of each layer.

Another class of approach is the enrichment of the intralaminar region. While equally considering only the cross-shape of the laminate, the modeling is including the behaviour of the resin rich region. Haboussi, Dumontet and Billoet [28] and [27] proposed two different models: a first model considering the graded property change and a second model using interface laws on the material surfaces having no physical thickness. Both models provide finite stress values at the free-edge.

Problems in traction as well as in bending were investigated by Reddy and Robbins [68] using a superposition of local LW elements on a global ESL model. Both element types are using only displacement unknowns. While in the before mentioned approaches, the elements were lying in the cross section, here the elements lie in the mid-plane of the plate. Since in the centre of the plate, the CPT is known to be valid, simple ESL elements provide a sufficient accuracy in this region. Close to the free edge in local regions of interest an additional mesh of LW elements is superposed on the global ESL mesh. Only linear variation of the displacement is used for the displacement components in the LW elements. However, Reddy and Robbins applied several mathematical layers per physical layer in order to provide more adequate

shapes of the transverse stress through the thickness of a single layer.

Caron et al [52] also used LW elements with linear variation through thickness. In contrast to Reddy and Robbins however no overlay was used. To overcome the limitation of the linear variation through thickness, Saeedi, Sab and Caron [69] applied several mathematical layers per physical layer, which are refined in an irregular manner towards the physical layers interfaces. The resulting piecewise linear combination was shown to be capable to provide a satisfying representation of the singular stresses.

Gruttmann and Wagner [25] also used LW elements in a mesh lying in the laminate's reference plane. While Reddy and Robbins had a linear variation of the displacements in thickness direction, Gruttmann and Wagner used polynomials up to the third order for the displacements. Besides problems in extension, a curved leaf spring under constant pressure load was considered. The mesh was continuously refined towards the edge and consisted of quadrilateral shell elements, capable to account for geometrical nonlinearity. No overlay of ESL and LW elements is used, Gruttmann and Wagner rather used entirely LW elements. Through the mesh consisting only of LW elements, a higher number of unknowns is present, compared to the approach by Reddy and Robbins. However, Gruttmann and Wagner showed that the LW technique is capable to produce accurate results. Further, they showed that the number of unknowns is nevertheless lower compared to a mesh consisting of three-dimensional elements.

A similar modeling approach as the one of Gruttmann and Wagner and Reddy and Robbins is followed by Carrera et al [9]: the Unified Formulation provides different two dimensional LW and ESL plate and shell models. They are available as displacement based or mixed formulations using displacement and transverse stress variables. The Unified Formulation will be used inside this work to assess free-edge effects in composites subjected to extension and bending.

Finally, investigations done by Mistou and Karama [47] about the edge effects in sandwich structures under bending will be mentioned. They compared two displacement-based methods, an analytical one-dimensional model using the Touratier Sinus kinematics, and the commercial FE code Ansys with displacement based quadratic shell elements. Those results were finally checked for the agreement with experimental results gained by photo-elasticity. A good accordance between the two modeling methods with the experimental results was demonstrated.

### 1.5.3 Comparison of Extension and Bending

Two works are addressed that proposed a quantitative comparison between the free-edge effect originated by extension and bending loads. Both are based on Finite Element models. The first study was published by Murthy and Chamis [51]. They accounted for problems in extension, in- and out of plane bending, as well as in-plane shear, twisting, uniform temperature and moisture effects assuming different layer orientations and plate widths. They considered the overall composite as a three-dimensional model and displacement-based cubic brick elements were used. In the

areas of interest where the maximum stresses were expected, according to the different load cases, a local refinement via global-local analysis was applied. For the global model, they used only one element through thickness and for the interlaminar resin-rich layer region between two layers one element through thickness was used. They stated that the smallest magnitude of interlaminar free-edge stresses was obtained for the axial tension case.

The second work was presented by Bar-Yoseph and Ben-David [4]. They investigated the difference of free-edge effects between extension and bending and between symmetric and unsymmetrical angle-ply laminates. In contrast to Murthy and Chamis, they used a two-dimensional mixed-hybrid element with linear approximations for displacement and stress. The mesh is distributed in a logarithmic manner in the cross section, refined towards the free edges. The solution was gained assuming an a priori equilibrated stress field in the cross section of the free edge. Their results showed that the free-edge effects are higher in extension than in bending. This is the contrary of the findings by Murthy and Chamis. Further, Bar-Yoseph and Ben-David found that free-edge effects are more pronounced in symmetric than in unsymmetrical angle-ply laminates.

#### 1.5.4 Comparison of Methods

All the methods reviewed before are compared in Table 1.1. The upper half lists the semi-analytical methods, the lower half the discrete methods, mainly Finite Element methods. Through comparing the common aspects, the computational efforts needed to solve the different systems of equation describing the problem can be estimated. An important factor is how the unknowns are describing the laminate. A common interest is to minimize the computational effort without loosing any accuracy to predict the free-edge effects. Therefore, the question arises, which approach provides the most suitable compromise between computational effort and accuracy. Many authors tried to reduce the dimensionality of the problem or even the description of the lay-up using for example ESL models. Others used rather simple models with few unknowns but used iterative techniques to improve the solution provided by the lower number of unknowns. From Table 1.1, it becomes evident that the vast majority of the methods described here based their modelling approaches on LW modelling using a two dimensional geometry. Hence, it seems to be the most adequate compromise between computational effort and accuracy.

### 1.6 Scope of this Work

In order to asses the capabilities of dimensional reduced model to reproduce local interlaminar stress concentrations, the free-edge effect is considered. Different types of loadings lead to high gradients localized at the intermediate vicinity of the free edges. In chapter 1 an introduction into the effects and the existing modeling techniques is given. In chapter 2 an overview of for different modeling approaches for two-dimensional multilayered structures is given. An special emphasis is here done

Table 1.1: Techniques used to calculate free-edge effects

Name	primary unknown		solution		model order	lay-up description	
	$\mathbf{u}$	$\sigma$	direct	iterative		ESL	LW
Kassapoglou		x	x		2D ( $y, z$ )		x
Cho and H. S. Kim		x		x	2D ( $y, z$ )		x
T. Kim and Atluri		x	x		3D		x
Tahani and Nosier	x		x		3D		x
Sarvestani and Sarvestani	x		x		2D ( $x, y$ )	x	x
Pipes and Pagano	x		x		2D ( $y, z$ )		x
Wang and Crossman	x		x		2D ( $y, z$ )		x
Bar-Yoseph and Ben-David	x	x	x		2D ( $y, z$ )		x
Ye	x		x		2D ( $y, z$ )		x
Yi	x		x		2D ( $y, z$ )		x
Reddy and Robbins	x		x		2D ( $x, y$ )	x	x
Gruttmann and Wagner	x		x		2D ( $x, y$ )		x
Unified Formulation	x	x	x		2D ( $x, y$ )	x	x
LS1 by Caron et al	x		x		2D ( $x, y$ )		x
Murthy an Chamis	x			x	3D		x
Mistou and Karama	x		x		1D / 2D ( $x, y$ )		x

on the Carrera's Unified Formulation (CUF), as unified tool to impose different kinematical hypothesis for the dimensional reduced models.

The free-edge effect is assessed for extension and bending in chapter 3. Therefore the different kinematical models available in the CUF are used. They are compare in order to find the best compromise between their computational cost and accuracy. As the high stress gradients at the free-edge tend to have a singular behaviour it is further assessed, which of the CUF models also provides the most accurate rendition of the singularity. The measurement of the singular behaviour itself is done via Power law fitting, based on the results of the different models. It is via the use of the parameters obtained from the fitting, that further comparison can be done. They are about the extend of the free-edge effects for the different laminates under consideration and about the amount of extend due to the different types of loading.

One finding is that higher order models are needed in the zones of high stress gradients, but no difference is present in other zones. A coupling of models with the same dimensionality but different kinematics seems desirable in order to further reduce the computational cost. Chapter 4 deals with this aspect, focusing for the sake of simplification on one-dimensional structures. Here the so-called extended Variational Formulation (XVF) is used to couple the different kinematically models. It will be demonstrated that XVF includes several other common techniques used to establish a coupling of different kinematical models. This work is closed with some final conclusion and an outlook on further future investigations.

## Chapter 2

# Boundary Value Problems and their Numerical Approaches

A brief overview of two fundamental variational statements will be given in the first section of this chapter. In a second section, different approaches to model the mechanical behaviour are given. Special attention is given to layered structures, by presenting their additional requirements and the resulting modelling approaches. The kinematical theories presented here can be employed to model one-dimensional beam and two-dimensional plate structures. An all-encompassing envelope for many theories is the Carrera Unified Formulation (CUF). The chapter is closed by the used Finite Element (FE) approximations for one-dimensional problems of beams and two-dimensional problems of plates. The beam approximations will be used in chapter 4.5 and appendix C, while the plate approximations will be studied in chapter 3.

### 2.1 Boundary Value Problem

Assume a general continuum body, occupying the domain  $\Omega$ , described in a cartesian system. The body is loaded by volumetric forces  $f_v$  and external traction forces  $t$ . Those forces will create a deformation of continuum. For a static problem, the deformation will create an inner state stress, represented by the stress  $\sigma$ . The stress state has to equilibrate those volumetric forces:

$$\begin{aligned}\frac{\partial \sigma_{xx}}{\partial x} + \frac{\partial \sigma_{xy}}{\partial y} + \frac{\partial \sigma_{xz}}{\partial z} + f_{v_x} &= 0 \\ \frac{\partial \sigma_{xy}}{\partial x} + \frac{\partial \sigma_{yy}}{\partial y} + \frac{\partial \sigma_{yz}}{\partial z} + f_{v_y} &= 0 \\ \frac{\partial \sigma_{xz}}{\partial x} + \frac{\partial \sigma_{yz}}{\partial y} + \frac{\partial \sigma_{zz}}{\partial z} + f_{v_z} &= 0\end{aligned}\tag{2.1}$$

At the outer boundary  $\Gamma_N$  the inner stress state has to be in an equilibrium with the outer forces acting on  $\Gamma_N$ :

$$\begin{aligned}\sigma_{xx}n_x + \sigma_{xy}n_y + \sigma_{xz}n_z &= t_x \\ \sigma_{xy}n_x + \sigma_{yy}n_y + \sigma_{yz}n_z &= t_y \\ \sigma_{xz}n_x + \sigma_{yz}n_y + \sigma_{zz}n_z &= t_z\end{aligned}\quad (2.2)$$

Further at the same boundary conditions about the displacements might be given:

$$\begin{aligned}u_x &= u_{\Gamma_{N_x}} \\ u_y &= u_{\Gamma_{N_y}} \\ u_z &= u_{\Gamma_{N_z}}\end{aligned}\quad (2.3)$$

The above stated equations describe the static equilibrium as well the boundary conditions. In order to solve the system further relations are needed. The unknown stresses have to be expressed, as well as the displacements. Via Hooke's law in Equation (1.4), the constitutive law of the material is given, linking stresses with strains. Via the kinematics the strains be linked with the displacements:

$$\begin{aligned}\epsilon_{xx} &= \frac{\partial u_x}{\partial x} \\ \epsilon_{yy} &= \frac{\partial u_y}{\partial y} \\ \epsilon_{zz} &= \frac{\partial u_z}{\partial z} \\ \epsilon_{xy} &= \frac{\partial u_x}{\partial y} + \frac{\partial u_y}{\partial x} \\ \epsilon_{yz} &= \frac{\partial u_y}{\partial z} + \frac{\partial u_z}{\partial y} \\ \epsilon_{xz} &= \frac{\partial u_x}{\partial z} + \frac{\partial u_z}{\partial x}\end{aligned}\quad (2.4)$$

This partial differential equation is hard to fulfill in the stated strong form for any body, any type of load and any type of boundary condition imposed. In order to find a suitable form for the unknowns  $\sigma$ ,  $\epsilon$  and  $u$ , the equations will be hereafter only fulfilled in an integral weak sense sense. Therefore two variational statements will be proposed.

## 2.2 Variational Statements

### 2.2.1 Principle of Virtual Displacements

Consider a static mechanical problem in the domain  $\Omega \subset \mathbb{R}^3$  with its boundary decomposed in a Dirichlet and Neumann boundary  $\Gamma = \Gamma_D \cup \Gamma_N$ , such that  $\Gamma_D \cap \Gamma_N = 0$ . By using a matrix notation with a variational formulation of the displacements, one can state for the balance between inner and outer energy:

Find  $\mathbf{u} \in \mathcal{U}$  such that:

$$\int_{\Omega} \boldsymbol{\sigma}(\mathbf{u})^T \delta \boldsymbol{\epsilon}(\mathbf{u}) d\Omega = \int_{\Omega} \mathbf{f}_v^T \delta \mathbf{u} d\Omega + \int_{\Gamma_N} \mathbf{t}^T \delta \mathbf{u} d\Gamma \quad \forall \delta \mathbf{u} \in \delta \mathcal{U} \quad (2.5)$$

where:

$$\mathcal{U} = \{\mathbf{u} \in \mathbf{H}^1(\Omega); \mathbf{u}|_{\Gamma_D} = \bar{\mathbf{u}}\} \quad (2.6)$$

and  $\delta\mathcal{U}$  is the space of the admissible virtual displacements. Here  $\Omega$  is the reference configuration,  $\sigma$  is the stress tensor,  $\mathbf{f}_v$  are volume forces and  $\mathbf{t}$  are tractions on the Neumann boundary  $\Gamma_N$ .

For further convenience, the strain  $\epsilon$  and the stress  $\sigma$  are split in their normal and in-plane parts. Hence we have:

$$\begin{aligned}\epsilon &= \epsilon_p + \epsilon_n \\ \sigma &= \sigma_p + \sigma_n\end{aligned} \quad (2.7)$$

with:

$$\begin{aligned}\sigma_p &= \begin{Bmatrix} \sigma_{xx} & \sigma_{yy} & \sigma_{xy} \end{Bmatrix}^T, & \epsilon_p &= \begin{Bmatrix} \epsilon_{xx} & \epsilon_{xy} & \epsilon_{xy} \end{Bmatrix}^T \\ \sigma_n &= \begin{Bmatrix} \sigma_{xz} & \sigma_{yz} & \sigma_{zz} \end{Bmatrix}^T, & \epsilon_n &= \begin{Bmatrix} \epsilon_{xz} & \epsilon_{yz} & \epsilon_{zz} \end{Bmatrix}^T\end{aligned} \quad (2.8)$$

The Principle of Virtual Displacements (PVD) finally reads:

$$\begin{aligned}\int_{\Omega} \sigma_p(\mathbf{u})^T \delta\epsilon_p(\mathbf{u}) + \sigma_n^T(\mathbf{u}) \delta\epsilon_n(\mathbf{u}) d\Omega &= \\ \int_{\Omega} \mathbf{f}_v^T \delta\mathbf{u} d\Omega + \int_{\Gamma_N} \mathbf{t}^T \delta\mathbf{u} d\Gamma &\quad \forall \delta\mathbf{u} \in \delta\mathcal{U}\end{aligned} \quad (2.9)$$

The inner and outer work can be identified as :

$$\delta\Pi_{int}(\mathbf{u}, \delta\mathbf{u}) = \int_{\Omega} (\sigma_p^T(\mathbf{u}) \delta\epsilon_p(\mathbf{u}) + \sigma_n^T(\mathbf{u}) \delta\epsilon_n(\mathbf{u})) d\Omega \quad (2.10)$$

$$\delta\Pi_{ext}(\delta\mathbf{u}) = \int_{\Omega} \mathbf{f}^T \delta\mathbf{u} d\Omega + \int_{\Gamma_N} \mathbf{t}^T \delta\mathbf{u} d\Gamma \quad (2.11)$$

**Constitutive Law** For the Principle of virtual Displacement we link the stresses with the strains according to the split in normal and in-plane components. Hooke's law (1.4) takes thus the form :

$$\begin{aligned}\sigma_p(\mathbf{u}) &= C_{pp} \epsilon_p(\mathbf{u}) + C_{pn} \epsilon_n(\mathbf{u}) \\ \sigma_n(\mathbf{u}) &= C_{np} \epsilon_p(\mathbf{u}) + C_{nn} \epsilon_n(\mathbf{u})\end{aligned} \quad (2.12)$$

The strain is calculated as a derivative of the displacement:

$$\epsilon_p(\mathbf{u}) = \mathbf{D}_p \mathbf{u} \quad \epsilon_n(\mathbf{u}) = (\mathbf{D}_{np} + \mathbf{D}_{nz}) \mathbf{u} \quad (2.13)$$

Where the explicit form of the differential operators  $\mathbf{D}_p$ ,  $\mathbf{D}_{np}$  and  $\mathbf{D}_{nz}$  adapts to the following forms due to the split:

$$\mathcal{D}_p = \begin{bmatrix} \frac{\partial}{\partial x} & 0 & 0 \\ 0 & \frac{\partial}{\partial y} & 0 \\ \frac{\partial}{\partial y} & \frac{\partial}{\partial x} & 0 \end{bmatrix} \quad \mathcal{D}_{np} = \begin{bmatrix} 0 & 0 & \frac{\partial}{\partial x} \\ 0 & 0 & \frac{\partial}{\partial y} \\ 0 & 0 & 0 \end{bmatrix} \quad \mathcal{D}_{nz} = \begin{bmatrix} \frac{\partial}{\partial z} & 0 & 0 \\ 0 & \frac{\partial}{\partial z} & 0 \\ 0 & 0 & \frac{\partial}{\partial z} \end{bmatrix}$$

Finally the stiffness matrices  $\mathbf{C}_{pp}$ ,  $\mathbf{C}_{pn}$ ,  $\mathbf{C}_{np}$  and  $\mathbf{C}_{nn}$  from the Equation (2.12) are ordered due to the split in the following form:

$$\mathbf{C}_{pp} = \begin{bmatrix} C_{11} & C_{12} & C_{16} \\ C_{12} & C_{22} & C_{26} \\ C_{16} & C_{26} & C_{66} \end{bmatrix}; \quad \mathbf{C}_{np} = \mathbf{C}_{pn}^T \begin{bmatrix} 0 & 0 & C_{13} \\ 0 & 0 & C_{23} \\ 0 & 0 & C_{36} \end{bmatrix}; \quad (2.14)$$

$$\mathbf{C}_{nn} = \begin{bmatrix} C_{44} & C_{45} & 0 \\ C_{45} & C_{55} & 0 \\ 0 & 0 & C_{66} \end{bmatrix}$$

It gets visible from the constitutive law, Equation (2.12), that all stress, through its identification of Hooke's law, depend on the stiffness parameters of each layer. They are hence generally discontinuous at the layers interface if the strain is continuous. This limits the capabilities of the PVD regarding the modeling of multilayered structures. In order to fulfill the ICs from Equation (1.2), additional efforts for the transverse stresses at the layers interfaces are needed. This motivates other variational formulations, delivering continuous transverse stresses.

### 2.2.2 Reissner's Mixed Variational Theorem

Reissner's Mixed Variational Theorem (RMVT), [64,65] is used to improve the transverse stress behaviour of composite structures by allowing to exactly fulfill the interlaminar continuity of  $\sigma_n$ . This mixed formulation permits to simultaneously and independently vary the in-plane strains  $\epsilon_p(\mathbf{u})$  as well as the transverse stress  $\sigma_n$ . Therefore the transverse stresses  $\sigma_{nM}$  will be introduced as independent variables in each layer, in addition to the independently formulated displacement  $\mathbf{u}$ .

Reissners Mixed Variational Theorem can be stated in the following form:

$$\int_{\Omega} \delta \epsilon_{pG}^T \boldsymbol{\sigma}_{pH} + \delta \epsilon_{nG}^T \boldsymbol{\sigma}_{nM} + \delta \boldsymbol{\sigma}_{nM}^T (\epsilon_{nG} - \epsilon_{nH}) d\Omega = \int_{\Omega} \mathbf{f}_v^T \delta \mathbf{u} d\Omega + \int_{\partial \Omega_N} \mathbf{t}^T \delta \mathbf{u} d\partial \Gamma \quad (2.15)$$

Note that the strain  $\epsilon_{nG}$  is calculated by geometrical relations and is denoted with the subscript  $G$ , while the strain  $\epsilon_{nH}$  is calculated via Hooke's law as emphasized by the subscript  $H$ .

Therefore, in the additional term  $\delta \boldsymbol{\sigma}_{nM} (\epsilon_{nG} - \epsilon_{nH})$ , the transverse stress  $\delta \boldsymbol{\sigma}_{nM}$  serves as Lagrange Multiplier to minimize the difference between the transverse strains calculated by Hooke's law and those defined by the geometric relations, given in Equation (2.13)

We can define the following forms for the inner and outer work:

$$\begin{aligned}\delta\Pi_{int_{RMVT}}(\boldsymbol{u}, \boldsymbol{\sigma}_{nM}, \delta\boldsymbol{u}, \delta\boldsymbol{\sigma}_{nM}) &= \\ \int_{\Omega} \delta\epsilon_{pG} \boldsymbol{\sigma}_{pH} + \delta\epsilon_{nG} \boldsymbol{\sigma}_{nM} + \delta\boldsymbol{\sigma}_{nM} (\boldsymbol{\epsilon}_{nG} - \boldsymbol{\epsilon}_{nH}) d\Omega & \\ \delta\Pi_{ext_{RMVT}}(\delta\boldsymbol{u}) &= \int_{\Omega} \boldsymbol{f} \cdot \delta\boldsymbol{u} d\Omega + \int_{\partial\Omega_N} \boldsymbol{t} \cdot \delta\boldsymbol{u} d\partial\Omega\end{aligned}\tag{2.16}$$

It is interesting to note that the external virtual work has the same expression as in the PVD.

The independent field variables of the RMVT are  $\boldsymbol{\epsilon}_p(\boldsymbol{u}) = \boldsymbol{\epsilon}_{pG}$  and  $\boldsymbol{\sigma}_{nM}$ , so that the Hooke's law has to be reformulated in the following mixed form:

$$\begin{aligned}\boldsymbol{\sigma}_{pH} &= C_{pp}^* \boldsymbol{\epsilon}_{pG} + C_{pn}^* \boldsymbol{\sigma}_{nM} \\ \boldsymbol{\epsilon}_{nH} &= C_{np}^* \boldsymbol{\epsilon}_{pG} + C_{nn}^* \boldsymbol{\sigma}_{nM}\end{aligned}\tag{2.17}$$

## 2.3 Reduced Models for Composite Plates

Hereafter, the formulation of two-dimensional plate models will be discussed. The reference coordinate system for a plate is given in Figure 2.1. Two-dimensional models are formulated by postulating a given behaviour in the transverse direction  $z$ : the integrals in the transverse direction appearing in the variational statements can then be exactly computed. This leaves only unknown functions that depend on the in-plane coordinates  $x, y$ .

Special attention will be paid towards the description of the mechanical behaviour of multilayered structures. Two different description techniques will be presented. The first one is ESL, where the description is given with respect to a reference surface for the whole plate. From this reference surface, the solution is expanded into the homogenized structure, along the thickness direction. The other alternative is the so-called Layer-Wise (LW) one, in which the mechanical behaviour of every single layer is explicitly described. Both will be discussed in detail and the adoption of different kinematical models used for both descriptions will be given.

### 2.3.1 Unified Formulation for Two Dimensional Plate Structures

The CUF, developed by Erasmo Carrera for plates and shells [9], is an all encompassing way to formulate two-dimensional models for multilayered structures on the basis of PVD and RMVT. It is referring to both, ESL and LW descriptions. The Unified Formulation consist in an abstract, compact index notation that is particulary suited for the numerical implementation. For two-dimensional plate models based

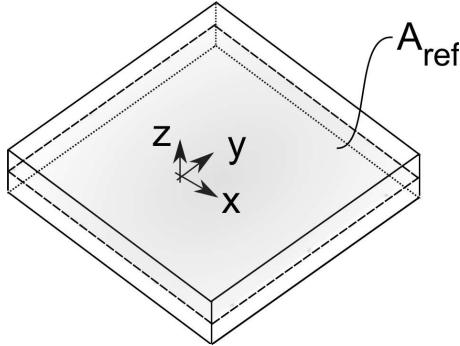


Figure 2.1: Coordinate system of a plate structure

on the PVD the unknown field variables  $\mathbf{u} = (u_x, u_y, u_z)$  are expressed in a generic manner as:

$$\mathbf{u}(x, y, z) = [u_x(x, y, z) \ u_y(x, y, z) \ u_z(x, y, z)]^T = \sum_{\tau=0}^N F_\tau(z) \mathbf{u}_\tau(x, y) \quad (2.18)$$

When referring to RMVT, the formally same expression is used for the transverse stress fields  $\boldsymbol{\sigma}_n = (\sigma_{xz}, \sigma_{yz}, \sigma_{zz})$ :

$$\boldsymbol{\sigma}_n(x, y, z) = [\sigma_{xz}(x, y, z) \ \sigma_{yz}(x, y, z) \ \sigma_{zz}(x, y, z)]^T = \sum_{\tau=0}^N F_\tau(z) \boldsymbol{\sigma}_{n\tau}(x, y) \quad (2.19)$$

Different functions  $F_\tau(z)$  can be chosen depending on the description used at the multilayered level (ESL or LW). The most frequent function used is a polynomial. The order  $N$  of its expansion is a free parameter of the formulation. In the Carrera's Unified Formulation, the same order  $N$  is used for all components of the unknown field variables. An augmented flexibility can be achieved by treating separately each component: this is the so-called Generalized Unified Formulation (GUF) by Demasi [15]

Both, analytical solutions as well as the implementation into FE approximations do profit from the CUF capabilities. In the present implementation of the CUF, mainly polynomials up to the forth order are used. Nevertheless other rational functions can be adapted, as recently shown by Carrera, Filippi and Zappino [11] through the use of sinus and exponential functions. It is worth mentioning that the compact index notation upon which the CUF relies, can be employed directly to multi field problems like electromagnetic, thermo-mechanic and electro-thermo-mechanic systems.

### 2.3.1.1 Equivalent Single Layer Models

The displacement field is here described in the global reference plane for the whole laminate. The kinematical assumptions are expressed via the functions  $F_\tau(z)$  that are defined over the global thickness coordinate  $z \in [-\frac{h}{2}, \frac{h}{2}]$ :

$$\mathbf{u}(x, y, z) = \sum_{\tau=0}^N F_\tau(z) \mathbf{u}_\tau(x, y) \quad \text{with } z \in \left[-\frac{h}{2}; \frac{h}{2}\right] \quad (2.20)$$

The function  $F_\tau(z)$  is defined in terms of the global coordinate  $z$  and is represented by a Taylor series expansion through the thickness. By denoting the coordinate  $z_0$ , providing the position of the reference surface  $A_{ref}$ , the approximating functions are defined as:

$$F_\tau(z) = (z - z_0)^\tau \quad (2.21)$$

The lowest order expansion is the first order one, with  $N = 1$ . Here two contributions are present, a constant term  $F_0$  and a linear  $F_1$ . Therefore they represent for each displacement component the membrane  $u_{i0}$  and its rotation  $u_{i1}$ . To keep the uniform and modular spirit of the CUF, hereafter the layer specific coordinate  $z_k$  will be used, which leads to a simple coordinate change:

$$F_\tau(z_k) = (z_k + z_{0k} - z_0)^\tau \quad \text{with } z_k \in \left[-\frac{h_k}{2}; \frac{h_k}{2}\right] \quad (2.22)$$

Where  $z_{0k}$  is the coordinate of the reference surface  $A_{ref}^k$  of the  $k^{th}$  layer. According to this, the values of the functions are the following, regarding also higher order terms, denoted by  $F_r$ :

$$\begin{aligned} F_0(z_k) &= 1 \\ F_1(z_k) &= (z_k + z_{0k} - z_0) \\ F_r(z_k) &= (z_k + z_{0k} - z_0)^r, \quad r = 2, \dots, N \end{aligned} \quad (2.23)$$

The ESL description with Taylor series expansion leads to a displacement field that is  $C_z^N$  continuous, which violates the slope discontinuity required at the inter-laminar interfaces. A very simple manner to overcome this excessive continuity is the adoption of Murakami's Zig-Zag functions (MZZF), [8, 50]:

$$F_{zz}(z_k) = (-1)^k \frac{2(z_k - z_{0k})}{h_k} \quad (2.24)$$

The unknown  $u_{zz}$  associated to  $F_{zz}(z_k)$  allows hence to introduce in an ESL manner a slope discontinuity at each interface thanks to the term  $(-1)^k$ . By introducing the non-dimensional layer-specific coordinate  $\zeta_k$ :

$$\zeta_k = \frac{2(z_k - z_{0k})}{h_k} \quad (2.25)$$

the MZZF can be written simply as:

$$F_{zz}(\zeta_k) = (-1)^k \zeta_k \quad (2.26)$$

An example for the resulting displacements and transverse stress fields for the second order expansion are displayed in Figure 2.2: the implementation of ESL theories in the PVD in (a), its extension with MZZF in (b) and the implementation into RMVT in (c). For all ESL models, the continuous displacement field but the discontinuous transverse stress are visible.

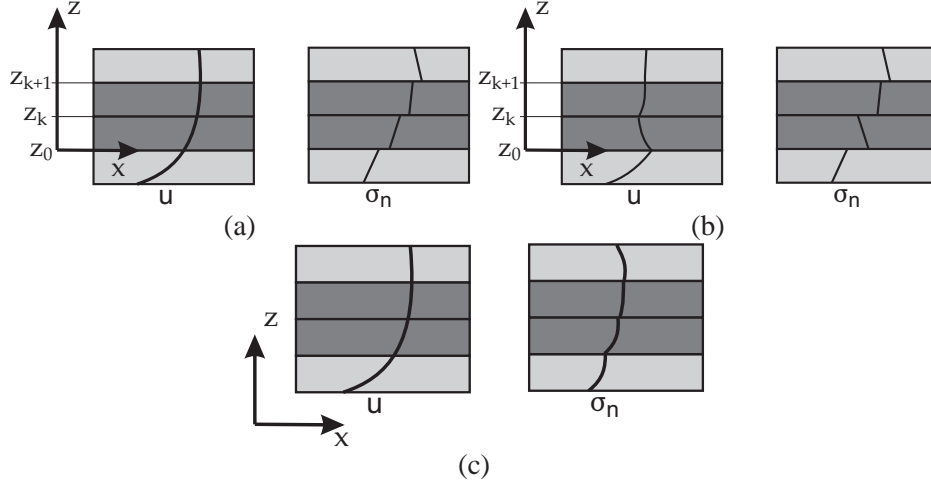


Figure 2.2: Displacement  $u$  and transverse stresses  $\sigma_n$  for (a) and ED2, (b) EDz2 and (c) EM2 model

### 2.3.1.2 Layer Wise Theories

In LW descriptions, the same expression (2.18) is formally used, where now the layer-specific coordinate  $\zeta_k(z_k)$  is used:

$$\mathbf{u}^k(x, y, z) = \sum_{\tau=0}^N F_\tau(z_k) \mathbf{u}_\tau^k(x, y) \quad \text{with } z_k \in \left[-\frac{h_k}{2}; \frac{h_k}{2}\right] \quad (2.27)$$

The same formalism applies to the transverse stress field  $\sigma_{nM}$  in the RMVT formulation:

$$\boldsymbol{\sigma}_{nM}^k(x, y, z) = \sum_{\tau=0}^N F_\tau(z_k) \boldsymbol{\sigma}_{nM\tau}^k(x, y) \quad \text{with } z_k \in \left[-\frac{h_k}{2}; \frac{h_k}{2}\right] \quad (2.28)$$

Remind that regardless of the multilayer description, the transverse stresses in the RMVT statement are always formulated Layer Wise. In this work, the thickness functions are constituted from Legendre polynomials as follows:

$$\begin{aligned}
 F_t(\zeta_k) &= F_0(\zeta_k) & = & \frac{P_0(\zeta_k) + P_1(\zeta_k)}{2} \\
 F_b(\zeta_k) &= F_1(\zeta_k) & = & \frac{P_0(\zeta_k) - P_1(\zeta_k)}{2} \\
 F_r(\zeta_k) &= P_r(\zeta_k) - P_{r-2}(\zeta_k), & r &= 2, \dots, N
 \end{aligned} \tag{2.29}$$

where the Legendre polynomials are the following:

$$\begin{aligned}
 P_0(\zeta_k) &= 1 & P_1(\zeta_k) &= \zeta_k \\
 P_{n+1}(\zeta_k) &= \frac{(2n+1)\zeta_k P_n(\zeta_k) - n P_{n-1}(\zeta_k)}{n+1} & \text{for } n = 1, \dots, N-1
 \end{aligned} \tag{2.30}$$

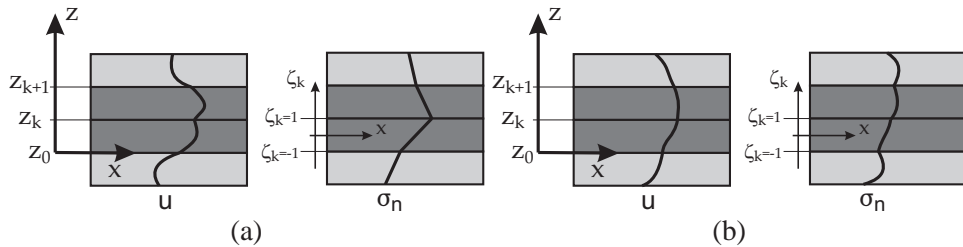


Figure 2.3: Displacement  $\mathbf{u}$  and transverse stresses  $\sigma_n$  for (a) and LD2, (b) LM2 model

Note that for the first two terms, related to the linear approximation, coincide with the Lagrange interpolation functions. When these layer-specific interpolations are assembled at multilayer level, the resulting approximation is automatically only of the class  $C_z^0$  at the interfaces between adjacent layers. Figure 2.3 provides an illustration for the LD2 (a) and LM2 (b) models, illustrating the continuous and layer-dependent displacements fields.

Further details about the mechanical behaviour as well as convergence studies can be found in [9], [17] and [24].

A summary of the different characteristics as well as capabilities of the CUF models is given in Table 2.1 as a function of the variational statement used, the lay-up description used and the expansion order  $N$ . Based on the different modeling techniques and the number of layers  $N_l$ , the total number of unknowns  $NDOF$  can be calculated.

Table 2.1: Capabilities and characteristics of the different CUF models

	N=1-4	ZZ	IC	NDOF
PVD	ED N	-	-	$3(N + 1)$
	EDz N	✓	-	$3(N + 1)$
	LD N	✓	-	$3(N_l N + 1)$
RMVT	EM N	-	✓	$6 + 3N(N_l + 1)$
	EMz N	✓	✓	$6 + 3N(N_l + 1)$
	LM N	✓	✓	$6(N_l N + 1)$

## 2.4 FE Approximations for CUF Plate Models

The solution for the in-plane distribution of each displacement component  $\mathbf{u}_\tau$  is given through the following FE approximation:

$$\begin{aligned}\mathbf{u}_\tau(x, y) &= F_\tau \mathbf{N}(x, y) \mathbf{q}_{\tau e} \\ \delta \mathbf{u}_s(x, y) &= F_s \mathbf{N}(x, y) \delta \mathbf{q}_{s e}\end{aligned}\quad (2.31)$$

The index  $\tau$  is used for the actual unknown and the index  $s$  is used for the virtual variation. In the case of the RMVT, the same approach is used for the stress components  $\boldsymbol{\sigma}_\tau$ . Regarding the FE implementation of the CUF models, four node bilinear Q4 plate elements are used for the in-plane discretisation. The numerical integration is done with classic Gauss point integration [10]. Shear locking can be handled via different reduced integration schemes, but is not an issue in this work.

Isoparametric bilinear four-node CUF elements have been implemented into the commercial FE code ABAQUS. A complete study of their behaviour for general multilayered structures is given by D’Ottavio [17].

### 2.4.1 FE Approximations for the PVD case

As stated before in Equation (2.13) the strain is split into in-plan and normal components. From the Equation (2.31) the strain can be expressed as a function of the independent nodal displacement  $\mathbf{q}_\tau$ :

$$\boldsymbol{\epsilon}_p(x, y, z) = F_\tau(z) (\mathcal{D}_p \mathbf{N}(x, y)) \mathbf{q}_\tau \quad (2.32)$$

$$\boldsymbol{\epsilon}_n(x, y, z) = F_\tau(z) (\mathcal{D}_{np} \mathbf{N}(x, y)) \mathbf{q}_\tau + F_\tau(z) (\mathcal{D}_{nz} \mathbf{N}(x, y)) \mathbf{q}_\tau \quad (2.33)$$

### 2.4.2 FE Approximations for the RMVT case

For the RMVT elements both, the displacements and the transverse stress unknowns use the same  $C^0$  bilinear approximation. For the stress unknowns the interpolation

of the stress fields is done in the same manner as to displacements in the PVD case, see Equation (2.31). Here the nodal stress values are denominated  $\mathbf{g}_n \tau$ :

$$\begin{aligned}\boldsymbol{\sigma}_{n\tau}^k(x, y, z) &= F_\tau(z) \mathbf{N}(x, y) \mathbf{g}_{n\tau}^k \\ \delta\boldsymbol{\sigma}_{ns}^k(x, y, z) &= F_s(z) \mathbf{N}(x, y) \delta\mathbf{g}_{ns}^k\end{aligned}\quad (2.34)$$

In the RMVT case, due to the two unknowns, pure displacement terms,  $\mathbf{K}_{uu}$ , pure stress terms  $\mathbf{K}_{\sigma\sigma}$  and the coupling terms  $\mathbf{K}_{u\sigma}$  and  $\mathbf{K}_{\sigma u}$ . The resulting linear system is as follows:

$$\begin{bmatrix} \mathbf{K}_{uu} & \mathbf{K}_{u\sigma} \\ \mathbf{K}_{\sigma u} & \mathbf{K}_{\sigma\sigma} \end{bmatrix} \begin{bmatrix} \mathbf{q} \\ \mathbf{g} \end{bmatrix} = \begin{bmatrix} \mathbf{F} \\ 0 \end{bmatrix} \quad (2.35)$$

Note that here the coupling matrices are symmetrical:  $\mathbf{K}_{\sigma u} = \mathbf{K}_{u\sigma}^T$

### 2.4.3 Assembling Strategy

After the FEM matrices are obtained for each layer  $k$  of the laminate, an assembly is required to build the matrices for the whole multilayer. The unknowns are either global for the overall compound in the ESL case or local per layer in the LW case. Hence different assembly strategies are needed for the two cases, regardless whether the variational statement is PVD or RMVT.

#### 2.4.3.1 Equivalent Single Layer Assembly

Thanks to the global defined unknowns, which are independent from the layers, it can be stated:

$$\mathbf{u}_\tau^{k=1} = \mathbf{u}_\tau^{k=2} = \dots = \mathbf{u}_\tau \quad (2.36)$$

$$\delta\mathbf{u}_s^{k=1} = \delta\mathbf{u}_s^{k=2} = \dots = \delta\mathbf{u}_s \quad (2.37)$$

Concerning only displacement based elements, the overall stiffness per element in the ESL case is simply the sum of the stiffness contributions of each layer. For the stress unknown however in the RMVT applications, the unknowns are always layer wise, as given by Equation (2.28). This leads hence to the second assembly strategy.

#### 2.4.3.2 Layerwise Assembly

As the unknowns are defined per layer, the strategy for assembling LW descriptions is different. The Interlaminar Continuity in Equation (1.1) imposes the identity of only the top and bottom unknowns of two interfacing layers. Therefore, only these will be adding their stiffness contributions. For displacement variables this leads to:

$$\begin{aligned}\mathbf{u}_{\tau t}^k &= \mathbf{u}_{\tau b}^{k+1} \\ \delta\mathbf{u}_{s t}^k &= \delta\mathbf{u}_{s b}^{k+1}\end{aligned}\quad (2.38)$$

The same procedure is applied to  $\boldsymbol{\sigma}_{n\tau}^k$  if RMVT is used.

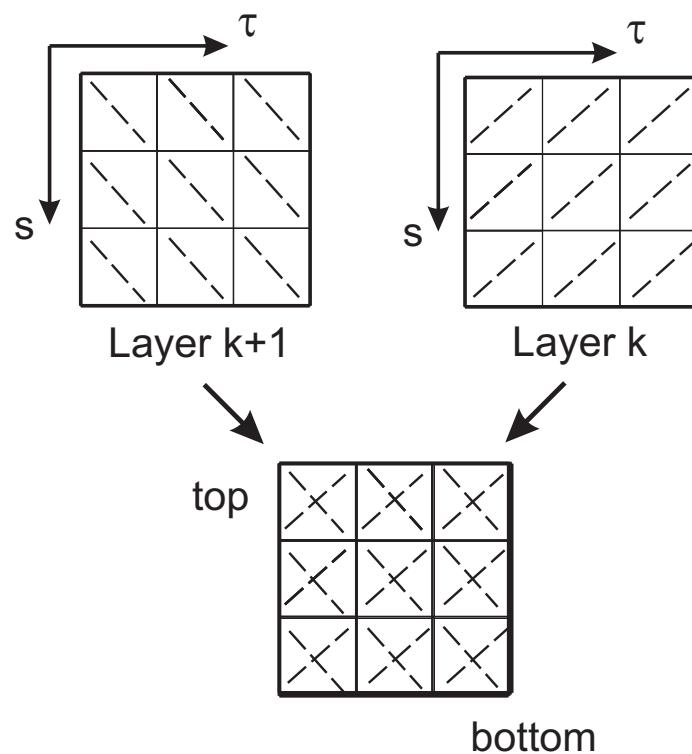


Figure 2.4: Assembly of the stiffness terms in Equivalent Single Layer description

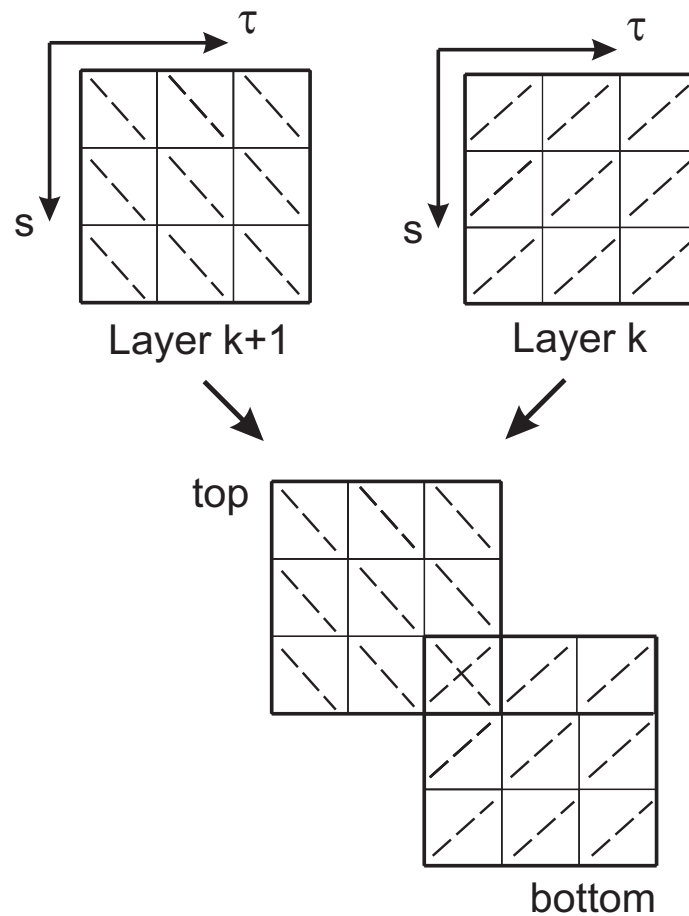


Figure 2.5: Assembly of Top and Bottom DOF in Layerwise Formulation

## Chapter 3

# Free Edge Effects of Composites in Plate Structures

This chapter discusses the free-edge effects in composites under two different types of loading: extension and bending. The aim is to compare this effect in different laminates and to estimate under which loading the effects are stronger. Therefore different two-dimensional plate models of the CUF will be used. They have been implemented as user elements in the commercial FE program ABAQUS, as described in Appendix E. The capability of these CUF plate models to reproduce very sharp gradients in the transverse stresses in the intermediate vicinity of free edges for the different laminates will be compared. Those gradients are expected to rise with the mesh refinement, in such an extend, that they do not converge. These appearing gradients are hence stress singularities. Hence the stress distributions provided by each model at the free edges will be investigated.

### 3.1 Free Edge Effects due to Extension

#### 3.1.1 Validation of the Models

In order to validate the accuracy of the CUF models, a reference test case from Wang and Crossman [78] is considered. The composite plate is according to Figure 1.5, while the geometric relations are  $a = 2b = 8h$ . Two cross-ply lay-ups were considered,  $[0, 90]_s$  and  $[90, 0]_s$ , as well as the angle-ply lay-up  $[\pm 45]_s$ . Further, two eight-layer quasi-isotropic lay-ups  $[90, 0, \pm 45]_s$  and  $[\pm 45, 0, 90]_s$  are compared, where the thickness of each layer is now half of that of the four-layer laminates, keeping the ratio  $a/h$  constant. Each layer has the same material properties listed in Table 3.1. A uniform axial strain is applied via a prescribed displacement on each of the plates short edges at  $x = \pm a$ . If not stated otherwise, all stress results are given in  $GPa$ .

The original numerical results by Wang and Crossman were based on a quasi three-dimensional plane strain model. They took advantage of the symmetries of

the problem, as three symmetry planes exist, thanks to the symmetric lay-ups used. Wang and Crossman considered therefore only a quarter of the cross section of the laminate,  $y \in [0, b = 4h]$   $z \in [0, 2h]$ . For the application of the CUF however, plate elements are considered. As shown by D’Ottavio et al [18], a total length of  $a = 8h$  is sufficient to provide a constant strain state along the lengthwise  $x$  axis in order to avoid disturbing effects of the load introduction at the short edges. In addition to the results by Wang and Crossman, values calculated with a three-dimensional model using the commercial code Ansys are given. The mesh used for the 3D Ansys model has the same in-plane pattern as that employed for the 2D CUF model. This mesh consists of  $30 \times 30$  elements that become smaller as the plate centre ( $x = 0$ ) and the free edge ( $y = \pm b$ ) are approached. In the three-dimensional model, six elements are used per layer in the thickness direction for the Quasi-isotropic laminates and twelve for the four-ply laminates. Quadratic brick elements are used in Ansys while the in-plane mesh for the CUF is based on bilinear quad elements. Finally, the results of Wang and Crossman have been validated by other authors, among them Tahani and Nosier [73], Spilker and Chou [71], Robbins and Reddy [67] as well as Mittelstedt and Becker [48].

Table 3.1: Single Layer Material properties

$E_1 = 137900 \text{ MPa}$
$E_2 = E_3 = 14480 \text{ MPa}$
$G_{12} = G_{13} = G_{23} = 5860 \text{ MPa}$
$\nu_{12} = \nu_{13} = \nu_{23} = 0.21$

### 3.1.1.1 Cross-Ply Laminates

Figures 3.1 and 3.3 report the through-thickness distribution of  $\sigma_{zz}$  for the two layups  $[0, 90]_s$  and  $[90, 0]_s$  respectively. In each figure, RMVT on the left and PVD on the right, as well as ESL and LW models are compared along with Ansys three-dimensional as well as with Wang and Crossman reference results. From the first criterion, the superiority of the LW description is visible. The distributions through the thickness for both laminates are in good accordance with those by Wang and Crossman and the three-dimensional results from Ansys. For the ESL description, the distributions through the thickness show that a kind of a mean value is achieved. The mixed RMVT elements do generally deliver better results. For the PVD statement a discontinuity of the transverse stress at the layers interface is visible, as has been pointed out in Table 2.1. Figures 3.1 and 3.3 indicate clearly that low-order expansions generally do not match the reference result. It appears that using a lower order expansion in combination with LW description yield a better result than a higher-order ESL descriptions.

The distributions along the width at the bilateral interface between two differently orientated layers of the cross-ply laminates, are shown in Figures 3.2 and 3.4.

For the PVD models, the stresses have been taken from the lower layer. The given results indicate as well a superiority of the Layerwise models. Especially the steep gradients close to the free edge are in perfect match with the three-dimensional solutions of Ansys. It is remarkable to see a twice occurring sign change for the  $[90, 0]_s$  lay-up. The ESL models are not able to achieve the same maximum stresses. In the width distributions, for the PVD statement it can be observed that from the free edge towards the plate's centre no vanishing transverse normal stress is achieved, while the RMVT provides it perfectly. This effect is more pronounced for the ESL models than for the LW models, as the LW descriptions helps to minimize the occurring difference. It has been shown in [17], that one can overcome the incomplete fulfilment of the ICs for the PVD based models by simply adding several mathematical layers per physical layer. Concerning the order of expansion, it can be stated, that the higher the order, the higher the maximum stress achieved at the free edge. Two last aspects about the ESL models are notable: while the ED4 and EDz3 model have the same number of DOFs, the Figures indicate that higher order expansion is more important than the inclusion of the discontinuity at the interface from the Zig-Zag model. That the inclusion of the Zig-Zag itself is not the best choice for the modeling of free-edge effects is also indicated by the comparison of the EM2 and EMz2 model. The additional Zig-Zag DOF in the EMz2 model does provide a worse behaviour compared to the EM2 model.

A last remark is about the different phenomena occurring for the presented cross-ply laminates: As the 0 degree layer is at the top and the bottom of the laminate, a compressive behaviour is provoked by the Poisson's effect through the thickness by the uniform extension. The contrary is the case if the 90 degree layer is at the top and bottom layer as the load is applied normal to the fibre direction.

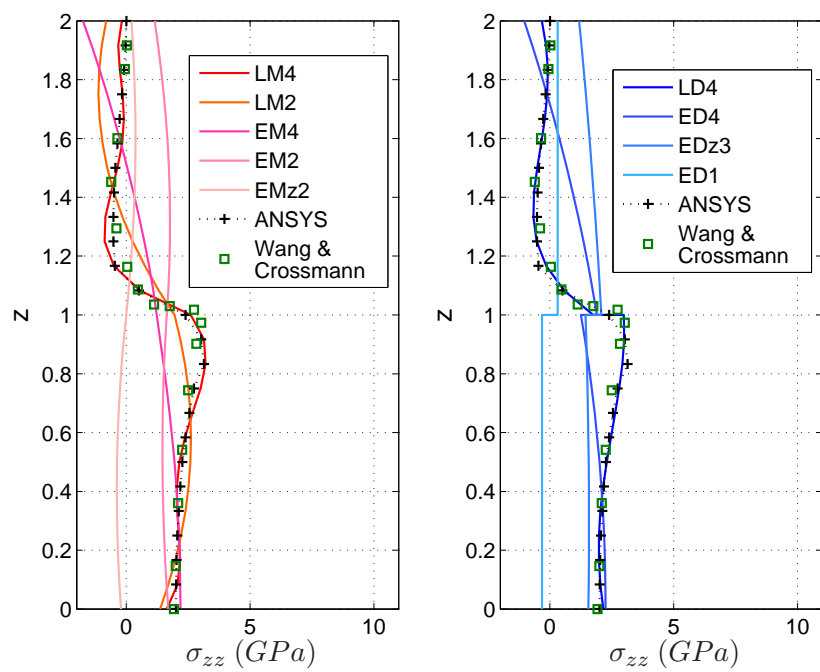


Figure 3.1: Extension:  $\sigma_{zz}$  at  $(x = 0, y = b, z)$  for  $[0, 90]_s$  using RMVT & PVD

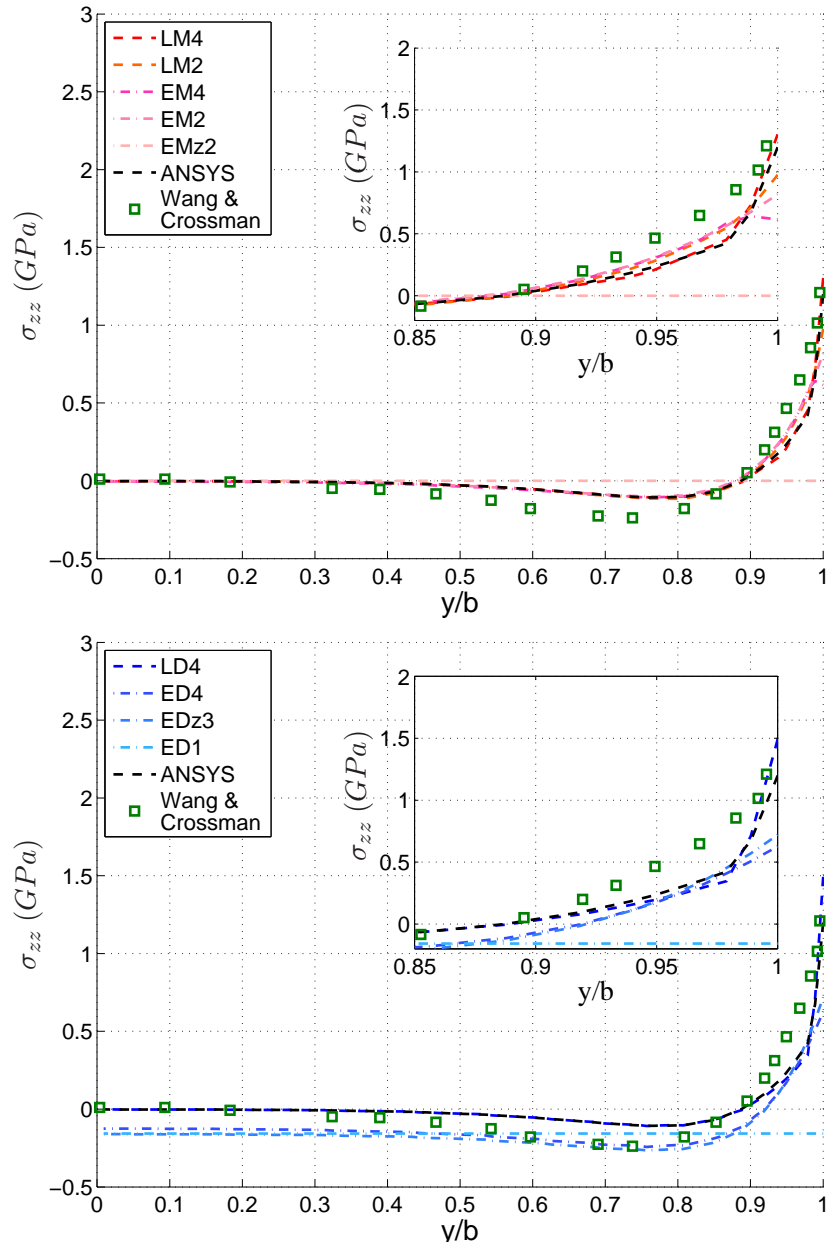


Figure 3.2: Extension:  $\sigma_{zz}$  at  $(x = 0, y, z = \frac{h}{4})$  for  $[0, 90]_s$  using RMVT & PVD

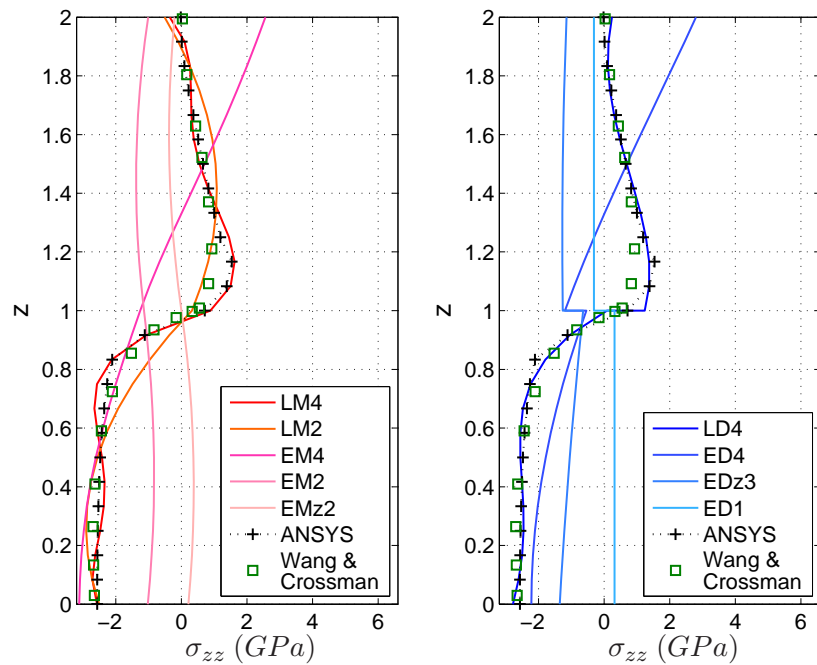


Figure 3.3: Extension:  $\sigma_{zz}$  at  $(x = 0, y = b, z)$  for  $[90, 0]_s$  using RMVT & PVD

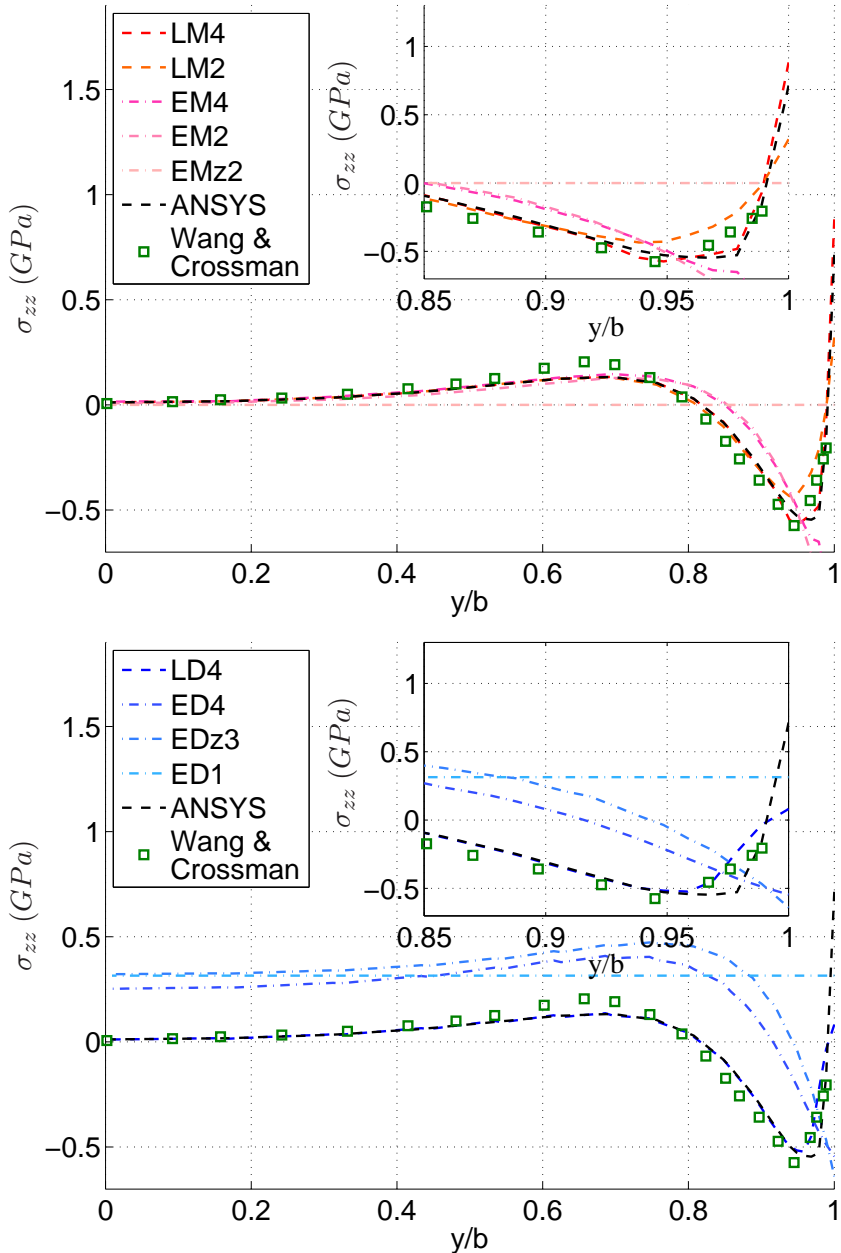


Figure 3.4: Extension:  $\sigma_{zz}$  at  $(x = 0, y, z = \frac{h}{4})$  for  $[90, 0]_s$  using RMVT & PVD

### 3.1.1.2 Angle-Ply Laminates

The results for angle-ply laminate  $[\pm 45]_s$  are given in Figure 3.5. The Poisson's ratio mismatch is not present any more. Due to the in-plane shear coupling the role of the transverse shear  $\sigma_{xz}$  is more important than for the cross-ply laminates. The gradients of this stress component is more pronounced compared to the cross-ply laminates. The distribution through the thickness shows a perfect match of both LW models, regardless of the variational statement used. In the case of PVD, a different behaviour at the interface is visible. As the shear stiffnesses of the adjacent layers are equal through thickness, the transverse shear component is continuous throughout the thickness. This leads to a disappearance of the jump of the transverse stress levels at the interface. ESL models still fail to predict the local maximum, for both PVD and RMVT, and provide only a mean value. For the angle-ply laminate the influence of the expansion order is as before: the higher the order, the higher the maximum stress. Summing up those aspects, only the forth order LW models are able to match the results by Wang and Crosman and the three-dimensional FE results.

The distribution along the width towards the free edge is given in Figure 3.6 for the upper  $\pm 45$  interface. The higher order LW models further confirm their superiority. Higher order PVD or RMVT models achieve higher stresses, the ESL description fails to have a good agreement close to the free edge with the three-dimensional FE results and the results by Wang and Crossman.

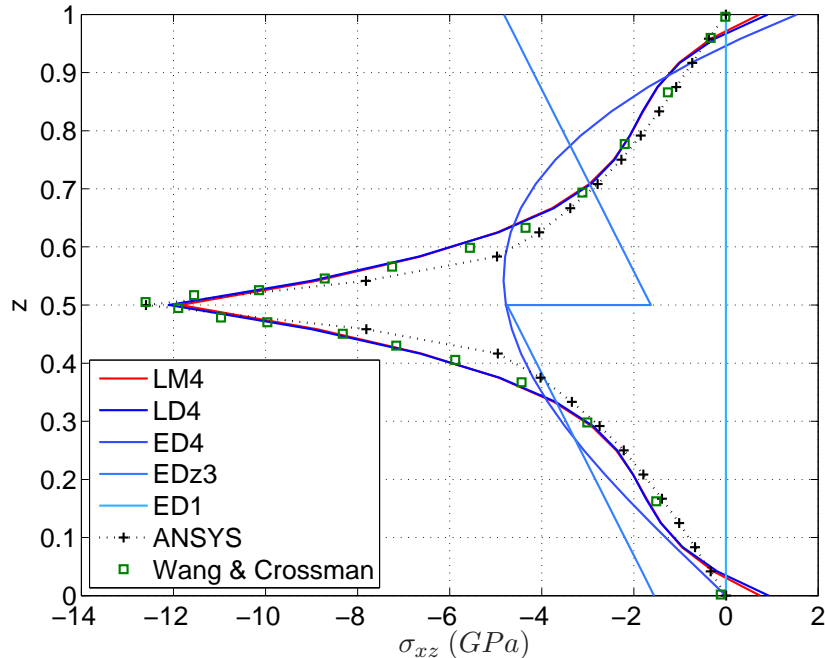


Figure 3.5: Extension:  $\sigma_{xz}$  at  $(x = 0, y = b, z)$  for  $[\pm 45]_s$  using RMVT & PVD

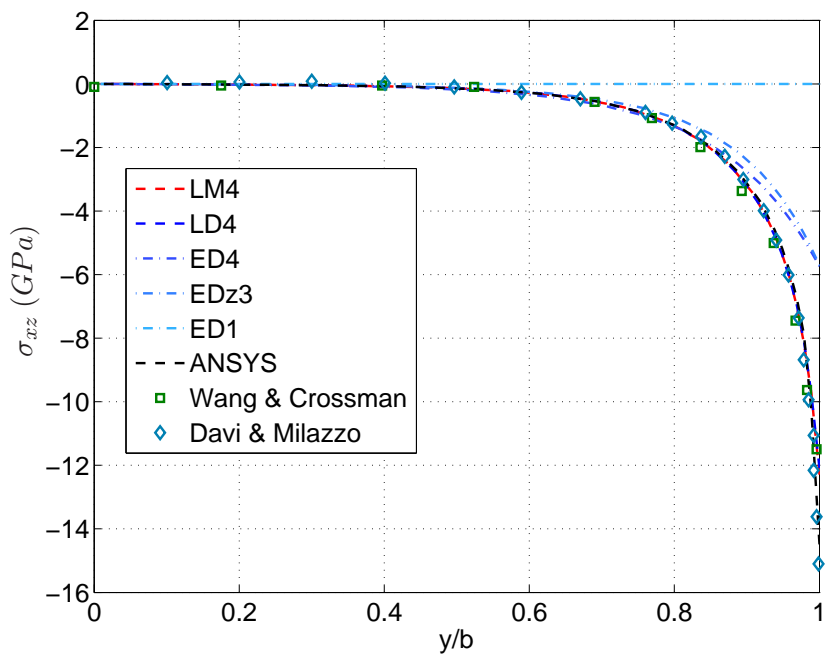


Figure 3.6: Extension:  $\sigma_{xz}$  at  $(x = -a, y, z = \frac{h}{4})$  for  $[\pm 45]_s$  using RMVT & PVD

### 3.1.1.3 Quasi-Isotropic Laminates

Two quasi-isotropic laminates, the  $[90, 0, \pm 45]_s$  and  $[\pm 45, 0, 90]_s$ , are presented here, which include the before stated angle-ply and cross-ply interfaces, plus one interface of only 45 degree difference between the layers. Results for these laminates are also provided by Wang and Crossman. Their results distributions through the thickness of the CUF models are given in Figure 3.7. For the first laminate, the thickness distribution of  $\sigma_{zz}$  shows a perfect accordance with the previous findings. Through the multiple interfaces, all of the before mentioned effects of the cross- and angle-ply lay-ups are present. The performance of the different LW and ESL descriptions, the remarks on PVD and RMVT statements and the expansion order is as stated before. The higher order PVD and RMVT LW models perfectly match the results obtained with the commercial three-dimensional code Ansys and the results given by Wang and Crossman. The same applies for the thickness distribution of the  $[\pm 45, 0, 90]_s$  lay-up, which is not shown for the sake of brevity. An example of a distribution along the width is given in Figure 3.8, where  $\sigma_{xz}$  is reported for the upper  $\pm 45$  interface.

For the cross-ply and angle-ply laminates it was stated that the ESL models have a good accordance with the three-dimensional results and the reference results far from the free edge. This does also hold true for the quasi-isotropic laminates. For both, PVD and RMVT models, with rising order of the polynomial, the point though width up to which the distributions are in good accordance with the reference is reaching further out.

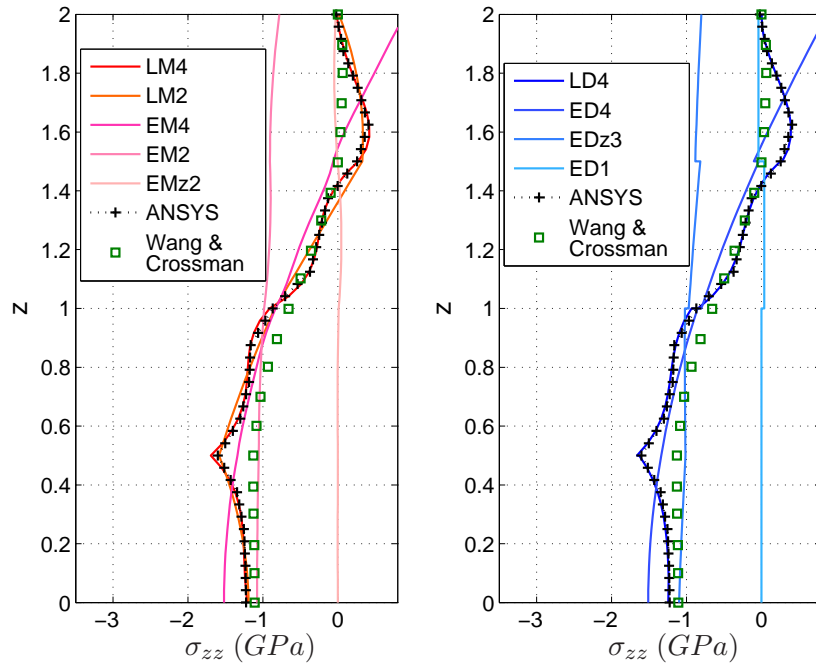


Figure 3.7: Extension:  $\sigma_{zz}$  at  $(x = -a, y = b, z)$  for  $[90, 0, \pm 45]_s$  using RMVT & PVD

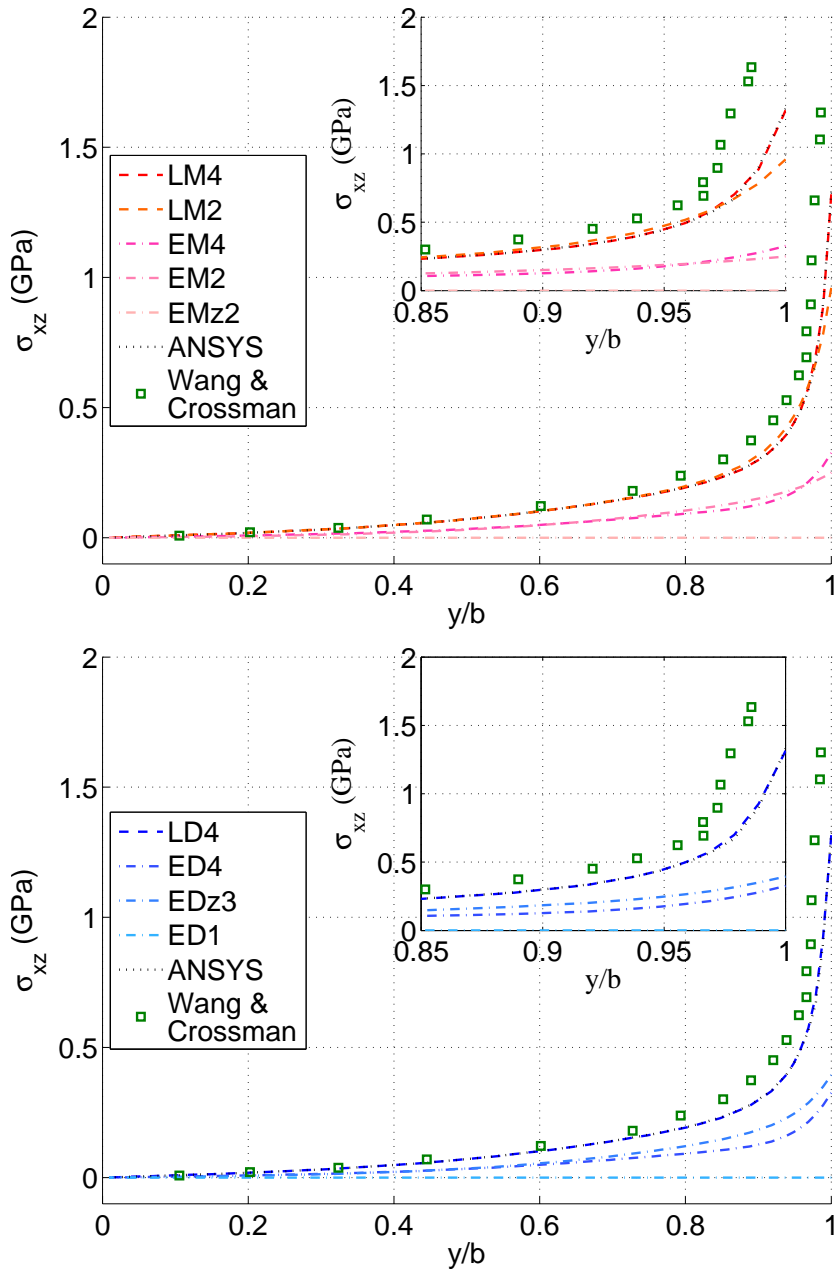


Figure 3.8: Extension:  $\sigma_{xz}$  at  $(x = 0, y, z = \frac{3h}{8})$  for  $[\pm 45, 0, 90]_s$  using RMVT & PVD

### 3.1.2 Mesh Sensitivity

In the previous sections, the sharp gradients for the different laminates have been shown for a fixed FE mesh. Here the sensitivity of those gradients to different FE meshes is discussed. Only the most accurate LM4 and LD4 models will be considered.

All meshes used before are refined in a regular manner, using a spacing ratio towards the plate's center along the plate's length and towards the free edges across its half-width, see Figure 3.9. The spacing of the elements is chosen so that the smallest element lies at the free edge ( $y = \pm b$ ) and at  $x = 0$  and that it has a square shape. Starting with a rather raw mesh of  $16 \times 16$  elements, the mesh is stepwise refined up to  $72 \times 72$  elements. This mesh will be called hereafter mesh ( $I$ ).

Figure 3.10 gives a zoom on the bimaterial interface of the  $[\pm 45]_s$  laminate. For different meshes the distributions through thickness of  $\sigma_{xz}$  are given. With refining the mesh, slightly higher stresses are obtained. However the difference is seen to be quite low for the angle-ply laminate. A different picture can be seen for the  $[0, 90]_s$  cross-ply laminate in Figure 3.11, concerning  $\sigma_{zz}$ . Here a zoom towards the free edge for the width distribution is given for the same meshes and models. The stress values are taken at the nodes of the meshes. It can be noticed that: the stress is increasing with a refined mesh. Comparing the effect of the refinements for cross-ply and angle-ply laminates leads to the conclusion that the stress increase is more pronounced in the cross-ply laminates.

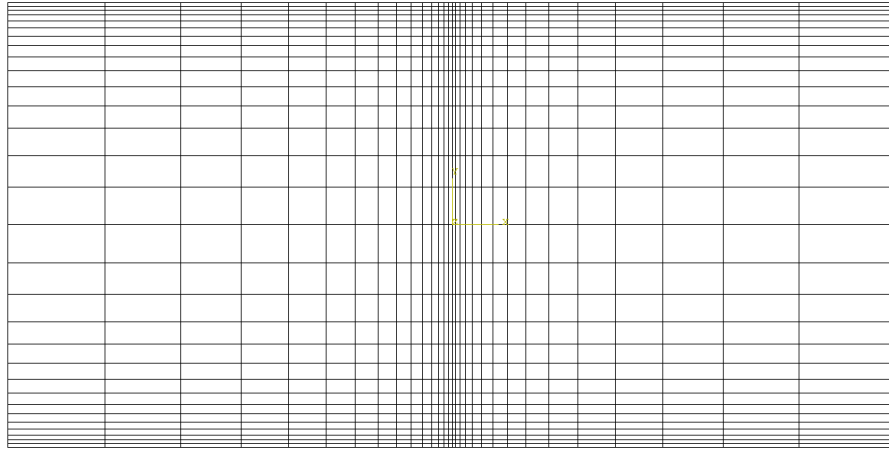


Figure 3.9: Principle of the regularly and continuously refined in-plane mesh ( $I$ )

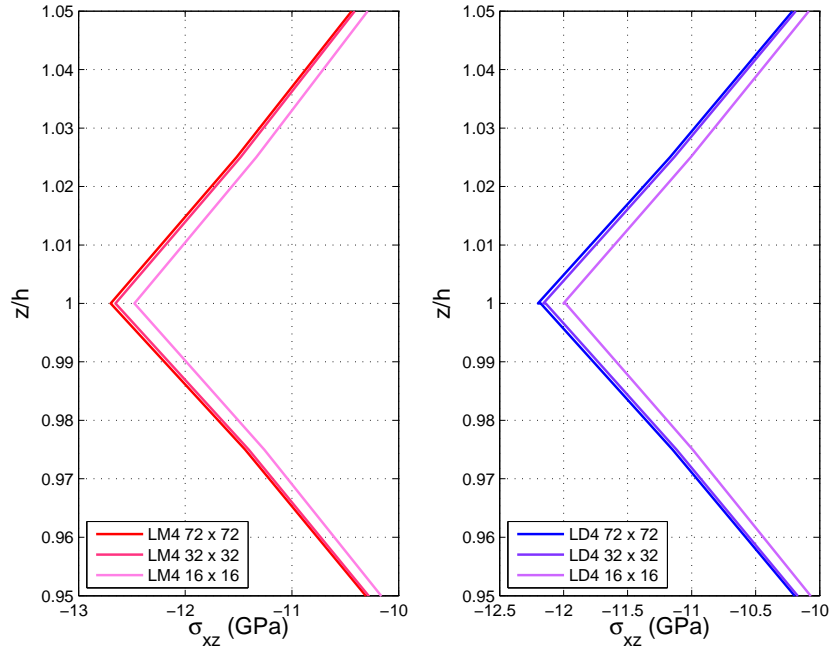


Figure 3.10: Extension: sensitivity of regular meshes of  $\sigma_{xz}$  at  $(x = 0, y = b, z)$  for  $[\pm 45]_s$  using LM4 & LD4

While the regular refinement revealed only a small increase of the stresses, in a second step, an irregularly mesh refinement is used, called hereafter mesh (II). This is done in order to have a high number of elements in the immediate vicinity of the free edge. For this region, it is tested whether a regular spacing or an irregular refinement towards the free edge does visibly affect the stress intensity. Hence, two different zones for the spacing ratios are defined along the plate's width, in order to mesh the plate's borders along the free edges separately. Further, a significantly higher number of elements in the width direction  $y$  is used, compared to the plate length in the  $x$ -direction, with very small elements close to the free edge. As has been shown by D'Ottavio [17], only few elements are needed in the  $x$ -direction in the extension case, to match the condition of  $\epsilon_{xx} = 1$  and in order to have congruent results with the references. Hence only 8 elements are used in length direction, while a finer discretization with  $N_{ey}^{in} = 30$  elements is applied in width. The border region, which has a width of  $0.1h_k$ , contains now additional  $N_{ey}^{br} = 15$  or 30 elements in width. A scheme of the employed meshing strategy is illustrated in Figure 3.12. Figure 3.13 shows for the separated meshing, that no visible impact of the regular or irregular spacing appears as long as only one mathematical layer is applied per physical layer. Comparing with the maximum stress levels in Figure 3.11, higher maximum stresses are obtained.

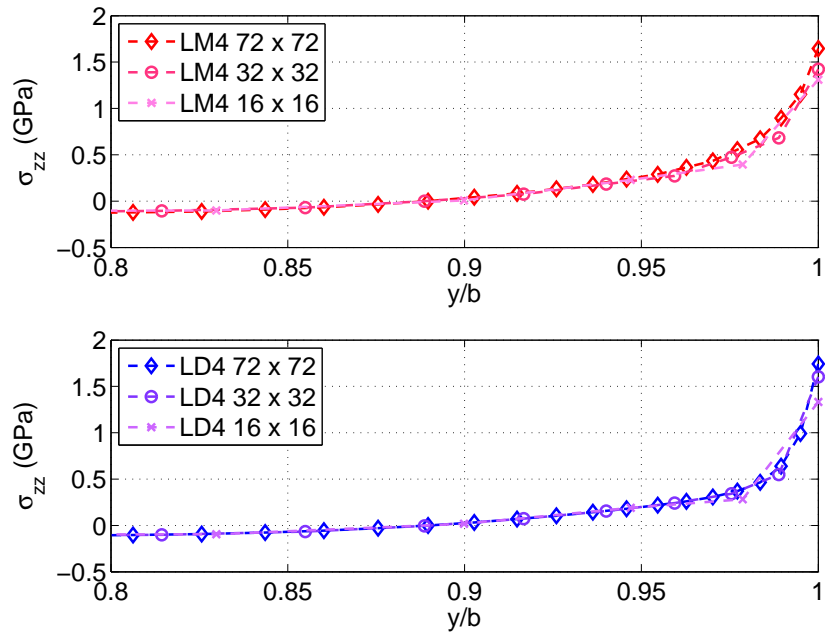


Figure 3.11: Extension: sensitivity of regular meshes on  $\sigma_{zz}$  at  $(x = 0, y, z = \frac{h}{4})$  for  $[0, 90]_s$  using LM4 & LD4

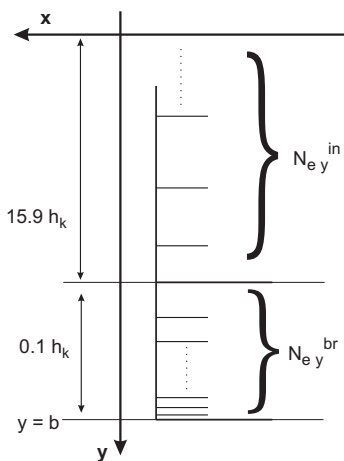


Figure 3.12: Principle of partly refinement through width for mesh (II)

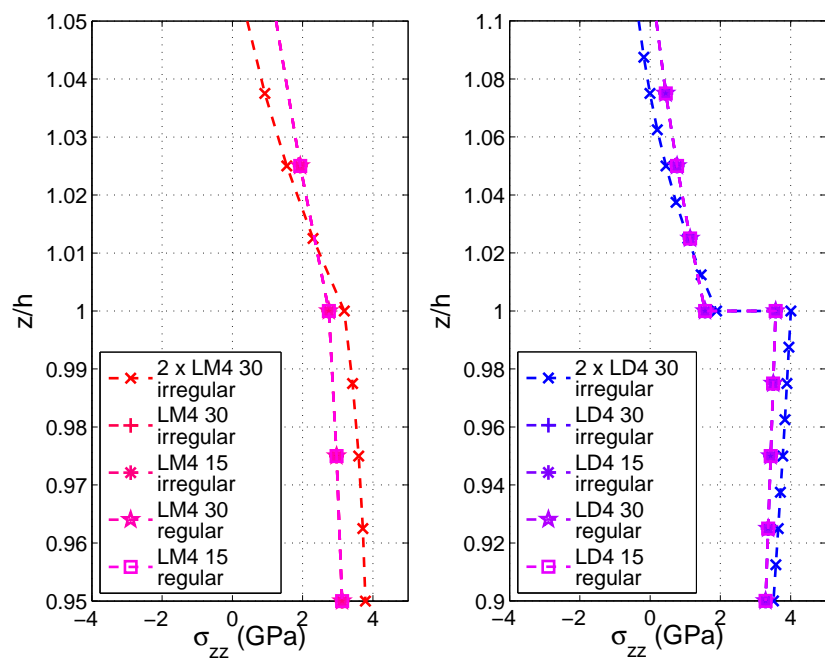


Figure 3.13: Extension: sensitivity of refined meshes of  $\sigma_{zz}$  at  $(x = 0, y = b, z)$  for  $[0, 90]_s$  using LM4 & LD4

### 3.1.3 Influence of through the thickness refinement

In Figure 3.13, the stress level does significantly rise for the application of two mathematical layers per physical layer. Therefore the use of a number of mathematical layers  $N_{ml} > 1$  per physical layer is investigated here. The use of several regular distributed mathematical layers per physical layer has already been suggested by D’Ottavio [17] to reduce the incomplete fulfillment of the ICs in of the LD models and further to provide a better distribution across the width close to the free edge. A further investigation by Sab et al. [69] for a similar class of two-dimensional elements with a suitable thickness expansion highlighted the advantages of using several mathematical layers per physical layer. Further they highlighted the advantage of having an irregular distribution of the mathematical layers through the thickness of one physical layer, with the thickness  $h_{mk}$  of the mathematical layers getting smaller towards the interface of the physical layer.

The application of mathematical layers per physical layer is further studied for the  $[\pm 45]_s$  angle-ply laminate, where for more than two mathematical layers an irregular distribution is applied. The irregular distributed mathematical layers are as follows:

- for  $N_{ml} = 3$ :  $h_{mk} = [0.25, 0.5, 0.25]h_k$
- for  $N_{ml} = 4$ :  $h_{mk} = [0.075, 0.425, 0.425, 0.075]h_k$
- for  $N_{ml} = 5$ :  $h_{mk} = [0.05, 0.2, 0.5, 0.2, 0.05]h_k$

Figure 3.14 reports the results for the LD4 model, indicating a significant rise with the increase of  $N_{ml}$  per physical layer. For the case of three irregular distributed mathematical layers, the stress levels achieved are higher than for the four regular distributed mathematical layers. For mesh (I), the important increase in the stress levels at the free edge was not visible in the same manner as for the separated refinements in mesh (II). This is shown in Figure 3.15 for the irregular refinements with  $N_{ml} = 2$  and the regular refinement with only one mathematical layer per physical layer.

Concerning the sensitivity of the different models to reproduce the stress singularities, it is hard to judge this aspect based on the different distributions provided in the earlier sections and here. Both rise and seem to have quite comparable behaviour. Another criterion has to be used therefore, in order to provide a significant comparison. In order to do so, the mesh with the separated refinements will be used.

The effects of the refinement in thickness direction was validated by a generalized plane strain model in Ansys for the cross-ply laminate  $[0, 90]_s$ , representing only the cross-section of the laminate. For the mesh, made of quadratic elements, the same spacing could be applied through width as illustrated in Figure 3.12. Here the spacing of the elements through the thickness of the physical layer is changed. The form of the last element at the free edge and at the layers interface is changed through the

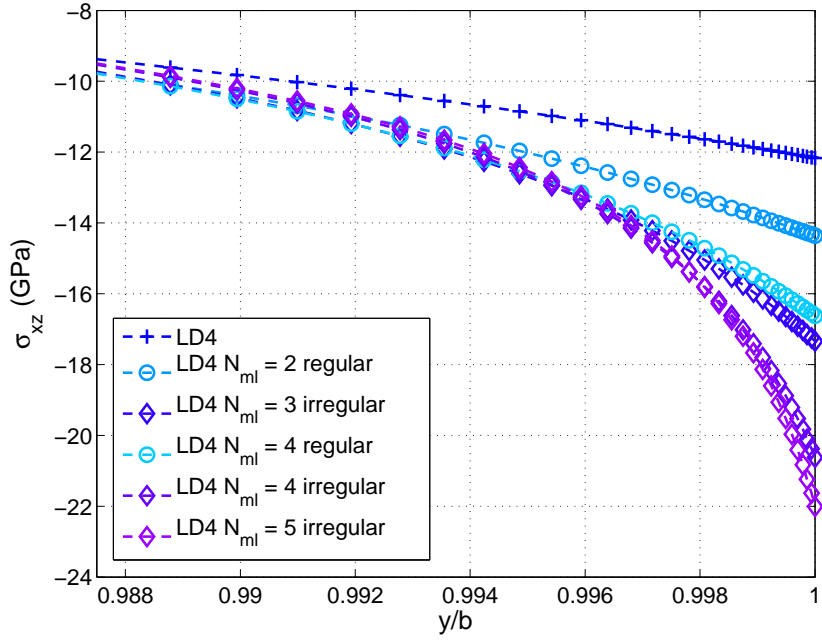


Figure 3.14: Extension: sensitivity of  $N_{ml}$  for  $\sigma_{xz}$  at  $(x = 0, y, z = \frac{h}{4})$  for  $[\pm 45]_s$  using LM4 & LD4

refinements from a rectangular towards a quadratic form. Figure 3.17 states the stress at the bimaterial interface along the width for the zone close to the free edge. Three curves, differing in the size of the last element at the bimaterial interface are given. They reveal that while having a rectangular form of 12 times the width, the transverse normal stresses  $\sigma_{zz}$  of the last elements before the free edge are not the increasing, but sinking. While refining, the spacing of the elements towards the interfaces, up to the the quadratic element a monotonous rise is provided.

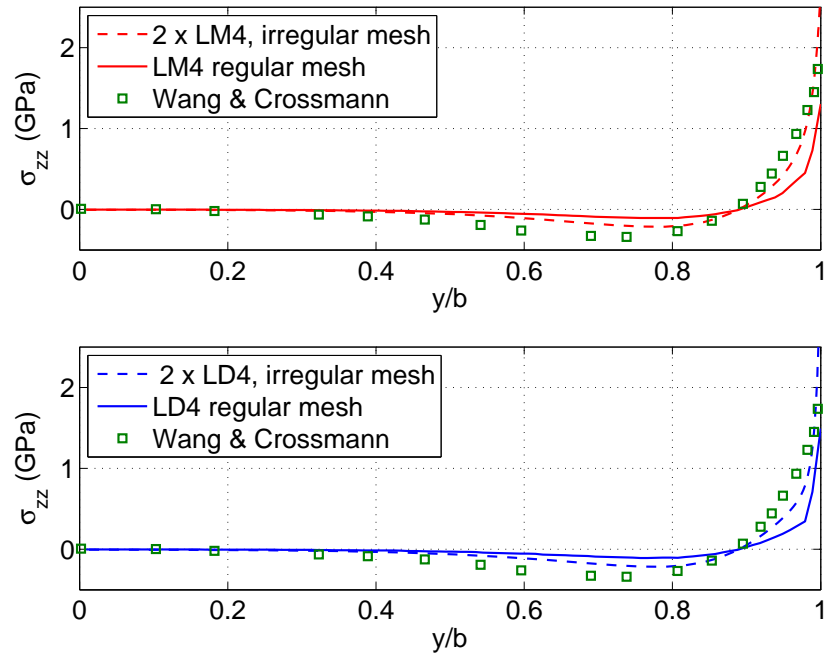


Figure 3.15: Extension: Confrontation of regular and irregular refined meshes;  $\sigma_{zz}$  at  $(x = 0, y, z = \frac{h}{4})$  for  $[0, 90]_s$  using LM4 & LD4

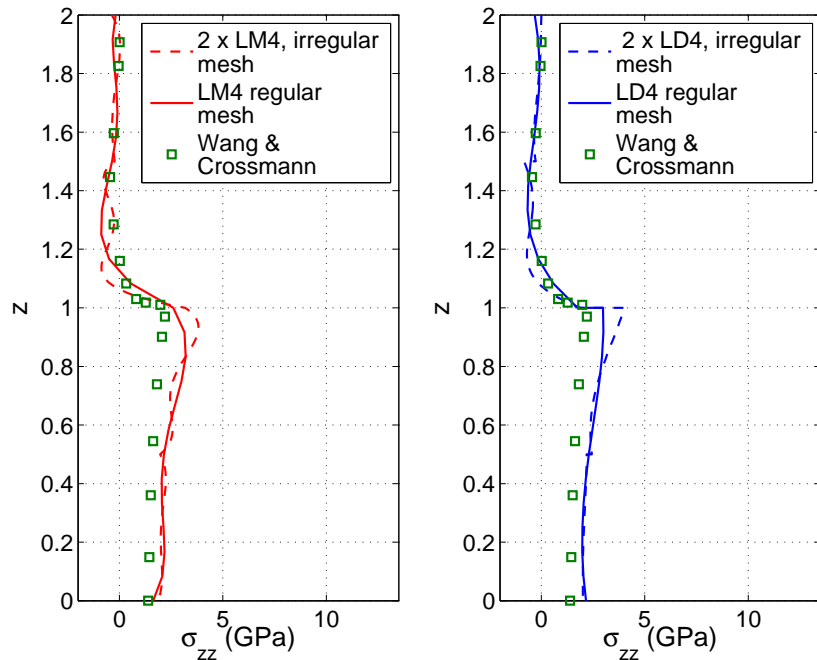


Figure 3.16: Extension: Confrontation of regular and irregular refined meshes;  $\sigma_{zz}$  at  $(x = 0, y = b, z)$  for  $[0, 90]_s$  using LM4 & LD4

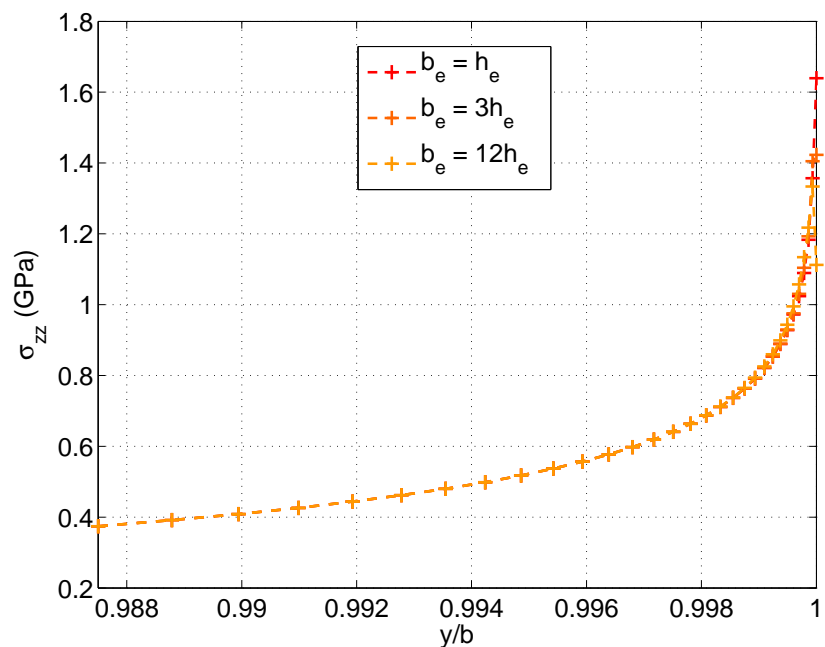


Figure 3.17: Extension: mesh sensitivity of  $\sigma_{zz}$  at  $(x = 0, y, z = \frac{h}{4})$  for  $[0, 90]_s$  using a generalized plain strain model within Ansys

### 3.1.4 Assessment of the Order of Singularity

#### 3.1.4.1 Power Law Representation

It has been shown, that the transverse stress components in the immediate vicinity of the free edge showed a monotonous rise towards the edge. Two components of the transverse stresses are unbounded through the traction free condition at the free edge: the transverse normal stress  $\sigma_{zz}$  at the cross-ply interfaces and the transverse shear stress  $\sigma_{xz}$  at the angle-ply interfaces. The previous section analyzed the sensitivity of the peaks of these stresses with respect to the in-plane FE mesh and the number of mathematical layers: this latter refinement appeared to greatly influence the maximum value of these stress components at the free edge. Therefore, different authors proposed to express these stress components close to the free edge via an exponential power law which represents the singular behaviour. Using the results of the different FE models, a fitting process derives the parameters of the power law. Comparing those parameters provides a measurement of the singularities and a tool to compare the different FE models at the same time. Among the authors who proposed this method were Raju and Crews [61], Zwiers, Ting and Spilker [66], Ghiringhelli and Sala [23] as well as Davì and Milazzo [14]. Similar works, assuming a slightly modified form of the power law were done by Bar-Yoseph and Avrashi [3] and Icardi and Beretto [35], while Mittelstedt and Becker [48] developed a special formulation in order to directly compute the order of singularity.

The stress in immediate vicinity to the free edge is supposed to have the following form, using the power  $\alpha_{ij}$  and the strength  $|A_{ij}|$  of the singularity:

$$\sigma_{ij}(y) \approx A_{ij} r(y)^{-\alpha_{ij}} \quad \text{with } 0 < \alpha_{ij} < 1 \quad (3.1)$$

where  $r$  denotes the distance from the free edge:

$$r(y) = \frac{b - y}{h_k} \quad \text{with } r \in ]0; 1] \quad (3.2)$$

Figure 3.18 shows that the distance  $r$  may be defined at any value of the angle  $\beta$ . In this work however, only the case of  $\beta = 0$  will be considered. This amounts to consider only the singularity occurring at the bimaterial interface.

According to Equation (3.1) infinite values of  $\sigma_{ij}$  are obtained for  $r \rightarrow 0$ . A convenient way to represent the singularity described by the power law is to plot the function in a double logarithmic scale, which yields a linear dependency on the distance  $r$ :

$$\log(\sigma_{ij}(r)) \approx \log(|A_{ij}|) - \alpha_{ij}r \quad (3.3)$$

This way, the power of the singularity  $\alpha_{ij}$  describes the slope of the singular trend, while the singularity strength  $|A_{ij}|$  is related to the length of the influence of the singularity itself or equivalently to the finite value of the stress at a distance  $r = 1$  (i.e.  $y = b - h_k$ ) from the free edge. Therefore low values of  $\alpha_{ij}$  correspond with high values of  $|A_{ij}|$  and vice versa. This is shown in Figure 3.19, where for powers

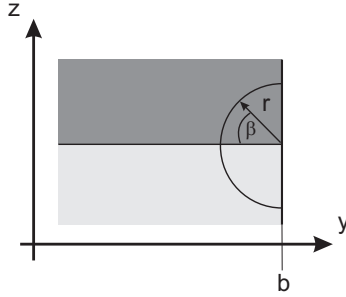


Figure 3.18: The distance  $r$  is measured from the free edge along the plate width and at the layers interface, ( $\beta = 0$ )

$\alpha_1 < \alpha_2$  two different singularity strengths  $A_1 < A_2$  are given. For a lower  $\alpha_{ij}$  the curve has to rise earlier and hence  $A_{ij}$  has to be higher. For the higher  $\alpha_{ij}$  the slope close to the free edge has a steeper rise.

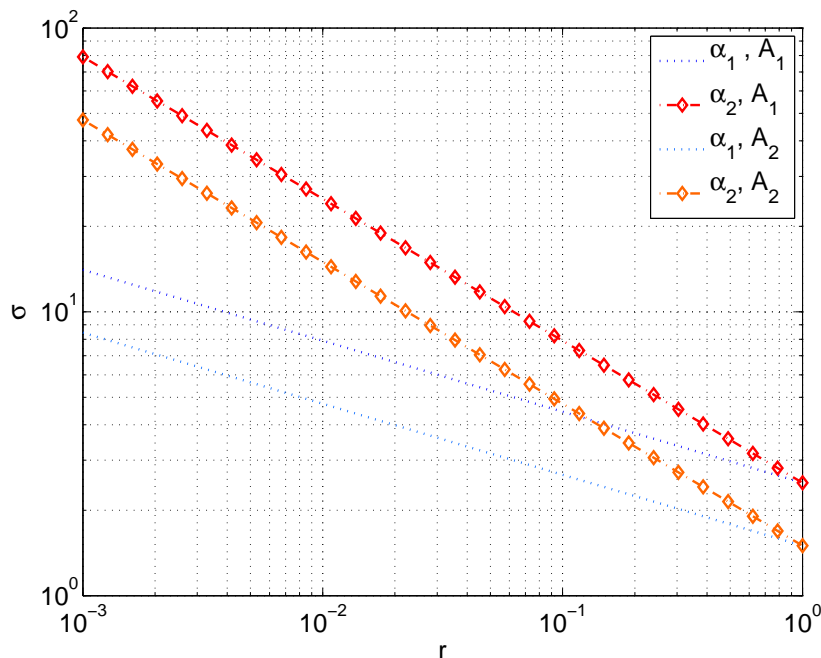


Figure 3.19: Stress representation using the power law; using:  $\alpha_1 < \alpha_2, A_1 < A_2$

In order to reconstruct the power law from the FE results, a curve fitting procedure is adopted based on a least squares interpolation and a 95 % trust regain. It is necessary to have as many stress values as possible in the immediate vicinity of the free edge if a reliable determination of the power law parameters is sought. Since the stress values are sampled at the nodes, a very fine mesh is assigned at the free edge. Note that if several stress values are taken inside one single element, these

are linearly dependent data points, that do not improve the interpolation process for obtaining the power law parameters. Therefore the mesh (*II*), as introduced before in section 3.1.2, is used, as illustrated in Figure 3.12. Only the nodes contained in the narrow region close to the free edge are used for determining the power law parameters. It is noted that the selected interval corresponds to that used by Davì and Milazzo [14]. These authors followed a similar approach for determining the power law parameters, however starting from stress values obtained by means of a Boundary Element Method. Their results obtained for  $\sigma_{xz}$  singularity occurring in the angle-ply  $[\pm 45]_s$  laminate loaded in extension will be used as a reference values.

The in-plane mesh used for the present CUF models employs 30 elements in the region  $y \in [0, 0.9875b]$  with a spacing ratio of 60, which leads to a small element width of  $0.0088h_k$ . In the region  $y \in [0.9875b, b]$ , 30 elements are used with a spacing ratio of 20, which leads to a smallest element of  $0.002h_k$ . Remind that through the geometry of the plate  $b = 8h_k$ . The role of increasing the number of mathematical layers is investigated in Figure 3.20. From the Figure, two regions can be identified: a first region with a linear rise starting at  $r = 0.1$  and a second region with a horizontal distribution close to the free edge itself. In between a very small transition zone is present, too. The size of the region with the linear rise does vary visibly depending on the number of mathematical layers per physical layer: the stress levels show a significant rise and also an increase of the size of the zone with the linear rise. Depending on how many mathematical layers are used, this region extends within  $10^{-2} < r < 10^{-1}$ . In an attempt to enlarge this interval upon increasing the resolution next to the interfaces, Lagrange polynomials interpolated at Chebyshev nodes [44] have been used instead of the standard Legendre polynomials of CUF. However, no relevant improvement could be remarked for the present application.

The convergence behaviour of the via power law fitting extracted coefficients  $\alpha_{xz}$  and  $|A_{xz}|$  is given in Table 3.2. Only the linear rising part of the curves has been considered, which is in the interval of  $2 \cdot 10^{-2} < r < 10^{-1}$ .

Table 3.2: Extension: Convergence of  $\alpha_{xz}$  and  $|A_{xz}|$  for the  $[\pm 45]_s$  lay-up

Method/Mesh	$ A_{xz} $	$\alpha_{xz}$
Davi Milazzo	5.0280	0.2630
Ansys	4.9758	0.2884
LM4, $N_{ml} = 1$	7.0380	0.1460
LD4, $N_{ml} = 1$	6.9099	0.1399
LM4, $N_{ml} = 2$	6.2170	0.2123
LD4, $N_{ml} = 2$	6.3246	0.1979
LD4, $N_{ml} = 3$	4.9793	0.2894
LD4, $N_{ml} = 4$ regular	5.5611	0.2529
LD4, $N_{ml} = 4$ irregular	4.9186	0.2920
LD4, $N_{ml} = 5$ irregular	4.9212	0.2895
$ A_{xz} $ in [GPa]		

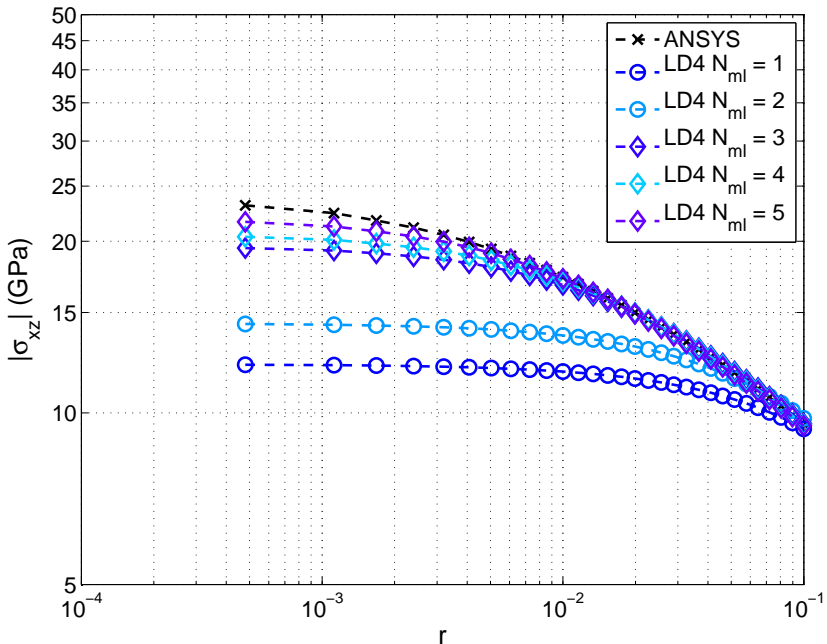


Figure 3.20: Extension: width distribution of  $\sigma_{xz}$ ; application of several irregular distributed mathematical layer per physical layer using LD4 for the  $[\pm 45]_s$  laminate

From Table 3.2 it gets further visible, that the use of LM4 was limited up to two mathematical layers per physical layer. In the following therefore, two mathematical layers for each physical layer are used. Even if it is desirable to have more mathematical layers per physical layer, it is limited by the maximum main memory of the CUF implementation into ABAQUS. The calculations were carried out on a four core Pentium *IV* computer with 48 GB of RAM. Having more than two mathematical layers per physical layer in the most demanding LM4 case with a mesh of 80\*120 elements and four physical layers was not possible. This configuration needed about two hours of calculation for the configuration of five mathematical layers using LD4. In contrast the FE calculations carried out with the three-dimensional model in Ansys needed about four hours.

A last statement concerning the horizontal plateau is done. One might even decrease the region of the horizontal plateau even more, through the application of even a higher number of mathematical layers, decreasing further the size of the mathematical layers  $h_{mk}$ . The before stated Figure 3.17, giving the stress for the generalized plain strain elements, is now also given in a double logarithmic plot. From Figure 3.21 a longer region for the horizontal rise can be observed here with an decreasing height  $h_e$ .

After assuring the convergence trend behaviour as a function of the number of mathematical layers, a comparison of the attempted values and the values by the CUF is done. Due to the computational architecture used, the precious LM4 model

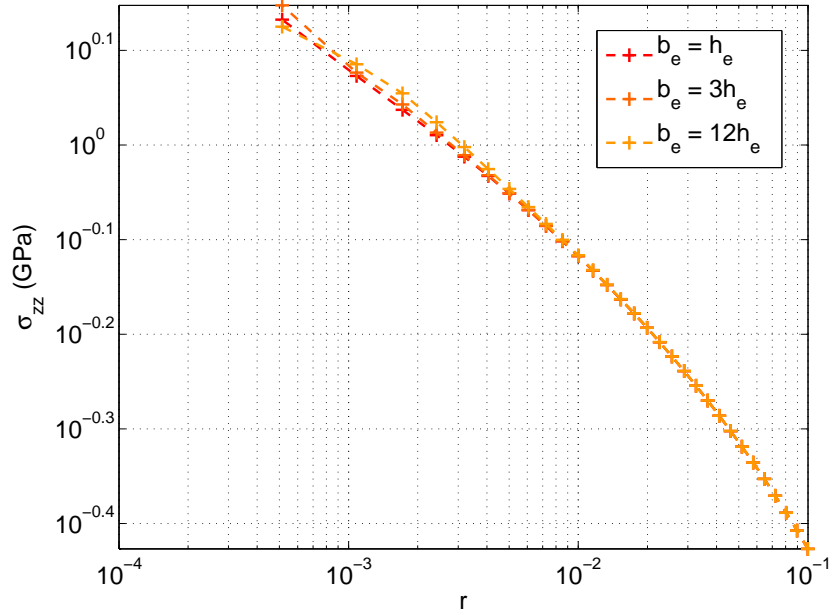


Figure 3.21: Extension: mesh sensitivity of  $\sigma_{zz}$  at  $(x = 0, y, z = \frac{h}{4})$  for  $[0, 90]_s$  using an Ansys Quasi three-dimensional model

is restricted to  $N_{ml} = 2$ . Davì and Milazzo's value, as well as the value obtained within Ansys are compared with the fitting points as well as the fitted curves for LM4 and LD4 in Figure 3.22. The mentioned difference in singularity strength  $|A_{xz}|$  between Davì and Milazzo and LM4 and LD4 are visible, where the slope of all three curves is identical. However, in the distribution through width, see Figure 3.6, all values showed a good accordance. The identical slopes, together with a good accordance of  $\alpha_{xz}$  indicates that the FE mesh is sufficiently fine and converged for the purposes of the assessment of the singularities.

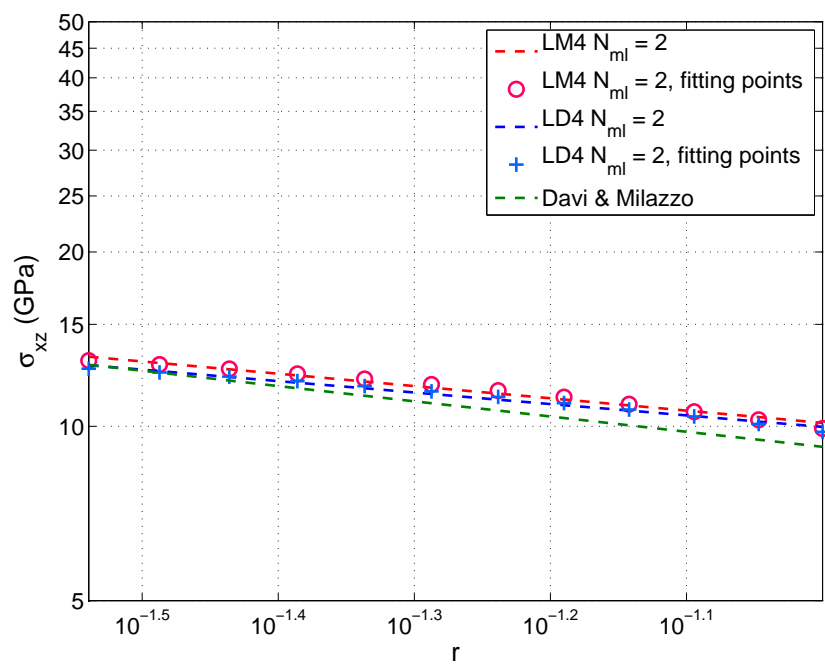


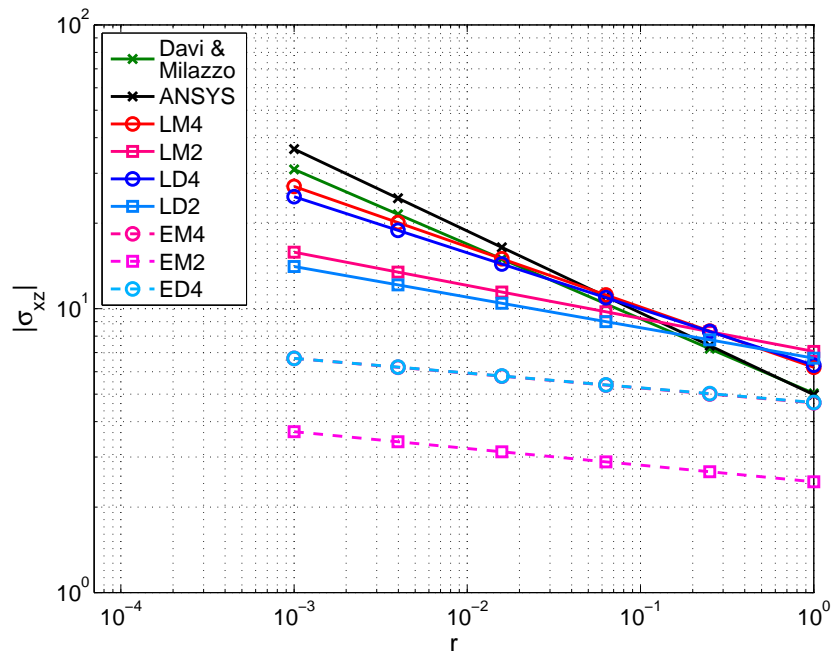
Figure 3.22: Quality of fit of  $\sigma_{xz}$  according to power law representation for the  $[\pm 45]_s$  laminate at  $(x = 0, y, z = \frac{h}{4})$

### 3.1.4.2 Assessement

With the help of the parameters an assessment of the performance of the CUF models to provide the singularities appearing is now possible. Comparing the results from Table 3.3 with the distribution through width in Figure 3.6 provides us with two pieces of information: the first its that for a value of  $\alpha_{xz}$  matching with the reference and the value computed with the help of Ansys, a proper distribution is expected. If the values is in good accordance, it is the provided singularity strength  $|A_{xz}|$  which indicates how critical the appearing singularity according to the used model is. It is again the three criterion of comparison for the CUF models which are used here: the lay-up description used, the variational statement and the expansion order. While using the LW model, values close to the three-dimensional FE results by Ansys are obtained. ESL models do provide lower values for the singularity power. Comparing the variational statements it gets especially visible for the ESL description, that while the RMVT statement is used, a singularity power closer to the value provided by Ansys is obtained. Nevertheless, the error is quite high. As highlighted before, it is the higher order expansions which provide better accordance, lower order models are not able to properly reproduce the overall singular behaviour. Note that for the singular fitting, also LD2 is listed, which was not presented before in the given distributions. This is due to its PVD characteristic, providing only linear stresses through thickness per mathematical layer. However, while using two mathematical layers through thickness, as used here for the fitting, a better accordance with the reference solution is obtained. Summing up all aspects about the CUF models, the LM4 and LD4 model provide the best prediction of the singularity. For the best performing models, in Figure 3.23 the stress is expressed via the power law parameters. It illustrates the good accordance of the higher order LW models with the reference given by Davi' and Milazzo and the results gained with Ansys.

Table 3.3: Extension:  $\alpha_{xz}$  and  $|A_{xz}|$  towards the  $[\pm 45]_s$  lay-up

Method/Mesh	$ A_{xz} $	$\alpha_{xz}$
Davì Milazzo	5.0280	0.2630
Ansys	4.9758	0.2884
LM4	6.2170	0.2123
LM2	7.0658	0.1165
LD4	6.3246	0.1979
LD2	6.6906	0.1077
EM4	4.6581	0.0522
EM2	2.4543	0.0589
EMz2	7.6374	0.3916
ED4	4.6722	0.0518
EDz3	2.4559	0.0584
ED1	3.1530	0.0496
$ A_{xz} $ in [GPa]		


 Figure 3.23: Assessment of power law fitting parameters: stress  $\sigma_{xz}$  for the  $[\pm 45]_s$  laminate at  $(x = 0, y, z = \frac{h}{4})$ 

Above it was described that low values of  $|A_{ij}|$  correspond with high values of  $\alpha_{ij}$  due to the nature of the fitting process. The forth order ESL models in Tables 3.3 have a singularity strength  $|A_{xz}|$  close to the value provided by Ansys, but the singu-

larity power  $\alpha_{xz}$  has a large difference. Comparing their distributions through width in Figure 3.6 showed a modest rise of the stress towards the free edge, compared with the higher order LW models and the three-dimensional models results. As the values of the fitting points are based on the stress values at the nodes, it is this modest rise which enforces the fitting process to adapt to a lower  $\alpha_{xz}$ . By enlarging the interval of  $r$ , a convergence towards higher values of  $\alpha_{ij}$  may be obtained. Before reviewing the issue of the interaction between  $\alpha_{ij}$  and  $|A_{ij}|$  in further detail, the results of the other four layer lay-ups will be compared.

Before passing to the other laminates, a further investigation of the different LW models is carried out. In order to gain better parameters, it was described above that the number of mathematical layers  $N_{ml}$  has to be increased. In Table 3.4 a comparison for the LM4 and LM2 as well as the LD4 and the LD2 elements is given. The sensitivity analysis shows that it is advantageous to apply twice the number  $N_{ml}$  with only half the expansion order. The same test was done for the EM elements, however they show an insensitivity towards the increase of  $N_{ml}$ . In the variational formulation of RMVT, Equation (2.15) a term for the minimization of the difference between the strains obtained via the displacement unknowns and the ones obtained via the stress unknowns is present. As the displacement-field is invariant to  $N_{ml}$  it prevents the refined stress field to obtain higher values.

Table 3.4: Extension: Sensitivity of  $\alpha_{xz}$  and  $|A_{xz}|$  concerning  $N_{ml}$  of the  $[\pm 45]_s$  lay-up

Model	$N_{ml} = 2$		$N_{ml} = 3$		$N_{ml} = 4$	
	$ A_{xz} $	$\alpha_{xz}$	$ A_{xz} $	$\alpha_{xz}$	$ A_{xz} $	$\alpha_{xz}$
LM4	6.2170	0.2123	-	-	-	-
LM2	7.0658	0.1165	6.4837	0.1731	4.9596	0.2437
LD4	6.3246	0.1979	4.9793	0.2894	4.9186	0.2920
LD2	6.6906	0.1077	6.6135	0.1551	5.6617	0.2437
Davì Milazzo: $ A_{xz}  = 5.0280 \quad \alpha_{xz} = 0.2630$						
Ansys: $ A_{xz}  = 4.9758 \quad \alpha_{xz} = 0.2884$						
$ A_{xz} $ in [GPa]						

Based on the results of the  $[\pm 45]_s$  laminate, the values of the  $[0, 90]_s$  and  $[90, 0]_s$  laminates can be verified. Through the comparison of the values of the singularity strength  $|A_{ij}|$  of all three laminates in Tables 3.3 and 3.5, it gets visible that the angle-ply laminate has the highest stress concentration at the free edge.

For the  $[0, 90]_s$  laminate with its monotonous rise of the transverse normal stress  $\sigma_{zz}$  towards the free edge, a slightly lower singularity strength can be found, compared to the angle-ply laminate. However for the  $[90, 0]_s$  cross-ply laminate a complete different behaviour is observed and no exploitable result can be obtained. As it is visible from the distribution across the width in Figure 3.4, the rise is not monotonous and hence no straight line will be present in the fitting zone for the

$[90, 0]_s$  cross-ply laminate. This gets visible by the values of  $\alpha_{zz}$ , which are out of its interval definition. In theoretical part in chapter 1, it was shown that the local stress gradient of  $\sigma_{zz}$  close to the free edge had to be balanced by a gradient of another transverse stress component. Through the occurring inflection in  $\sigma_{zz}$  inside the interval of  $r$ , also the other stress transverse components are not fully usable with the fitting approach.

From the results of the cross-ply and the angle-ply laminates, further remarks on the CUF models can be done, concerning the values of the power  $\alpha_{ij}$  and the strength  $|A_{ij}|$ : The higher the order of expansion, the easier it is for the model to capture the harsh gradient of the expected singularity. Models of lower than the forth order partly reproduce the singularity. The quality depends on both, the lay-up description used as well as the variational statement. As mentioned before, the best results are obtained with LW description and for expansion orders lower than the forth order a further improvement can be provided by the RMVT statement.

EM2, EMz2 and EDz3 were shown also before to not fully provide the same pronounced singularity. The values given in Table 3.5 for  $\alpha_{ij}$  shown that the models have however better capabilities than ED1. Except EMz2, they have also a still reasonable value of the singularity strength  $|A_{ij}|$ . Obviously, EMz2 does not benefit from the inclusion of Zig-Zag while compared with EM2.

Table 3.5: Extension:  $\alpha_{zz}$  and  $|A_{zz}|$  for the  $[0, 90]_s$  and  $[90, 0]_s$  lay-ups

Model	$[0, 90]_s$		$[90, 0]_s$	
	$ A_{zz} $	$\alpha_{zz}$	$ A_{zz} $	$\alpha_{zz}$
Ansys	1.7581	0.3320	0.1628	3.3100
LM4	0.3925	0.4775	0.6943	3.8122
LM2	0.6766	0.3229	0.3299	2.0462
LD4	0.2776	0.5646	0.2515	2.1387
LD2	0.5638	0.4161	0.1292	0.1158
EM4	1.0442	0.1069	0.7426	0.0407
EM2	1.0212	0.1193	0.7610	0.1027
EMz2	0.0002	0.2271	0.0005	1.2899
ED4	0.7351	0.1380	0.4200	0.0670
EDz3	1.0670	0.1174	0.8465	0.0966
ED1	0.3145	0.0002	0.3145	0.0005
$ A_{zz}  \text{ in } [GPa]$				

In the quasi-isotropic eight layer laminates, through the multiple interfaces, multiple singularities are present. The interfaces are numbered consecutively for the upper half, beginning at the reference plane at  $z = 0$ , Figure 3.24. Their results are listed in Tables 3.6 and 3.7. For the interfaces of the bottom half, the results are the same due to the symmetry. In order to better compare the role of the two transverse stress components  $\sigma_{zz}$  and  $\sigma_{xz}$ , both are given for the two laminates in the accord-

ing tables. This permits to identify the most critical component at the concerned interface.

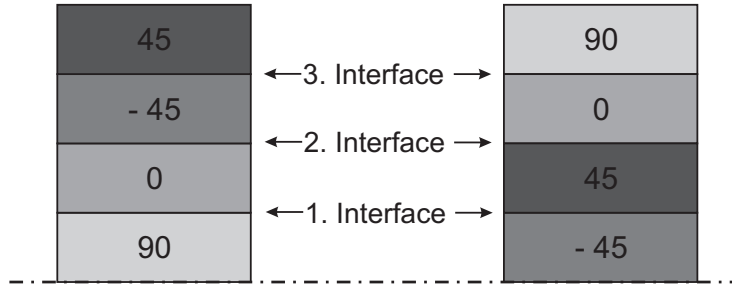


Figure 3.24: Denomination of the interfaces for the quasi-isotropic laminates

Regarding the transverse shear component  $\sigma_{xz}$ , the positioning of the  $\pm 45$  interface is relatively important for the laminate. The singularity strength values are rising for the  $[\pm 45, 0, 90]_s$  from the inner interface towards the outermost interface, the  $\pm 45$  interface. In the  $[90, 0, \pm 45]_s$  laminate it is the contrary. The highest singularity strengths are at the innermost interface. For both laminates however, the highest singularity strength concerning the transverse normal stress  $\sigma_{zz}$  is at the innermost laminate, as no transverse normal loads are present at the laminates top and bottom surface.

For the  $[90, 0]_s$  cross-ply laminate it was shown it was not possible to apply the fitting process. The same applies here for the quasi-isotropic  $[90, 0, \pm 45]_s$  laminate. For the same laminate, the  $\pm 45$  interface concerning the transverse normal stress  $\sigma_{zz}$  as well as transverse shear stress  $\sigma_{xz}$  are problematic. It is not possible to achieve a good fitting of this stress component at these interfaces.

Concerning the interfaces of the  $[\pm 45, 0, 90]_s$  laminate, it is the transverse normal stress  $\sigma_{zz}$  which is dominant at the first, the 0, 90 interface. The second interface, the 0, 45 interface, is dominated by the transverse shear stress  $\sigma_{xz}$ , as indicated by the better congruence of the fitting parameters with the Ansys solution. Finally, the third interface, the  $\pm 45$  interface, is clearly dominated by the transverse shear stress  $\sigma_{xz}$ . Accordingly, for the transverse normal stress  $\sigma_{zz}$  the obtained fitting parameters have a rather large scatter.

While regarding the accordance of the CUF models with the 3D reference solution, a higher difference is visible for the  $[\pm 45, 0, 90]_s$ , especially for the transverse shear stress. Here the higher order LW elements cannot always provide the before seen accuracy compared to the 3D reference, especially the LM elements seem to slightly overestimate the singularities. In the  $[90, 0, \pm 45]_s$  laminate, the accordance for the fitting parameters of the transverse shear components with the reference is higher compared to the  $[\pm 45, 0, 90]_s$  laminate, but still not perfect. For the outermost interface, it is especially troublesome to reliably predict the effects of the transverse shear component  $\sigma_{xz}$  as the stress level is relatively low. Also for the  $[90, 0, \pm 45]_s$ , a slight tendency to overestimate the appearing singularities can be seen for the LM

elements, increasing with the expansion order. However, the findings for the provided parameters is as before for the angle-ply and the cross-ply laminate: the LW elements have a significantly better performance as the ESL elements, which is for both increasing with the order of expansion.

Table 3.6: Extension:  $\alpha_{xz}$  and  $|A_{xz}|$  as well as  $\alpha_{zz}$  and  $|A_{zz}|$  for the  $[\pm 45, 0, 90]_s$  laminate

Model	$[\pm 45, 0, 90]_s$					
	1. Interface		2. Interface		3. Interface	
	$ A_{xz} $	$\alpha_{xz}$	$ A_{xz} $	$\alpha_{xz}$	$ A_{xz} $	$\alpha_{xz}$
Ansys	0.6005	0.2831	1.2005	0.3694	5.5994	0.2573
LM4	0.6407	0.1046	1.3617	0.3102	6.9354	0.2009
LM2	0.6182	0.1089	1.6759	0.1518	7.8000	0.1700
LD4	0.5045	0.0030	1.1662	0.3671	7.0618	0.1883
LD2	0.4788	0.0171	1.5932	0.2231	7.6353	0.0999
EM4	0.4419	0.1401	1.1717	0.0093	2.6530	0.0523
EM2	0.7609	0.0234	1.5219	0.0234	2.2828	0.0234
EMz2	0.0001	0.6853	0.0001	0.4132	0.0005	0.0948
ED4	0.4439	0.1395	1.1750	0.0097	2.6550	0.0518
EDz3	0.7620	0.0233	1.5242	0.0233	2.2861	0.0233
ED1	0.0001	0.2045	0.0002	0.2690	0.0002	0.3043
$ A_{xz}  \text{ in [GPa]}$						
Model	1. Interface		2. Interface		3. Interface	
	$ A_{zz} $	$\alpha_{zz}$	$ A_{zz} $	$\alpha_{zz}$	$ A_{zz} $	$\alpha_{zz}$
	8.3451	0.1622	4.7368	0.2117	0.4891	0.6837
LM4	9.2643	0.1385	6.2118	0.3263	0.2956	0.7654
LM2	9.9990	0.1203	4.7480	0.2546	0.7364	0.5149
LD4	8.9696	0.1458	4.5432	0.2399	0.3723	0.6966
LD2	9.8183	0.1374	2.7016	0.0177	0.9476	0.4256
EM4	1.0301	0.0625	6.2703	0.0257	0.4056	0.4659
EM2	8.5240	0.0486	8.0224	0.0515	6.7469	0.0601
EMz2	0.0733	0.0002	0.1379	0.0001	0.0217	0.0001
ED4	9.9447	0.0644	6.5130	0.0250	0.4213	0.4592
EDz3	8.7451	0.0485	7.3268	0.0540	7.7385	0.0552
ED1	0.3940	0.0001	0.3940	0.0001	0.0002	2.4043
$ A_{zz}  \text{ in [GPa]}$						

Table 3.7: Extension:  $\alpha_{xz}$  and  $|A_{xz}|$  as well as  $\alpha_{zz}$  and  $|A_{zz}|$  for the  $[90, 0, \pm 45]_s$  laminate

Model	$[90, 0, \pm 45]_s$					
	1. Interface		2. Interface		3. Interface	
	$ A_{xz} $	$\alpha_{xz}$	$ A_{xz} $	$\alpha_{xz}$	$ A_{xz} $	$\alpha_{xz}$
Ansys	3.2587	0.2836	1.1086	0.3750	0.5326	0.0062
LM4	7.6094	0.2115	1.5241	0.3211	0.6837	0.1206
LM2	8.5704	0.1158	1.8734	0.2068	0.6646	0.2004
LD4	7.7457	0.1982	1.9959	0.1908	0.5151	0.0095
LD2	8.2866	0.1067	1.5848	0.1219	0.5806	0.0606
EM4	0.9006	0.0593	1.5489	0.0468	2.0883	0.5558
EM2	0.3296	0.0399	0.6591	0.0399	0.9887	0.0399
EMz2	0.0008	0.8715	0.0004	0.4314	0.0008	0.5164
ED4	1.5459	0.0592	2.0451	0.0467	0.9916	0.5791
EDz3	0.3279	0.0397	0.6565	0.0397	0.9842	0.0397
ED1	0.0001	0.0763	0.0002	0.2072	0.0001	0.1625

$ A_{xz}  \text{ in [GPa]}$						
Model	1. Interface		2. Interface		3. Interface	
	$ A_{zz} $	$\alpha_{zz}$	$ A_{zz} $	$\alpha_{zz}$	$ A_{zz} $	$\alpha_{zz}$
Ansys	2.1094	0.1492	1.0527	0.1010	-	-
LM4	7.7710	0.2034	5.4627	0.1343	-	-
LM2	9.3987	0.1535	6.3088	0.0921	-	-
LD4	8.1647	0.1887	4.9513	0.1579	-	-
LD2	1.0076	0.1271	5.6137	0.1511	-	-
EM4	1.0803	0.0538	7.1208	0.0372	-	-
EM2	8.7857	0.0465	8.0082	0.0507	-	-
EMz2	0.0120	0.0003	0.1044	0.0001	-	-
ED4	1.0788	0.0541	7.3583	0.0365	-	-
EDz3	9.4209	0.0446	7.1543	0.0541	-	-
ED1	0.0001	4.2736	0.0001	4.2735	-	-

$ A_{zz}  \text{ in [GPa]}$						
-----------------------------	--	--	--	--	--	--

## 3.2 Free Edge Effects due to Bending

In this section, a convergence study and model validation is first presented, and then followed by the assessment for the different laminates. The CUF models are compared with results available in literature. At first, the determination which FE mesh and model refinement is needed to properly capture the singularities under bending loads is presented.

### 3.2.1 Convergence Study

To validate the different models of the CUF, a bending test with a uniform pressure load was considered. This test was first shown by Tahani and Nosier [72]. They presented the results for a symmetric  $[0, 90]_s$  and unsymmetrical  $[90_3, 0]$  laminate, loaded on the top surface with a constant pressure load  $q_0$  and simply supported at the two short edges at  $x = \pm a$ . Only the results of the forth order LW models are compared with the results given by Tahani and Nosier. Differently from the presented extension cases, the composite plate's geometric relations are here  $a = 2b = 10h$ . Remind that  $h$  its the overall thickness and is  $h = 4h_k$ . The changed geometric relations will change the values of the stress, while the form of the distributions are fixed by the mechanical behaviour, determined by the laminate and the loading.

In order to compare the results given in this subsection with results from literature, the stress components are normalized using the definition of Pagano [53]:

$$(\bar{\sigma}_{xx}, \bar{\sigma}_{yy}, \bar{\sigma}_{xy}) = (\sigma_{xx}, \sigma_{yy}, \sigma_{xy}) \frac{h^2}{q_0 a^2} \quad (3.4)$$

$$\bar{\sigma}_{zz} = \frac{\sigma_{zz}}{q_0}; \quad (\bar{\sigma}_{xz}, \bar{\sigma}_{yz}) = (\sigma_{xz}, \sigma_{yz}) \frac{h}{q_0 a} \quad (3.5)$$

In order to study the evolution of the results provided by the CUF as a function of the discretization, the same approach was used as Section 3.1.2. One of the main goals is to evaluate if the same mesh of the extension test case could be used, or if it is necessary to modify the mesh. Before, the assessment was mainly focused on achieving a convergence for the power of the singularity  $\alpha_{ij}$  and its strength  $|A_{ij}|$ . As no reference exists for the power law in the bending case, the convergence study aims towards obtaining a good congruence with the stress distributions provided by Tahani and Nosier and to obtain a good accordance on the calculated fitting parameters  $\alpha_{ij}$  and its strength  $|A_{ij}|$ .

At first, the classical distributions through thickness are compared with the references of Tahani and Nosier. The convergence study begins with the continuous refined in-plane mesh ( $I$ ), having a very small quadratic element at the free edges centre, while in the inside rather large elements are present, see Figure 3.9. For the  $[0, 90]_s$  laminate, three in-plane meshes for the fourth order LW models are given in Figure 3.25 concerning LM4 and in Figure 3.26 concerning LD4. The maximum stresses increase for both variational statements as a function of the mesh refinement.

For the same distribution, a zoom on the upper interface is provided in Figure 3.27 for LM4 and Figure 3.28 for LD4. In the solution of Tahani and Nosier some oscillations close to the bimaterial interface, inside the 0 degree layers appear for  $\bar{\sigma}_{zz}$ . Tahani and Nosier identified this as an additional singularity as it grew for an increasing number of subdivisions [72]. In their analytical solution method, this means the introduction of additional mathematical layers per physical layer, each having a linear approximation. Further, they stated, that no proof for this additional singularity could be provided by the use of approximate theories. This behaviour is studied also for the CUF models. If each physical layer is modelled with one mathematical layer as shown in the left half of each graph, the oscillations rise with a refinement of the in-plane mesh. In the right half two mathematical layers are used per physical layer. The oscillations are reduced significantly. This shows a better overall fit with the reference result by Tahani and Nosier. For the LD4 model, it also helps to significantly reduce the discontinuity of  $\sigma_{zz}$  at the layers interface. Therefore, as proven by the CUF results, there are no additional singularities.

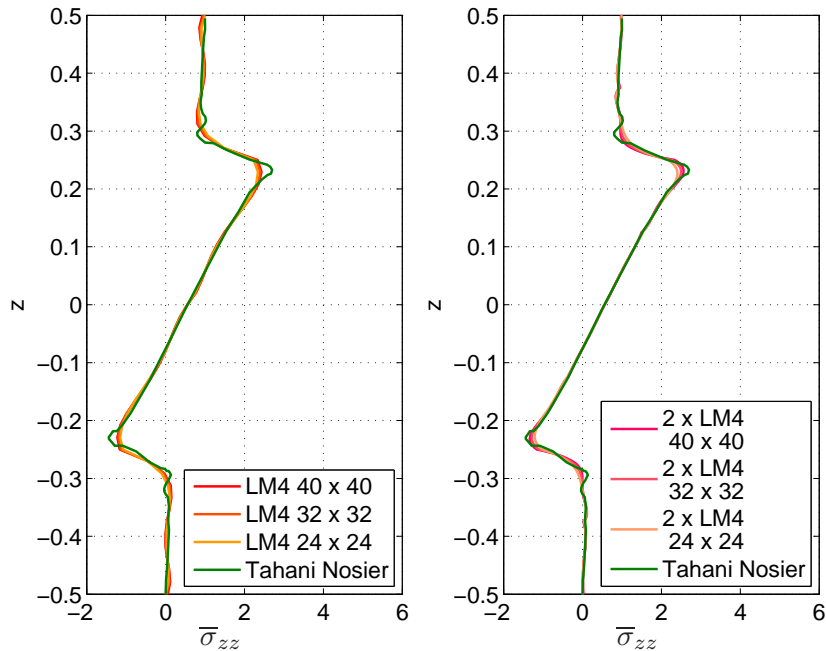
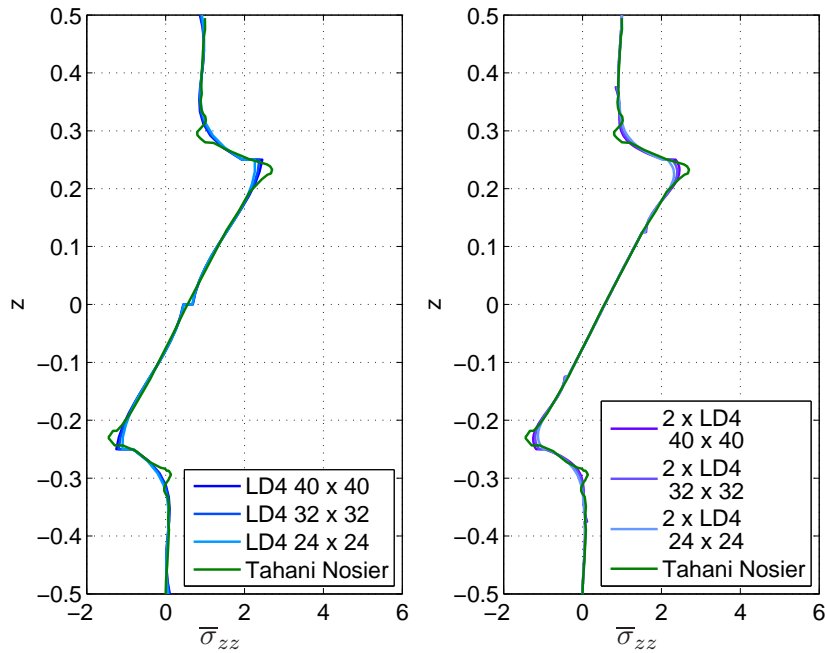
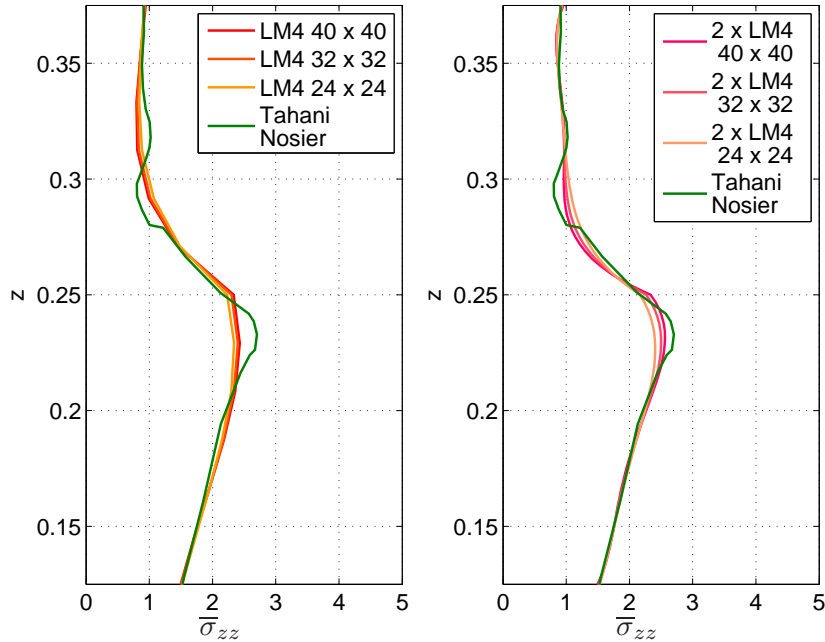


Figure 3.25: Bending:  $\bar{\sigma}_{zz}$  at  $(x = 0, y = b, z)$  for  $[0, 90]_s$  using LM4


 Figure 3.26: Bending:  $\bar{\sigma}_{zz}$  at  $(x = 0, y = b, z)$  for  $[0, 90]_s$  using LD4

 Figure 3.27: Bending: oscillations in  $\bar{\sigma}_{zz}$  at  $(x = 0, y = b, z)$  for  $[0, 90]_s$  using RMVT

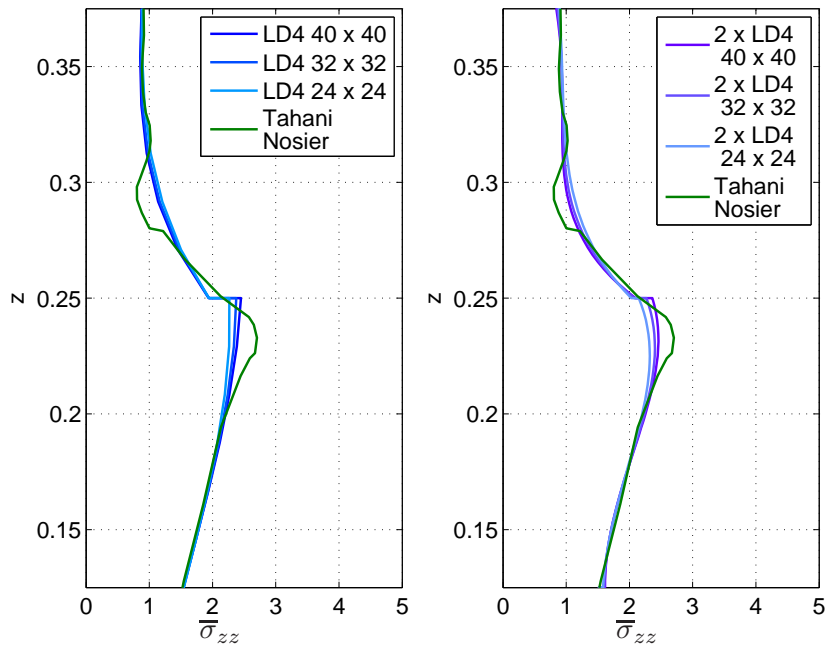


Figure 3.28: Bending: oscillations in  $\bar{\sigma}_{zz}$  at  $(x = 0, y = b, z)$  for  $[0, 90]_s$  using PVD

Concerning the distributions along the width, the same rise of the maximum stresses with rising number of elements is found, see Figure 3.29 for LM4 and Figure 3.30 for LD4. The maximum stress rises in while the mesh is refined. However, the distributions with  $N_{ml} = 2$  do, regardless of the variational statement used, not significantly improve the gradients of the transverse shear stress close to the free edge. It is worth noting however, that the rise in stress is more sensitive in bending than in extension for the simple regular in-plane mesh refinement. The Figures from the extension test case, 3.10 and 3.11, required a stronger mesh refinement to reach a notable difference in stresses. For the same LM4 and LD4 model in bending, the visible stress increase happens already with a moderate mesh refinement.

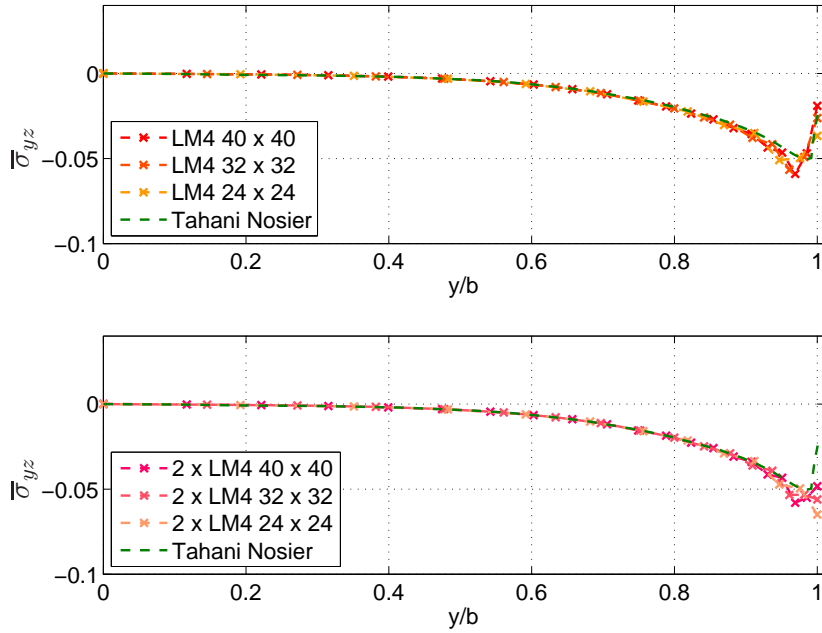


Figure 3.29: Bending:  $\bar{\sigma}_{yz}$  at  $(x = 0, y, z = \frac{h}{4})$  for  $[0, 90]_s$  using RMVT

In order to test the sensitivity of the stresses for the model refinement in mesh (II), the fitting process for the stress singularities was applied to the Tahani-Nosier bending test. Here, the transverse normal stress  $\bar{\sigma}_{zz}$  is concerned as a cross-ply laminate is considered. A mesh with 24 elements along the length (x-axis) is used, while along the width  $N_{ey98.75\%} = 20$  elements are used plus  $N_{e y 0.1hk} = 30$ . A sufficient congruence with the Tahani-Nosier reference results can be appreciated. For one mathematical layer per physical layer, matching width and thickness distributions are obtained as with the  $32 \times 32$  mesh used before. For this fixed in-plane mesh, the refinement through the thickness by the introduction of several mathematical layers per physical layer is next studied. The width distributions next to the free edge ( $0 < r \leq 1$ ) is given in Figure 3.31 showing a considerable rise with the increase of the number of  $N_{ml}$ . When more than two mathematical layers are used per phys-

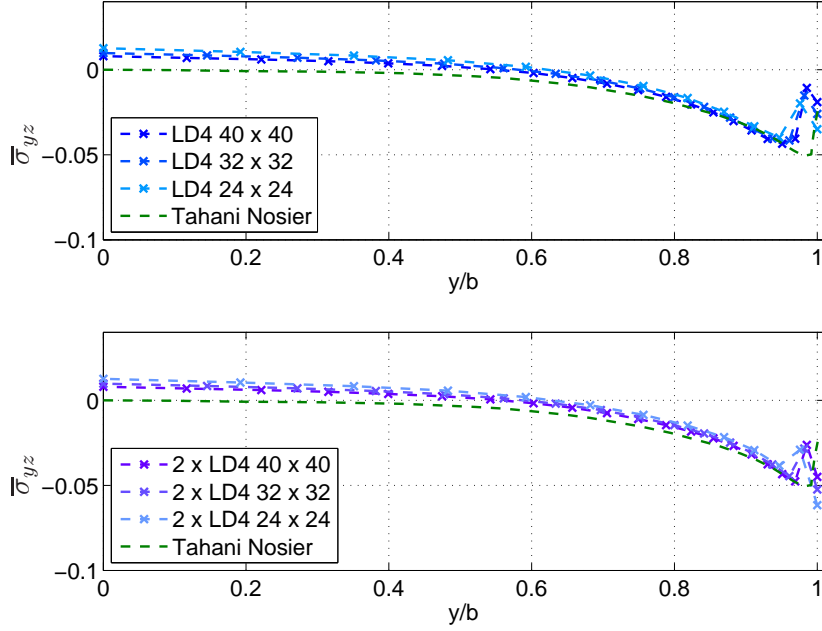


Figure 3.30: Bending:  $\bar{\sigma}_{yz}$  at  $(x = 0, y, z = \frac{h}{4})$  for  $[0, 90]_s$  using PVD

ical layer, they are irregularly distributed as in the extension case. The power law parameters  $\alpha_{zz}$  and  $|A_{zz}|$  are extracted from these Figures, given in Table 3.8.

These findings confirm that the conclusion found for the extension case is also valid in bending: While only interested in the distribution of the stresses in order to locate stress concentrations, a simple in-plane refinement is sufficient. However for the singularity fitting, a refinement through thickness is needed in order to reliably capture the stress singularities.

Table 3.8: Bending: Convergence of  $\alpha_{zz}$  and  $|A_{zz}|$  for the  $[0, 90]_s$  lay-up in Tahani Nosier test case

Method/Mesh	$ A_{zz} $	$\alpha_{zz}$
LM4, $N_{ml} = 1$	0.4083	0.3598
LD4, $N_{ml} = 1$	0.4384	0.3335
LM4, $N_{ml} = 2$	0.4828	0.3024
LD4, $N_{ml} = 2$	0.5091	0.2859
LD4, $N_{ml} = 3$	0.5083	0.2925
LD4, $N_{ml} = 4$	0.4881	0.3093
LD4, $N_{ml} = 5$	0.4872	0.3099
$ A_{zz} $ in [GPa]		

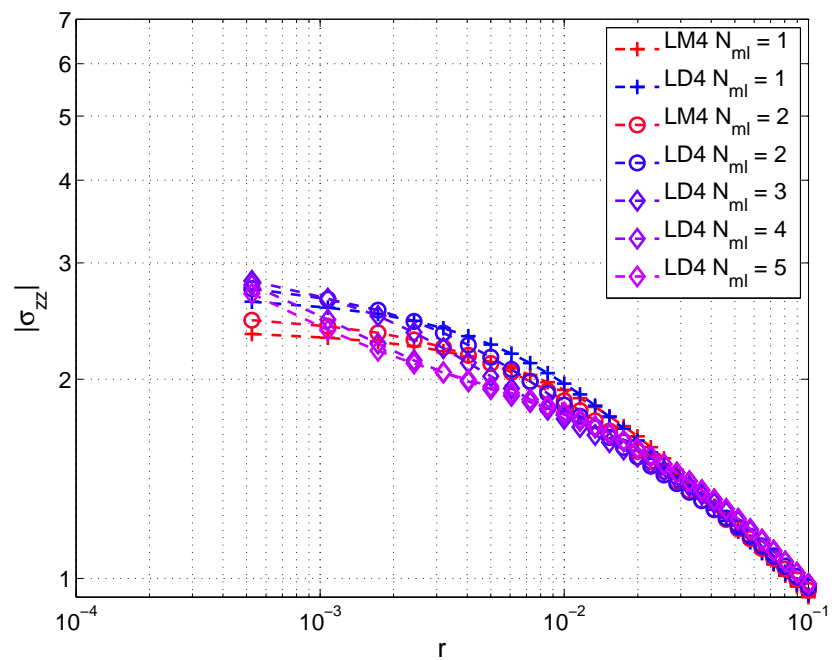


Figure 3.31: Bending: convergence for different mathematical layers of  $\sigma_{zz}$  in  $[0, 90]_s$  laminate using LM4 and LD4

### 3.2.2 Validation of Models

As for the extension test case, results are also presented using a three-dimensional model in Ansys. Here quadratic brick elements are used, where the in-plane mesh is equal to that used for the two-dimensional CUF elements. In contrast to the extensional case, 12 elements are applied per layer along the thickness direction.

At first, the results for the symmetric  $[0, 90]_s$  laminate are presented for only the highest order (fourth order) LW and ESL models based on PVD and RMVT statements. A very good agreement for the results using LW models is visible in the distribution through thickness at the free edge in Figure 3.32 ( $\bar{\sigma}_{zz}$ ) and Figure 3.33 ( $\bar{\sigma}_{xz}$ ). These results are in perfect match with the results computed with the three-dimensional model as well as the results by Tahani and Nosier. Regarding the ESL models, the same kind of adapting towards a mean value is visible as in the extension cases. The distribution of  $\bar{\sigma}_{zz}$  towards the free edge over the width is given in Figure 3.34. The upper curve corresponds to the mid plane interface at  $z = 0$ , while the lower corresponds to the upper interface at  $z = \frac{h}{4}$ . The three-dimensional results as well as the LW descriptions match the reference. Finally, all ESL techniques provide the same tendencies in bending as in traction: the distributions are significantly lower and do not capture the steep gradient at the free edge in a reliable manner.

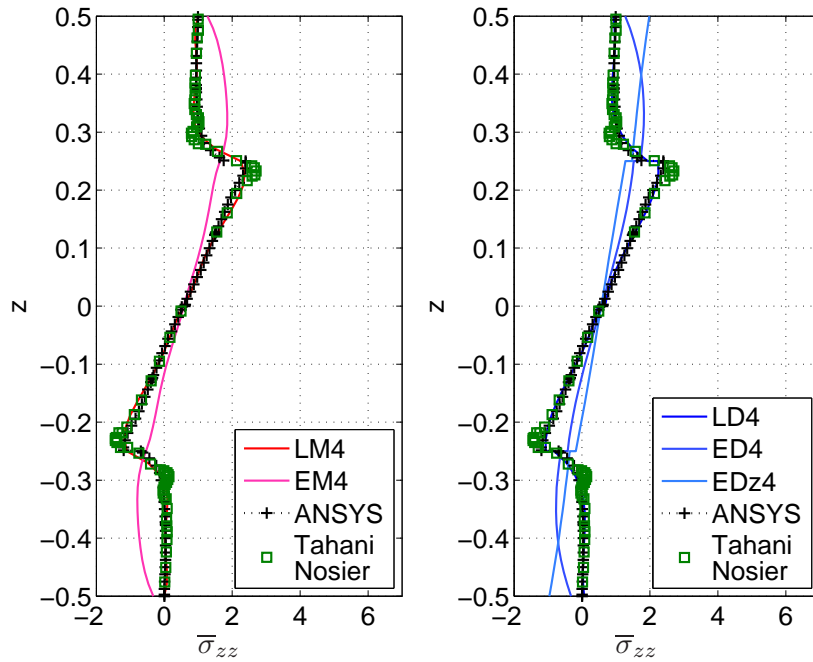


Figure 3.32: Bending:  $\bar{\sigma}_{zz}$  at  $(x = 0, y = b, z)$  for  $[0, 90]_s$  using RMVT & PVD

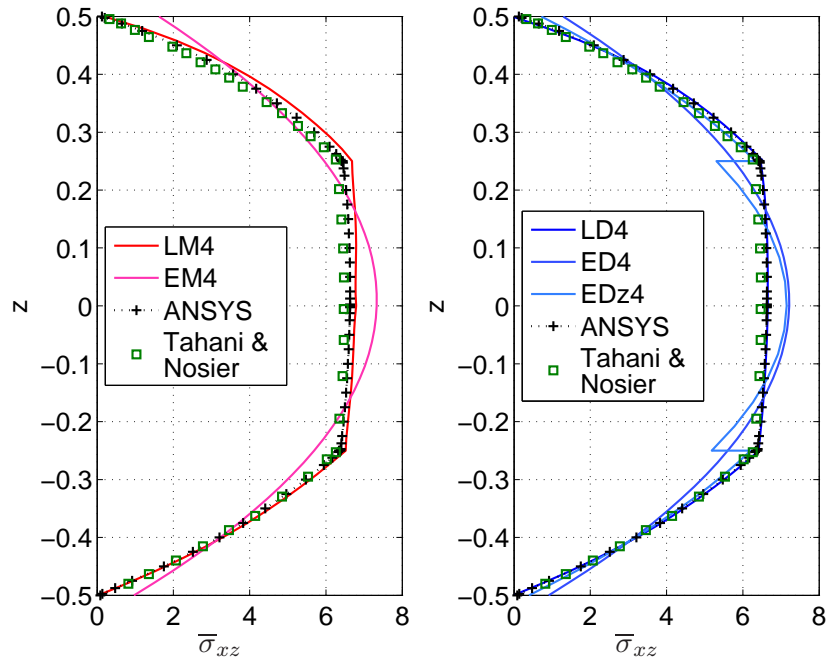


Figure 3.33: Bending:  $\bar{\sigma}_{xz}$  at  $(x = a, y = b, z)$  for  $[0, 90]_s$  using RMVT & PVD

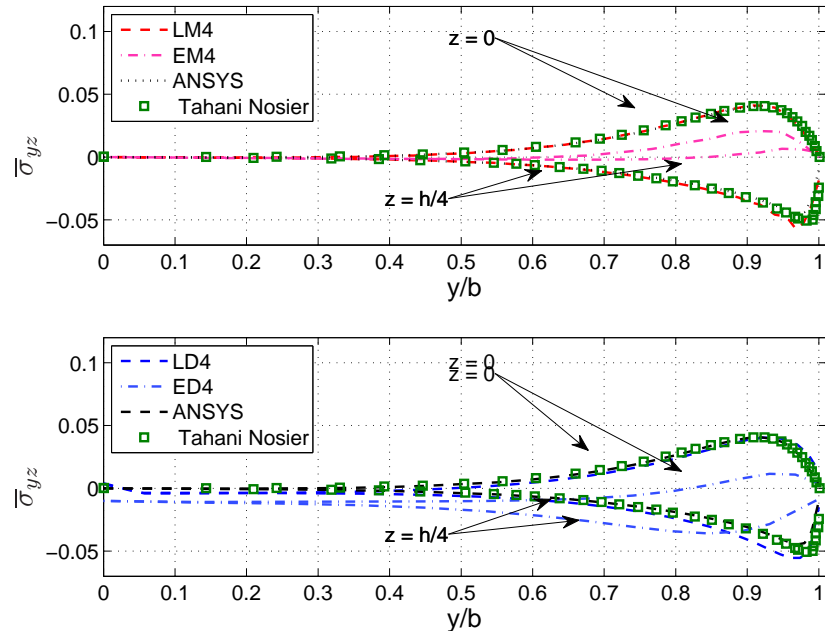


Figure 3.34: Bending:  $\bar{\sigma}_{yz}$  with upper Figure at  $(x = 0, y, z = 0)$  and lower Figure at  $(x = 0, y, z = \frac{h}{4})$  for  $[0, 90]_s$  using RMVT & PVD

Hereafter, the situation for the unsymmetrical laminate  $[90_3, 0]$  is described. The distributions through thickness for  $\bar{\sigma}_{xz}$  are shown in Figure 3.35 and for  $\bar{\sigma}_{zz}$  in Figure 3.36. Note that for this laminate  $\sigma_{zz} > 0$  are in the tension regime. The LW description confirms its superiority compared to the ESL description. Regarding the variational statement used, no significant difference can be found, except the failure to fulfil the interlaminar continuity of the transverse stress when the PVD statement is used. The distribution along the width and towards the free edge of  $\bar{\sigma}_{zz}$ , Figure 3.37, shows a better performance of the ESL description, compared to the  $[0, 90]_s$  laminate. Here, the lower curve is for  $z = 0$  while the upper curves corresponds to the bimaterial interfaces located at  $z = \frac{h}{4}$ . Even close to the free edge, the values are very close to the reference, which again is in perfect match with the 3D results in Ansys. Also for the width distributions, no further significant difference between the PVD and the RMVT statement can be found for both descriptions.

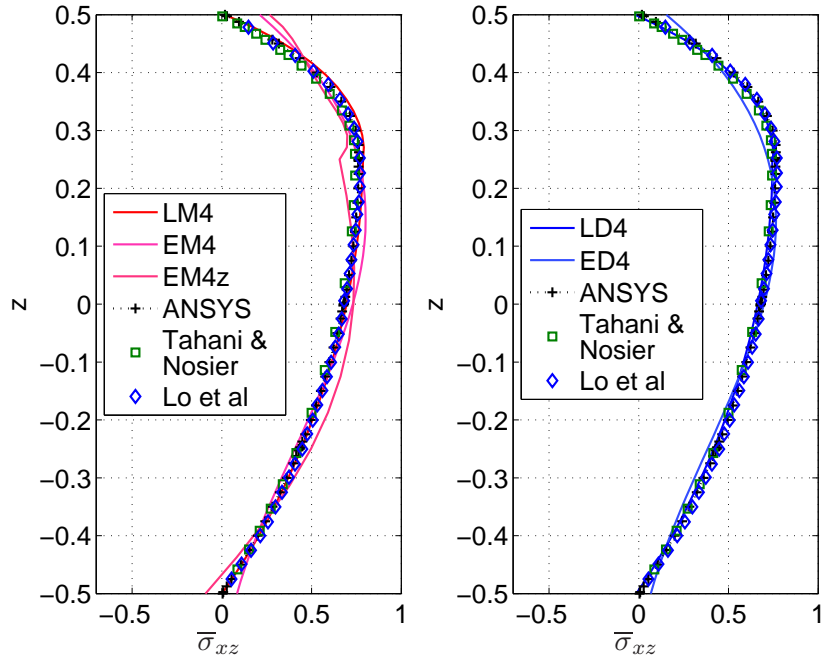
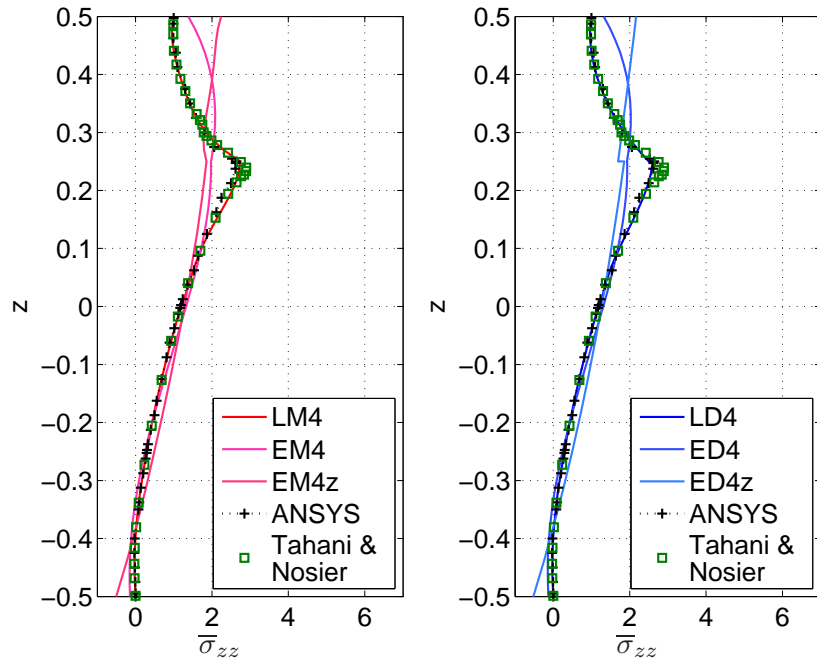
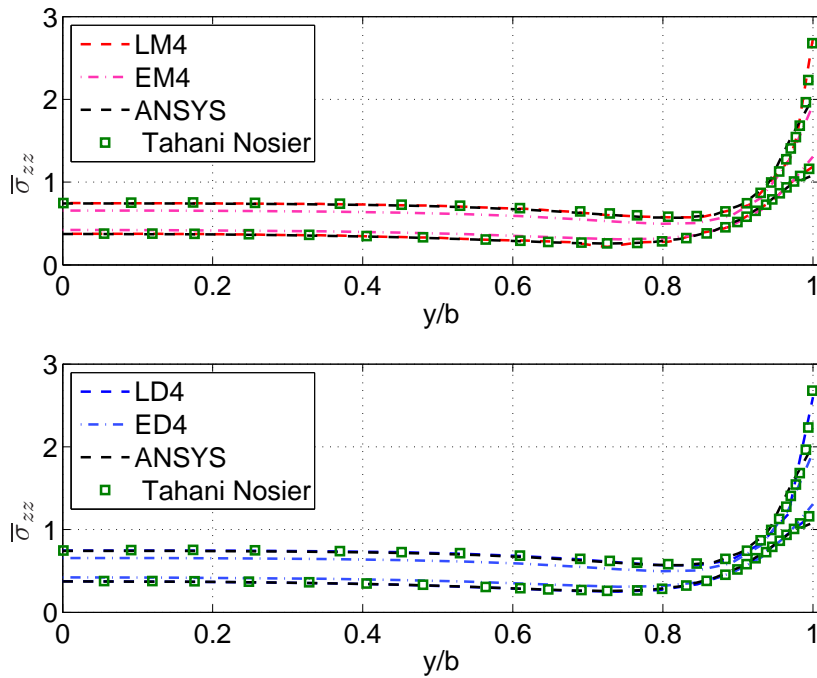


Figure 3.35: Bending:  $\bar{\sigma}_{xz}$  at  $(x = -a, y = b, z)$  for  $[90_3, 0]$  using RMVT & PVD


 Figure 3.36: Bending:  $\bar{\sigma}_{zz}$  at  $(x = 0, y = b, z)$  for  $[90_3, 0]$  using RMVT & PVD

 Figure 3.37: Bending:  $\bar{\sigma}_{zz}$  with upper Figure at  $(x = 0, y, z = \frac{h}{4})$  and lower Figure at  $(x = 0, y, z = 0)$  for  $[90_3, 0]$  using RMVT & PVD

### 3.2.3 Lay-Up Sensitivity

In this section, the free-edge effects are addressed that occur in different laminates occurring under bending load. Since in the subsequent section the free-edge effects due to extension and bending will be compared, the following modifications to the bending test case considered in the previous section will be made: (1) the geometry is kept identical to that used in the extension test case, (2) the uniform pressure load magnitude  $q_0$  is defined in such a manner, that the resulting deformation energy of the laminate is the same as that of the extension load ( $\epsilon_0 = 1$ ). Therefore  $q_0$  depends on the stacking sequence of the laminate. The magnitudes are given in Table 3.9. (3) No adimensionalization is used for the stress components. Moreover, an assessment of the different CUF models is proposed for the different laminates in bending. As reference, the results calculated via the three-dimensional model in Ansys is used.

Table 3.9: Bending: load magnitude  $q_0$  for the different laminates

laminate	$q_0$
$[\pm 45]_s$	5130.060
$[0, 90]_s$	253.453
$[90, 0]_s$	870.315
$[\pm 45, 0, 90]_s$	298.798
$[90, 0, \pm 45]_s$	213.531
$q_0$ in [MPa]	

#### 3.2.3.1 Angle-Ply Laminates

At first, the  $[\pm 45]_s$  laminate is considered. Figure 3.38 reports the trough thickness distribution of  $\sigma_{xz}$  at the free edge ( $x = 0, y = b, z$ ) obtained with LW models. Regardless of the variational statement used, with rising order of the polynomial, the flexibility is increased, hence the maximum stress. Figure 3.38 indicates that at least a third order expansion is needed to reliably capture sharp gradients occurring at the layer interfaces. Lower orders, as LM1 do not deliver any benefit while using only one mathematical layer per physical layer. Besides their drawback of not fully satisfying the ICs, PVD models show the same behaviour as LM models. Figure 3.39 reports the distribution of  $\sigma_{xz}$  at the free edge ( $x = 0, y = b, z$ ) obtained with ESL models. For both variational statements, regardless of their expansion order used, no gradient is present at the bimaterials interface. As for the LW models, with rising order of the polynomial the maximum stress rises. The results obtained by Zig-Zag models are finally reported in Figure 3.40. A gradient at the layers interface is now present for the distribution through thickness, but still the ESL description using Zig-Zag is not fully providing the sharp gradients occurring at the interfaces as shown by Ansys. As before without Zig-Zag, the maximum stresses are still lower in magnitude compared to the stresses provided by the LW models. These three

Figures show, that for the angle-ply laminates, it is rather difficult to capture properly the singularities.

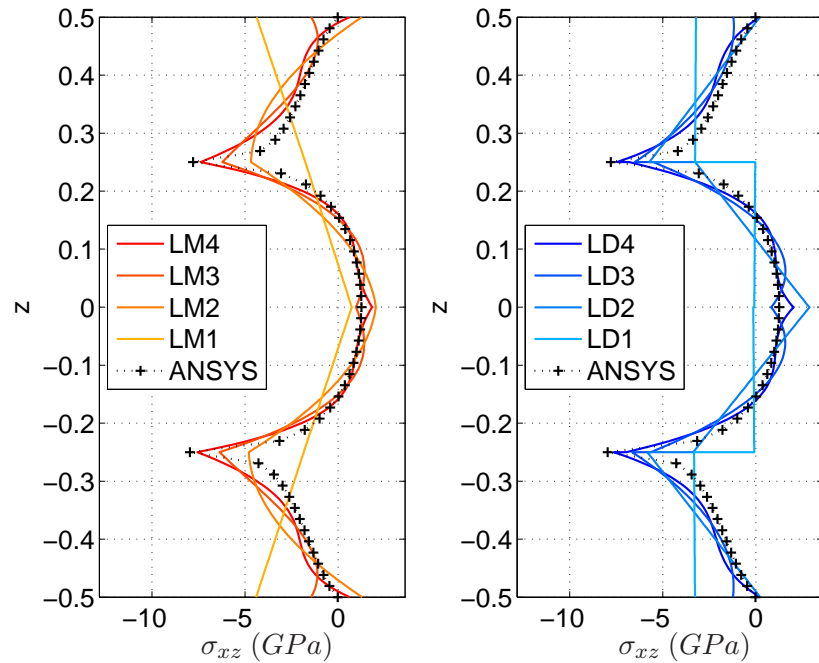


Figure 3.38: Bending:  $\sigma_{xz}$  at  $(x = 0, y = b, z)$  for  $[\pm 45]_s$  using RMVT & PVD LW models

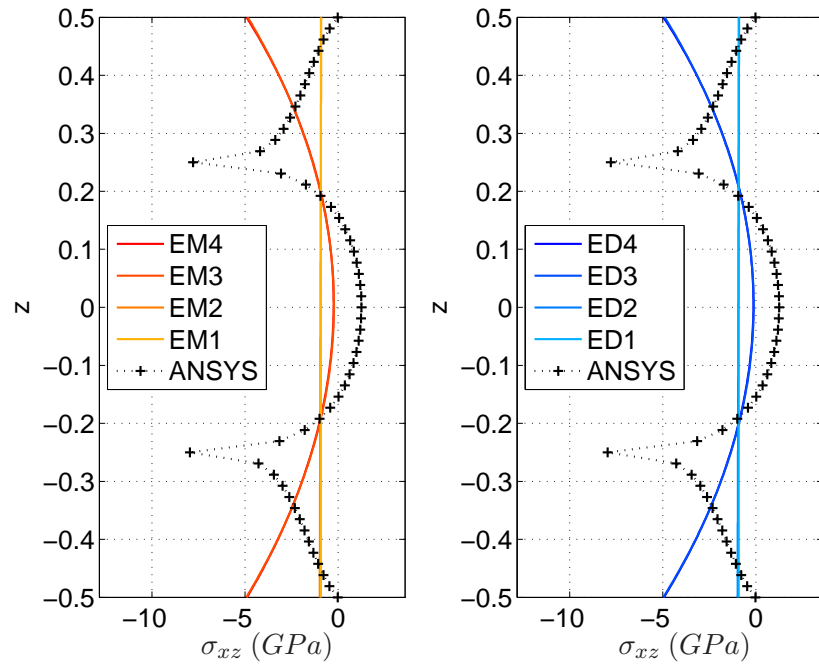


Figure 3.39: Bending:  $\sigma_{xz}$  at  $(x = 0, y = b, z)$  for  $[\pm 45]_s$  using RMVT & PVD ESL models

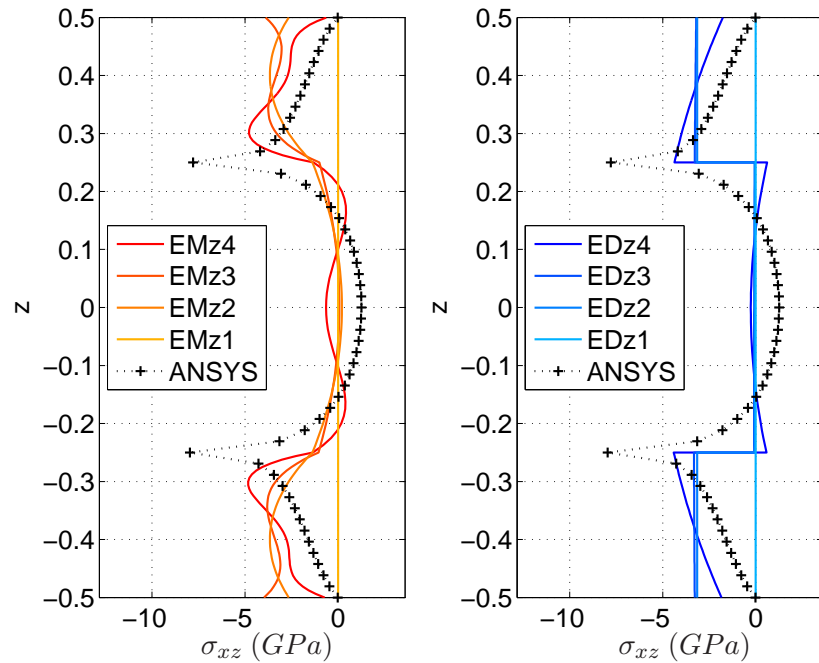


Figure 3.40: Bending:  $\sigma_{xz}$  at  $(x = 0, y = b, z)$  for  $[\pm 45]_s$  using RMVT & PVD ESL Zig-Zag models

As further comparison, the width distributions of  $\sigma_{xz}$  at the upper bimaterial interface are given. Due to the test configuration, the distributions are symmetric through thickness, therefore only the upper layer interfaces will be considered. From here on, the distributions are limited to the same CUF models considered in the assessment for the extension case.

Figure 3.41 shows that the LW models have the best congruence with the three-dimensional solution computed by Ansys. However, they do not fully match. The models using the ESL description provide not even half of the maximum transverse shears stress. The RMVT statement helps to improve the distributions of the models using the ESL description, while for the models using the LW description no significant difference is visible between the PVD and RMVT statement. Note that, since the transverse shear modulus  $G_{xz}$  is actually the same in the +45 and the -45 plies, the interlaminar continuity is assured by the PVD models. The stress distributions through thickness showed that with rising expansion order the maximum stress is rising. The same conclusion can be drawn on the basis of the distribution along the width. Moreover, despite their insufficient representation of the step gradients at the free edge, ESL models with higher-order expansion can provide satisfactory results far from the free edge.

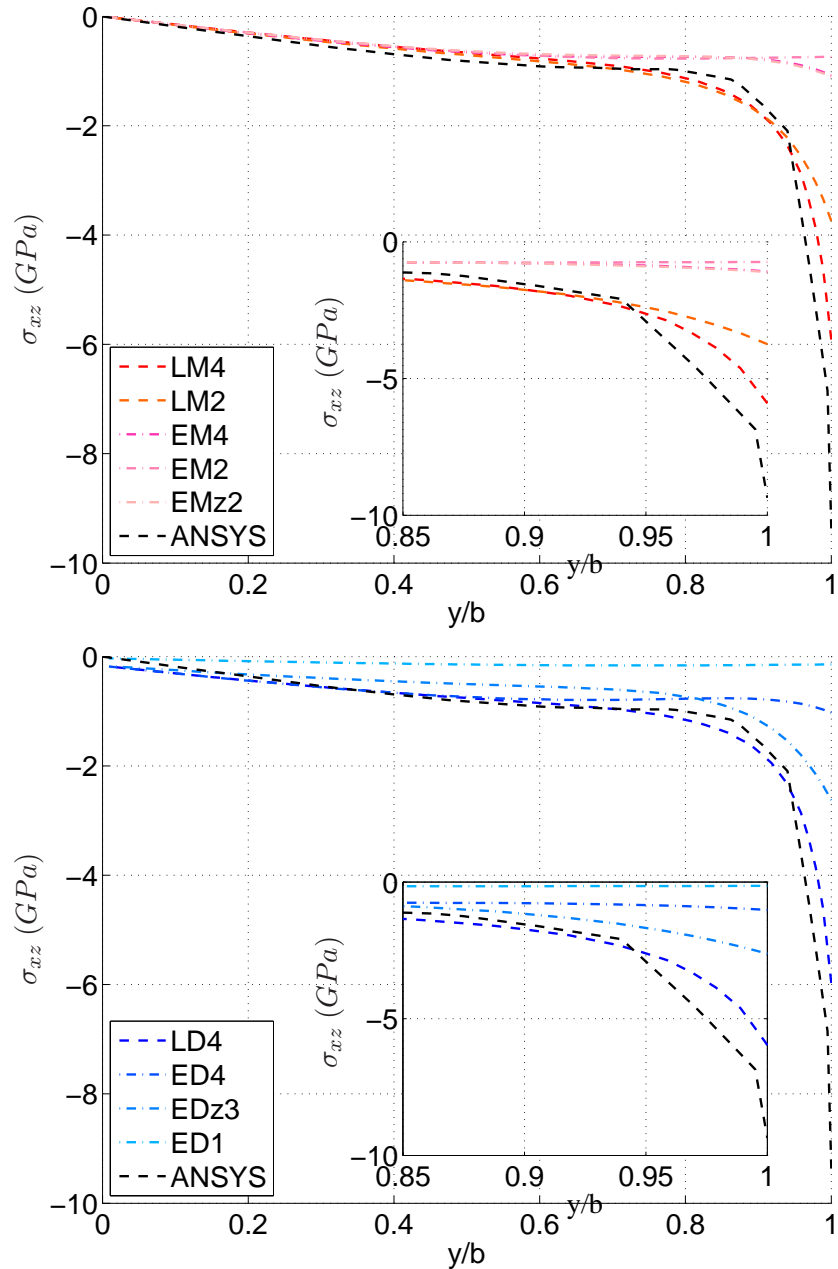


Figure 3.41: Bending:  $\sigma_{xz}$  at  $(x = 0, y, z = \frac{h}{4})$  for  $[\pm 45]_s$  using RMVT & PVD

### 3.2.3.2 Cross-Ply Laminates

For the case of the two cross-ply laminates  $[0, 90]_s$  and  $[90, 0]_s$ , different phenomena occur. Due to the different position of the rigid 0 degree layer, the different laminates will have different bending behaviour. The highest rigidity is expected for the  $[0, 90]_s$  lay-up.

In the two thickness distributions of  $\sigma_{zz}$  in Figures 3.42 and 3.44 both show that the highest layer is in compression and in the lowest in tension. Further, for the  $[90, 0]_s$ , the neutral axis separating the part from compression and tension is in the middle, while in the  $[0, 90]_s$  lay-up, it is at a slightly lower position. Additionally, through the Poisson's mismatch, the  $[90, 0]_s$  lay-up is alternating between tension and compression at each interface through thickness. This leads to higher overall stresses in the  $[90, 0]_s$  lay-up.

Comparing the different CUF models, provides the following findings: Only the LW description provides the gradients between the layer interfaces, while the ESL descriptions provide only an averaged transverse normal stress distribution through thickness. It is worthwhile to note that for the ESL models, the results are in a better coherence with the  $[0, 90]_s$  lay-up. In contrast to the angle-ply laminates, the PVD statement does not fulfil the ICs concerning the transverse stresses. Only the RMVT statement provides the continuity at the layers interfaces. The higher the expansion order, the higher the maximum stresses achieved and therefore the better the congruency with the result of the three-dimensional model.

Based on the distributions across width, further conclusions on the CUF models behaviour can be made. Figures 3.43 and 3.45 for the upper bimaterial interface show that the  $[0, 90]_s$  laminate is completely in compression, while the  $[90, 0]_s$  laminate has a complete tension state. Regarding the expansion order, the first and second order models have severe difficulties to adapt to the singular behaviour. The first order models fail totally. These two Figures show, that for those two low expansion orders the inclusion of Zig-Zag does not improve the overall behaviour.

Based on the mesh (*II*) configuration for bending, the values of the power law parameters were gained. All parameter values for all four laminates are given in Table 3.10. They show a very good coherence with the before stated characteristics of the different models for the distributions through width. High singularity strength values are obtained for the  $[0, 90]_s$  laminate, having also a low singularity order, which indicates the steepest rise towards infinite values. The  $[\pm 45]_s$  angle-ply laminate has a higher singularity order and hence a smoother rise. An exception concerning the fitting is the  $[90, 0]_s$  laminate. The power law for this laminate is not applicable as  $\sigma_{zz}(y)$  is not monotonous in the fitting interval. Therefore, no power law parameters can be given for this laminate.

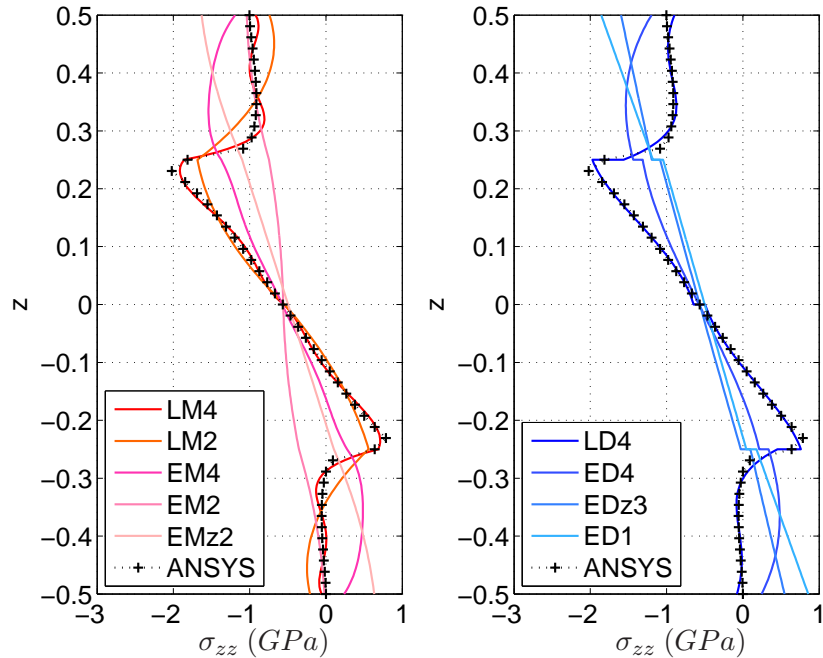

 Figure 3.42: Bending:  $\sigma_{zz}$  at  $(x = 0, y = b, z)$  for  $[0, 90]_s$  using RMVT & PVD

 Table 3.10: Bending:  $\alpha_{ij}$  and  $|A_{ij}|$  for the  $[\pm 45]_s$ ,  $[0, 90]_s$  and  $[90, 0]_s$  lay-ups

Model	$[\pm 45]_s$		$[0, 90]_s$		$[90, 0]_s$	
	$ A_{xz} $	$\alpha_{zz}$	$ A_{zz} $	$\alpha_{zz}$	$ A_{zz} $	$\alpha_{zz}$
Ansys	0.6868	0.3498	3.5357	0.1778	-	-
LM4	1.0953	0.2254	3.1364	0.2014	-	-
LM2	1.2261	0.1205	3.7038	0.1580	-	-
LD4	0.7685	0.2507	2.9985	0.2115	-	-
LD2	0.6931	0.1367	3.5550	0.1871	-	-
EM4	0.3575	0.0363	4.1739	0.0655	-	-
EM2	0.2853	0.0019	2.8712	0.0073	-	-
EMz2	0.3691	0.0336	4.2935	0.0024	-	-
ED4	1.0959	1.8888	3.9740	0.0680	-	-
EDz3	0.2918	0.0587	3.3530	0.0616	-	-
ED1	0.0731	0.0393	4.1270	0.0002	-	-
$ A_{ij} $ in [GPa]						

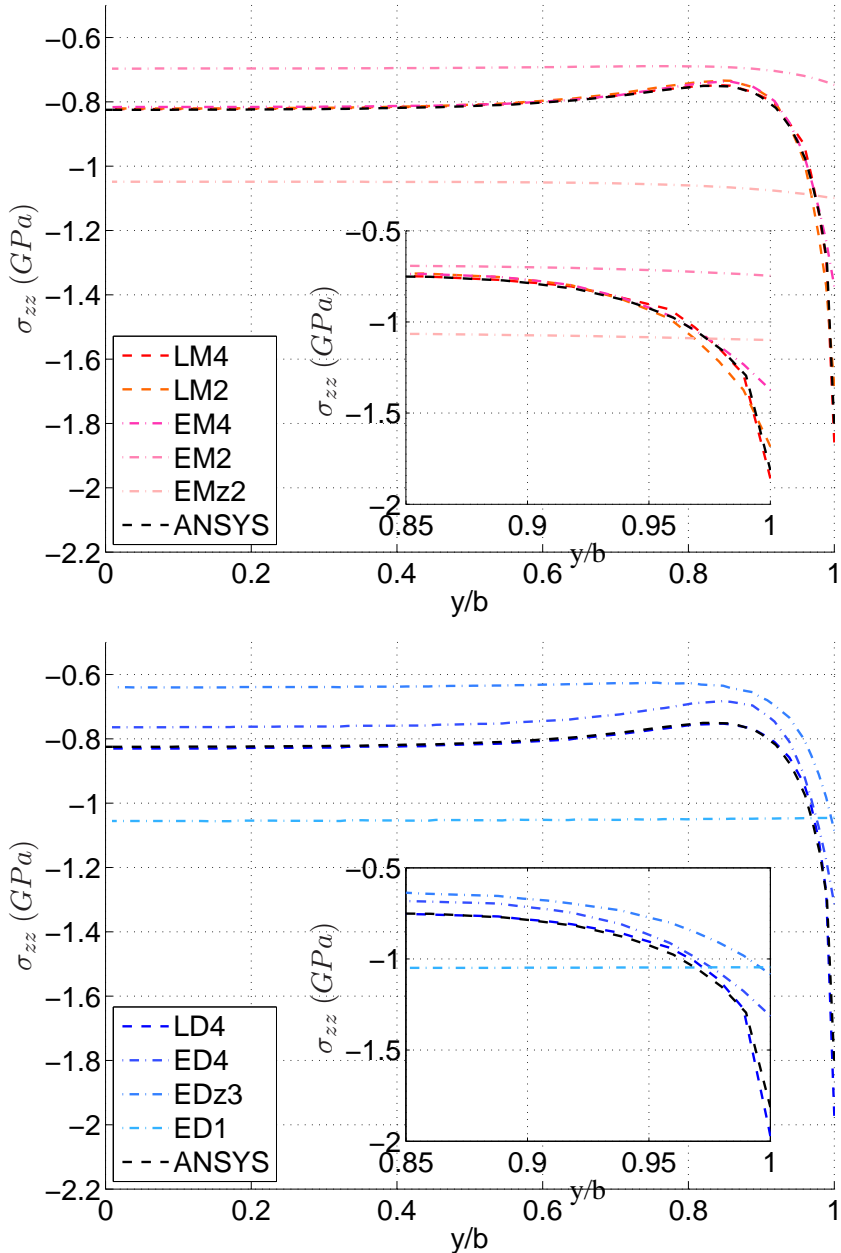


Figure 3.43: Bending:  $\sigma_{zz}$  at  $(x = 0, y, z = \frac{h}{4})$  for  $[0, 90]_s$  using RMVT & PVD

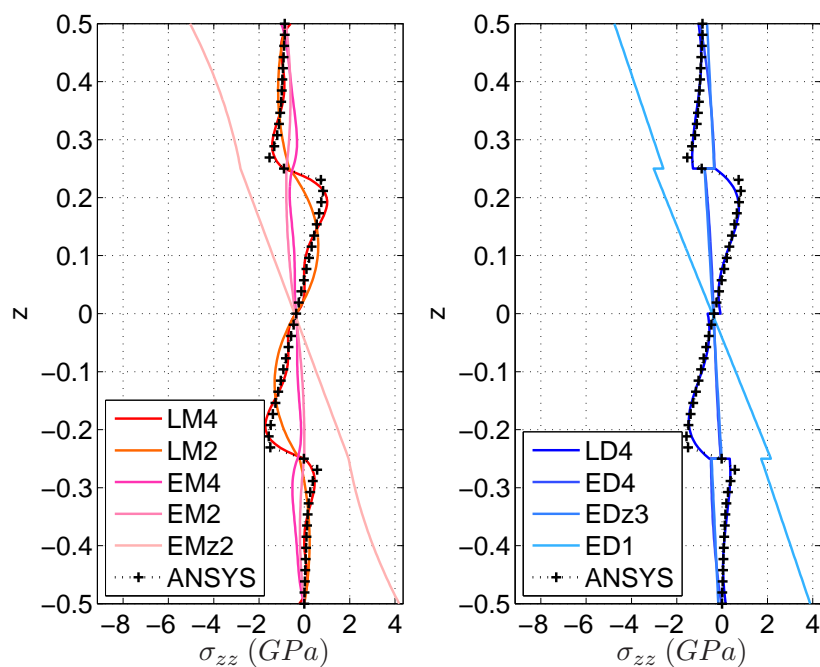


Figure 3.44: Bending:  $\sigma_{zz}$  at  $(x = 0, y = b, z)$  for  $[90, 0]_s$  using RMVT & PVD

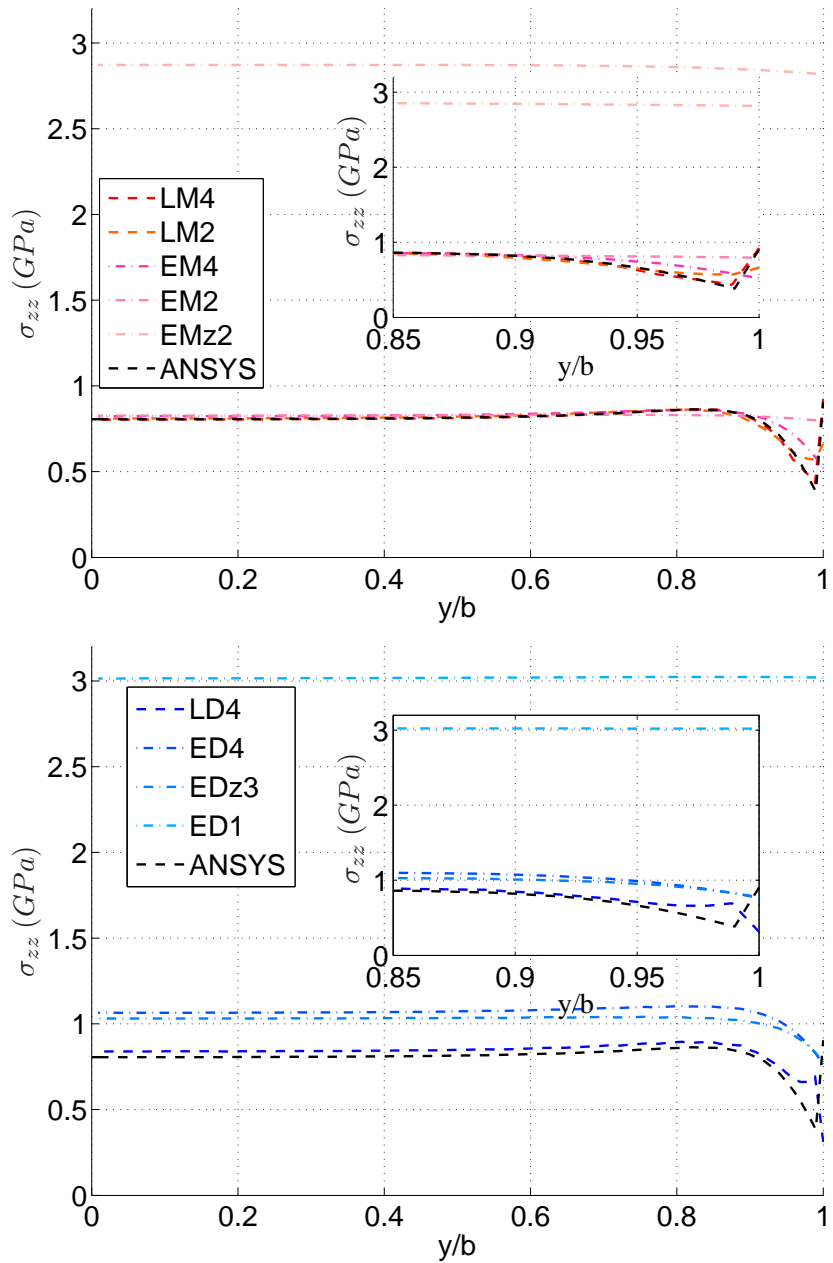


Figure 3.45: Bending:  $\sigma_{zz}$  at  $(x = 0, y, z = \frac{h}{4})$  for  $[90, 0]_s$  using RMVT & PVD

### 3.2.3.3 Quasi-Isotropic Laminates

Thickness distributions of the transverse normal stress  $\sigma_{zz}$  for the quasi-isotropic laminates, are shown in Figure 3.46 and 3.47. The orientation of the outer layers is very important for the rigidity of the overall lay-up. Besides the singularity in the  $\pm 45$  layers, the overall stresses are lower than in the  $90, 0$  layers. In total, the  $[90, 0, \pm 45]_s$  laminate shows a smoother distribution through thickness, with less sharp changes than the  $[\pm 45, 0, 90]_s$  laminate. The last has a two times higher maximum stresses in the tension and compression regime, which are located at the interfaces of the  $0, 90$  layers. Note that around 1.4 times the load magnitude  $q_0$  is applied for this laminate, compared to the  $[90, 0, \pm 45]_s$  laminate. Equally for the transverse shear stress  $\sigma_{xz}$  a factor of nearly five times higher stresses are visible compared to the  $[90, 0, \pm 45]_s$  laminate. This indicates that the  $[\pm 45, 0, 90]_s$  laminate is more prone to delamination. Not so in the case of  $[90, 0, \pm 45]_s$ , here, the maximum transverse normal stresses and transverse shear stress are located at the  $0, 45$  interfaces. Except the  $\pm 45$  interface, most interfaces possess lower maximum stresses. This indicates further that it is recommended to use the  $\pm 45$  layer in the inner of the structure where normally the maximum shear are expected. Depending on the load, the maximum tensional stresses are expected at the outer layers, which therefore calls for the use of 0 or 90 degree layers.

The higher number of interfaces and discontinuities through thickness is reliably predicted using the LW description. The ESL description is not able to reproduce the sharp gradient, even if Zig-Zag functions are included. No significant differences can be identified between RMVT and PVD models: both model families distributions provide for the same expansion orders comparable distributions with similar stress magnitudes.

Concerning the transverse shear stress  $\sigma_{xz}$ , the results for the  $[\pm 45, 0, 90]_s$  laminate are given in Figure 3.48 and for the  $[90, 0, \pm 45]_s$  laminate are given in Figure 3.49. The maximum stress intensity is for both present at the  $\pm 45$  interfaces. For the first lay-up, having the angle-ply layers at the outer faces, the intensity is significantly lower. For the other layers of both laminates, the transverse shear stress is nearly zero. A clear difference between LW and ESL description becomes visible. Regardless of the expansion order and the variational statement used, only the LW description is able to provide a solution being coherent with the solution provided by the three-dimensional model. The ESL models completely fail to predict the local stress gradients and can only give an approximate indication on the sign of the stress.

For the sake of brevity, only two stress distributions across width are shown for both laminates. For the  $[\pm 45, 0, 90]_s$  laminate, the distributions of  $\sigma_{xz}$  are shown in Figure 3.50 at  $z = \frac{h}{8}$  and Figure 3.51 show the distributions at  $z = \frac{3h}{8}$ . A rather mild rise is visible at the first interface at  $z = \frac{h}{8}$ . The LW description is as reliable as before. For the ESL description, only the forth order expansion provides results in accordance with the three-dimensional result. This is not the case in the third interface at  $z = \frac{3h}{8}$ , where a stronger singularity appears at the  $\pm 45$  interface. Here,

the forth order ESL models do not have the same congruency as provided for the interface at  $z = \frac{h}{8}$ .

For the  $[90, 0, \pm 45]_s$  laminate, the distributions of  $\sigma_{zz}$  are shown in Figure 3.52 for  $z = \frac{3h}{8}$  and Figure 3.53 for  $z = \frac{h}{4}$ . In contrast to the  $[\pm 45, 0, 90]_s$  laminate, not both interfaces have relatively pronounced singular behaviour. The non-monotonous distribution through width is difficult to capture, also the LM2 model does not provide a sufficient response. In contrary the second interface at  $z = \frac{h}{4}$ , the 0, 45 interface. It has a more pronounced singularity leading to a better performance of all LW models and the higher order ESL models.

The other interface width distributions are according to the effects shown before and posses the same behaviour for the different models studied. Further, the stress singularities and the performance of the different models to reproduce them can be extracted as before from the singularity fitting process. The obtained values for the distributions through width get visible in Tables 3.12 and 3.11. As before, the singularity fitting results are given for the upper interfaces counting them from the first interface after the laminates symmetry plane, outwards. As could be seen before for the two cross-ply and the angle-ply laminates, certain interfaces are more pronounced with one of the two transverse stress components and some are not applicable to the fitting process. As indicated by Figure 3.52, this is the case for the 90, 0 interface of the  $[90, 0, \pm 45]_s$  laminate. For this quasi-isotropic laminate however, a rather good performance of the fitting is expected by Figure 3.53. For the first, the  $\pm 45$  interface, a domination of the transverse shear stress  $\sigma_{xz}$  is expected. For the  $[\pm 45, 0, 90]_s$  laminate, Figure 3.51 shows that the poor increase of the transverse shear stress does not provide a sufficient singular behaviour. Again the  $\pm 45$  interface in Figure 3.50 indicates a domination of the transverse shear  $\sigma_{xz}$ , while the fitting process fails for the transverse normal stress.

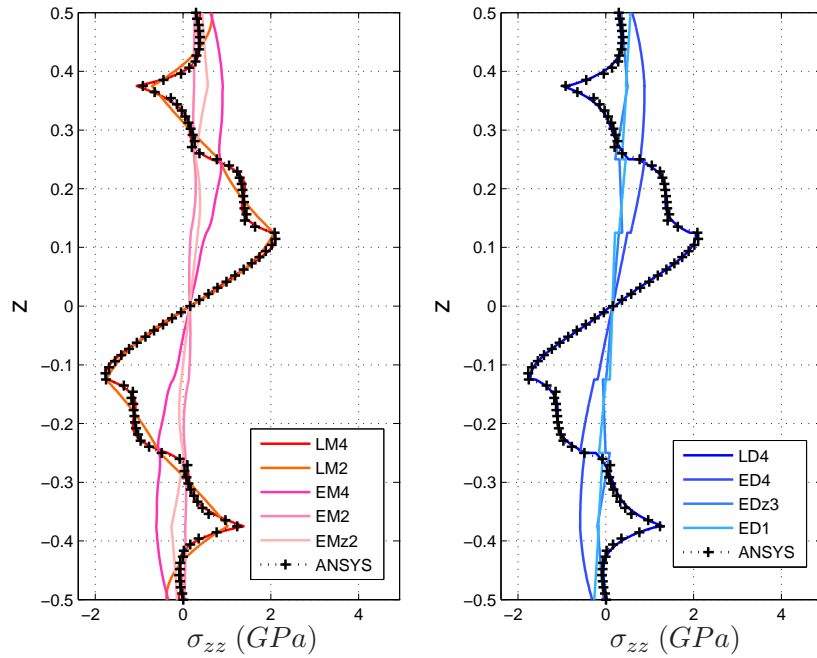


Figure 3.46: Bending:  $\sigma_{zz}$  at  $(x = 0, y = b, z)$  for  $[\pm 45, 0, 90]_s$  using RMVVT & PVD

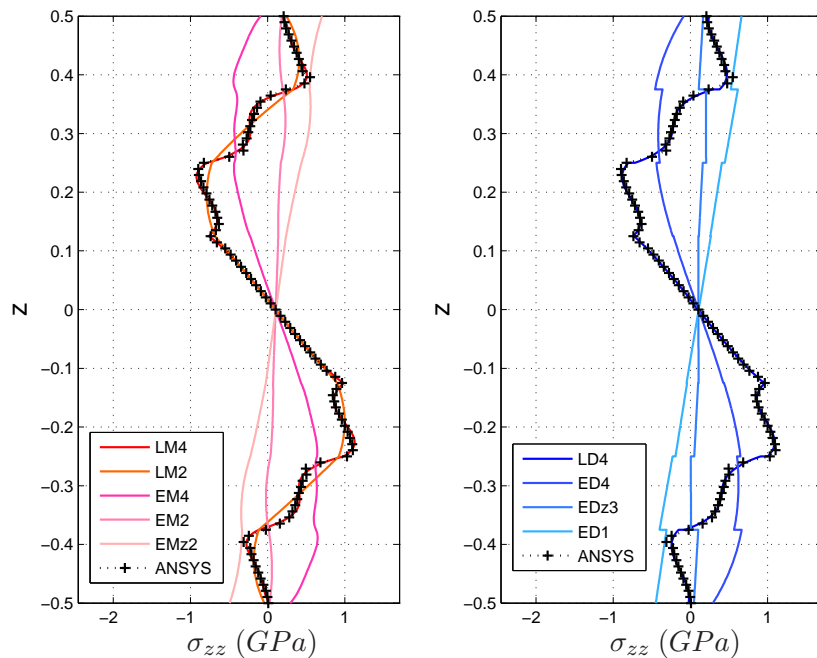


Figure 3.47: Bending:  $\sigma_{zz}$  at  $(x = 0, y = b, z)$  for  $[90, 0, \pm 45]_s$  using RMVVT & PVD

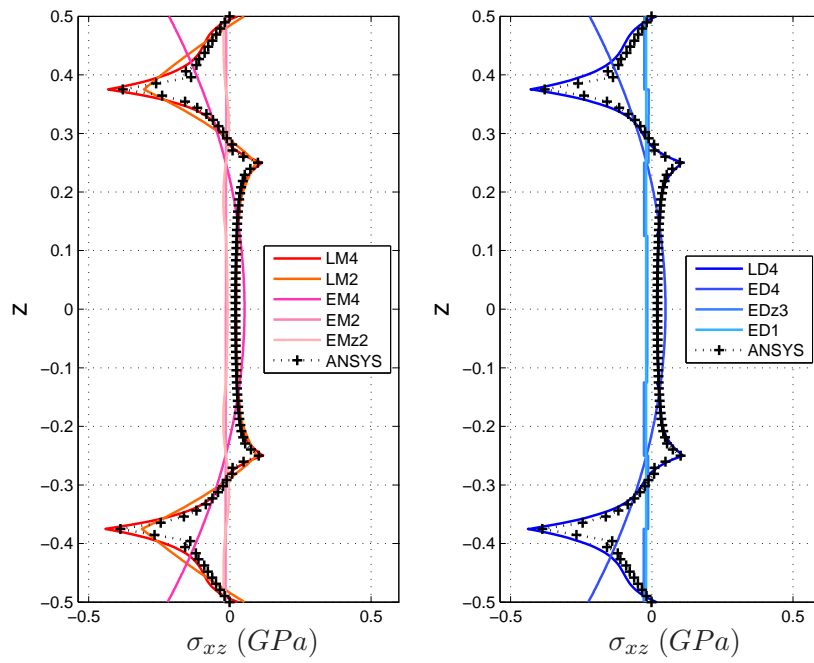


Figure 3.48: Bending:  $\sigma_{xz}$  at  $(x = 0, y = b, z)$  for  $[\pm 45, 0, 90]_s$  using RMVT & PVD

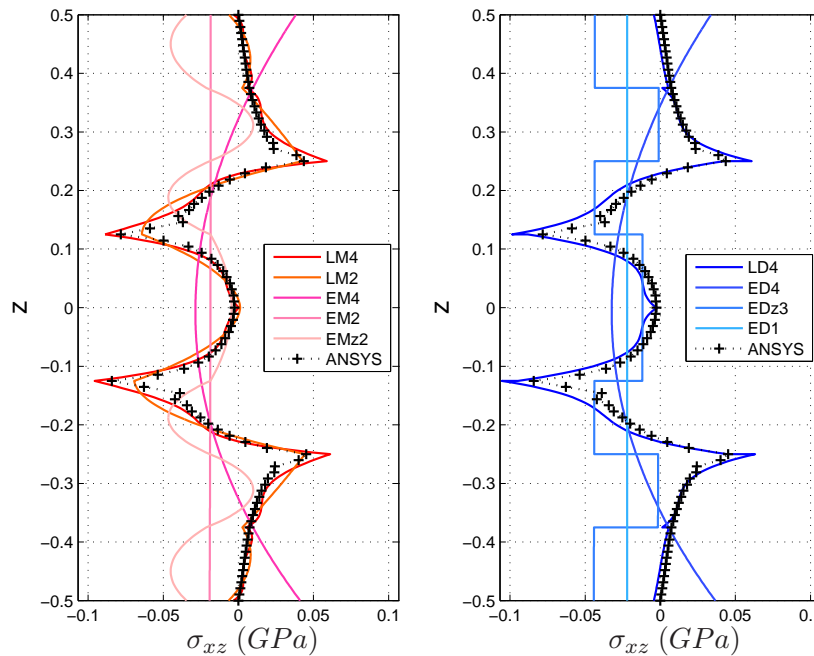


Figure 3.49: Bending:  $\sigma_{xz}$  at  $(x = 0, y = b, z)$  for  $[90, 0, \pm 45]_s$  using RMVT & PVD

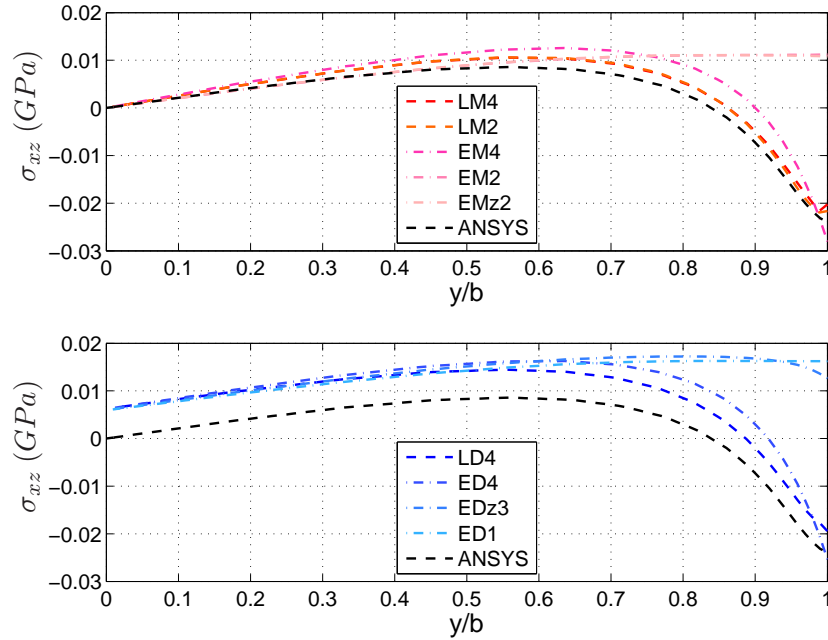


Figure 3.50: Bending:  $\sigma_{xz}$  at  $(x = 0, y, z = \frac{h}{8})$  for  $[\pm 45, 0, 90]_s$  using RMVT & PVD

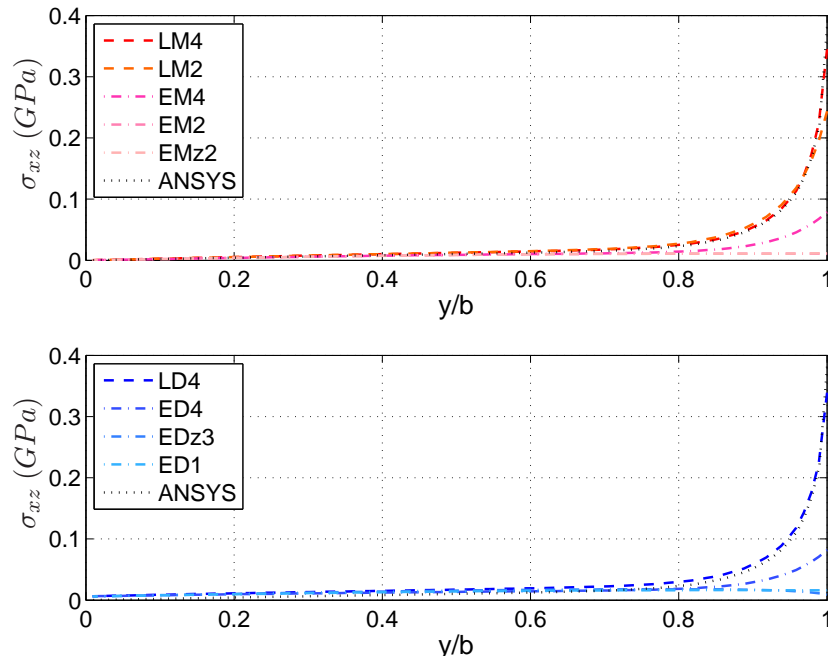


Figure 3.51: Bending:  $\sigma_{xz}$  at  $(x = 0, y, z = \frac{3h}{8})$  for  $[\pm 45, 0, 90]_s$  using RMVT & PVD

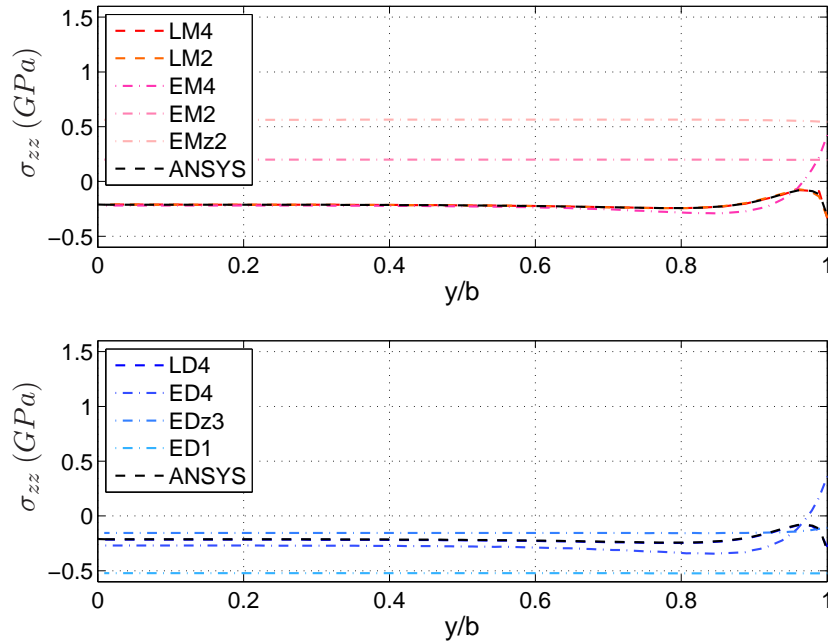


Figure 3.52: Bending:  $\sigma_{zz}$  at  $(x = 0, y, z = \frac{3h}{8})$  for  $[90, 0, \pm 45]_s$  using RMVT & PVD

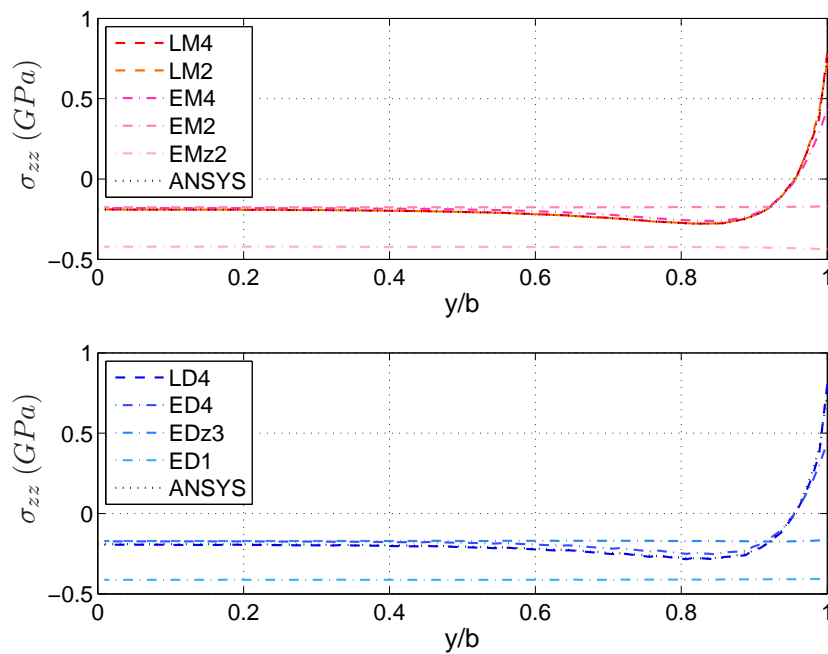


Figure 3.53: Bending:  $\sigma_{zz}$  at  $(x = 0, y, z = \frac{h}{4})$  for  $[90, 0, \pm 45]_s$  using RMVT & PVD

Table 3.11: Bending:  $\alpha_{xz}$  and  $|A_{xz}|$  for the  $[\pm 45, 0, 90]_s$  laminate

Model	$[\pm 45, 0, 90]_s$					
	1. Interface		2. Interface		3. Interface	
	$ A_{xz} $	$\alpha_{xz}$	$ A_{xz} $	$\alpha_{xz}$	$ A_{xz} $	$\alpha_{xz}$
Ansys	2.2125	1.6220	1.0780	0.1080	8.8947	0.2716
LM4	0.2328	0.0413	0.3788	0.2238	1.9842	0.1413
LM2	0.2219	0.0100	0.4350	0.1341	1.8369	0.0719
LD4	0.5142	0.0154	0.6642	0.1531	1.4928	0.2176
LD2	0.5108	0.0168	0.6164	0.1778	1.5475	0.1708
EM4	0.2174	0.0624	0.1076	0.0294	0.6518	0.0482
EM2	0.1121	0.0004	0.1100	0.0004	0.1079	0.0013
EMz2	0.1092	0.0014	0.1099	0.0004	0.1137	0.0050
ED4	0.5376	0.0286	0.2138	0.0125	0.3384	0.0804
EDz3	0.1918	0.0191	0.1380	0.0424	0.2158	0.0305
ED1	0.1669	0.0028	0.1669	0.0028	0.1669	0.0028
Model	1. Interface		2. Interface		3. Interface	
	$ A_{zz} $	$\alpha_{zz}$	$ A_{zz} $	$\alpha_{zz}$	$ A_{zz} $	$\alpha_{zz}$
	2.6473	0.1205	0.5975	0.0548	5.7141	0.7968
Ansys	0.9904	0.1819	0.6639	0.0071	0.0200	1.0523
LM4	1.1517	0.1463	0.6113	0.0725	0.0636	0.6217
LM2	0.9356	0.2014	0.6082	0.0507	0.0216	1.0379
LD4	1.2658	0.1269	0.7572	0.0188	0.1269	0.4763
LD2	0.4467	0.0435	0.6857	0.0528	0.6786	0.0739
EM4	0.1739	0.0005	0.2544	0.0002	0.2526	0.0004
EM2	0.3179	0.0164	0.3072	0.0198	0.5512	0.0081
EMz2	0.4137	0.0458	0.7369	0.0489	0.6720	0.0724
ED4	0.2608	0.0401	0.2757	0.0235	0.4168	0.0474
ED1	0.2082	0.0002	0.4516	0.0008	0.4720	0.0007
$ A_{ij} $ in [GPa]						

Table 3.12: Bending:  $\alpha_{zz}$  and  $|A_{zz}|$  for the  $[90, 0, \pm 45]_s$  laminate

Model	$[90, 0, \pm 45]_s$					
	1. Interface		2. Interface		3. Interface	
	$ A_{xz} $	$\alpha_{xz}$	$ A_{xz} $	$\alpha_{xz}$	$ A_{xz} $	$\alpha_{xz}$
Ansys	1.5812	0.2370	0.9994	0.2474	-	-
LM4	2.0250	0.1260	0.9824	0.2068	-	-
LM2	1.9268	0.0563	1.0123	0.1178	-	-
LD4	1.4123	0.1488	1.6038	0.0925	-	-
LD2	0.9742	0.0678	1.1351	0.0588	-	-
EM4	0.8296	0.0189	0.4194	0.0048	-	-
EM2	0.6311	0.0230	0.6295	0.0229	-	-
EMz2	0.6335	0.0232	0.6387	0.0343	-	-
ED4	0.2257	0.0599	0.1796	0.0119	-	-
EDz3	0.2062	0.0790	0.5906	0.1119	-	-
ED1	0.0616	0.1544	0.0616	0.1543	-	-
Model	1. Interface		2. Interface		3. Interface	
	$ A_{zz} $	$\alpha_{zz}$	$ A_{zz} $	$\alpha_{zz}$	$ A_{zz} $	$\alpha_{zz}$
	1.0664	0.1726	1.1189	0.1648	-	-
Ansys	1.4543	0.2249	1.5713	0.2141	-	-
LM4	1.7511	0.1509	1.8487	0.1514	-	-
LM2	1.4501	0.2223	1.3635	0.2655	-	-
LD4	1.9078	0.1207	2.1250	0.1379	-	-
LD2	0.6782	0.1150	1.2807	0.1169	-	-
EM4	0.6420	0.0009	0.8018	0.0011	-	-
EM2	0.4856	0.0012	2.0339	0.0015	-	-
EMz2	0.6283	0.1205	1.3026	0.1151	-	-
ED4	0.5234	0.0282	0.7859	0.0125	-	-
ED1	1.2362	0.0002	1.9038	0.0004	-	-
$ A_{ij} $ in [GPa]						

### 3.3 On the Difference between Bending and Extension

As criterion for the confrontation of the free-edge effects due to bending or extensional load, the same total deformation energy is imposed. The uniform bending load was applied with a magnitude, producing for the same laminate the same deformation energy as in the extension case. Evidently this varies quite a lot for the laminates in consideration in the bending compared to the extension case. In the extension case, the uniform load is equally distributed to all the layers of the laminate. Therefore, the order of the layers orientations in the laminate show less importance compared to bending.

For the two cross-ply laminates,  $[0, 90]_s$  and  $[90, 0]_s$ , a similar behaviour in extension is observed, while in bending the  $[0, 90]_s$  is more than three times stiffer than the  $[90, 0]_s$  laminate. This originates from the outer layers, having their predominant stiffness orientated into the highest stress direction. The same considerations hold for the quasi-isotropic laminates. In extension, they have a comparable, but only slightly lower stiffness as both cross-ply laminates. However, in bending both are quite different: the  $[90, 0, \pm 45]_s$  has the 0 degree layers further outwards compared to the other quasi-isotropic laminate, plus the  $\pm 45$  layers in the centre, where the maximal shear stress can be found. This makes it in comparison to the  $[\pm 45, 0, 90]_s$  laminate about 50 % stiffer. The  $[\pm 45]_s$  angle-ply laminate is a special case in both, bending and extension. Through its layers orientation, the stiffness in the direction of the extension drops significantly, which makes it the weakest of all five laminates in extension. In bending, a similar observation can be found because the stiffness in the outer layers is comparatively low to that provided by a 0 degree layer. Also, through its strong in-plane coupling an additional shear deformation is present.

The rigidity alone is not a decisive factor for the comparison of the free-edge effect. Here, two factors were introduced to measure the singularities. The order of singularity  $\alpha_{ij}$ , providing the slope, and the singularity strength  $|A_{ij}|$ , providing the magnitude in a distance of  $r = 1$  of the fitted curve. Its magnitude gives at the same time an indirect measurement for the length of influence. Due to the nature of a monotonous rise, a higher value of  $|A_{ij}|$  is linked to a longer length of influence of the singularity. With other words, the length share through width of elevated stress levels is higher, as the rise towards the singular behaviour starts at an earlier point in the distribution across width. Hence the decisive criteria for a comparison is first the singularity strength  $|A_{ij}|$  and afterwards the order of singularity  $\alpha_{ij}$ . This rise in width is influenced by load type and stacking order. Comparing the singularity strength for the two cross-ply laminates in extension in Tables 3.3 and 3.5 and for bending in Table 3.10, generally a more pronounced singularity can be found in extension. An exception is the  $[0, 90]_s$ , which has a higher singularity strength in bending. From the graphs, Figure 3.2 for extension and Figure 3.43 for bending, a similar behaviour of the transverse normal stress can be seen. Even if the calculated magnitudes seem comparable, the predicted rise at the free edge itself is more pronounced in bending. This leads to the conclusion that in bending, the free-edge effect is more pronounced compared to extension. As the outer layers 0 degree layers

have a higher rigidity as the inner 90 degree layers, they are capable of introducing higher stress in the bending case. Therefore, they provide a higher strength and order of singularity, compared to the other cross-ply laminate with the inverse stacking sequence.

In the case of the angle-ply laminate, a higher gap in-between the singularity strength provided by Ansys and by the CUF elements can be seen, see Table 3.3 for extension and the first two columns of Table 3.10 for bending. The computation of angle-ply laminates was found to be quite challenging for the CUF elements. This applies equally to bending and extension. Regardless to the difference of Ansys and CUF models, the results achieved are comparable. The quantitative values are of the same orders in the obtained distributions, and the tendency for the different elements are the same as in the cross-ply laminates. For the angle-ply laminate, higher singularity strength values are present than for the cross-ply laminates. Also, as stated before, generally for extension higher values are achieved as for the angle-ply laminate in bending.

The singularity strength  $|A_{ij}|$  was identified as being equally influenced by the length of influence of the singularity. The distributions through the width confirm the findings of higher singularity strength in extension. For the angle-ply laminate the begin of the singular behaviour starts at a width ratio of  $y/b = 0.6$ , shown in Figure 3.6, and for the cross-ply laminates it starts at about  $y/b = 0.8$ , see Figures 3.2 and 3.4. In bending the rise towards the singularity starts for the angle-ply laminate in Figure 3.41 as well as for the  $[90, 0]_s$  cross-ply laminate in Figures 3.43 and 3.45 at about  $y/b = 0.9$ . An exception is the before stated  $[0, 90]_s$  laminate, rising from the same starting point up to the same maxima values, as shown in Figure 3.43.

As an exception for both load cases, the  $[90, 0]_s$  laminate has to be stated. Due to its sharp in flexion close to the free edge, it has a non monotonous stress distribution in the interval used for the fitting. Another fitting approach has to be applied to this case.

The same difference in singularity strength between bending and extension pursues for the quasi-isotropic laminates. Compared between extension in Tables 3.7 as well as 3.6, and bending, 3.12 as well as 3.11, the resulting singularity strength is always lower for bending. The decay for the singularity as shown in Figure 3.8 for the extension case starts at  $y/b = 0.8$  while in bending in Figure 3.50 the decay can be found at around  $y/b = 0.9$ . This concerns the interface in-between the  $\pm 45$  layers, which has the highest, respectively the most pronounced singularity of all the interfaces in the lay-up. Hence also for the quasi-isotropic laminates, the free-edge effects are stronger in extension.

In the introduction of the singularity fitting, a link between the strength  $|A_{ij}|$  and the order of singularity  $\alpha_{ij}$  was given. Having a low singularity order  $\alpha_{ij}$  results in a higher singularity strength. A lower order means having a steeper rise in the immediate vicinity of the free edge towards the maximum stress. Further, this results as well in comparatively stronger rise before  $r = 1$ . This is equally shown by the width distributions: through this earlier rise towards the singularity in extension, lower values for the singularity order  $\alpha_{ij}$  are obtained and hence higher singularity

strength  $|A_{ij}|$  in extension.

By using the fitting parameters, the assessment of the critical interface for each laminate under both loading is possible. This is displayed for the quasi-isotropic laminates hereafter, as they contain all of the cross-ply and angle-ply interfaces stated before. For both quasi-isotropic laminates only the usable stress components  $\sigma_{xz}$  and  $\sigma_{zz}$  are given using the LD4 model. From Figure 3.54 for extension from the  $[\pm 45, 0, 90]_s$  laminates the  $\sigma_{zz}$  at the 0, 90 interface is identified as the most critical one, through its high stress values across the whole fitting interval of  $r$ . For bending, stated in Figure 3.55, the stress component  $\sigma_{xz}$  at the  $\pm 45$  interface has the highest values. For the  $[90, 0, \pm 45]_s$  laminates in Figure 3.56 for extension,  $\sigma_{xz}$  at the  $\pm 45$  interface has the highest stress values, while Figure 3.57 for bending identifies  $\sigma_{zz}$  at the 0, 45 interface as the most likely interface to initiate delamination.

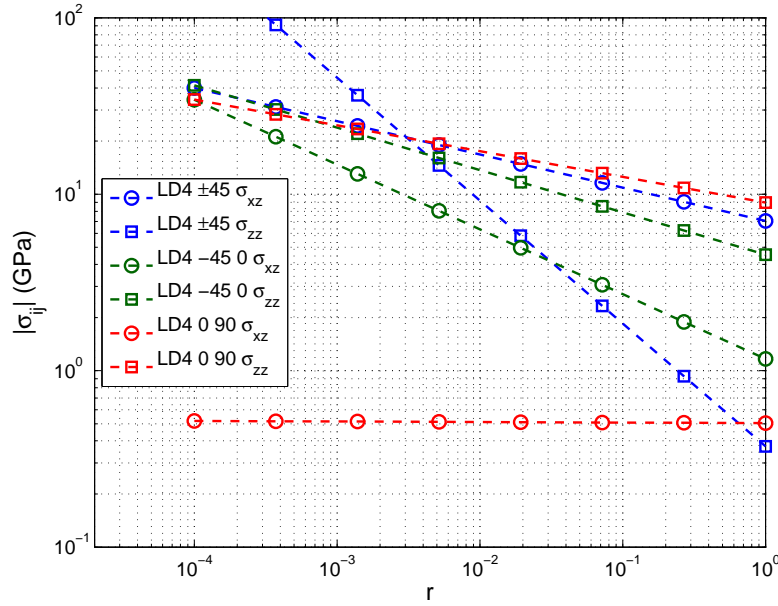


Figure 3.54: Extension: fitted transverse stresses close to the free edge of the  $[\pm 45, 0, 90]_s$  using LD4

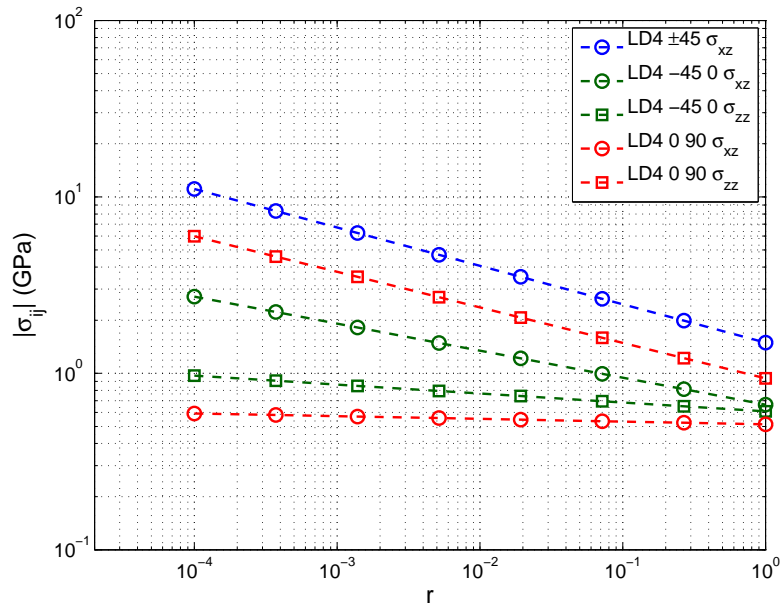


Figure 3.55: Bending: fitted transverse stresses close to the free edge of the  $[\pm 45, 0, 90]_s$  using LD4

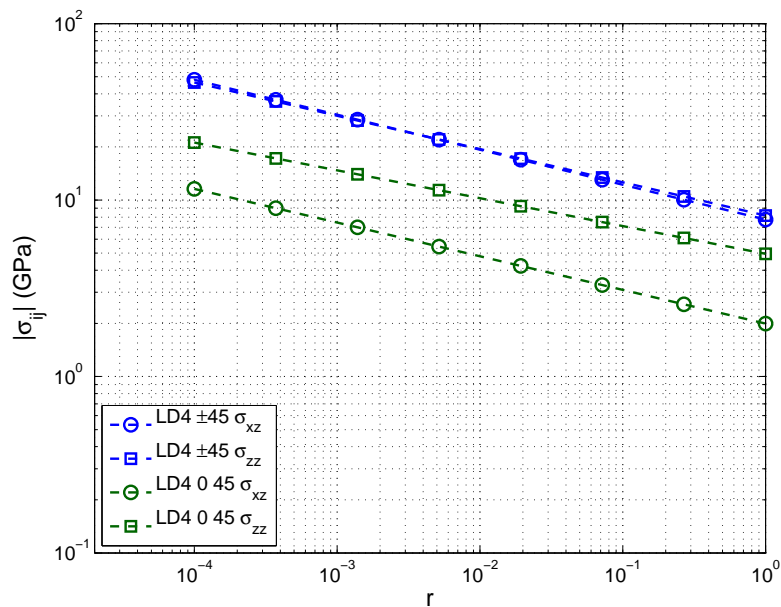


Figure 3.56: Extension: fitted transverse stresses close to the free edge of the  $[90, 0, \pm 45]_s$  using LD4

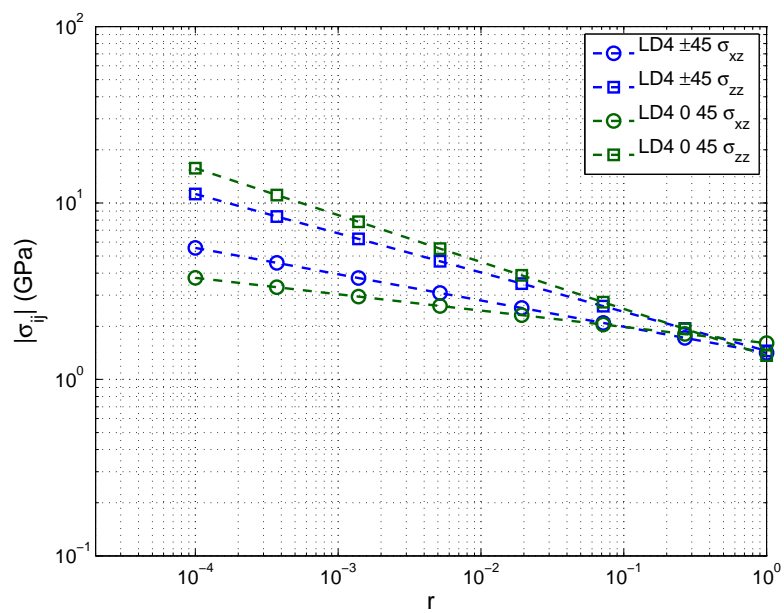


Figure 3.57: Bending: fitted transverse stresses close to the free edge of the  $[90, 0, \pm 45]_s$  using LD4

### 3.4 Conclusion

Three class of symmetric laminates were addressed with respect to the free-edge effects: the angle-ply laminate  $[\pm 45]_s$ , two cross-ply laminates  $[0, 90]_s$  and  $[90, 0]_s$  and two quasi-isotropic laminates  $[90, 0, \pm 45]_s$  and  $[\pm 45, 0, 90]_s$ . Moreover, the free edge response of each laminate has been considered for two loading configuration: in-plane extension and out-of-plane bending under uniform pressure load. In angle-ply laminates the singularities occur essentially due to the transverse shear  $\sigma_{xz}$ , which is the predominant stress. The cross-ply laminates are dominated by the Poisson's ratio mismatch, which makes the transverse normal stress the most remarkable stress component.

The quasi-isotropic laminates include both effects, which occur to different extents, depending on the stacking sequence. In order to reduce the computational cost associated to a full three-dimensional FEM analysis, the application of two-dimensional plate elements may be interesting. Comparing the computed three-dimensional results in Ansys, as well as the presented results from literature with the performance of the different CUF models, the following conclusions could be made:

- Generally modelling the free-edge effects with the LW models of at least second order provide results close to those obtained by commercial three-dimensional codes.
- Using a simple in-plane mesh refinement is a very economic way to asses the behaviour of a laminate. Refining through the thickness, through the introduction of several mathematical layers per physical layer, provides further information about the singular behaviour.
- LW models provide the most accurate results for free-edge effects.
- ESL models are able to provide satisfactory results far from the free edge: in these regions these models may represent a good compromise between computational cost and accuracy. However, in the free-edge region, ESL models only approximate the steep stress gradients.
- The inclusion of Zig-Zag for ESL based models does only improve slightly their comparatively poor performance concerning the free-edge effect.
- RMVT models fulfill the ICs a priori and provide better results compared to PVD bases models of the same expansion order.
- The higher the expansion order, the better the congruence with the reference

While applying LW models with higher expansion orders to the free-edge effect in extension and bending, the results provide the following conclusions:

- The Power Law fitting is a reliable way to measure the singular behaviour of the stress components.
- The Power Law parameters provide an intuitive way to compare different laminates.
- The strongest singularities appear for both, bending and extension, in angle-ply laminates.
- The stacking sequence has a higher influence on the free-edge effect in bending compared to extension.
- With the exception of the  $[0, 90]_s$  laminate, the singularities are lower in strength while comparing bending to extension.

In the following an estimate of the computational cost of two-dimensional CUF models and three-dimensional models is discussed. The in-plane discretization of the plate surface is the same in the three-dimensional models and the two-dimensional CUF models: mesh (*I*) has  $32 \times 32$  elements. However, bilinear approximations are used in the CUF elements, while quadratic brick elements are used in Ansys. This results in only 1089 nodes in total for the CUF models, and 3201 nodes for the three-dimensional model in the in-plane direction. The same mesh of a total of 48 elements in thickness is used in the three-dimensional mesh for the four layer configurations. In the CUF we have for the LW elements a dependency on the number of layers additionally to the dependency on the order of the thickness function. The total number of unknowns are listed in Table 3.13. Note that the LM4 model has still a lower number of total unknowns than the three-dimensional model. For the four layer configurations, half the unknowns are needed to achieve the same results and only a quarter if the LD4 model is used. Compared with the ESL models, even more than six times less unknowns were used for EM4 and about a thirteenth for the ED4 model.

Table 3.13: Total number of unknowns for the four layer laminates

Model	total Unknowns
Ansys	217156
LM4	111078
LM2	58806
LD4	55539
EM4	32670
EM2	19602
EMz2	26136
ED4	16335
EDz3	16335
ED1	6534

## Chapter 4

# System Reduction via Model Coupling

In the previous chapter, different kinematical models have been applied to problems having very strong stress gradients in a small local region. It could be seen, that far from the free-edge, the stress gradients are rather smooth, hence simple kinematical models deliver accurate results. On the contrary, refined models are needed in the vicinity of the free-edge. This Chapter therefore deals with the methods how to couple models with different kinematics but same dimensionality. The main issue consists in saving computational time. In fact, only the refined higher-order model is used in the localized domain of interest, while the remaining overall global domain will be using a lower order kinematical model. In this way, the computational effort is focused only in a small domain. In order to properly connect those different models in their different domains, several techniques will be compared from a theoretical point of view as well as their implementation into the FE Method.

In this first overview the concepts of how the different domains can be arranged and how the connection can be established is presented is discussed. From this global overview of different concepts, it will be the eXtended Variational Formulation (XVF), which shows to be the most suitable one. Originally it was designed for coupling models with different dimensionality. Hence its adoption to couple models with the same dimensionality but different kinematics will be presented. The chapter is concluded by a numerical study on the XVF. For the sake of simplicity, the studies are carried out on one-dimensional structures. Homogenous and sandwich materials are addressed.

### 4.1 Literature Overview

#### 4.1.1 Differentiation of Techniques

In the past, different modeling approaches have been developed, which have been often motivated by a multi physics context. Mainly domains with heterogenous di-

mensionality but homogenous kinematical descriptions have been taken into account, or domains of homogenous dimensionality with heterogenous kinematics. Heterogenous dimensionality means that local domains of interest are modeled in a higher dimensionality, often three-dimensional models. Consequently, the global domains are made of models of lower dimensionality, like one-dimensional beam or two-dimensional plate or shell models. In the context of this work, no dimensional heterogeneity is used. This work focuses on the use of different kinematics for each sub region of the structure. Therefore, at least two different sub regions can be identified: one containing a rather complex kinematics, named complex domain hereafter, and the global domain, using a simple kinematics, which is consequently the simple domain.

Regardless of the aspect of the geometric order of the two domains, three possible configurations can be distinguished in order to combine a complex with a simple domain. They are displayed in Figure 4.1. In (a) no overlap between the simple domain  $\Omega_s$  and the complex mechanical  $\Omega_c$  is shown  $\Omega_s \cap \Omega_c = \Gamma$ ; (b) shows a partial overlap between both domains  $\Omega_s$  and  $\Omega_c$  such as  $\Omega_s \cap \Omega_c = \Omega_a$ ; in (c)  $\Omega_c$  is fully overlaid to the simple domain  $\Omega_s$ .

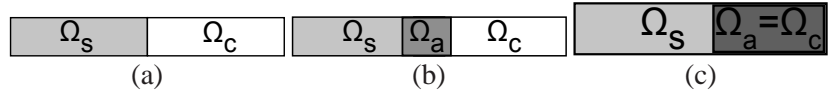


Figure 4.1: Domain arrangement: no (a), partial (b) or complete overlap (c)

The decision of how the domains are arranged is mainly influenced by the way the problem is treated. Having an overlapping arrangement like in (b) and (c) is of advantageous especially for techniques using heterogeneous dimensional models. However also some techniques considering homogenous dimensionality considered this type of arrangement. This is due to a rather strong difference in the kinematical models used.

#### 4.1.1.1 Non Overlapping Techniques

A classical method to link kinematical heterogeneous models is the Lagrange Multiplier Technique. To the mathematical formulation of the mechanical problem an interface constraint function is added in order to minimize the difference between the domains containing the different kinematics. Prager was the first to propose an interface potential for a physical discontinuity through a single Lagrange multiplier field, in the context of variational formulation in elastostatics [59]. On the basis of this classical two-fields formulation a method to combine variable kinematical beam models in the context of the CUF was developed [12]. They considered different classical as well as higher order kinematical models by a Taylor Series Expansion from the neutral fibre of the beam structure. A chosen number and location of points were used to set up a Lagrange Multiplier field to establish the coupling at the com-

mon Interface. Different homogenous material structures with complex geometries were considered, providing results of the kinematical heterogeneous model close to the kinematical homogenous model.

Extensive studies have been done to give a flexible formulation of the Lagrange Multipliers used for the connection at the interfaces between local and global domain. Aminpour, Ransom and Cleary investigated the possibility of directly connecting two completely different, non matching meshes in one single calculation [1]. Therefore they used a spline method to model the common border between the domains, as illustrated in Figure 4.2. Three independently handled unknowns are present: unknowns in the subdomains, the unknowns at the common interfaces and the unknown representing the interaction at the interfaces. The last ones are mainly the Interface forces. All the three sets of unknowns are treated independently. This type of technique is regarded as Three-field formulation. Ransom expanded this technique by a general approach using different solution techniques, like finite differences, finite elements and finite volumes, which have favourable characteristics for each domain [62]. Therefore, he showed how the interface conditions have to be formulated to pass from one solution method in one domain to the method used in the opposing domain. This is shown in Figure 4.2 through the additional intermediate Interface  $\Gamma_{intermediate}$ .

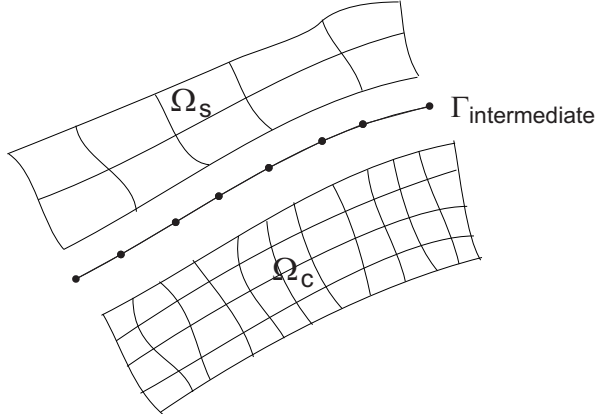


Figure 4.2: Continuous spline formulation based on an independent discretization to pass between incompatible domain repartitions

Different efforts by a series of authors have been done to unify the three-field method in the context of coupling independently modelled domains . The most notable one was done by K. C. Park and Felippa [55]. Here the independently modelled domains are coupled via localized Lagrange Multipliers, instead of one global Lagrange Multiplier set. They considered previous works like from Atluri [2] as well as the FETI (Finite Element Tearing and Interconnecting) algorithm by Farhat and Roux [19] on coupling independently modelled domains. K. C. Park and Felippa

method expanded the previous ones by adding the possibilities of rigid body motion and floating sub-domains of non matching meshes in order to enable the method to be used for crack propagation problems.

A possible reduction of this three-field formulation while still retaining a local description is the elimination of the independent unknowns at the common interfaces. Through the construction of a suitable interface approximation, it can be reduced towards a Two-field formulation. This technique is known as Mortar Method presented by Lacour and Maday [45] or Puso [60]. It still uses an independent Lagrange Multiplier field in-between the independently modelled domains. Equally to the before mentioned methods, the Lagrange Multipliers are defined locally, based on the description of the adjacent sub-domains. However they are not based on a Lagrange polynomial like in the FETI method, but rather on piecewise linear functions. Here the piecewise linear functions are established using the nodes of the non-matching meshes of the independently modelled domains.

An alternative technique has been presented by Blanco et al. [7]. Based on the two different kinematical descriptions, two Lagrange Multiplier spaces are introduced. The classical principle of virtual variations is therefore enriched by a dual space between the kinematical variables and Lagrange Multipliers. It allows to couple heterogenous dimensionality and kinematics. Further details of this technique will be given later in this chapter in the section 4.3.1.

The introduction of Lagrange Multipliers prohibits the band structure of the linear system describing the mechanical problem. H.G. Kim [40] developed therefore a special interface element in order to avoid Lagrange Multipliers. In a moving least squares approach, the new specific shape functions are introduced in an interface element domain. This domain assures the continuity of the displacement. Through this localized approach, the numerical integration is a difficult task.

Commercial FE Codes offer the possibility of the so-called global local analysis. The overall domain is described with a simple or low order kinematical model and one or more local sub-domains can be chosen for applying refined geometric or model representations. So, heterogeneous dimensionality and kinematics are possible. Both domains have a common border. The results of the simple local model at this common border are used as boundary conditions for the local sub-domain having the higher order kinematical model inside. Calculations are normally done in at least two subsequently steps, but also iterative methods have been applied. Equally another classical method available in commercial codes are Multiple Point Constraints (MPC). They are frequently used in different applications, mainly to couple geometric heterogenous models. In the case of kinematical heterogeneous modes, the two domains are connected at the common interface through an imposed relation between the models used. This relation is applied at the discrete level of the kinematical description, hence the available degrees of freedom (DOF) are therefore linked in a suitable manner. This technique does not add new DOFs but imposes a behaviour at the interface between both domains. In Figure 4.3, two simplified displacement fields through thickness of beam structures are shown. The two different behaviours need to be matched at the common interface. The complex model on the right is

enforced through the applied condition to take the form of the simple model on the left. Among the stated techniques, it is an exception as it is purely numerically motivated and does not rely on an energy principle. Recently, a MPC formulation for eigenfrequency calculation and dynamic contact problems have been developed by Hetherington et al. [30].

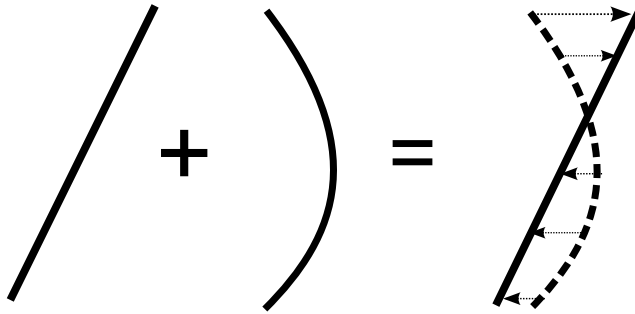


Figure 4.3: MPC enforces complex model to be compatible with simple model

#### 4.1.1.2 Partial Overlap

At least a partial overlap is used inside for the Arlequin Method introduced by Ben Dhia et al [16]. This technique defines three zones: A domain using a simple kinematical model, a domain using a complex kinematical model and the sub-domain where both domains overlap. See configuration (b) in Figure 4.1. Inside the overlapping domain, Lagrange Multipliers are used to establish the connection in a weak sense formulation, representing a form of glueing force along the common domain. Due to the overlap, a partition of the energy between both domains is introduced. Different possibilities to do so are studied in [26]. Applications of this technique to receive detailed local results in sandwich structures have been done by Hu et al for geometrically linear [32] and nonlinear problems, [34] and [82]. In this work, the Arlequin method was used to combine dimensional heterogeneous models. For the local domain of interest, a higher dimensionality than in the rest of the structure was used to gain the desired detailed results. However Biscani and Giunta applied the Arlequin Method to homogenous dimensional problems. The potential of the local refinement using the partial superposition of a lower order and higher order kinematics in the context of the CUF are shown for beams [24] and plates [6]. Arlequin can be reduced to surface coupling of the domains. This however is not used frequently as perturbations occur in results [26]. This technique will be discussed in further details in the Appendix A.

### 4.1.1.3 Complete Overlap

Several authors have studied the possibility to overlay a global mesh with a local mesh having different element size and different element order.

One of the most remarkable contributions were done by Fish et al [20]. They introduced the superposition version of the FE Method, denoted as the s-Version or S-FEM. Higher order hierarchical elements in the local domain are overlaid onto the global finite element mesh. Homogenous boundary conditions along its common boundary are applied to keep compatibility and  $C^0$  continuity. The overall displacement in the local area is the addition of the higher order mesh and the global mesh. The solution for homogenous dimensional problems is obtained in one direct step with the possibility of incompatible meshes for the global and local domains. Fish and Markolefas [21] used the s-Version equally for the computation of layered structures, where they used ESL elements for the global domain and LW elements as local overlays. Different polynomial orders are used for the displacement field. In this application, only the cross-shape of the laminate is meshed.

A Similar method was developed by J.W. Park et al, [54], adapted to classical displacement based and two-field assumed strain FE formulations. This method is capable of providing adaptive refinements inside the sub-domain of interest and further needs no additional transition region or Multi-Point Constraints.

Refining locally element order and element size, is known as  $p$  and  $h$  refinement. Including these ideas into the coupling techniques was the subject of several authors. One attempt to combine the  $p$  refinement with the ideas of the s-Version are the works on variable kinematics of Reddy and Robbins [63]. The difference to the s-Version is in the hierarchical element family considered, here the variable kinematics finite elements. While in the s-Version for composites, the elements model the laminates cross-shape, elements in the variable kinematics approach model the in-plane section of the laminate. As the variable kinematics formulation was developed for layered structures, the higher order elements use a LW description. The elements in the global domain use an ESL description. Different orders of expansion were used. Reddy and Robbins considered up to second order polynomials through thickness on purely displacement based LW elements and up to third order polynomials for the ESL type elements. Unlike the s-Version, the global and local elements have for the in-plane direction the same order polynomial of their shape functions.

Spectral methods are applied in [56] as an overlay of simultaneously refined element order ( $p$ -refinement) and size ( $h$  refinement). The laborios domain of the problem  $\Omega$  is brought towards a simpler and larger domain  $\Pi$ , containing  $\Omega$ . The chosen  $\Pi$  which will be used for the solution process, has to be formulated in a way that in the common regions of both domains the results will be coincident.

An iterative two scale analysis method for local sub-domains has been developed by Gendre et al [22]. The method combines local and global contributions. The global domain is assumed to have linear elastic properties, which can be also homogenized, while material and geometric non-linearity can be included for the local domain. It uses a two-scale approximation of the Schur complement of the lo-

cal domain's stiffness matrix. The use of a weighted combination of Dirichlet and Neumann boundary conditions on the local domain enables relatively low number of iterations and assures the convergence of the solution.

Finally, the zooming method [31] is a scale descending iterative FE technique. Inside a global domain, a local domain of interest is defined. The mesh of the local region is refined at each step. At the same time, the local domain of interest is redefined. The refined local domain will be a cut-out of the previous analysis, so the new local domain is narrowed down in each so-called zooming step, shown by Figure 4.4. Therefore the zooming method is used to locate and asses local stress concentrations.

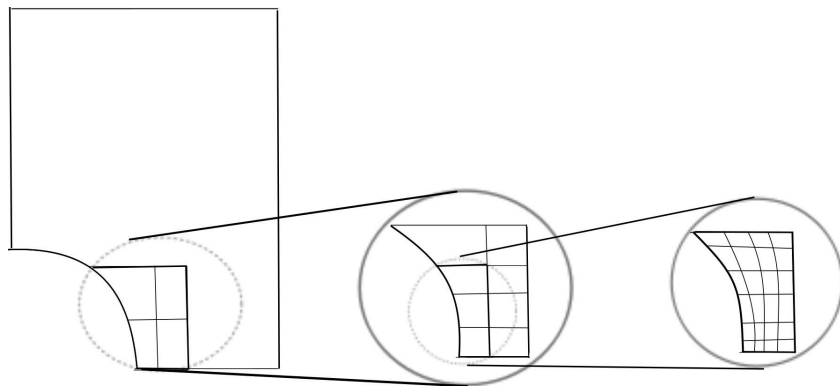


Figure 4.4: Principle of the scale descending Zooming Method

### 4.1.2 Comparison of methods

Based on the division of the three different domain arrangements, a more detailed comparison of those existing techniques is done in Table 4.1. For each technique some common aspects are compared. The first column is about the orientation of the domain and the exchange of informations. This means for example if the exchange happens origins from a coarse model  $c$  towards a fine model  $f$  or vice versa the fine model is defined before the coarse model or even both at the same time. Further, due to the different mathematical modellisations used, the establishment of the connection is regarded via the unknowns included. Some are based on the displacements  $\mathbf{u}$ , some on the stresses  $\sigma$ , while some consider the sum of the total work, denoted by  $\Sigma\mathbf{W}$ . As a consequence, this requires for some techniques an iterative calculation, while some other profit from the possibility of a direct calculation of the solution. The domain arrangement is listed again for convenience, indicating also for some techniques the possibility to provide other domain arrangements. Some techniques however need some additional interface formulations.

The most desirable technique seems to be a technique having no overlap and a global matching mesh, avoiding extensive additional efforts for the transfer between the domains. The recently developed eXtended Variational Formulation (XVF) seems

a promising candidate through the adoption of the different Lagrange Multipliers. These additional unknowns have the benefit to be of the same form as the kinematical models used and are strictly localized to the domains interface. The XVF will be therefore used within this chapter to establish the connection between the different domains. Further, it will be identified as an encompassing formulation for different existing techniques. Among the different techniques to combine heterogeneous kinematics, the most used today are the Multi-Point Constraints. Its relation with the XVF will be given as well as for another recent technique, the Arlequin Method.

Table 4.1: Techniques for Coupling heterogenous Kinematics

Name	model direction coarse / fine	connection via			solution		overlap no	overlap partial	additional Interface yes
		$\mathbf{u}$	$\sigma$	$\Sigma \mathbf{W}$	direct	iterative			
MPC	$c \leftrightarrow f$	x	x		x		x	x	x
Submodelling	$c \rightarrow f$	x				x	x		
Spline method [1].	$c \rightarrow f$	x			x		x		x
Collaborative by Ransom [62]	$f \rightarrow c$			x	x		x		x
FETI [19]	$c \leftrightarrow f$			x	x		x		x
XVF [7]	$c \rightarrow f$			x	x		x		x
Interface Element [40]	$f \leftrightarrow c$	x			x		x	x	x
Arlequin [16]	$c \leftrightarrow f$			x	x			x	x
S-FEM [20]	$c \rightarrow f$			x	x				x
Mesh Superposition Method [54]	$c \rightarrow f$	x	x		x				x
Variable Kinematics [63]	$c \rightarrow f$			x		x			x
Spectral by Parussini [56]	$c \rightarrow f$			x		x			x
Zooming method [31]	$c \leftrightarrow f$	x				x			x
iterative two scale [22]	$c \rightarrow f$	x	x			x			x

## 4.2 Modeling of One Dimensional Structures

The kinematics used in the present approach are discussed. This section deals with the modeling of beam structures, and in particular for multilayered structures, as presented in section 2.3.

In the following, the reference coordinate system, given in Figure 4.5 is used. The cross-section of the beam is denoted  $S$  and its thickness  $h$ .

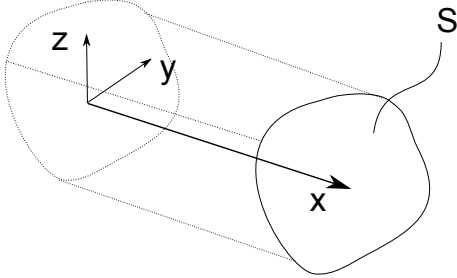


Figure 4.5: Coordinate system of a beam structure

### 4.2.1 Kinematical Models

The basis for all classical and advanced kinematical theories is made up by the thickness expansion function  $f(z)$ . In the displacement based ESL approaches, it describes the assumed deformation behavior through thickness.

A general displacement field can be expressed as:

$$\begin{cases} u_1(x, z) = v_0(x) - z v_1(x) + f(z) (\theta(x) + v_1(x)) \\ u_3(x, z) = w_0(x) + z w_1(x) + z^2 w_2(x) \end{cases} \quad (4.1)$$

The membrane elongation is represented by  $v_0$  and the deflection of the neutral fibre by  $w_0$ . The rotation of the section is given by  $\theta$ , while  $v_1$  represents a contribution of the transverse shear deformation. This leads to a deformable section along with the beam's length and the thickness. In this expression, the stretching effect is also taken into account by two additional unknown functions  $w_1$  and  $w_2$ . The linear term  $w_1$  represents the coupling with the membrane component and the quadratic term  $w_2$  the actual thickness dilatation. The according strains can be deduced as:

$$\begin{cases} \epsilon_{11}(x, z) = v'_0(x) - z v'_1(x) + f(z) (\theta'(x) + v'_1(x)) \\ \gamma_{13}(x, z) = w'_0(x) + z w'_1(x) + z^2 w'_2(x) - v_1(x) + f'(z) (\theta(x) + v_1(x)) \\ \epsilon_{33}(x, z) = w_1(x) + 2z w_2(x) \end{cases} \quad (4.2)$$

Note that the transverse normal strain,  $\epsilon_{33}$  is available with this displacement formulation.

Some classical kinematical theories can be deduced depending on the expression of the thickness expansion function  $f(z)$  and the suppression of the transverse normal effects. Each of the assumptions and resulting capabilities of those classical theories are discussed hereafter.

#### 4.2.1.1 Euler-Bernoulli Theory

The simplest kinematical model is known as the Euler-Bernoulli kinematics for beams and as Kirchhoff kinematics for plates [43]. As this theory does not include transverse shear effects, the section will remain normal to the neutral fibre. Due to this strong relation between the deflection and the non-existing rotation, the shear deformation  $v_1$  is replaced by  $w'_0$ . For the beam structure the mechanical behavior is simplified towards a generalized plane stress behavior in the  $x-z$  plane. No rotation of the section is present, which leads to the thickness expansion function  $f(z) = 0$ . The formulation of the displacement field for a beam structure is the following:

$$\begin{cases} u_1(x, z) &= v_0(x) - z w'_0(x) \\ u_3(x, z) &= w_0(x) \end{cases} \quad (4.3)$$

As shear is one of the important components for layered structures, the kinematical hypothesis assumed are not sufficient for their description. Therefore, for beams made of isotropic material of medium or thin slenderness, this theory provides good results.

#### 4.2.1.2 Timoshenko Theory

The inclusion of constant transverse shear into the model assumptions leads to the First-Order Shear Deformation Theory, for beams also known as the Timoshenko Theory [74] and for plates equally known as Reissner-Mindlin Theory. The section is not forced any more to remain perpendicular to the reference line or surface. In contrast to the Euler-Bernoulli Theory, an additional rotation  $\theta$  is present, but constant through the thickness. Therefore, a constant shear strain in the section is present. In this case  $f(z) = z$ . Hence, the displacement field can be written as follows:

$$\begin{cases} u_1(x, z) &= v_0(x) + z \theta(x) \\ u_3(x, z) &= w(x) \end{cases} \quad (4.4)$$

No transverse normal effects are included. From the strains, stresses can be calculated via Hook's law, which is given in Equation (2.12). A constant shear strain gives a constant shear stress, which requires therefore the introduction of a shear correction factor for the shear stiffness. As the shear correction factors depend on the geometry, loadings and boundary conditions, this solution is not very convenient. This model however is able to deliver good results also for beams with inhomogenous material for medium to thin slenderness.

For other types of beams, a quadratic distribution of the shear is expected, which vanishes at the bottom and the top of the layup. Hence it is favorable to directly gain a

parabolic distribution of transverse shears strains. Therefore a model with a variable rotation of the cross section through the thickness is needed.

#### 4.2.1.3 Touratier Sinus Kinematics

In order to achieve a higher order distribution of the shear, a sinusoidal displacement distribution was proposed by Touratier et al [36]. The displacement field in its classical form, considering the derivative of the deflection  $w'_0$  instead of  $v_1$ , is:

$$\begin{cases} u_1(x, z) = v_0(x) - z w'_0(x) + \left(\frac{h}{\pi} \sin \frac{\pi z}{h}\right) (\theta(x) + w'_0(x)) \\ u_3(x, z) = w_0(x) \end{cases} \quad (4.5)$$

Due to the sinusoidal distribution of the displacement, the shear strains have a cosinusoidal form. This kinematical theory now also provides good results for thick beams, made of inhomogenous material.

#### 4.2.1.4 Touratier Sinus Theory with Transverse Normal Effect

Finally the Touratier Sinus can be enhanced to include deformation in the transverse direction, named Sin-z2 Theory. The displacement field in the 3 or  $z$  direction is expanded with the terms up to the second order. A strong relation between deflection and its derivative is not implied any more:

$$\begin{cases} u_1(x, z) = v_0(x) - z v_1(x) + \left(\frac{h}{\pi} \sin \frac{\pi z}{h}\right) (\theta(x) + v_1(x)) \\ u_3(x, z) = w_0(x) + z w_1(x) + z^2 w_2(x) \end{cases} \quad (4.6)$$

This theory is of interest for thick beams of homogenous and inhomogenous materials, which are exerted to transverse effects on the top or bottom surface of the beam.

#### 4.2.1.5 Comparison of kinematical models

The deformation behaviour of those different theories is compared in Figure 4.6, showing the increasing flexibility from Euler-Bernoulli Theory towards the Sinus  $z^2$  Theory.

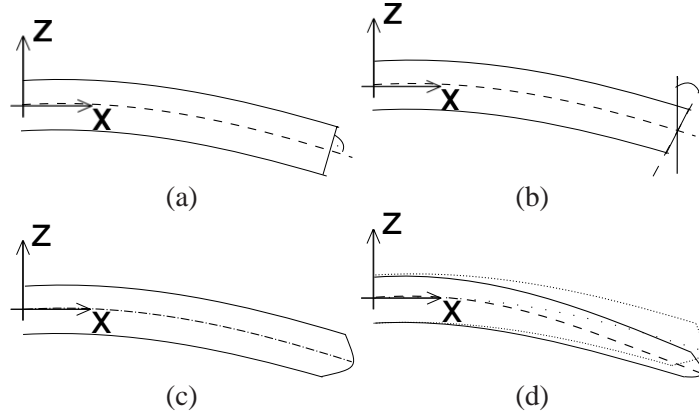


Figure 4.6: Deformation of Euler-Bernoulli Theory (a), Timoshenko Theory (b), Sinus Theory (c) and Sinus  $z^2$  Theory (d).

Based on the unified expression in Equation (4.1), these models can be expressed using:

$$\begin{aligned}
 f(z) &= 0, w_1 = w_2 = 0, v_1 = w'_0, && \text{representing the Euler-Bernoulli Theory} \\
 f(z) &= z, w_1 = w_2 = 0, v_1 = w'_0, && \text{representing the Timoshenko Theory} \\
 f(z) &= \frac{h}{\pi} \sin \frac{\pi z}{h}, w_1 = w_2 = 0, v_1 = w'_0, && \text{for the Touratier Sinus Theory} \\
 f(z) &= \frac{h}{\pi} \sin \frac{\pi z}{h}, && \text{for the Sinus } z^2 \text{ Theory}
 \end{aligned} \tag{4.7}$$

Other thickness expansions can be imagined from this compact notation, enabling even more flexible deformation through the thickness. It is visible that for layered structures, more refined kinematics with a non constant rotation can provide a good answer of the local deformation. Regarding the FE implementation using different approximation functions, a complete description is provided in Appendix C.

### 4.3 eXtended Variational Formulation for One Dimensional Approaches

In this section the XVF will be adapted in the framework of the presented one-dimensional models with different kinematical models. Its resulting systems and the coupling terms, the dual products, will be discussed for the case of homogenous dimensionality. Finally its FE implementation is sketched.

#### 4.3.1 eXtended Variational Formulation (XVF)

##### 4.3.1.1 Problem Formulation

Coupling models of heterogenous dimensionality and kinematics was the original aim of the formulation of Blanco et al [7]. The structure is divided by a smooth

artificial internal boundary, or Interface,  $\Gamma_a$  into two domains: the complex domain  $\Omega_c$  and the simple domain  $\Omega_s$  such that  $\Omega = \Omega_s \cup \Omega_c$  and  $\Gamma_a = \Omega_s \cap \Omega_c$ , see Figure 4.7. Recall that the simple domain  $\Omega_s$  contains the simple kinematical model using  $^s\mathbf{u}$  and the complex domain  $\Omega_c$  the complex kinematical model using  $^c\mathbf{u}$ .

The original Principle of virtual Displacements in Equation (2.5) is therefore considered by a pair of displacements,  $\mathbf{u} = (^s\mathbf{u}, ^c\mathbf{u})$ . Over the common Interface  $\Gamma_a$  a continuity conditions for displacements and stresses has to be fulfilled:

$$^s\mathbf{u} = ^c\mathbf{u} \quad \text{in } \mathbf{H}^{1/2}(\Gamma_a) \quad (4.8)$$

$$^s\boldsymbol{\sigma} \cdot ^s\mathbf{n} = ^c\boldsymbol{\sigma} \cdot ^c\mathbf{n} \quad \text{in } \mathbf{H}^{-1/2}(\Gamma_a) \quad (4.9)$$

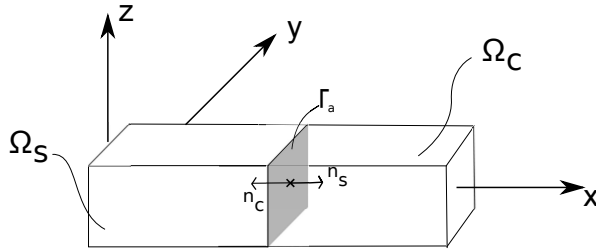


Figure 4.7:  $\Omega_c$  and  $\Omega_s$  with common interface  $\Gamma_a$  in a Beam Structure

The classical variational form of inner and outer work, like in Equation (2.5), needs to be expanded with the terms regarding the interface  $\Gamma_s$ . These terms are expressed as a vanishing difference in the weak sense between the displacements of both domains at the interface. The scalar parameter  $\gamma \in [0, 1]$  is introduced in the variational formulation of the problem. It will be assigned to either use a pure expansion of the simple model with a value of  $\gamma = 0$  or a reduction of the complex model with  $\gamma = 1$ .

Additional to the inner and outer work of Equation (2.11) new variables at the interface are introduced: a pair of two Lagrange Multipliers  $\boldsymbol{\lambda} = (^s\boldsymbol{\lambda}, ^c\boldsymbol{\lambda})$ , according to the kinematics used in each subdomain. For a better overview, all unknowns of the XVF are written in the Table 4.2. The additional coupling terms are:

$$\begin{aligned} \delta\Pi_{couple}(^s\mathbf{u}, ^c\mathbf{u}, ^s\boldsymbol{\lambda}, ^c\boldsymbol{\lambda}, \delta^s\mathbf{u}, \delta^c\mathbf{u}, \delta^s\boldsymbol{\lambda}, \delta^c\boldsymbol{\lambda}) = \\ \gamma \int_{\Gamma_a} ^s\boldsymbol{\lambda} \cdot (\delta^s\mathbf{u} - \delta^c\mathbf{u}) d\Gamma + (1 - \gamma) \int_{\Gamma_a} ^c\boldsymbol{\lambda} \cdot (\delta^s\mathbf{u} - \delta^c\mathbf{u}) d\Gamma \\ + \gamma \int_{\Gamma_a} \delta^s\boldsymbol{\lambda} \cdot (^s\mathbf{u} - ^c\mathbf{u}) d\Gamma + (1 - \gamma) \int_{\Gamma_a} \delta^c\boldsymbol{\lambda} \cdot (^s\mathbf{u} - ^c\mathbf{u}) d\Gamma \end{aligned} \quad (4.10)$$

Therefore the mechanical problems reads:

Table 4.2: Overview of variables in the two sub-domains

	$\Omega_s$	$\Omega_c$
stress tensor	${}^s\boldsymbol{\sigma}$	${}^c\boldsymbol{\sigma}$
strain tensor	${}^s\boldsymbol{\epsilon}$	${}^c\boldsymbol{\epsilon}$
displacement	${}^s\mathbf{u}$	${}^c\mathbf{u}$
virtual displacement	$\delta{}^s\mathbf{u}$	$\delta{}^c\mathbf{u}$
external traction	${}^s\mathbf{t}$	${}^c\mathbf{t}$
external force	${}^s\mathbf{f}$	${}^c\mathbf{f}$
traction at interface	${}^s\boldsymbol{\lambda}$	${}^c\boldsymbol{\lambda}$
virtual traction at interface	$\delta{}^s\boldsymbol{\lambda}$	$\delta{}^c\boldsymbol{\lambda}$

For a given  $\gamma \in [0, 1]$  find  $({}^s\mathbf{u}, {}^c\mathbf{u}, {}^s\boldsymbol{\lambda}, {}^c\boldsymbol{\lambda}) \in \mathcal{U}_s \times \mathcal{U}_c \times \mathcal{L}_s \times \mathcal{L}_c$  such that:

$$\begin{aligned} & \delta\Pi_{int}({}^s\mathbf{u}, \delta{}^s\mathbf{u}) + \delta\Pi_{int}({}^c\mathbf{u}, \delta{}^c\mathbf{u}) = \\ & \delta\Pi_{couple}({}^s\mathbf{u}, {}^c\mathbf{u}, {}^s\boldsymbol{\lambda}, {}^c\boldsymbol{\lambda}, {}^s\mathbf{u}, \delta{}^c\mathbf{u}, \delta{}^s\boldsymbol{\lambda}, \delta{}^c\boldsymbol{\lambda}) \\ & + \delta\Pi_{ext}({}^s\mathbf{u}) + \delta\Pi_{ext}({}^c\mathbf{u}) \\ & \forall (\delta{}^s\mathbf{u}, \delta{}^c\mathbf{u}, \delta{}^s\boldsymbol{\lambda}, \delta{}^c\boldsymbol{\lambda}) \in \delta\mathcal{U}_s \times \delta\mathcal{U}_c \times \delta\mathcal{L}_s \times \delta\mathcal{L}_c \end{aligned} \quad (4.11)$$

with the following definitions for both domains:

$$\begin{aligned} \mathcal{U}_s &= \{{}^s\mathbf{u} \in \mathbf{H}^1(\Omega_s); {}^s\mathbf{u}|_{\Gamma_D} = {}^s\bar{\mathbf{u}}\} \\ \mathcal{U}_c &= \{{}^c\mathbf{u} \in \mathbf{H}^1(\Omega_c); {}^c\mathbf{u}|_{\Gamma_D} = {}^c\bar{\mathbf{u}}\} \end{aligned} \quad (4.12)$$

$\delta\mathcal{U}_s$  and  $\delta\mathcal{U}_c$  are spaces of the admissible displacements  $\mathcal{U}_s$  and  $\mathcal{U}_c$ . Therefore  $\mathcal{L}_s = \mathcal{L}_c = \mathbf{H}^{-1/2}(\Gamma_a)$ . All other definitions remain as in the initial problem mentioned before.

The Euler-Lagrange Equations, derived from Equation (4.10), at the interface provide the following relations:

$$\begin{cases} \gamma ({}^s\mathbf{u} - {}^c\mathbf{u}) = 0 & \text{on } \Gamma_a \\ (1 - \gamma) ({}^s\mathbf{u} - {}^c\mathbf{u}) = 0 & \text{on } \Gamma_a \\ {}^s\boldsymbol{\sigma} {}^s\mathbf{n} = \gamma {}^s\boldsymbol{\lambda} + (1 - \gamma) {}^c\boldsymbol{\lambda} & \text{on } \Gamma_a \\ {}^c\boldsymbol{\sigma} {}^c\mathbf{n} = \gamma {}^s\boldsymbol{\lambda} + (1 - \gamma) {}^c\boldsymbol{\lambda} & \text{on } \Gamma_a \end{cases} \quad (4.13)$$

The Euler-Lagrange Equations identify the new unknowns, the Lagrange Multipliers, as the tractions at the interface. It can be noticed that these tractions correspond to  ${}^s\boldsymbol{\lambda}$  for  $\gamma = 1$  and  ${}^c\boldsymbol{\lambda}$  for  $\gamma = 0$  which characterizes the originality of the XVF approach. Equally the Euler-Lagrange Equations show that the displacements have a vanishing difference in the integral sense.

### 4.3.1.2 XVF Dual Products

Several dual products are constructed in Equation (4.10) to establish a vanishing difference in weak form between the displacements at their common interface. These dual products are of the form  $\int_{\Gamma_a} \delta\boldsymbol{\lambda} \cdot \mathbf{u} d\Gamma$ . Dual products of the same space can

be evaluated without further efforts, however those products coupling two different spaces need a projection. As given by Blanco et al [7], the complex space has to be projected into the simple space. In the sense of the dual product,  ${}^c\boldsymbol{u}$  has components which will deliver no work together with  $\delta^s \boldsymbol{\lambda}$ .

A decomposition into parallel and orthogonal parts of the complex displacement field  ${}^c\boldsymbol{u}$  is done:

$${}^c\boldsymbol{u} = {}^c\boldsymbol{u}_{\parallel} + {}^c\boldsymbol{u}_{\perp} \quad (4.14)$$

Where the orthogonal parts of the displacement fields will not deliver any work in the sense of the dual product:

$$\int_{\Gamma_a} \delta^s \boldsymbol{\lambda} \cdot {}^c\boldsymbol{u}_{\perp} d\Gamma = 0 \quad (4.15)$$

The projected displacement field  ${}^c\boldsymbol{u}_{\parallel}$  is expressed in the same form as the simple displacement field  ${}^s\boldsymbol{u}$ . With the Equations (4.14) and (4.15), the relations between the components of the unknowns  ${}^c\boldsymbol{u}_{\parallel}$  and the initial complex displacement field  ${}^c\boldsymbol{u}$  can be expressed. This is shown hereafter by coupling the Sinus  $z^2$  with the Euler Bernoulli models.

**Coupling of Sinus  $z^2$  with Euler Bernoulli Theory** The simple and complex displacement fields are given in Equation (4.3) and Equation (4.6) respectively. The parallel complex displacement field is expressed as the simple displacement field  ${}^s\boldsymbol{u}$ . Therefore we have:

$$\begin{cases} {}^s u_1(x, z) &= {}^s v_0(x) - z {}^s w'_0(x) \\ {}^s u_3(x, z) &= {}^s w_0(x) \end{cases} \quad (4.16)$$

$$\begin{cases} {}^c u_1(x, z) &= {}^c v_0(x) - z {}^c v_1(x) + f(z) ({}^c v_1(x) + \theta(x)) \\ {}^c u_3(x, z) &= {}^c w_0(x) + z {}^c w_1(x) + z^2 {}^c w_2(x) \end{cases} \quad (4.17)$$

$$\begin{cases} {}^c u_{1\parallel}(x, z) &= {}^c v_{0\parallel}(x) - z {}^c w'_{0\parallel}(x) \\ {}^c u_{3\parallel}(x, z) &= {}^c w_{0\parallel}(x) \end{cases} \quad (4.18)$$

The Lagrange Multipliers are only active on the interface and they are constructed analogue to its according kinematical field. The number of additional unknowns for the Lagrange Multipliers are hence according:

$$\begin{cases} {}^s \lambda_1(x, z) &= {}^s \lambda_{v_0} - z {}^s \lambda_{w'_0} \\ {}^s \lambda_3(x, z) &= {}^s \lambda_{w_0} \end{cases} \quad (4.19)$$

The applied projection using Equations (4.14) and (4.15) implies:

$$\begin{aligned}
 0 &= \int_{\Gamma_a} \delta^s \boldsymbol{\lambda} \cdot ({}^c \mathbf{u} - {}^c \mathbf{u}_{\parallel}) d\Gamma = \\
 &\quad \int_{\Gamma} \delta^s \lambda_{v_0} \left[ ({}^c v_0 - {}^c v_{0\parallel}) + (f(z) - z) {}^c v_1 + f(z) {}^c \theta - z {}^c w'_{0\parallel} \right] \\
 &\quad - z \delta^s \lambda_{w'_0} \left[ ({}^c v_0 - {}^c v_{0\parallel}) + (f(z) - z) {}^c v_1 + f(z) {}^c \theta - z {}^c w'_{0\parallel} \right] \\
 &\quad + \delta^s \lambda_{w_0} \left[ ({}^c w_0 + z {}^c w_1 + z^2 {}^c w_2 - {}^c w_{0\parallel}) \right] d\Gamma
 \end{aligned} \tag{4.20}$$

From Equation (4.20) the following identities can be extracted:

$$\begin{aligned}
 \forall \delta^s \lambda_{v_0} : {}^c v_{0\parallel} &= \frac{1}{A} \int_{\Gamma_a} \left( {}^c v_0 + (f(z) - z) {}^c v_1 + f(z) {}^c \theta - z {}^c w'_{0\parallel} \right) d\Gamma \\
 \forall \delta^s \lambda_{w_0} : {}^c w_{0\parallel} &= \frac{1}{A} \int_{\Gamma_a} ({}^c w_0 + z {}^c w_1 + z^2 {}^c w_2) d\Gamma \\
 \forall \delta^s \lambda_{w'_0} : {}^c w'_{0\parallel} &= \frac{1}{I} \int_{\Gamma_a} \left( z ({}^c v_0 - {}^c v_{0\parallel}) + z (f(z) - z) {}^c v_1 + z f(z) {}^c \theta \right) d\Gamma \\
 \text{with } \int_{\Gamma_a} 1 d\Gamma &= A \quad \text{and} \quad \int_{\Gamma_a} z^2 d\Gamma = I
 \end{aligned} \tag{4.21}$$

For a symmetric cross shape, Equation (4.21) gives the following relations between the parallel and the complex displacement field:

$$\begin{aligned}
 \forall \delta^s \lambda_{v_0} : {}^c v_{0\parallel} &= {}^c v_0 \\
 \forall \delta^s \lambda_{w_0} : {}^c w_{0\parallel} &= {}^c w_0 + \frac{h^2}{12} {}^c w_2 \\
 \forall \delta^s \lambda_{w'_0} : {}^c w'_{0\parallel} &= -\frac{24}{\pi^3} {}^c \theta - \left( \frac{24}{\pi^3} - 1 \right) {}^c v_1
 \end{aligned} \tag{4.22}$$

In the Appendix B, the same calculations are presented for the coupling between Sinus  $z^2$  and Timoshenko models.

**Matrix Formulation** A matrix notation is introduced for both the displacement fields and the Lagrange Multipliers. Based on the unified expression given in Equation (4.1), a generalized compact notation can be introduced:

$$\begin{aligned}
 {}^i \mathbf{u} &= {}^i \mathbf{F} {}^i \boldsymbol{\epsilon}_u, \quad i \in \{c, s\} \\
 \text{with } \boldsymbol{\epsilon}_u &= [v_0 \ w_0 \ v_1 \ \theta \ w_1 \ w_2]^T
 \end{aligned} \tag{4.23}$$

and

$$\mathbf{F} = \begin{bmatrix} 1 & 0 & f(z) - z & f(z) & 0 & 0 \\ 0 & 1 & 0 & 0 & z & z^2 \end{bmatrix} \tag{4.24}$$

Following Equations (4.23) and (4.24), the Lagrange Multiplier are the same:

$$\begin{aligned}
 {}^i \boldsymbol{\lambda} &= {}^i \mathbf{F} {}^i \boldsymbol{\epsilon}_\lambda \\
 \text{with } \boldsymbol{\epsilon}_\lambda &= [\lambda_{v_0} \ \lambda_{w_0} \ \lambda_{v_1} \ \lambda_\theta \ \lambda_{w_1} \ \lambda_{w_2}]^T
 \end{aligned} \tag{4.25}$$

In the case of the Sinus  $z^2$  and Euler Bernoulli kinematics, the following thickness functions are:

$${}^c\mathbf{F} = \begin{bmatrix} 1 & 0 & f(z) - z & f(z) & 0 & 0 \\ 0 & 1 & 0 & 0 & z & z^2 \end{bmatrix} \quad {}^s\mathbf{F} = \begin{bmatrix} 1 & 0 & -z \\ 0 & 1 & 0 \end{bmatrix} \quad (4.26)$$

with the adapted generalized vectors:

$$\begin{aligned} {}^c\boldsymbol{\mathcal{E}}_u &= [v_0 \ w_0 \ v_1 \ \theta \ w_1 \ w_2]^T & {}^s\boldsymbol{\mathcal{E}}_u &= [v_0 \ w_0 \ w'_0]^T \\ {}^c\boldsymbol{\mathcal{E}}_\lambda &= [\lambda_{v_0} \ \lambda_{w_0} \ \lambda_{v_1} \ \lambda_\theta \ \lambda_{w_1} \ \lambda_{w_2}]^T & {}^s\boldsymbol{\mathcal{E}}_\lambda &= [\lambda_{v_0} \ \lambda_{w_0} \ \lambda_{w'_0}]^T \end{aligned} \quad (4.27)$$

Using these expressions, the coupling matrices  $\mathbf{B}$  can be established. For the case of the simple kinematics with the simple Lagrange multipliers, the following is obtained:

$$\int_{\Gamma_a} \delta^s \boldsymbol{\lambda} \cdot {}^s\mathbf{u} \ d\Gamma = \int_{\Gamma} \delta^s \boldsymbol{\mathcal{E}}_\lambda^T {}^s\mathbf{F}^T {}^s\mathbf{F} {}^s\boldsymbol{\mathcal{E}}_u \ d\Gamma = \delta^s \boldsymbol{\mathcal{E}}_\lambda^T \mathbf{B}_{ss} {}^s\boldsymbol{\mathcal{E}}_u \quad (4.28)$$

with  $\mathbf{B}_{ss} = \int_{-\frac{h}{2}}^{\frac{h}{2}} \begin{pmatrix} 1 & 0 & -z \\ 0 & 1 & 0 \\ -z & 0 & z^2 \end{pmatrix} dz$

Applying directly the dual product on the unprojected vector  ${}^c\mathbf{u}$  with the simple Lagrange Multipliers  ${}^s\boldsymbol{\lambda}$  delivers:

$$\int_{\Gamma_a} \delta^s \boldsymbol{\lambda} \cdot {}^c\mathbf{u} \ d\Gamma = \delta^s \boldsymbol{\mathcal{E}}_\lambda^T \mathbf{B}_{sc} {}^c\boldsymbol{\mathcal{E}}_u \quad (4.29)$$

with  $\mathbf{B}_{sc} = \int_{-\frac{h}{2}}^{\frac{h}{2}} \begin{pmatrix} 1 & 0 & -z \\ 0 & 1 & 0 \\ -\frac{24z}{\pi^3} & 0 & -\frac{24z^2}{\pi^3} \\ (1 - \frac{24}{\pi^3})z & 0 & -(1 - \frac{24}{\pi^3})z^2 \\ 0 & z & 0 \\ 0 & z^2 & 0 \end{pmatrix} dz$

According to Equation (4.15), the dual product has to be calculated as the product of  ${}^s\boldsymbol{\lambda} \cdot {}^c\mathbf{u}_\parallel$ . While doing so and inserting the obtained relations between  ${}^c\mathbf{u}_\parallel$  and  ${}^c\mathbf{u}$  in Equation (4.22), the same is obtained as if one directly calculates  ${}^s\boldsymbol{\lambda} \cdot {}^c\mathbf{u}$ , as shown in Equation (4.29). In the case of dimensional homogeneity, the same mathematical spaces are present due to same base kinematics. The space of the simple model is included in the complex model. The same is valid for the dual product of  ${}^s\mathbf{u}$  with  ${}^c\boldsymbol{\lambda}$  to deduce  $\mathbf{B}_{cs}$ , where we have  $\mathbf{B}_{cs} = \mathbf{B}_{sc}^T$ .

Finally  $\mathbf{B}_{cc}$  can be also defined as:

$$\int_{\Gamma_a} \delta^c \boldsymbol{\lambda} \cdot {}^c \mathbf{u} d\Gamma = \delta^c \boldsymbol{\mathcal{E}}_\lambda^T \mathbf{B}_{cc} {}^c \boldsymbol{\mathcal{E}}_u \quad (4.30)$$

with  $\mathbf{B}_{cc} = \int_{-\frac{h}{2}}^{\frac{h}{2}} \begin{pmatrix} 1 & 0 & f(z) - z & f(z) & 0 & 0 \\ 0 & 1 & 0 & 0 & z & z^2 \\ f(z) - z & 0 & (f(z) - z)^2 & (f(z) - z)f(z) & 0 & 0 \\ f(z) & 0 & (f(z) - z)f(z) & (f(z))^2 & 0 & 0 \\ 0 & z & 0 & 0 & z^2 & z^3 \\ 0 & z^2 & 0 & 0 & z^3 & z^4 \end{pmatrix} dz$

This gives a matrix form of Equation (4.10) as:

$$\delta \Pi_{couple}({}^s \boldsymbol{\mathcal{E}}_u, {}^c \boldsymbol{\mathcal{E}}_u, {}^s \boldsymbol{\mathcal{E}}_\lambda, {}^c \boldsymbol{\mathcal{E}}_\lambda, \delta {}^s \boldsymbol{\mathcal{E}}_u, \delta {}^c \boldsymbol{\mathcal{E}}_u, \delta {}^s \boldsymbol{\mathcal{E}}_\lambda, \delta {}^c \boldsymbol{\mathcal{E}}_\lambda) =$$

$$\begin{bmatrix} \delta {}^s \boldsymbol{\mathcal{E}}_u \\ \delta {}^c \boldsymbol{\mathcal{E}}_u \\ \delta {}^s \boldsymbol{\mathcal{E}}_\lambda \\ \delta {}^c \boldsymbol{\mathcal{E}}_\lambda \end{bmatrix}^T \begin{bmatrix} 0 & 0 & \gamma \mathbf{B}_{ss} & (1 - \gamma) \mathbf{B}_{sc} \\ 0 & 0 & \gamma \mathbf{B}_{sc} & (1 - \gamma) \mathbf{B}_{cc} \\ \gamma \mathbf{B}_{ss} & \gamma \mathbf{B}_{sc} & 0 & 0 \\ (1 - \gamma) \mathbf{B}_{sc} & (1 - \gamma) \mathbf{B}_{cc} & 0 & 0 \end{bmatrix} \begin{bmatrix} {}^s \boldsymbol{\mathcal{E}}_u \\ {}^c \boldsymbol{\mathcal{E}}_u \\ {}^s \boldsymbol{\mathcal{E}}_\lambda \\ {}^c \boldsymbol{\mathcal{E}}_\lambda \end{bmatrix} \quad (4.31)$$

### 4.3.1.3 About the Choice of $\gamma$ in XVF

In Equation (4.10), the scalar parameter  $\gamma \in [0, 1]$  is introduced. From the compact form in Equation (4.31), different interface conditions are imposed with adoption of different values of the scalar  $\gamma$ . In order to evaluate the role of this parameter, the equations are rewritten, considering the two previously involved kinematics.

Only the terms associated with the variation of the Lagrange Multipliers are given:

$$\begin{aligned} & \delta {}^s \boldsymbol{\mathcal{E}}_\lambda^T \gamma \mathbf{B}_{ss} {}^s \boldsymbol{\mathcal{E}}_u - \delta {}^s \boldsymbol{\mathcal{E}}_\lambda^T \gamma \mathbf{B}_{sc} {}^c \boldsymbol{\mathcal{E}}_u + \delta {}^c \boldsymbol{\mathcal{E}}_\lambda^T (1 - \gamma) \mathbf{B}_{cs} {}^s \boldsymbol{\mathcal{E}}_u - \delta {}^c \boldsymbol{\mathcal{E}}_\lambda^T (1 - \gamma) \mathbf{B}_{cc} {}^c \boldsymbol{\mathcal{E}}_u = \\ & \gamma \delta {}^s \lambda_{v_0} [{}^s v_0 - {}^c v_0] h + (1 - \gamma) \delta {}^c \lambda_{v_0} [{}^s v_0 - {}^c v_0] h \\ & + \gamma \delta {}^s \lambda_{w_0} \left[ {}^s w_0 - {}^c w_0 - \frac{h^2 c}{12} w_2 \right] h + (1 - \gamma) \delta {}^c \lambda_{w_0} \left[ {}^s w_0 - {}^c w_0 - \frac{h^2 c}{12} w_2 \right] h \\ & + \gamma \underbrace{\delta {}^s \lambda_{w'_0} \left[ \frac{h^3}{12} {}^s w'_0 - \frac{h^3 (\pi^3 - 24)}{12\pi^3} {}^c v_1 + \frac{2h^3}{\pi^3} {}^c \theta \right]}_I \\ & + (1 - \gamma) \underbrace{\delta {}^c \lambda_\theta \left[ -\frac{2h^3}{\pi^3} {}^s w'_0 - \frac{h^3 (\pi - 4)}{2\pi^3} {}^c v_1 - \frac{h^3}{2\pi^2} {}^c \theta \right]}_II \\ & + (1 - \gamma) \underbrace{\delta {}^c \lambda_{v_1} \left[ \frac{h^3 (\pi^3 - 24)}{12\pi^3} {}^s w'_0 - \frac{h^3 (\pi^3 + 6\pi - 48)}{12\pi^3} {}^c v_1 - \frac{h^3 (\pi - 4)}{2\pi^3} {}^c \theta \right]}_III \end{aligned} \quad (4.32)$$

Applying factorization on the terms  $I$ ,  $II$  and  $III$  gives:

$$\begin{aligned}
 \text{I} : & \quad \delta^s \lambda_{w'_0} \left[ ({}^s w'_0 - {}^c v_1) \frac{h^3}{12} + ({}^c \theta + {}^c v_1) \frac{2h^3}{\pi^3} \right] \\
 \text{II} : & \quad -\delta^c \lambda_\theta \left[ ({}^s w'_0 - {}^c v_1) \frac{2h^3}{\pi^3} + ({}^c \theta + {}^c v_1) \frac{h^3}{2\pi^2} \right] \\
 \text{III} : & \quad -\delta^c \lambda_{v_1} \left[ -({}^s w'_0 - {}^c v_1) \frac{h^3}{12} + ({}^s w'_0 - {}^c \theta - 2{}^c v_1) \frac{2h^3}{\pi^3} + ({}^c \theta + {}^c v_1) \frac{h^3}{2\pi^2} \right]
 \end{aligned} \tag{4.33}$$

Therefore, we can identify the restrictions satisfying the conditions at the interface. The deduced sets of relations on the displacement components are now discussed. From Equation (4.32), two cases can be distinguished:

(i) For  $\gamma \in [0, 1[$

$$\begin{aligned}
 {}^s v_0 &= {}^c v_0 \\
 {}^s w_0 &= {}^c w_0 + \frac{h^2}{12} {}^c w_2 \\
 {}^c v_1 &= -{}^c \theta = {}^s w'_0
 \end{aligned} \tag{4.34}$$

For this case, the conditions show that the rotation of the cross-section and the unknown  $v_1$  of the complex model have the same value as the derivative of the deflection of the simple model at the interface. It seems to be a strong restriction, the additional variable of the complex model being reduced as only one unique variable of the simple one.

(ii) For  $\gamma = 1$

$$\begin{aligned}
 {}^s v_0 &= {}^c v_0 \\
 {}^s w_0 &= {}^c w_0 + \frac{h^2}{12} {}^c w_2 \\
 {}^s w'_0 &= \left(1 - \frac{24}{\pi^3}\right) {}^c v_1 - \frac{24}{\pi^3} {}^c \theta
 \end{aligned} \tag{4.35}$$

For the case of ( $\gamma \in [0, 1[$ ) the most constrained conditions are implied as it involves 4 conditions at the interface. Only 3 are implied for the case of ( $\gamma = 1$ ). **III** and **II** can only be satisfied simultaneously if both complex rotational variables  ${}^c \theta$  and  ${}^c v_1$  have the same value as the rotational variable of the simple kinematics  ${}^s w'_0$ . As a consequence, the Sinus  $z^2$  theory gets restricted to equal the form of the Euler-Bernoulli theory at the interface. As final remark, it is interesting to note, that both condition do not provide any link for  ${}^c w_1$ , representing a symmetric linear membrane effect in the thickness dilatation.

In the numerical examples in the following, only two cases will be considered:  
 (i)  $\gamma = 0$  and (ii)  $\gamma = 1$ . As shown before, the weak condition of  $\gamma = 1$  gives a more flexible solution.

#### 4.3.1.4 Finite Element Formulation of XVF

In the FE system of the eXtended Variational Formulation, classic terms and the additional entries of the dual products from Equation (4.31) have to be expressed in a discrete form. The stiffness matrices of the domains  $\Omega_s$  and  $\Omega_c$  are classically constructed according to Equation (C.6) given in Appendix C, and are:

$$\begin{aligned}\delta\Pi_{int}(^s\boldsymbol{u}) &= \delta^s\boldsymbol{q} \boldsymbol{K}_{\Omega_s} {}^s\boldsymbol{q} \quad \text{for } \Omega_s \\ \delta\Pi_{int}(^c\boldsymbol{u}) &= \delta^c\boldsymbol{q} \boldsymbol{K}_{\Omega_c} {}^c\boldsymbol{q} \quad \text{for } \Omega_c\end{aligned}\tag{4.36}$$

The additional coupling entries become visible at the outer diagonal. For the use in a discrete FE formulation, the matrices from Equation (4.31) are multiplied with the according shape functions of the concerned node, therefore it is  $\boldsymbol{B} = \boldsymbol{N}^T \boldsymbol{\mathcal{B}} \boldsymbol{N}$ . The discrete Lagrange Multiplier DOFs are denoted by  ${}^s\boldsymbol{L}$ ,  ${}^c\boldsymbol{L}$ .

For the coupling of two sub-domains having one interface, the finite element system is:

$$\begin{pmatrix} \boldsymbol{K}_{\Omega_s} & 0 & \gamma \boldsymbol{B}_{ss} & (1-\gamma) \boldsymbol{B}_{sc} \\ 0 & \boldsymbol{K}_{\Omega_c} & \gamma \boldsymbol{B}_{sc} & (1-\gamma) \boldsymbol{B}_{cc} \\ \gamma \boldsymbol{B}_{ss} & \gamma \boldsymbol{B}_{sc}^T & 0 & 0 \\ (1-\gamma) \boldsymbol{B}_{sc} & (1-\gamma) \boldsymbol{B}_{cc} & 0 & 0 \end{pmatrix} \begin{pmatrix} {}^s\boldsymbol{q} \\ {}^c\boldsymbol{q} \\ {}^s\boldsymbol{L} \\ {}^c\boldsymbol{L} \end{pmatrix} = \begin{pmatrix} {}^s\boldsymbol{f} \\ {}^c\boldsymbol{f} \\ 0 \\ 0 \end{pmatrix} \tag{4.37}$$

Note that this system has zero components on the diagonal. This prohibits the advantageous banded form of a homogen FE system. Therefore standard solvers cannot be used as they do not cope with all configurations possible. Especially while having differing domains sizes and multiple interfaces require adapted solver algorithms. Either solvers with preconditioning and matrix decomposition have to be used, or algorithms considering block systems. Two approaches can deliver a solution: for only small  $\boldsymbol{B}$  compared to  $\boldsymbol{K}_{\Omega_s}$  and  $\boldsymbol{K}_{\Omega_c}$ , a preconditioning can be sufficient. For larger block matrices, a complete LU decomposition is needed. A short introduction of the XVF implementation in the FE code EvalEF is given in Appendix D.

## 4.4 Unification of Approaches using the XVF

Through the assignment of value to the scalar parameter  $\gamma \in [0, 1]$ , the XVF adapts for the homogenous dimensional problems presented here, to two main cases. According to Equation (4.11), two sets of Interface conditions could be found, one imposed with  $\gamma = 1$  and one imposed with  $\gamma \neq 1$ . This simplification allows to further identify identical interface conditions imposed by other techniques.

### 4.4.1 The Arlequin Method without Overlap

Considering the Arlequin Method [16], a complete discussion can be found in the Annex A. In this section, only the parts needed to have an equivalence with the XVF

are presented.

In the section 4.1, the Arlequin Method is considered as technique having a partial overlap. The zone of the partial overlap  $\Omega_a$ , indicated in Figure 4.8, can be reduced to a surface coupling at a common interface  $\Gamma_a$ . As in XVF, a coupling formulation has to be established. Two coupling operators have been formulated in the Arlequin Method: The purely displacement based  $L^2$  operator and the  $H^1$  operator, which equally consider at the same time the strain and the displacement field. Here only the first one, the purely displacement based operator, is considered:

$$L^2 : \quad C(\boldsymbol{\lambda}, \mathbf{u}) = \int_{\Omega_a} \boldsymbol{\lambda} \delta \mathbf{u} d\Omega_a \quad (4.38)$$

Equal to Equations (4.11) and (4.10), related to the XVF approach, the internal and external work, as well as the coupling term can be expressed using the  $L^2$  operator:

$$\begin{aligned} \delta \Pi_{int} &= \int_{\Omega_s} {}^s \boldsymbol{\sigma} \delta^s \boldsymbol{\epsilon} d\Omega + \int_{\Omega_c} {}^c \boldsymbol{\sigma} \delta^c \boldsymbol{\epsilon} d\Omega \\ \delta \Pi_{ext} &= \int_{\Omega_a} \mathbf{f}_d \delta^s \mathbf{u} d\Omega + \int_{\Omega_c} \mathbf{f}_d \delta^c \mathbf{u} d\Omega \\ &\quad + \int_{\partial \Omega_s} \mathbf{f}_d \delta^s \mathbf{u} d\Omega + \int_{\partial \Omega_c} \mathbf{f}_d \delta^c \mathbf{u} d\Omega \\ \delta \Pi_{couple} &= \int_{\Gamma_a} \boldsymbol{\lambda} (\delta^s \mathbf{u} - \delta^c \mathbf{u}) d\Gamma \end{aligned} \quad (4.39)$$

The jump over the displacement fields is here restricted to the common interface, which restricts also the Lagrange Multipliers  $\boldsymbol{\lambda}$ , to be defined only at the interface. In an article by Belytschko and Guidault [26], the construction of the Lagrange Multipliers according to the coarser discretisation of the two sub-domains showed to provide better and more robust results. Hence, restricting the Arlequin Method to surface coupling with the  $L^2$  operator, will provide the same results as in XVF, while using  $\gamma = 1$ .

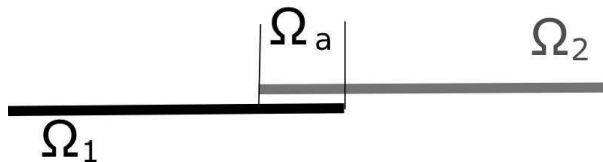


Figure 4.8: Arrangements of domains in the Arlequin Method

### 4.4.2 Penalty Technique

In order to impose a predefined relation between several DOFs of the different kinematical theories, Multi-Point Constraints can be applied at discrete level at the common nodes on the interface. Several techniques are available in order to impose them on the systems of Equations: penalty or least squares or even the introduction of Lagrange Multipliers as new unknowns. According to [5] all these techniques are sub cases of Multi-Point Constraints. Here penalty technique is used in comparison.

As a simple preliminary example Euler Bernoulli theory is connected with Timoshenko theory. In order to establish the connection, a relation between the derivative of the flexional DOF of Euler Bernoulli and the cross section rotation in Timoshenko at their common node on the interface is needed. In the penalty technique a value of  $\hat{u}$  is imposed on a combination of several different degrees of freedom  $u_1$  to  $u_n$ . They are multiplied with factors  $a_1$  to  $a_n$  whose signs and values are according to the imposed relation. They are grouped into a global vector  $a$ , respecting the global order of the DOFs in the total system of equations. At the affected nodes it contains the imposed value, otherwise only zeros:

$$\hat{u} = a_1 u_1 + \cdots + a_n u_n \quad (4.40)$$

In this first preliminary example, the difference between the relevant variables of both kinematical fields has to vanish at the interface, therefore  $\hat{u} = 0$ . Equally to Equation (4.10) a potential in variational form can be written for the Penalty technique:

$$\delta\Pi_{\text{Penalty}}({}^s\boldsymbol{u}, {}^c\boldsymbol{u}, {}^P\boldsymbol{\lambda}, \delta{}^s\boldsymbol{u}, \delta{}^c\boldsymbol{u}, \delta{}^P\boldsymbol{\lambda}) = \frac{1}{2} \int_{\Gamma_a} {}^P\boldsymbol{\lambda} \cdot (\delta{}^s\boldsymbol{u}) \quad (4.41)$$

In the case of penalty technique,  ${}^P\boldsymbol{\lambda}$  is fixed and not a additional unknown. Therefore the relations applied have to be valid in strong form over the whole Interface  $\Gamma_a$ . For the example of coupling Sinus  $z^2$  with Euler Bernoulli theory the potential in variational formulation gives:

$$\begin{aligned} \delta\Pi_{\text{Penalty}}({}^s\boldsymbol{u}, {}^c\boldsymbol{u}, {}^P\boldsymbol{\lambda}, \delta{}^s\boldsymbol{u}, \delta{}^c\boldsymbol{u}) &= \\ \frac{1}{2} {}^P\boldsymbol{\lambda} [({}^s v_0 - {}^c v_0) + ({}^s w'_0 - {}^c v_1 - {}^c v_1 - {}^c q_\theta)] & \\ + \frac{1}{2} {}^P\boldsymbol{\lambda} [({}^s w_0 - {}^c w_0 - {}^c w_1 - {}^c w_2)] & \\ + \frac{1}{2} {}^P\boldsymbol{\lambda} \cdot ({}^s \delta\boldsymbol{u} - {}^c \delta\boldsymbol{u}) & \end{aligned} \quad (4.42)$$

From which the following restrictions for a given  ${}^P\boldsymbol{\lambda}$  are obtained by:

$$\begin{aligned} \forall {}^P\boldsymbol{\lambda} : {}^s v_0 &= {}^c v_0 \\ \forall {}^P\boldsymbol{\lambda} : {}^s w'_0 &= {}^c v_1 \\ \forall {}^P\boldsymbol{\lambda} : {}^c v_1 &= -{}^c \theta \\ \forall {}^P\boldsymbol{\lambda} : {}^s w_0 &= -{}^c w_0 + w_1 + w_2 \end{aligned} \quad (4.43)$$

This is giving the same as restrictions as  $\gamma = 0$  in Equation (4.34).

In general we can state, that having a higher number of unknowns in the complex domain, which are related to a lower number of unknowns of the simple domain, XVF using  $\gamma = 0$  will match the Penalty technique. In contrast, XVF using  $\gamma = 1$  provides a more flexible formulation.

For the adaption to the discrete FE system, the predefined  ${}^P\boldsymbol{\lambda}$  will be denoted as  $G$ . For numerical efficiency it has to be 3 or 4 orders higher than the highest stiffness term in the overall FE system. The modified stiffness matrix  $\mathbf{K}'$  is constructed together with  $\mathbf{a}$ :

$$0 = (\mathbf{K} + G \mathbf{a}^T \mathbf{a}) \mathbf{q} - \mathbf{f} = \mathbf{K}' \mathbf{q} - \mathbf{f} \quad (4.44)$$

The Results obtained by inside this study where calculated with a Penalty factor  $G$  of  $10^{10}$ .

## 4.5 Numerical Study of One Dimensional Structures

This sections treats the numerical implementation of the theoretical formulations. Two materials are considered: a homogenous material and a sandwich material. Both will be tested on a simple supported beam under a patch load is chosen. As the configuration is symmetrical, only half of the configuration is used for the FE solution. The maximum axial stress will occur at the beams middle and the maximum shear stress will be present at the support. The coupled models test start with the introduction of one interface at first. This test is carried out in order to evaluate the influence of the refinement with complex kinematic elements. Afterwards two interfaces are applied in order to capture the appearing maxima of both stress components, each one appearing at one of the half models extremes. This is followed by set study of a sandwich structure. For this case a new coupling operator is proposed and tested. This section will be concluded with a study concerning the reduction of the overall number of unknowns without the loss of local precision.

The test case is described as follows:

- Geometry: rectangular beam with  $l = 10$  and slenderness ratio  $s = \frac{l}{h}$  of 5, 10 and 1000
- Boundary conditions: simply supported beam
- Load: patch load  $q_0$  on 10 per cent of the beam's length, located at the beams center
- Material properties:
  1. Homogeneous Material:  $E = 1$  MPa and  $\nu = 0.3$

2. Sandwich Material: Layer thicknesses:  $0.1h/0.8h/0.1h$
- a) Face:  $E_{11} = 131.1 \text{ GPa}$ ,  $E_{22} = E_{33} = 6.9 \text{ GPa}$ ,  $G_{12} = 3.588 \text{ GPa}$ ,  $G_{13} = 3.088 \text{ GPa}$ ,  $G_{23} = 2.3322 \text{ GPa}$ ,  $\nu_{12} = \nu_{13} = 0.32$ ,  $\nu_{23} = 0.49$
  - b) Core:  $E_{11} = 0.2208 \text{ MPa}$ ,  $E_{22} = 0.2001 \text{ MPa}$ ,  $E_{33} = 2760 \text{ MPa}$ ,  $G_{12} = 16.56 \text{ MPa}$ ,  $G_{13} = 545.1 \text{ MPa}$ ,  $G_{23} = 455.4 \text{ MPa}$ ,  $\nu_{12} = 0.99$ ,  $\nu_{13} = 0.00003$ ,  $\nu_{23} = 0.00003$
- Mesh: number of the elements  $N_x$  along the half length = 20, 40, 60, 80
  - Results: normalized using:  $\bar{u}_3 = 100 u_3 \frac{Y_0}{hs^4 q_0}$ ,  $\bar{\sigma}_{11} = \frac{\sigma_{11}}{s^2 q_0}$ ,  $\bar{\sigma}_{13} = \frac{\sigma_{13}}{sq_0}$ , with  $Y_0 = E_{33}^{Face}$

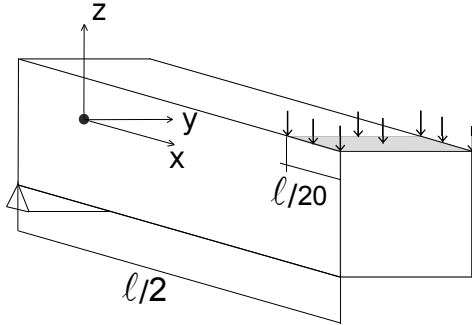


Figure 4.9: Test configuration of a beam subjected to a patch load at the beams center

#### 4.5.1 Assessment of Models

In this section, only one model will be used for the whole structure (denoted monomodel) without any application of any coupling technique. This allows to highlight the effect of each model on the results. The different models (Euler-Bernoulli denoted Euler, Timoshenko denoted Timo, Sin-z2) are assessed on both a homogeneous and a sandwich beam for various slenderness ratios and for different meshes. The results are summarized in Tables 4.4 and 4.5. They are compared with FE results issued from a 2D analysis performed with the commercial code ANSYS with converged meshes. These are reported in Table 4.3.

These tables show that a mesh of  $N_x = 20$  elements provides converged results for thick to very thin beams with  $s = 5, 10, 1000$ .

For the very thin case, the results are rather similar for the three models except for the transverse shear stress. The Sin-z2 yield more accurate results. For very thick and moderately thick structures, the accuracy of the deflection and the transverse shear stress is also improved by the use of the Sin-z2 model.

Table 4.3: ANSYS meshes with PLANE82 elements for homogeneous and sandwich beams

s	homogeneous		sandwich	
	$N_x$	$N_z$	$N_x$	$N_{face} / N_{core} / N_{face}$
5	80	20	80	12/48/12
10	80	10	80	6/24/6
1000	720	6	720	2/4/2

$N_z$  is the number of elements across the thickness

For further comparison, Figures 4.10 and 4.12 show the deflection of the beam for the two materials. The main differences occur for the sandwich structure. Euler-Bernoulli model yields poor results. The maximum deflection of the Timoshenko model is 20% less stiff when compared with the reference solution, whereas the Sin-z2 results are satisfactory with error rate less than 4.5%. The distribution of the transverse shear stress along the thickness is also represented in Figures 4.11 and 4.13. As expected, the results computed from the constitutive relation for the Sin-z2 model are closer to the reference solution than these obtained from the simple models. Using the integration of the equilibrium equations, all the results are in rather good agreement with the ANSYS solutions.

In the following, the simple kinematical model will be either Euler-Bernoulli or Timoshenko kinematics; the complex model will be the Sin-z2 kinematics. While Tables 4.4 and 4.5 show that a  $N_x = 20$  mesh is converged,  $N_x = 40$  will be used in the following in order to ensure that all the observed effects are due to the coupling method only.

Table 4.4: Homogeneous Material: assessment of different FE approximations

s	N		$\bar{u}_3$ ( $x = \frac{l}{2}, z = 0$ )	$\bar{\sigma}_{11}$ ( $x = \frac{l}{2}, z = -\frac{h}{2}$ )	$\bar{\sigma}_{13}$ ( $x = 0, z = 0$ )	$\bar{\sigma}_{13_{EQ}}$ ( $x = 0, z = 0$ )
5	20	Euler	-8583.05	0.7141	-	-0.3750
	40		-8583.05	0.7129	-	-0.3750
	60		-8583.05	0.7127	-	-0.3750
	80		-8583.05 (9.59%)	0.7126 (0.30%)	-	-0.3750 (1.42%)
5	20	Timo	-9607.01	0.7140	-0.2512	-0.3662
	40		-9607.01	0.7129	-0.2503	-0.3690
	60		-9607.01	0.7127	-0.2501	-0.3696
	80		-9607.01 (1.19%)	0.7126 (0.30%)	-0.2501 (34.25%)	-0.3698 (2.79%)
5	20	Sin-z2	-9454.10	0.7581	-0.3833	-0.4118
	40		-9454.10	0.7565	-0.3822	-0.4120
	60		-9454.10	0.7562	-0.3820	-0.4121
	80		-9454.10 (0.42%)	0.7560 (6.40%)	-0.3819 (0.39%)	-0.4121 (8.33%)
5		Ansys	-9493.85	0.7105	-0.3804	-
	20	Euler	-8582.91	0.7141	-	-0.3750
	40		-8582.91	0.7129	-	-0.3750
	60		-8582.91	0.7127	-	-0.3750
10	20	Timo	-8838.90	0.7140	-0.2550	-0.3735
	40		-8838.90	0.7129	-0.2513	-0.3746
	60		-8838.90	0.7127	-0.2506	-0.3748
	80		-8838.90 (0.54%)	0.7126 (0.67%)	-0.2503 (34.17%)	-0.3749 (1.39%)
10	20	Sin-z2	-8783.70	0.7272	-0.3879	-0.4111
	40		-8783.01	0.7261	-0.3833	-0.4119
	60		-8783.01	0.7251	-0.3825	-0.4120
	80		-8783.01 (0.09%)	0.7258 (1.17%)	-0.3822 (0.53%)	-0.4120 (8.36%)
10		Ansys	-8471.34	0.7105	-0.3804	-
	20	Euler	-8582.91	0.7141	-	-0.3750
	40		-8582.91	0.7129	-	-0.3750
	60		-8582.91	0.7127	-	-0.3750
1000	20	Timo	-8582.91	0.7141	-0.2500	-0.3750
	40		-8582.91	0.7129	-0.2500	-0.3750
	60		-8582.91	0.7127	-0.2500	-0.3750
	80		-8582.91 (0.02%)	0.7126 (0.01%)	-0.2500 (34.02%)	-0.3750 (1.03%)
1000	20	Sin-z2	-8583.00	0.7141	-0.3627	-0.4121
	40		-8582.91	0.7129	-0.3627	-0.4121
	60		-8582.91	0.7127	-0.3627	-0.4121
	80		-8582.91 (0.02%)	0.7126 (0.01%)	-0.3627 (4.28%)	-0.4121 (8.76%)
1000		Ansys	-8584.50	0.7125	-0.3789	-

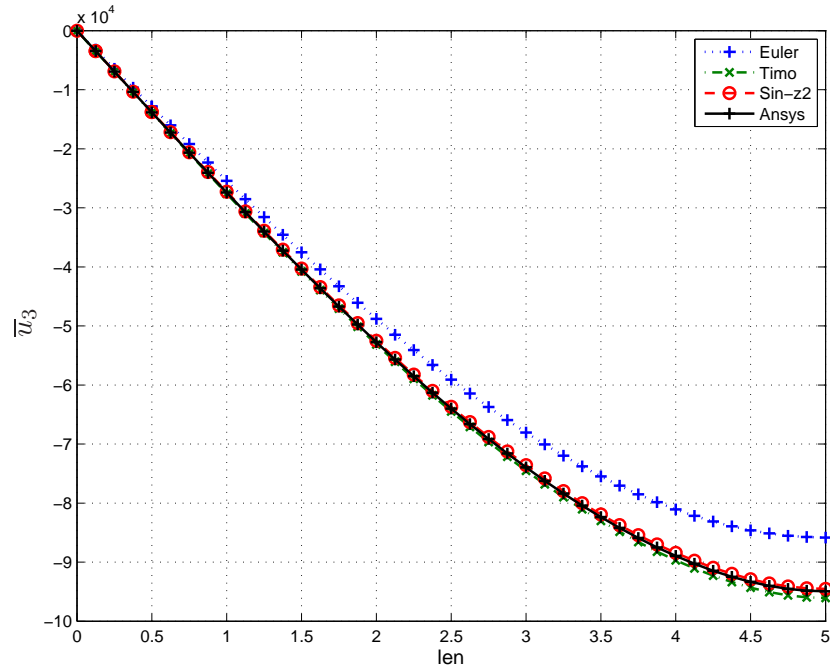
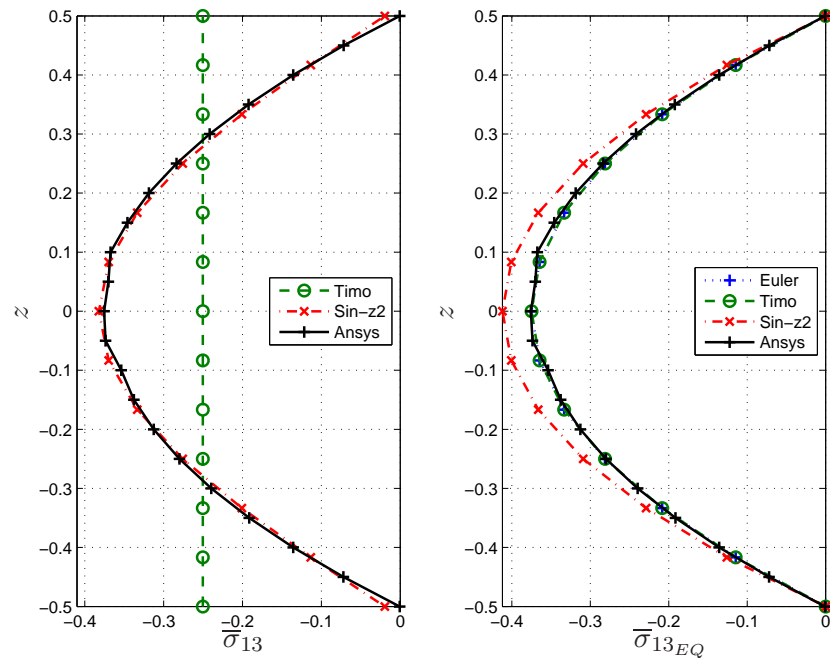

 Figure 4.10: Homogeneous Material: deflection of the different Kinematics;  $s = 5$ 

 Figure 4.11: Homogeneous Material:  $\bar{\sigma}_{13}$  through thickness  $z$  for different kinematics;  $s = 5$

Table 4.5: Sandwich Material: assessment of different FE approximations

s	N		$\bar{u}_3$ ( $x = \frac{l}{2}, z = 0$ )	$\bar{\sigma}_{11}$ ( $x = \frac{l}{2}, z = -\frac{h}{2}$ )	$\bar{\sigma}_{13}$ ( $x = 0, z = 0$ )	$\bar{\sigma}_{13EQ}$ ( $x = 0, z = 0$ )
5	20	Euler	-0.26832	0.29265	-	-0.05533
	40		-0.26832	0.29265	-	-0.05533
	60		-0.26832	0.29208	-	-0.05533
	80		-0.26832 (80.95%)	0.29205 (37.29%)	-	-0.05533 (0.02%)
10	20	Timo	-1.01485	0.29265	-0.02587	-0.05533
	40		-1.01485	0.29217	-0.02587	-0.05533
	60		-1.01485	0.29208	-0.02587	-0.05533
	80		-1.01485 (27.95%)	0.29205 (37.29%)	-0.02587 (53.24%)	-0.05533 (0.02%)
1000	20	Sin-z2	-1.32690	0.53668	-0.06613	-0.05562
	40		-1.32690	0.53388	-0.06612	-0.05563
	60		-1.32690	0.53336	-0.06612	-0.05563
	80		-1.32690 (5.80%)	0.53316 (14.48%)	-0.06612 (19.52%)	-0.05563 (0.56%)
		Ansys	-1.40859	0.46572	-0.05532	-
20	20	Euler	-0.26831	0.29265	-	-0.05533
	40		-0.26831	0.29217	-	-0.05533
	60		-0.26831	0.29208	-	-0.05533
	80		-0.26831 (52.31%)	0.29205 (21.40%)	-	-0.05533 (0%)
40	20	Timo	-0.45494	0.29265	-0.02589	-0.05532
	40		-0.45494	0.29217	-0.02587	-0.05533
	60		-0.45494	0.29208	-0.02587	-0.05533
	80		-0.45494 (19.13%)	0.29205 (21.40%)	-0.02587 (53.24%)	-0.05533 (0%)
60	20	Sin-z2	-0.53710	0.37522	-0.06615	-0.05562
	40		-0.53709	0.37388	-0.06613	-0.05563
	60		-0.53709	0.37365	-0.06613	-0.05563
	80		-0.53709 (4.53%)	0.37357 (0.54%)	-0.06613 (19.52%)	-0.05563 (0.54%)
		Ansys	-0.56258	0.37157	-0.05533	-
80	20	Euler	-0.26831	0.29265	-	-0.05533
	40		-0.26831	0.29217	-	-0.05533
	60		-0.26831	0.29208	-	-0.05533
	80		-0.26831 (0.02%)	0.29205 (0.01%)	-	-0.05533 (0%)
1000	20	Timo	-0.26833	0.29265	-0.02587	-0.05533
	40		-0.26833	0.29217	-0.02587	-0.05533
	60		-0.26833	0.29208	-0.02587	-0.05533
	80		-0.26833 (0.01%)	0.29205 (0.01%)	-0.02587 (53.24%)	-0.05533 (0%)
1000	20	Sin-z2	-0.26833	0.29266	-0.06761	-0.05563
	40		-0.26833	0.29218	-0.06761	-0.05563
	60		-0.26833	0.29209	-0.06761	-0.05563
	80		-0.26833 (0.01%)	0.29206 (0.01%)	-0.06761 (22.19%)	-0.05563 (0.54%)
		Ansys	-0.26836	0.29203	-0.05533	-

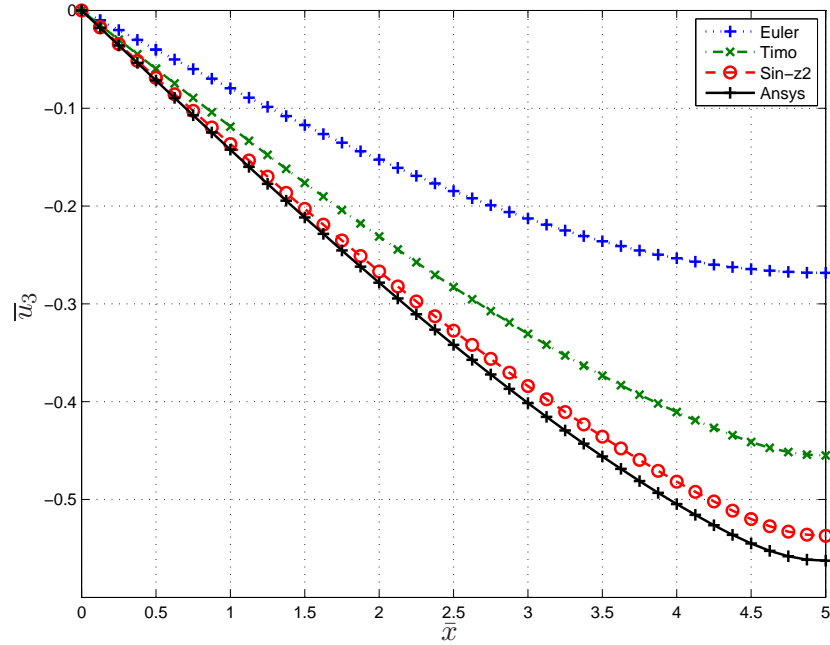


Figure 4.12: Sandwich Material: deflection of the different kinematics;  $s = 10$

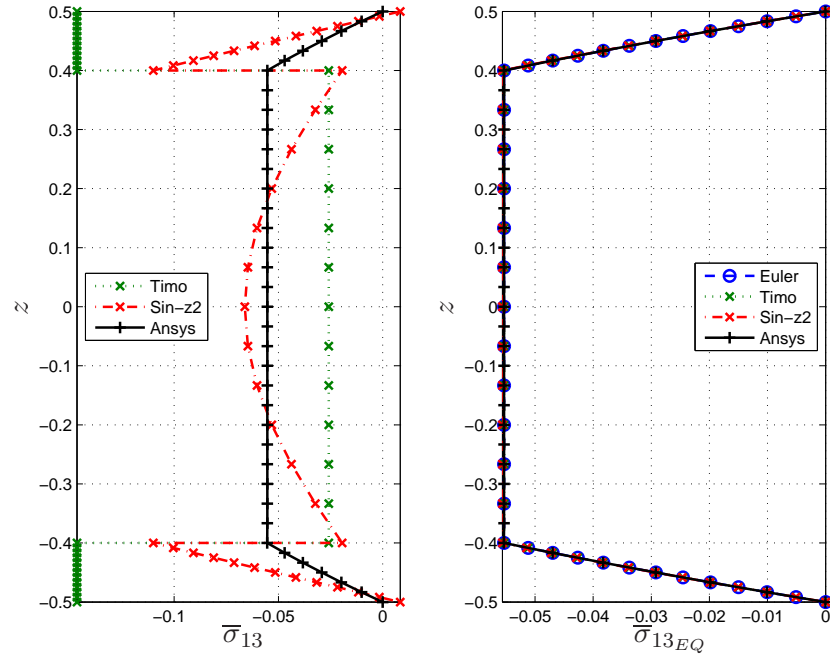


Figure 4.13: Sandwich Material:  $\bar{\sigma}_{13}$  through thickness  $z$  for different kinematics;  $s = 10$

## 4.5.2 Homogen Beam Test

### 4.5.2.1 One Interface

Using one interface between the complex and the simple domain, two configurations are possible. Therefore, it has to be evaluated, which configuration is the more effective one. As shown in Figure 4.14, either the complex zone is close to the simple support or under the load. Three test are carried out for these two configurations: XVF with  $\gamma = 0, \gamma = 1$ , and the Penalty technique.

In Figure 4.15 both configurations were applied, using Euler-Bernoulli kinematics as simple model and Sinus kinematics as complex model. The interface positioned at half the length of the model, so at  $\bar{x} = 2.5 = \frac{l}{4}$ . Only  $\gamma = 1$  is displayed. The same tendencies are obtained for  $\gamma = 0$  and penalty method. The momomodel results are provided for comparison in order to measure the influence of the coupling. The curves show, that the kinematical heterogenous models are keeping the tendency of the local model used within the subdomain. Moreover, the maximum deflection is influenced by the coupling. The maximum values are in between the results of the two monomodels. An overall higher deflection is obtained for those heterogeneous kinematical models using Sinus kinematics at the left half, were the support is located.

The according numerical values to the two configurations for the three tests are listed in the Table 4.6 for the thick structure which is the most severe case. It gives the maximum deflection and the maximum stresses. All values are compared with the according values of the monomodels. First of all, it can be noticed that the XVF approach with  $\gamma = 0$  and the penalty method gives always the same results. Furthermore, only the value of the maximal deflection changes with the involved technique of coupling. Since the displacement is a global quantity, it depends on both the choice of the simple model (Euler-Bernoulli or Timoshenko) and the domain modeled by the complex kinematics. On the contrary, the stresses computed in the complex domain is independent on of the coupling of the models and of the choice of the simple model. The numerical value achieved corresponds only to these of the complex kinematics. This feature is very attractive in the framework of the design of composite structures in which the computation of the stresses in the region of interest is of major importance. Further this is a very promising result for the aim of reducing the total number of unknowns. This effect needs a further study in order to see how much of the complex elements are really needed. Up to now the interface was fixed at  $\bar{x} = 2.5 = \frac{l}{4}$ .

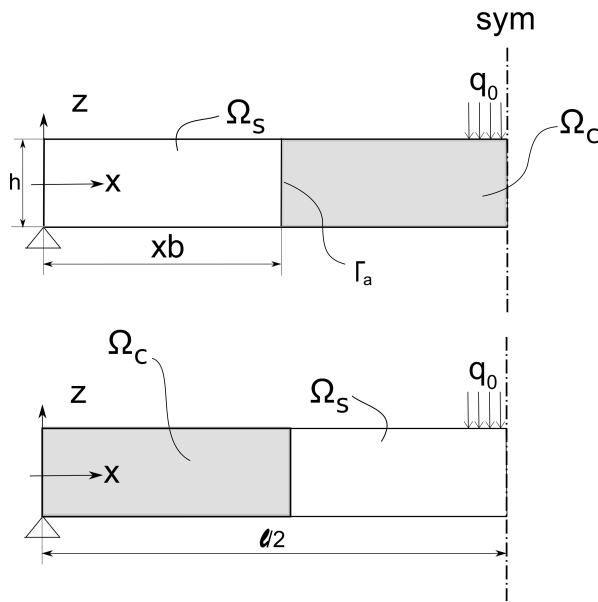


Figure 4.14: One interface: configuration of simple and complex domains

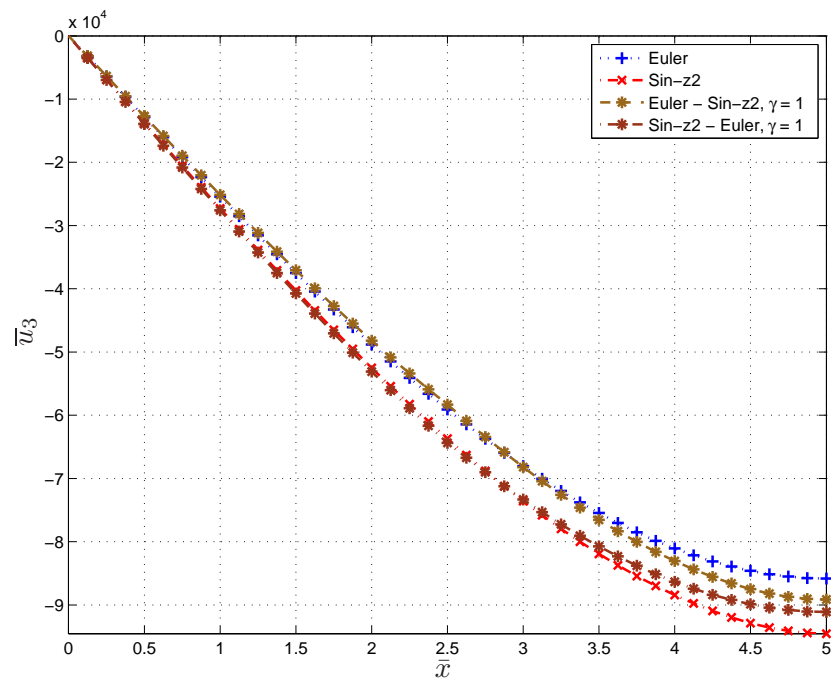

 Figure 4.15: Homogeneous Material: deflection for  $\gamma = 1$ ;  $\Gamma_a$  at  $\bar{x} = 2.5$ ;  $s = 5$

Table 4.6: Homogeneous Material: values of  $\bar{u}_3$ ,  $\bar{\sigma}_{11}$  and  $\bar{\sigma}_{13}$  for  $\Gamma_a$  at  $\bar{x} = 2.5$ , s = 5

	Euler - Sin-z2		Sin-z2 - Euler	
Type	$\bar{u}_3$	$\bar{\sigma}_{11}$	$\bar{u}_3$	$\bar{\sigma}_{13}$
<i>Penalty</i>	-8904.31	0.7564	-9111.31	-0.3821
$\gamma = 0$	-8904.31	0.7564	-9111.31	-0.3821
$\gamma = 1$	-8915.35	0.7565	-9121.80	-0.3822
	Timo - Sin-z2		Sin-z2 - Timo	
Type	$\bar{u}_3$	$\bar{\sigma}_{11}$	$\bar{u}_3$	$\bar{\sigma}_{13}$
<i>Penalty</i>	-9443.62	0.7564	-9595.97	-0.3821
$\gamma = 0$	-9443.62	0.7564	-9595.97	-0.3821
$\gamma = 1$	-9454.10	0.7565	-9607.01	-0.3822
	monomodels			
Type	$\bar{u}_3$	$\bar{\sigma}_{11}$	$\bar{\sigma}_{13}$	
Euler Bernoulli	-8583.05	0.7129	-	
Timoshenko	-9607.01	0.7129	-0.2503	
Sin-z2	-9454.10	0.7565	-0.3822	

In the following, the positioning of the interface is reviewed in further detail. The Interface is therefore shifted from one of the beams ends towards the beams center. The distance is varied each time with a length increment equal to half a the beams height. This results in  $ah$  with  $a \in \{0.5, 1, 1.5, 2\}$ . For a slenderness ratio of  $s = \frac{l}{h} = 5$  the length is hence  $\alpha \frac{l}{5}$ . The deflection and stresses are evaluated at the location of their maximum values:  $(x = \frac{l}{2}, z = -\frac{h}{2})$  for  $u_3$  and  $\bar{\sigma}_{11}$  respectively ( $x = 0, z = 0$ ) for  $\bar{\sigma}_{13}$ . Table 4.7 gives the value for the displacements, while Tables 4.8 and 4.9 provide the values for the stresses. The results indicate that the size of the complex zone has very little influence on the result of the deflection and the in-plane stress. It is only the transverse stress who seems to be a little bit more sensitive. This is shown in Figure 4.17, where the distributions of  $\bar{\sigma}_{13}$  through thickness at  $x = 0$  is shown. In (a) for  $\Omega_c = 1 \cdot h$  and in (b) for  $\Omega_c = 2 \cdot h$ . In (a) the same distributions for Penalty and  $\gamma = 0$  are obtained, while  $\gamma = 1$  is already matching the Sin-z2 Monomodel. In Figure 4.17 (b) we can see, that all the three coupled models have the same distribution as the Sin-z2 theory. In both configurations we always retrieve for the coupled models the distribution of the complex model.

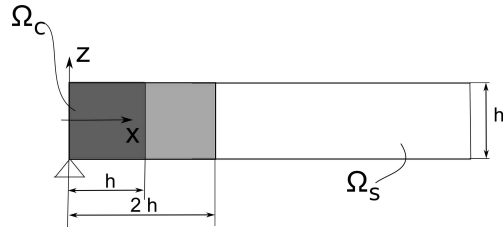


Figure 4.16: Principal of refinement zone corresponding several times the height

Table 4.7: Homogeneous Material: sensitivity on  $\bar{u}_3$ ; refined with Sin-z2 at each of beam ends separately , s = 5

refined at support				
	$\bar{u}_3$			
Type	$0.5 \cdot h$	$1 \cdot h$	$1.5 \cdot h$	$2 \cdot h$
<i>Penalty</i>	-9596.52	-9596.52	-9595.97	-9595.97
$\gamma = 0$	-9596.52	-9596.52	-9595.97	-9595.97
$\gamma = 1$	-9607.01	-9607.01	-9607.01	-9606.46
refined under load				
Type	$0.5 \cdot h$	$1 \cdot h$	$1.5 \cdot h$	$2 \cdot h$
<i>Penalty</i>	-9445.80	-9443.62	-9443.62	-9443.62
$\gamma = 0$	-9445.80	-9443.62	-9443.62	-9443.62
$\gamma = 1$	-9454.66	-9454.10	-9454.10	-9454.10
monomodel values				
Timo	$\bar{u}_3 = -9607.01$			
Sin-z2	$\bar{u}_3 = -9454.10$			

Table 4.8: Homogeneous Material: sensitivity on  $\bar{\sigma}_{11}$ ; refined with Sin-z2 at each of beam ends separately , s = 5

refined under load				
Type	$0.5 \cdot h$	$1 \cdot h$	$1.5 \cdot h$	$2 \cdot h$
<i>Penalty</i>	0.7502	0.7562	0.7565	0.7565
$\gamma = 0$	0.7502	0.7562	0.7565	0.7565
$\gamma = 1$	0.7561	0.7565	0.7565	0.7565
monomodel values				
Timo	$\bar{\sigma}_{11} = 0.7129$			
Sin-z2	$\bar{\sigma}_{11} = 0.7565$			

Table 4.9: Homogeneous Material: sensitivity on  $\bar{\sigma}_{13}$ ; refined with Sin-z2 at each of beam ends separately , s = 5

refined at support				
	$\bar{\sigma}_{13}$			
Type	$0.5 \cdot h$	$1 \cdot h$	$1.5 \cdot h$	$2 \cdot h$
<i>Penalty</i>	-0.3731	-0.3819	-0.3822	-0.3822
$\gamma = 0$	-0.3731	-0.3819	-0.3822	-0.3822
$\gamma = 1$	-0.3822	-0.3822	-0.3822	-0.3822

monomodel values	
Timo	$\bar{\sigma}_{13} = -0.2503$
Sin-z2	$\bar{\sigma}_{13} = -0.3822$

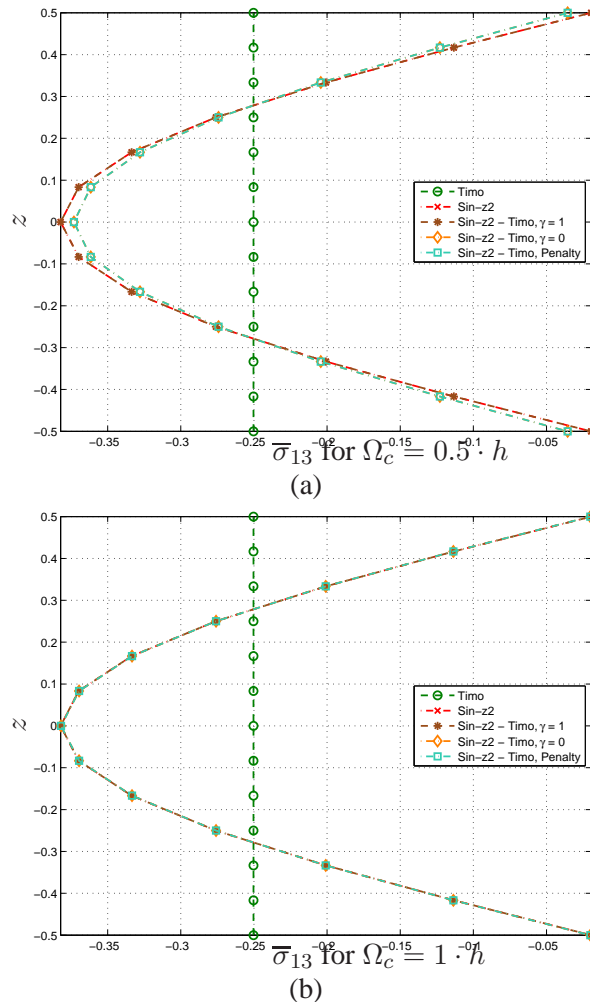


Figure 4.17: Homogeneous Material: (a):  $\bar{\sigma}_{13}$  for  $\Omega_c = 0.5 \cdot h$ ; (b):  $\bar{\sigma}_{13}$  for  $\Omega_c = 1 \cdot h$ ; refined at support;  $s = 5$

Equation (4.33) imposed a stringent condition for  $\gamma = 0$  at the interface, which could be only satisfied by having all rotational and shear components of the same absolute value. In the variational formulation, the same vanishing displacement difference at the interface is enforced by different factors for two Lagrange Multipliers. This concerns the couple  $\delta^c \lambda_\theta ({}^s w'_0 - {}^c v_1)$  together with  $\delta^c \lambda_{v_1} ({}^s w'_0 - {}^c v_1)$  as well as the couple  $\delta^c \lambda_\theta ({}^c v_1 - {}^c \theta)$  together with  $\delta^c \lambda_{v_1} ({}^c v_1 - {}^c \theta)$ . Therefore one might think of easing this stringent condition by loosening one part of one of the couples. This leads to canceling one of the double occurring Lagrange Multipliers. This is done in Figure 4.18. While canceling one of the double occurring jump minimizations, it can bee seen that the overall system gets to rigid and does not provide a smooth displacement distribution around the interface any more. The stringent condition for  $\gamma = 0$ , which implies the restriction of the complex model to the form of the simple model, cannot be loosened.

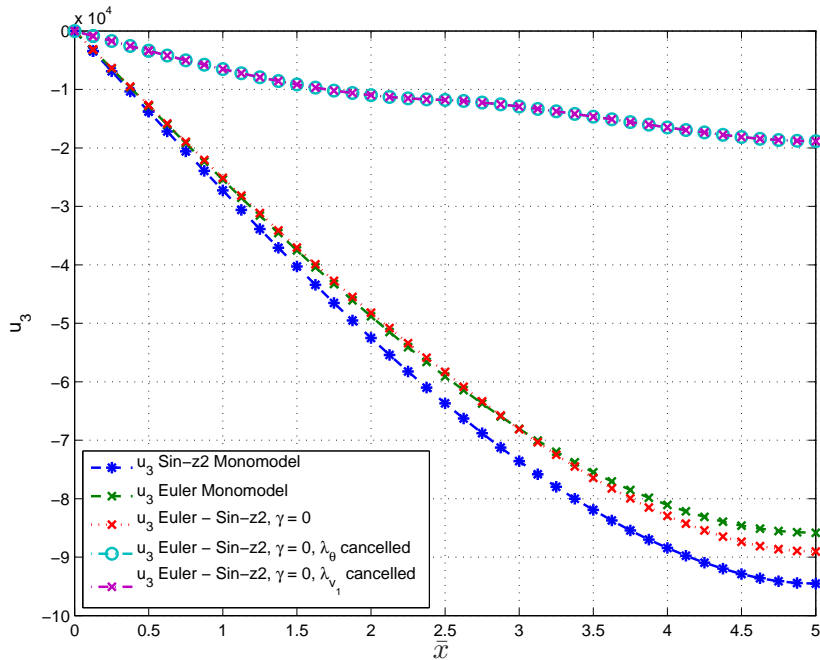


Figure 4.18: Propagation of  $\bar{u}_3$  over length  $x$  for cancelled double conditions;  $s = 5$

#### 4.5.2.2 Two Interfaces

As the general interest is to capture all the maximum stresses at the same time, elements with the complex kinematics will be applied at both ends at the same time. Hence two interfaces will be used. The mesh with  $N_x = 40$  elements is used having 20 elements in the centre associated with the simple model and at each end 10 elements using the Sin-z2 model, as shown in Figure 4.19. For a regular mesh, the positions of the interfaces are  $\bar{x}_1 = \frac{l}{8}$  and  $\bar{x}_2 = \frac{3l}{8}$ . At first, the impact of the local refinements on the global behavior of the kinematical heterogenous model is studied. Therefore results gained with Ansys are given for comparison. Figure 4.20 shows the distribution of  $\bar{\sigma}_{11}$  at the beam's lower surface,  $z = -\frac{h}{2}$ , along the beam's axis for monomodels and coupling models. Also for all models, Figure 4.21 shows the distribution for  $\bar{\sigma}_{13}$  at the beam's mid-fibre surface,  $z = 0$ , along the beam's axis. For both, monomodel references and Ansys references are given in the upper part, while the values obtained by with the XVF are shown in the lower part of the graphs. Note that the penalty technique was identified before to have the same conditions and distributions as  $\gamma = 0$  in the lowest graph. For convince it is not shown hereafter.

For the two values of  $\gamma$ , two different characteristics can be obtained. While having  $\gamma = 1$ , no difference is visible along the length for  $\bar{\sigma}_{11}$ . However, for  $\bar{\sigma}_{13}$  a sudden change between the levels at the interface can be seen. Note that for Euler Bernoulli theory,  $\bar{\sigma}_{13}$  is not present, but for the kinematical heterogenous models it can still be perfectly recovered in the domains using Sin-z2 kinematics. While having  $\gamma = 0$ , a transition between the models close to the interface is visible. In the case of  $\bar{\sigma}_{11}$  this is rather a disturbance in the value, as all kinematical models deliver very close results. However for both values of  $\gamma$ , starting from a point with a certain distance from the interface, the mono model results are recovered.

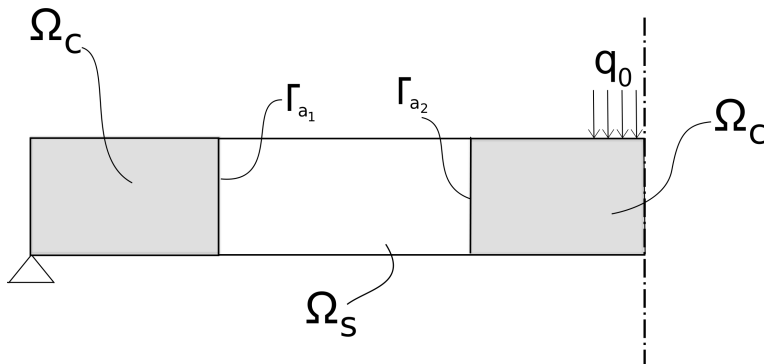


Figure 4.19: Position of refined zones in beam model

The occurring transition for  $\gamma = 0$  is further studied. In Figure 4.22, the position of the interface is changed. From the initial positions they are moved further inwards in order to have two times 40 per cent of the model using complex kinematics. Hence the positions of the interface are  $\bar{x}_1 = \frac{l}{5}$  and  $\bar{x}_2 = \frac{3l}{10}$ . It is shown, that along the length, the distributions of  $\bar{\sigma}_{11}$  and  $\bar{\sigma}_{13}$  have the same transition zone and magnitude

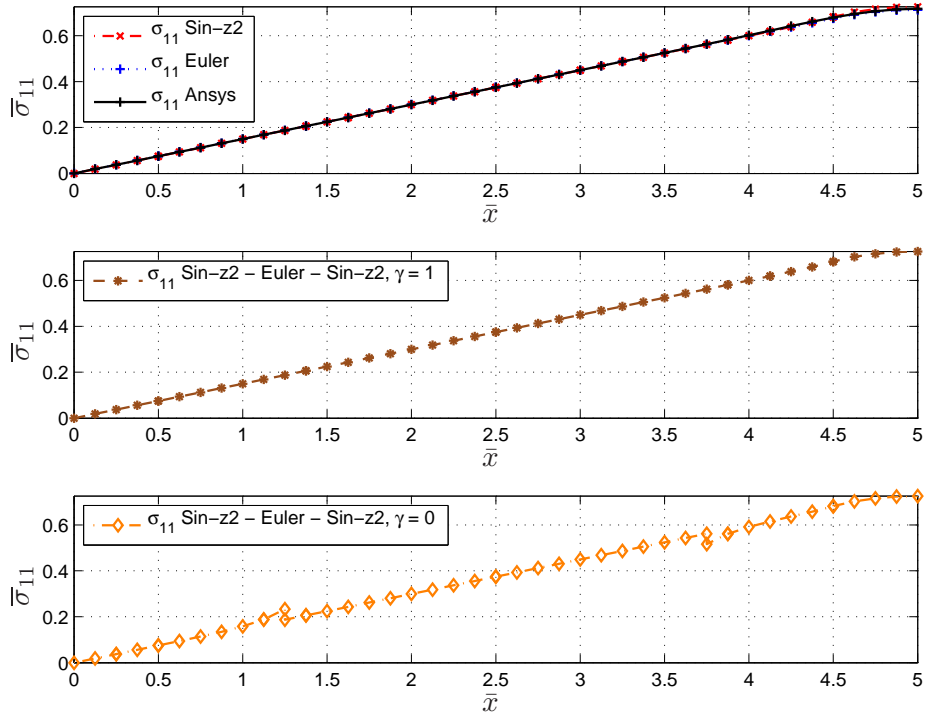


Figure 4.20: Homogenous Material:  $\bar{\sigma}_{11}$  at  $z = -\frac{h}{2}$  with the different kinematical models;  $s = 10$

in disturbance, which is hence independent from the interface position for a given mesh. In Figure, 4.23, the number of elements is changed therefore, while the position of the interface is kept the same. A mesh with 80 elements result is overlaid onto the results obtained with 40 elements. The distributions across the beam's length of  $\bar{\sigma}_{11}$  and  $\bar{\sigma}_{13}$  are given. Here it is shown, that the transition zone and magnitude are also independent from the number of elements used. The terms in (4.33) for  $\gamma = 0$ , have shown, that the occurring disturbance can be minimized, by reducing the difference in the values of the DOFs, provided by the different kinematical models. For a thin beam, having  $s = 1000$  all kinematical models showed in Table 4.4 to provide the same values. The length distribution for  $s = 1000$  in Figure 4.24 shows that for  $\gamma = 0$  no more disturbance of transition is present. All DOFs of the two kinematical models adapt to the same absolute values. No significant minimization effort is needed by the Lagrange Multipliers any more. Note two occurring particularities for  $\bar{\sigma}_{13}$ : as for the Euler model no transverse shear stress is present, for the kinematical heterogenous model a jump at the interface occurs. Further due to the very thin beam, the FE approximation is not able to deliver a continuous distribution of  $\bar{\sigma}_{13}$  any more.

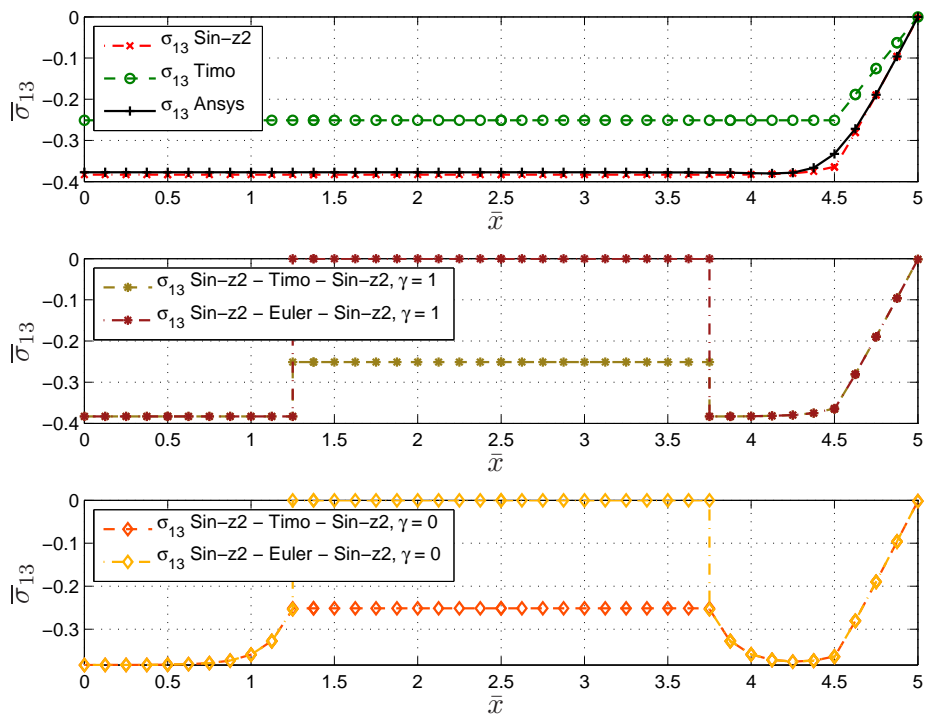


Figure 4.21: Homogeneous Material:  $\bar{\sigma}_{13}$  at  $z = 0$  with the different kinematical models;  $s = 10$

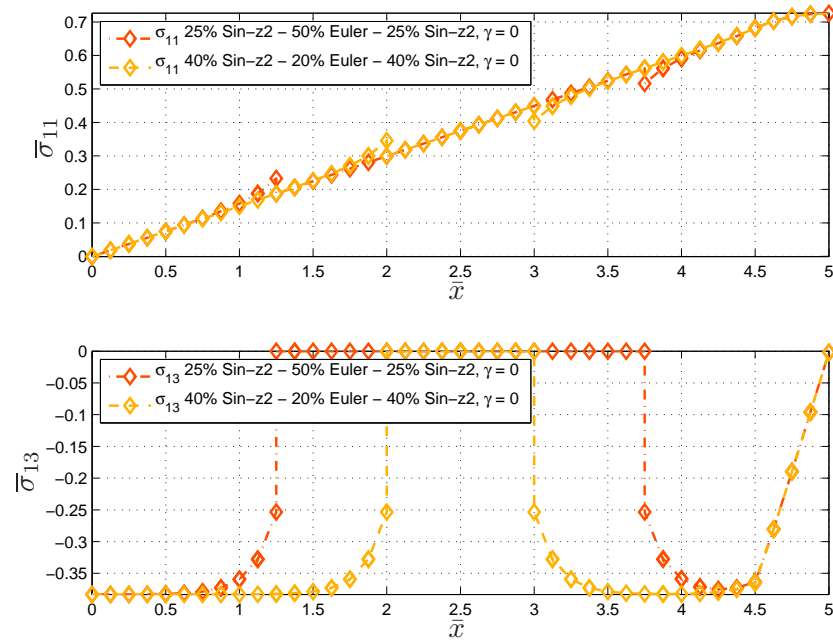


Figure 4.22: Homogenous Material:  $\bar{\sigma}_{11}$  and  $\bar{\sigma}_{13}$  for different positions of  $\Gamma_a$ ;  $\gamma = 0$ ;  $s = 10$

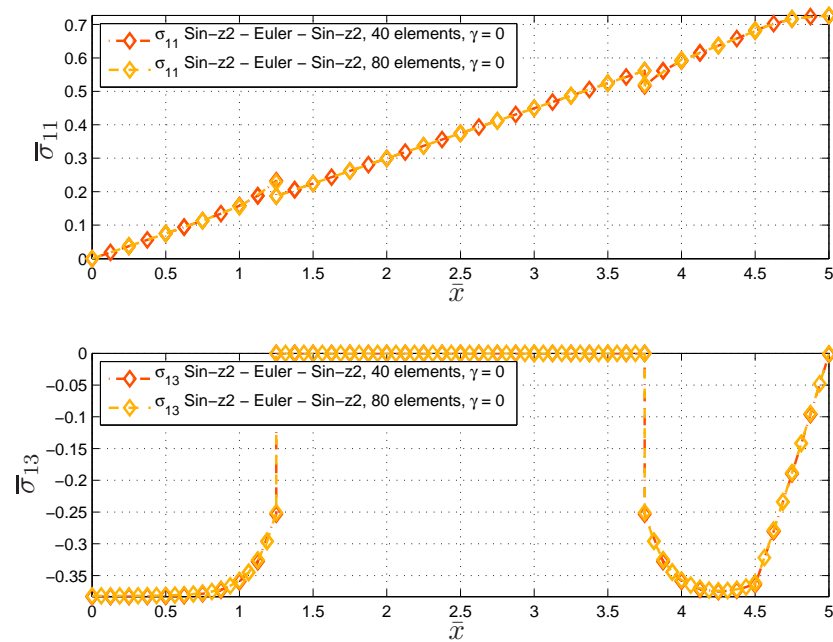
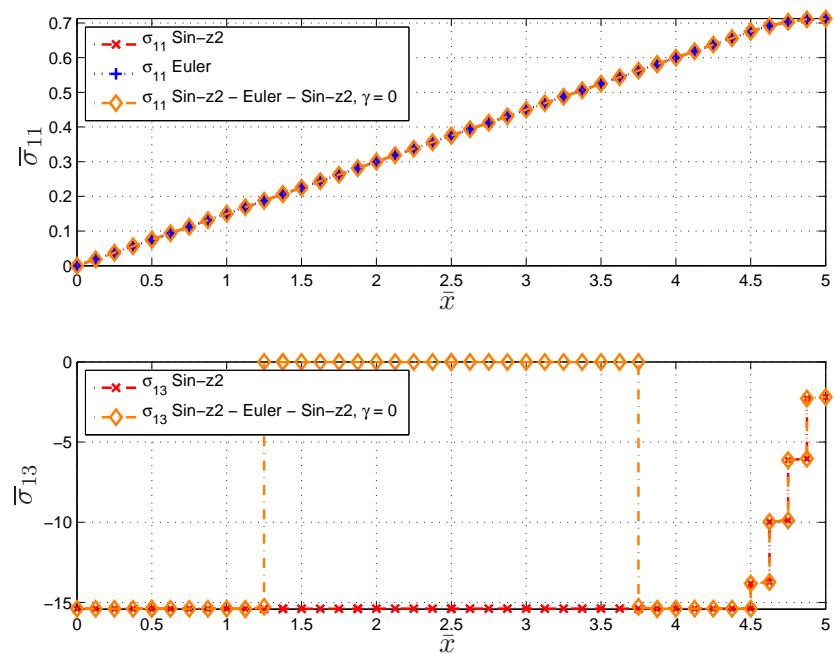


Figure 4.23: Homogenous Material:  $\bar{\sigma}_{11}$  and  $\bar{\sigma}_{13}$  for different discretisations;  $\gamma = 0$ ;  $s = 10$


 Figure 4.24: Homogenous Material:  $\bar{\sigma}_{11}$  and  $\bar{\sigma}_{13}$ ;  $\gamma = 0$ ;  $s = 1000$

### 4.5.3 Layered Structures

For the layered and the Sandwich Material tests, the double interface configuration from Figure 4.19 is used. Results are presented again for thick beams with  $s = 10$  and thin beams with  $s = 1000$ , for configurations as shown in Figure 4.25. At first it will be shown, that a new coupling operator is needed, which is able to take into account the material characteristics of the layers by considering a highly anisotropic sandwich beam. The behaviour of the new coupling operator will be assessed first and this section is then completed by its application.

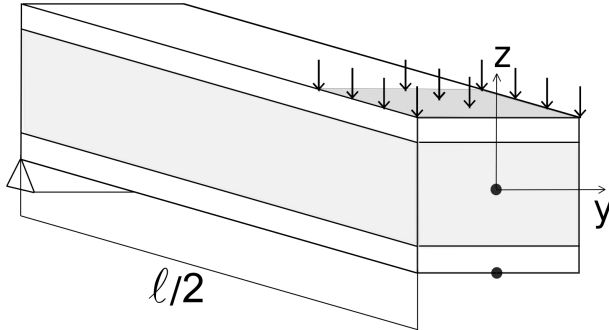


Figure 4.25: Sandwich Beam Configuration with Local Pressure Load

#### 4.5.3.1 Modified Coupling Operator

For XVF, a modification to Equation (4.10) is applied. The stiffness coefficient  $C_{11}$  of each layer is now included into the duality product, besides the geometry, which alone is not sufficient. The four duality products for layered structures are integrated over all  $N_L$  layers, counting from  $k = 1, \dots, N_L$ :

$$\delta^i \mathcal{E}_\lambda^T \mathcal{B}_{ij_{mod}}^j \mathcal{E}_u \quad \text{with } \mathcal{B}_{ij_{mod}} = \sum_{k=1}^{N_L} C_{11}^k \int_{h_{k-1}}^{h_k} {}^i \mathbf{F}^T {}^j \mathbf{F} dz \quad (4.45)$$

$$(4.46)$$

The sandwich test described in the beginning of this section 4.5 is considered with two interfaces, but the material properties is chosen such that  $C_{11,face} = 1000 \cdot C_{11,core}$  so as to highlight the interest of the new coupling operator. Therefore, results are provided with and without the inclusion of the stiffness coefficient  $C_{11}$ . The effect of this modification is shown in Figure 4.26 where the transverse shear stress over the beam length is given.

For  $\gamma = 1$  without the modified dual product, the distribution of the stress has a , while the same abrupt change from one model to another one as in the homogeneous material case can be observed with the modified duality product. In the Euler Lagrange Equations (4.13), the Lagrange Multipliers were identified as stresses. For

the proper establishment of the Multipliers not only the geometric informations are needed but also about the materials stiffness. As a consequence the origin of the peak is a ill-conditioning problem of the original dual product formulation. The values of the Lagrange Multipliers of the original dual product are excessive and, as shown, do not fulfill their role as to satisfactorily minimize the difference in the two displacement fields. As a ESL formulation is used for the one dimensional beam structures, this effect was not visible for homogenous materials. Here the stiffness coefficient  $C_{11}$  is only a constant factor, regardless of the kinematical model chosen. Due to the ESL formulation, the ridigity terms of each kinematical model can be of several orders difference in magnitude. Therefore not only the geometric share of the compound does contribute to the overall ridigity. This modification is done accordingly to a proposition for the Arlequin Method by Hu [32] and [33].

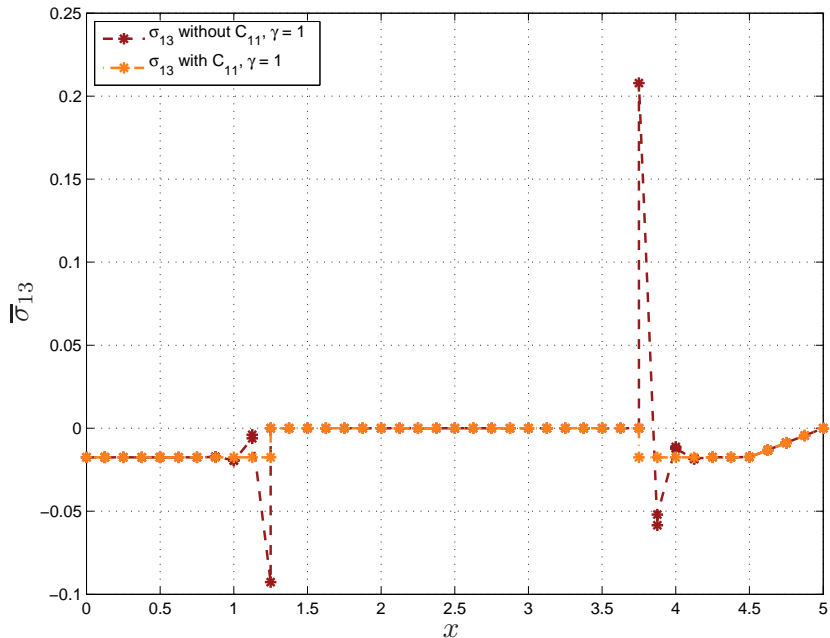


Figure 4.26: Sandwich Material:  $\bar{\sigma}_{13}$  over length  $x$  for  $\gamma = 1$ ;  $1000 \cdot C_{11_{core}} = C_{11_{face}}$ ;  $s = 10$

The influence of the Youngs modulus  $C_{11}$  is now further studied. Therefore the same test configuration is used. The difference here is the material used: the same soft core material times a factor is applied to the different layers. It can be stated:  $C_{11_{face}} = \alpha_{mat} C_{11_{core}}$ , where  $\alpha_{mat}$  is varied from 1 to 1000. The results are listed in Tables 4.10 to 4.12.

The Tables for the first interface, 4.10 and 4.11, show a decreasing Lagrange Multipliers with a growing factor  $\alpha_{mat}$ . While comparing the results of the unmodified with the modified duality product in the same Tables, no changes for the Lagrange Multipliers with  $\gamma = 1$  are visible. Comparing the values of  $\gamma = 0$  shows a slight

increase with the rising factor for the rotational DOFs. The stringent interface condition imposed helps the Lagrange Multipliers of the rotational DOFs, even without the modified coupling operator, to adapt with the growing factor  $\alpha_{mat}$ . Further it can be noted, that for the factors of  ${}^c\lambda_{v_1}$  always a value close to  $10^{10}$  is needed. In the Penalty technique the factor  $G$  was chosen to be  $10^{10}$ , according to recommendation by Wissman and Schwarz [79], in order to provide stable results. A further justification for the chosen magnitude of  $G$  and the equivalence of both techniques. On the second interface, located at  $\bar{x}_2 = 3.75$ , the same values for the unmodified duality product occur, but having inverted signs, as shown in Table 4.12 .

Table 4.10: Sandwich Material: Lagrange Multipliers on  $\Gamma_{a_1}$  at  $\bar{x}_1 = 1.25$ ; Sin-z2 & Euler;  $\gamma = 1$ ;  $s = 10$

$\alpha_{mat}$	${}^s\lambda_{v_0}$	${}^s\lambda_{w_0}$	${}^s\lambda'_{w_0}$
with $C_{11}$ conditioning			
1	$-0.50951 \cdot 10^{-3}$	$-0.22645 \cdot 10^3$	$0.33967 \cdot 10^4$
10	$-0.18197 \cdot 10^{-3}$	$-0.80875 \cdot 10^2$	$0.62996 \cdot 10^3$
100	$-0.24496 \cdot 10^{-4}$	$-0.10887 \cdot 10^2$	$0.68883 \cdot 10^2$
1000	$-0.25374 \cdot 10^{-5}$	$-0.11277 \cdot 10^1$	$0.69532 \cdot 10^1$
without $C_{11}$ conditioning			
1	$-0.11250 \cdot 10^3$	$-0.50000 \cdot 10^8$	$0.75000 \cdot 10^9$
10	$-0.11250 \cdot 10^3$	$-0.50000 \cdot 10^8$	$0.75000 \cdot 10^9$
100	$-0.11250 \cdot 10^3$	$-0.50000 \cdot 10^8$	$0.75000 \cdot 10^9$
1000	$-0.11250 \cdot 10^3$	$-0.50000 \cdot 10^8$	$0.75000 \cdot 10^9$

Table 4.11: Sandwich Material: Lagrange Multipliers on  $\Gamma_{a_1}$  at  $\bar{x}_1 = 1.25$ ; Sin-z2 & Euler;  $\gamma = 0$ ;  $s = 10$

$\alpha_{mat}$	${}^c\lambda_{v_0}$	${}^c\lambda_{w_0}$	${}^c\lambda_\theta$	${}^c\lambda_{v_1}$
with $C_{11}$ conditioning				
1	$-0.50951 \cdot 10^{-3}$	$-0.22645 \cdot 10^3$	$-0.26392 \cdot 10^4$	$0.59915 \cdot 10^4$
10	$-0.18197 \cdot 10^{-3}$	$-0.80875 \cdot 10^2$	$0.40819 \cdot 10^3$	$0.31531 \cdot 10^4$
100	$-0.24496 \cdot 10^{-4}$	$-0.10887 \cdot 10^2$	$0.21116 \cdot 10^3$	$0.70761 \cdot 10^3$
1000	$-0.25374 \cdot 10^{-5}$	$-0.11277 \cdot 10^1$	$0.24176 \cdot 10^2$	$0.77464 \cdot 10^2$
without $C_{11}$ conditioning				
1	$-0.11250 \cdot 10^3$	$-0.50000 \cdot 10^8$	$-0.58275 \cdot 10^9$	$0.13229 \cdot 10^{10}$
10	$-0.11250 \cdot 10^3$	$-0.50000 \cdot 10^8$	$0.90352 \cdot 10^9$	$0.64141 \cdot 10^{10}$
100	$-0.11250 \cdot 10^3$	$-0.50000 \cdot 10^8$	$0.11493 \cdot 10^{10}$	$0.72561 \cdot 10^{10}$
1000	$-0.11250 \cdot 10^3$	$-0.50000 \cdot 10^8$	$0.11425 \cdot 10^{10}$	$0.72328 \cdot 10^{10}$

Table 4.12: Sandwich Material: Lagrange Multipliers on  $\Gamma_{a_2}$  at  $\bar{x}_2 = 3.75$ ; Sin-z2 & Euler; without  $C_{11}$ ;  $\gamma = 1$ ;  $s = 10$

$\alpha_{mat}$	${}^s\lambda_{v_0}$	${}^s\lambda_{w_0}$	${}^s\lambda_{w'_0}$
1	$0.11250 \cdot 10^3$	$0.50000 \cdot 10^8$	$-0.22500 \cdot 10^{10}$
10	$0.11250 \cdot 10^3$	$0.50000 \cdot 10^8$	$-0.22500 \cdot 10^{10}$
100	$0.11250 \cdot 10^3$	$0.50000 \cdot 10^8$	$-0.22500 \cdot 10^{10}$
1000	$0.11250 \cdot 10^3$	$0.50000 \cdot 10^8$	$-0.22500 \cdot 10^{10}$

#### 4.5.3.2 Sandwich Structure

Hereafter the sandwich structure with its face and core material is tested. As desired with the complex kinematics at both extremes to reliably capture the maximum values of both stress components. Only the modified duality product from Equation (4.45) is used.

The normal stress  $\bar{\sigma}_{11}$  distribution along the beam length is shown in Figure 4.27 for the monomodels and the Sin-z2 - Euler - Sin-z2 as well as the Sin-z2 - Timo - Sin-z2 coupling. For the normal stress, the choice of the simple model has no influence, so only one result with the Euler model is represented. While having  $\gamma = 0$  the discontinuity with the transition is present at the interface, in the zone of the complex model where far from the interface the effect of the localized load is well captured. Continuous distributions can be achieved with  $\gamma = 1$ . Accordingly for the transverse stress  $\bar{\sigma}_{13}$  in Figure 4.28, where for  $\gamma = 0$  the transition is present. Far from the interface, the values are in good accordance with the monomodel results. For  $\gamma = 1$  an abrupt change of the levels is observed. Here the undisturbed monomodel distributions are recovered right at the interface in both, the simple and the complex model.

Evaluating the thickness distributions of the stress at the beam middle for  $\bar{\sigma}_{11}$  or at support  $\bar{\sigma}_{13}$  are given in Figure 4.29. The kinematical heterogenous models follow perfectly the distribution of the complex kinematics, hence also in the layered case, the local models response is preserved. It is also the case for  $\gamma = 0$ , the end of the beam being not affected by the transition zone of the coupling.

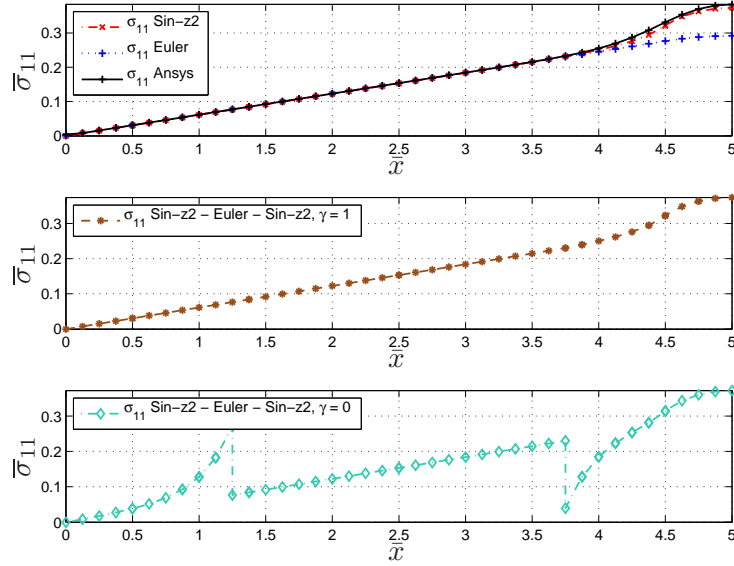


Figure 4.27: Sandwich Material:  $\bar{\sigma}_{11}$  at  $z = -\frac{h}{2}$  with Euler combinations over  $x$ ;  $s = 10$

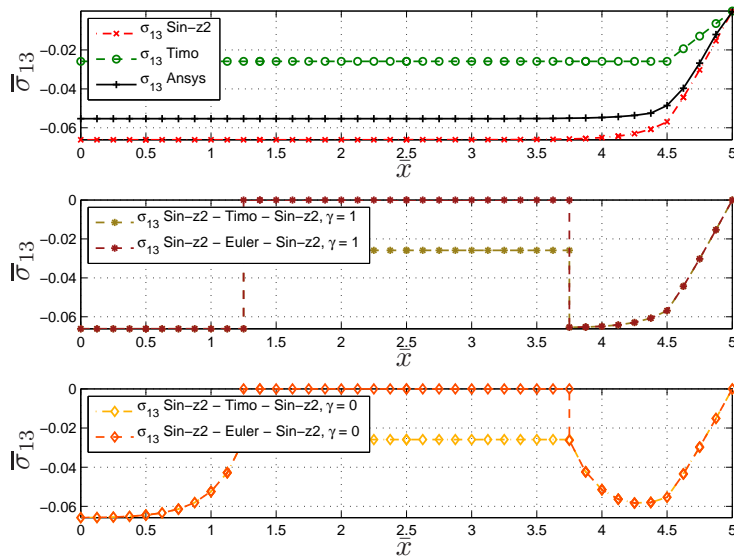


Figure 4.28: Sandwich Material:  $\bar{\sigma}_{13}$  at  $z = 0$  with Timoshenko and Euler combinations over  $x$ ;  $s = 10$

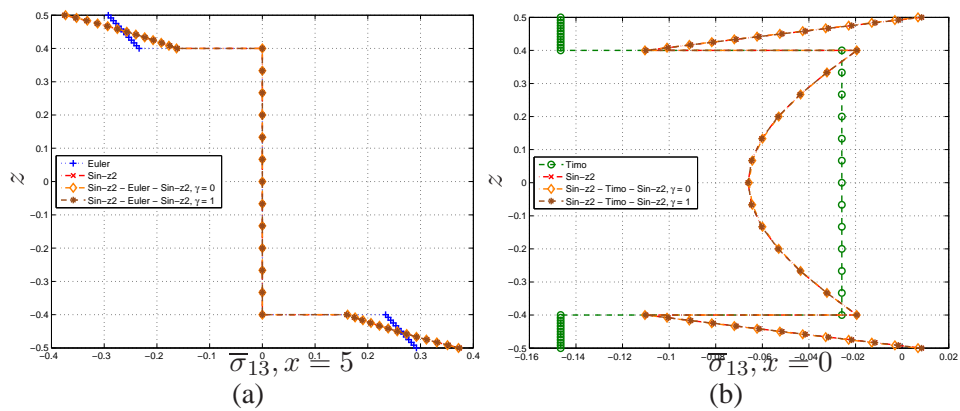


Figure 4.29: Sandwich Material: (a):  $\bar{\sigma}_{11}$  with Euler; (b):  $\bar{\sigma}_{13}$  with Timoshenko through thickness  $z$ ;  $s = 10$

A last study on the sandwich beam is presented hereafter, dedicated to the influence of the size of the complex zone. Before for  $\gamma = 0$  a transition zone was present, which must not disturb the results. Hence, the influence of the size of the complex zone is next studied for two cases  $\gamma = 0$  and  $\gamma = 1$ . A regular mesh of 20 elements is used for the half beam. The number of elements using the simple kinematical model is varied in the central portion of the half-beam. This results in a change of the size of the simple and complex regions. From a mesh consisting of only Sin-z2 models the number of elements with changed stepwise up to 18 elements, having only one complex element at both extreme of the half-beam. The maximum normal stress  $\sigma_{11}$  and shear stresses  $\bar{\sigma}_{13}$  are evaluate for each step. An error rate is defined as follows  $\Delta\sigma_{ij} = 100 \frac{\bar{\sigma}_{ij} - \bar{\sigma}_{ij}^{Sin-z2}}{\bar{\sigma}_{ij}^{Sin-z2}}$ , representing the variation of the maximum value of the according stress. Figures 4.30 and 4.31 show the error-rate for an increasing number of simple kinematics elements.

The presented results lead to the conclusion, that  $\gamma = 1$  yields better results, in particular for the transverse shear stress. Only one complex element can be used without affecting the quality of the results at the end of the beam. For  $\gamma = 0$ , the size of the complex zone must be multiplied by four to achieve an error rate of 2% for the transverse stress. For the in-plane stress only a gain of 2 is obtained. In contrast to the transverse shear stress, which is affected mainly by local effects, the in-plan stress is dominated by the global behaviour of the whole model, here especially in therms of the deflection  $u_3$ . An unbalanced kinematically heterogenous model will not provide a smooth global behaviour.

An illustration of the efficiency of the XVF approach is given in Figure 4.32, concerning the transverse stress distribution along the beam length. Here a configuration of only two complex element at each of the end is used. For  $\gamma = 0$  the stress distribution is disturbed by the transition zone, leading to lower maximum values in the zone of interest. For  $\gamma = 1$  however the stress distribution provides the desired maximum value and a better congruence for the last two complex elements, inside  $\frac{9}{20}l < x < \frac{l}{2}$ . This attractive feature allows to confine the richer and computational more expensive model in a very small region where accurate stresses are indispensable. This provides therefore a drastic reduction of the computational cost.

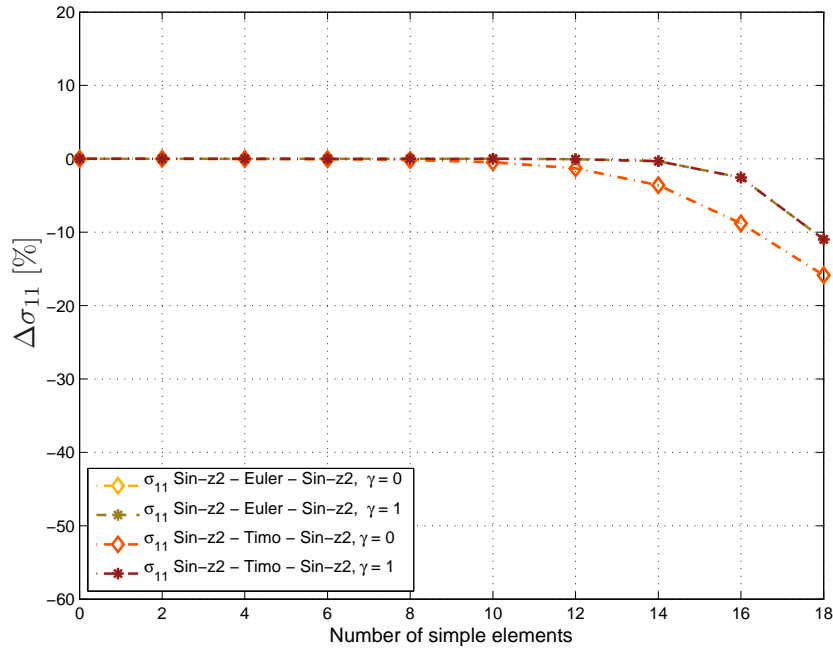


Figure 4.30: Sandwich Material: Error rate on  $\bar{\sigma}_{11}$  for increasing number of simple elements;  $s = 10$

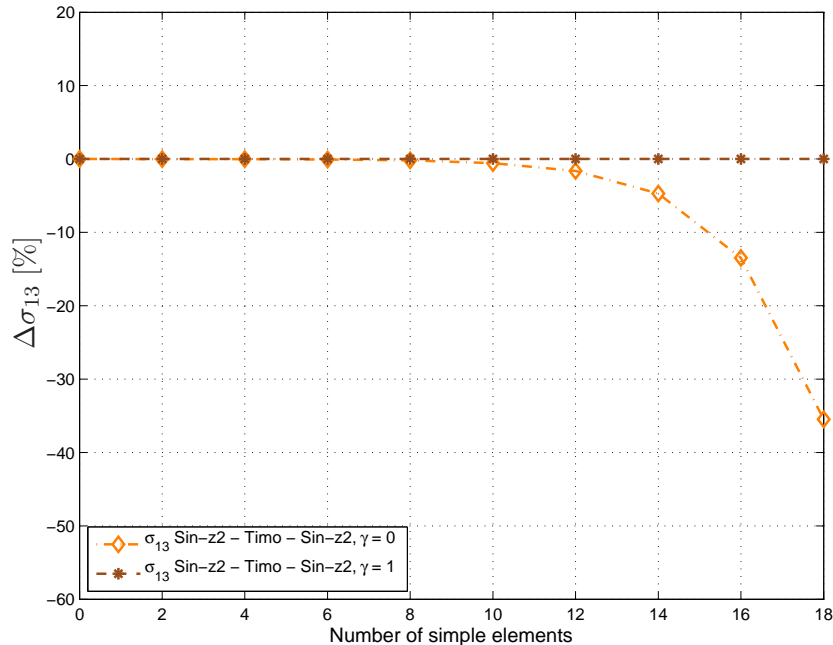


Figure 4.31: Sandwich Material: Error rate on  $\bar{\sigma}_{13}$  for increasing number of simple elements;  $s = 10$

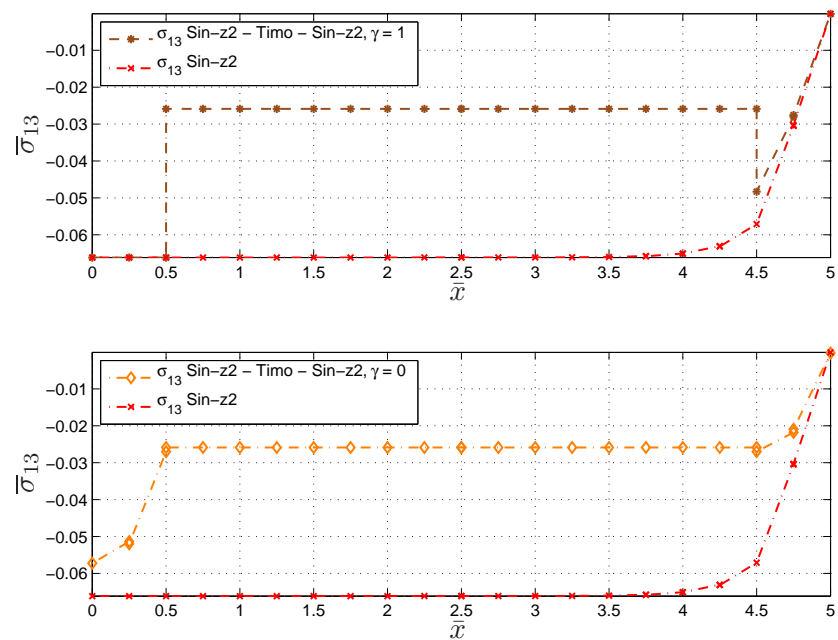


Figure 4.32: Sandwich Material:  $\bar{\sigma}_{13}$  over length  $x$  with 16 Timoshenko elements;  $s = 10$

## 4.6 Conclusion

The main goal of this study is to reduce overall computational effort, without loss of local precision. Therefore, different kinematical models with different FE approximations were used. Each within local sub-domains, where they are the most suitable to deliver the desired results. For the kinematical models used, different formulations of the Lagrange Multipliers were possible. In the presented case of dimensional homogeneity, the projection of the complex towards the simple kinematical model rendered the same results as without projection in the sense of the duality product. This lead to the identification of two different interface conditions, depending on the value assigned to the scalar parameter  $\gamma$ : one for  $\gamma = 1$  and one for  $\gamma \neq 1$ . It could be identified, that while  $\gamma \neq 1$ , the stringent interface conditions of  $\gamma = 0$  were present. Also an application of XVF towards multilayered structures was addressed. Through the introduction of a new coupling operator for multilayered structures, robust and mechanical correct results could be provided.

Summing up the key aspects, for coupling of kinematically heterogenous models via XVF and Penalty method, it can be stater that:

- the Penalty technique is included in XVF for  $\gamma = 0$ .
- the local response of each kinematical models is kept.
- for  $\gamma = 0$  perturbations in the complex model domain close to the interfaces can be found, having a transition from the complex model level towards the simple model level. Far from the interface the undisturbed complex model is achieved.
- for  $\gamma = 1$  an abrupt change from the complex model level towards the simple model level is obtained. This allows using smaller complex domains, which are covering only the zone of interest.
- a reduction of the number of total number of unknowns is possible, especially for  $\gamma = 1$ .

## Chapter 5

# Conclusion and Outlook

### 5.1 Conclusion

This work presented an overview of different techniques to model layered structures, especially composites. The modelling approach was mainly based on the all-encompassing CUF, which can also be adapted to the kinematical hypothesis used in the one-dimensional models. Two classes of descriptions were distinguished: The ESL type and the LW type descriptions. Kinematical hypothesizes used for the multilayer in the ESL descriptions was shown to be adaptable in a modified form per layer in the LW descriptions.

The different models were evaluated on the free edge effects in composite plates, applied to uniform extensional and bending loads. A simple in-plane mesh refinement was delivering reliable results for the CUF models. This provided detailed results in order to understand the general mechanics of each laminate, and at the same time was more economic than an equivalent 3D modeling approach. In the vicinity of the free edges high stress concentrations in the transverse stress components are present. In a linear elastic approach they are having a singular behaviour. Only higher order kinematical models were capable to provide elevated stresses close to the free edge. Further it was the LW models that could provide reliable results in the intralaminar region. These models did further profit from the needed model refinement in thickness direction via the use of several mathematical layers per physical layer, which enabled a better visibility of the singular behaviour. EM models showed to be not as capable to deliver the same amount of singular behaviour as LM models. Among the CUF models, the LM models were able to provide further detailed prediction of the singularities.

Via the power law fitting approach, it was possible to gain a measurement on the occurring singularities in the different laminates. Having only two parameters it provides an intuitive measurement for the singular stresses. Here, the singularity strength was based on a distance to the free edge, where a finite stress value is assured. The resulting material data was based on an effective modulus theory, using a homogenization via mixing rules of the volumetric share of fibres and matrix. Micro

mechanical effects were neglected. This has to be kept in mind if one wants to apply a failure criteria.

Via the power law parameters for the stress components it was possible to compare the free edge effects in extension and bending for the laminates under consideration. The confrontation showed, that for equal deformation energy, the effect in extension is in the most cases more pronounced compared to bending. In bending, the stacking sequence has a major impact on the singularities appearing. From the CLPT one can see that the stiffness terms for the membrane rigidity are invariant to the position in the lay-up, however the rigidity terms for bending are. Due to the high rigidity of the outer layers in the case of the  $[0, 90]_s$  laminate, the singularity strength is of the same order in extension and bending.

Via the CUF models, compared with the results obtained from the 3D code, it was shown that only the cost expensive higher order LW models provided reliable results close to the free edge. However far from the free edge, in the region where the hypotheses of the CLPT hold true, also ESL models provided good results. They are of special interest as they are very inexpensive regarding computational cost. Therefore it is desirable to model the laminate with the costly inexpensive ESL models in the plate's centre and use the precise LW elements only close to the free edges. The overall system size will be reduced and hence computational costs. The overall number of the degree of freedom determines them, which are the unknowns of the FE system. This calls for a suitable connection method, which at the same time does not provoke extensive additional computational costs. The XVF was identified as such a method. As it uses a non-overlapping domain arrangement, it does not involve a redundant set of unknowns from both, the complex and the simple kinematical model. Its particularity is that the overall mesh can be kept and only the element type change. Further, the construction of the Lagrange multipliers, which are used to establish the connection, is based on the kinematical models used. Hence two different formulations are possible, assigned by the scalar parameter  $\gamma$ . In this work, the connection between different one-dimensional ESL kinematic with different FE approximations has been studied. When the complex kinematical model is used with  $\gamma = 0$ , the conditions imposed at the interface were restricting the complex model towards the kinematics of the simple model. Therefore a transition in the complex model close to the interfaces was observed. In contrary, using the simple kinematical model, with  $\gamma = 1$ , less restrictive conditions were imposed, allowing an abrupt chance of the levels at the interface. Both formulations showed their capability to provide the detailed response of the complex model far from the interface. The XVF was shown to be able to reduce the overall computational costs, through the use of inexpensive simple models. It was further shown that the domain using simple kinematics could be extended with  $\gamma = 1$ . The advantages of the XVF using  $\gamma = 1$  are promising for further applications.

## 5.2 Outlook

As a base to measure the singularities occurring in the vicinity of free edges, the power law fitting was introduced. Its major drawback is its mathematical formulation, allowing only to be applied to monotonous and strictly positive or negative stress distributions. A sign-chance for monotonous distributions is frequent in the free edge effect, depending on the laminate considered. An expansion of the power law with a third parameter can be imagined, in order to account for this kind of distribution. Other types of singular stress distributions might be considered, as a waveform distribution which is occurring especially in  $[90, 0]_s$  cross-ply laminate. Nevertheless a new measurement for this type of distributions has to be treated apart in order to keep comparability between the formulations.

Up to now only symmetric laminates have been investigated. In order to further investigate the difference between the free edge effect in bending and extension, also other laminates have to be regarded. Therefore, unsymmetrical as well as asymmetrical laminates are of interest. As they have a strong coupling between the flexion and membrane behaviour, different response to the two load types are expected. Due to those coupling effects of those types of laminates, additional stress concentrations are expected.

Concerning the application of the XVF, further developments are needed in order to couple ESL with LW formulations. This concerns also the coupling of PVD and RMVT formulations. Due to the dimensional homogeneity, similar results would be expected. In contrary to the presented one-dimensional approach, using purely ESL models, additional sampling points through thickness appear in the LW formulation. Here the integral mean applied in the XVF will be formulated piecewise per layer. While using  $\gamma = 1$  the weak fulfilment of the interface conditions, based on the ESL kinematics, is very promising.

# Conclusions et perspectives

## Conclusions

Ce travail a présenté un aperçu des différentes techniques de modélisation des structures stratifiées, en particulier les matériaux composites. L'approche de modélisation a été principalement basée sur l'amplectif CUF, qui peut également être adapté aux hypothèses de la cinématique utilisée dans les modèles unidimensionnels. Deux classes de description ont été distinguées: le type de l'ESL et les descriptions de type LW. Il a été montré que les hypothèses cinématiques utilisées pour le multicouches dans les descriptions ESL peuvent être adapté dans une forme modifiée par couche dans les descriptions LW.

Les différents modèles ont été évalués sur les effets de bords libres des plaques composites, appliqués à des charges uniformes d'extension et de flexion. Un simple raffinement du maillage dans le plan a fourni des résultats fiables pour les modèles de la CUF. Cette technique de modélisation a permis de livrer des résultats détaillés afin de comprendre les mécanismes généraux de chaque stratifié, de plus, elle est plus économique qu'une approche de modélisation 3D équivalente. Au voisinage des bords libres, des concentrations élevées de contraintes des composantes transversales sont présents. Dans une approche élastique linéaire, ils ont un comportement singulier. Seulement les modèles cinématiques d'un ordre supérieur étaient capables de fournir des contraintes élevées à la proximité du bord libre. En outre, ce sont les modèles LW qui pourraient donner des résultats fiables dans la région intralaminaire. Ces modèles en outre ont profité du raffinement du modèle nécessaire en direction de l'épaisseur grâce à l'utilisation de plusieurs couches mathématiques par couche physique, ce qui a permis une meilleure visibilité du comportement singulier. Les modèles EM ont montré de ne pas être aussi capable de fournir la même quantité de comportement singulier comme les modèles LM. Parmi les modèles du CUF, les modèles LM étaient capables de fournir plus de détail des singularités.

L'expression des contraints sous la forme exponentielle, a permis d'obtenir une mesure sur les singularités qui se produisent dans les différents stratifiés. Avec seulement deux paramètres, il fournit une mesure intuitive pour les contraintes singulières. Ici, la résistance à la singularité est basée sur une distance du bord libre, où une valeur finie des contraintes est assurée. Les données du matériau résultant sont basées sur une théorie de module effectif, en utilisant une homogénéisation par les parts volumiques des fibres et la matrice. Les effets micromécaniques ont été négligés. Ceci

doit être gardé à l'esprit si l'on veut appliquer un critère de rupture.

Utilisant les paramètres de la forme exponentielle des différents composants des contraints c'était possible de comparer les effets de bord libre au lieu (pour dire à la place ?) des chargements d'extension et de flexion pour les stratifiés étudiés. La confrontation, en assurant la même énergie de déformation dans les deux chargements, a montré que l'effet en extension est dans la plupart des cas plus prononcé par rapport à la flexion. En flexion, la séquence d'empilement a un impact majeur sur l'apparition des singularités . De la CLPT on peut voir que les termes de rigidité de la membrane sont invariants à la position dans le stratifié, mais les termes de rigidité de flexion le sont. Grace à la rigidité importante des couches externes dans le cas du stratifié  $[0, 90]_s$ , la résistance à la singularité est du même ordre dans l'extension et la flexion.

Par l'intermédiaire des modèles de CUF, par rapport aux résultats obtenus avec le code commercial 3D, il a été montré que seulement les modèles coûteux d'ordre supérieur LW ont fourni des résultats fiables à proximité du bord libre. Cependant, loin du bord libre, dans la région où les hypothèses de la CLPT sont valides, les modèles ESL ont donné de bons résultats. Ils sont particulièrement intéressants pour leurs très bas coûts de calcul. Il est donc souhaitable de modéliser le stratifié avec les modèles ESL peu coûteux dans le centre de la plaque et d'utiliser les éléments de LW précises que près des bords libres. La taille globale du système est réduite, ce qui diminue le coût de calcul. Le nombre global de degré de liberté détermine la taille, à travers les inconnues des différents éléments du système FE. Il faut pour cela une méthode de connexion adaptée, qui, dans le même temps, ne provoque pas d'importants coûts de calcul. La XVF a été identifié avec un tel procédé. Comme il utilise un agencement de domaine sans recouvrement, il n'inclus pas des inconnues redondantes à la fois, du modèle de la cinématique complexe et simple. Sa particularité est que le maillage global peut être maintenu et on change seulement le type d'élément. En outre, la construction des multiplicateurs de Lagrange, qui sont utilisés pour établir la connexion, est basée sur les modèles cinématiques utilisés. Deux formulations différentes sont donc possibles, et sont attribuées par le paramètre scalaire  $\gamma$ . Dans ce travail, la connexion entre les différents unidimensionnels d'une cinématique ESL avec différentes approximations FE a été étudiée. Lorsque le modèle cinématique complexe est utilisé avec  $\gamma = 0$ , les conditions imposées à l'interface restreignaient le modèle complexe vers la cinématique du modèle simple. Par conséquent, une transition dans le modèle complexe dans la proximité des interfaces a été observée. En revanche, en utilisant le modèle cinématique simple, avec  $\gamma = 1$ , des conditions moins restrictives ont été imposées, ce qui permet un changement brutal des niveaux à l'interface. Les deux formulations ont montré leur capacité à fournir la réponse détaillée du modèle complexe loin de l'interface. La XVF a montré sa capacité de réduire les coûts des calculs globaux, grâce à l'utilisation de modèles simples peu coûteux. Il a également été démontré que le domaine utilisant une cinématique simple pourrait être étendu avec  $\gamma = 1$ . Les avantages de la XVF utilisant  $\gamma = 1$  sont prometteuses pour d'autres applications.

## Perspectives

Pour mesurer les singularités qui se produisent au voisinage du bord libre, l'expression des contraints sous la forme exponentielle a été introduite. Son inconvénient majeur est sa formulation mathématiquement, qui permet seulement une application sur des distributions des contraintes monotones et strictement positives ou négatives. Un changement de signe pour les distributions monotones est fréquent pour les effets du bord libre, selon le stratifié considéré. Une extension de la forme exponentielle avec un troisième paramètre peut être imaginé afin de tenir en compte de ce genre de distributions. D'autres types de distributions des contraintes singulières pourraient être envisagées, comme une forme de distribution d'onde qui se produit en particulier dans le stratifié  $[90, 0]_s$  cross-ply. Néanmoins, une nouvelle mesure de ce type de distributions doit être traitée indépendamment pour maintenir la comparabilité entre les formulations.

Jusqu'à présent, seulement les stratifiés symétriques ont été étudiés. Afin d'étudier plus en détail la différence entre l'effet de bord libre en flexion et en extension, aussi d'autres stratifiés doivent être considérés. Par exemple des stratifiés antisymétriques ainsi que des asymétriques. Comme ils ont un fort couplage entre la flexion et le comportement de la membrane, une réponse différente pour les deux types de charge est attendue. En raison des effets de couplage de ces types de stratifiés, des concentrations de contraintes supplémentaires sont attendues.

En ce qui concerne l'application de la XVF, de nouveaux développements sont nécessaires pour coupler des cinématiques ESL avec des cinématiques LW. Cela concerne aussi le couplage des descriptions PVD et RMVT. En raison de l'homogénéité dimensionnelle, des résultats similaires seraient attendus. Au contraire de l'approche unidimensionnelle présentée, en utilisant seulement des modèles ESL, des points supplémentaires pour les multiplicateurs de Lagrange apparaissent dans l'épaisseur dans la formulation LW. La moyenne intégrale appliquée dans le XVF sera formulée par couche tout en utilisant  $\gamma = 1$ . De plus, utiliser des conditions faibles à l'interface, basées sur la cinématique de l'ESL, s'avère très prometteur.

# Conclusioni e prospettive

## Conclusioni

Questo lavoro ha rappresentato una sintesi di modellizzazione delle strutture laminate, in particolar modo quelle composite. L'approccio alla modellizzazione era principalmente basato sulla complessiva CUF che può anche essere adattata alle ipotesi cinematice usate per i modelli unidimensionali. Si possono distinguere due classi di descrizioni: i tipi di ESL e le descrizioni LW. Le ipotesi cinematice usate per il multistrato nel caso delle descrizioni ESL hanno dimostrato di essere adattabili in forma modificata per le descrizioni LW.

I diversi modelli sono stati valutati per gli effetti del bordo libero nelle piastre composite, esposte a sforzi uniformi di trazione o flessione. Un semplice raffinamento del mesh nel piano della piastra può fornire dei risultati affidabili per i modelli CUF. Questa dimostrazione ha fornito dei risultati dettagliati per comprendere il comportamento generale di ogni laminato e nello stesso tempo ha rappresentato una soluzione più economica di una modellizzazione equivalente con elementi tridimensionali. Nella contiguità ai bordi liberi sono presenti delle concentrazioni considerabilmente elevate a sforzi trasversali. Utilizzando un approccio lineare elastico, loro hanno un comportamento singolare. Solo i modelli cinematici di ordine superiore erano capaci di fornire sforzi elevati vicino ai bordi liberi. Ulteriormente, i modelli LW hanno potuto fornire dei risultati affidabili nella regione intralaminare. Questi modelli hanno potuto usufruire inoltre del raffinamento del modello nella direzione dello spessore, utilizzando alcuni strati matematici per strato fisico, concretizzando una migliore visibilità del comportamento singolare. I modelli EM hanno comunque dimostrato di non essere così potenti nel fornire la proporzione del comportamento singolare come i modelli LM. Tra i modelli di CUF, i modelli LM erano i modelli che potevano dare predizioni più dettagliate di singolarità.

Utilizzando l'approccio della descrizione esponenziale era possibile ricevere una misura di singolarità nei diversi laminati. Con solo due parametri la descrizione ha dato una misura intuitiva per gli sforzi singolari. In questo caso, la potenza della singolarità era basata su una distanza dal bordo libero, dove fosse presente uno sforzo finito. I dati materiali erano basati su una teoria di un modulo effettivo, utilizzando una omogeneizzazione e rispettando la composizione volumetrica delle fibre e della matrice. Erano stati negati degli effetti micromecanici. Questo aspetto deve essere preso in considerazione se si vuole applicare un criterio di rottura.

Utilizzando i parametri della discrezione esponenziale era possibile confrontare gli effetti dei bordi liberi tra trazione e flessione per i laminati considerati. Questo confronto ha mostrato che per la stessa energia di deformazione totale gli effetti in trazione sono dominanti rispetto alla flessione per la maggior parte dei casi. Nella flessione la sequenza di laminazione ha un effetto importante per le singolarità risultanti. Dalla CLPT si può osservare che il termine della rigidezza membrane sono invariate della posizione nel dei strati nel laminato, ma le termine della flessione lo sono. Grazie alla rigidezza elevata dai strati esterni nel caso del  $[0, 90]_s$  laminato, la singolarità era dello stesso ordine in trazione e flessione.

Dai modelli CUF, confrontati con i risultati ottenuti dal codice tridimensionale, è stato dimostrato che solo i modelli più costosi LW dell'ordine elevato potevano fornire dei risultati affidabili vicino al bordo libero. Comunque lontano dal bordo libero, nella regione in cui la CLPT è valida, anche i modelli ESL forniscono dei buoni risultati. Questi modelli sono molto interessanti come anche molto economici dal punto di vista dei costi computazionali. Per questo è di gran lunga preferibile modellizzare il laminato con elementi economici ESL nel centro della piastra e usare elementi precisi LW solo vicino ai bordi liberi. Così, il taglio del sistema viene ridotto e con questo conseguentemente anche i costi computazionali. Il numero totale dei gradi di libertà sta determinando i costi computazionali. Questo richiede un metodo adatto che allo stesso tempo non fornisca dei considerevoli costi addizionali. La XVF era stato identificato come un metodo adatto. Utilizzando solo una configurazione dei domini senza recupero, non utilizza delle incognite ridondanti da tutte e due, il modello di cinematica complesso e semplice. La sua particolarità è che il mesh globale può essere tenuto invariato, si cambia solo il tipo di elemento. Poi, la costruzione dei moltiplicatori di Lagrange, che si usano per la connessione, sono basati sugli modelli cinematici usati. Di seguito due formulazioni sono possibili, assegnato dal parametro scalare  $\gamma$ . In questo lavoro è stata studiata la connessione tra diversi modelli cinematici unidimensionali del tipo ESL. Ogni modello usava la sua approssimazione di elementi finiti adattata. Quando si utilizza il modello della cinematica complessa con  $\gamma = 0$ , le condizioni imposte all'interfaccia costringono il modello complesso verso il modello semplice. Di seguito, vicino all'interfaccia, diventa visibile una transizione tra i livelli nel modello complesso. In contrario, quando si utilizza il modello della cinematica semplice con  $\gamma = 1$ , dei condizioni più liberi sono imposti che permettono un cambio bruscamente dei livelli al interfaccia. Tutti e due le formulazioni hanno dimostrato la loro capacità di fornire dei risultati dettagliati nei modelli complessi lontano dall'interfaccia. La XVF ha dimostrato di essere capace di ridurre i costi totali di computazione quando si usano dei modelli semplici ed economici. In seguito, è stato dimostrato che il dominio che usa i modelli semplici può essere esteso con  $\gamma = 1$ . I vantaggi con  $\gamma = 1$  sono molto promettenti per future applicazioni.

## Prospettive

Come base della misura delle singolarità che compaiono nella contiguità ai bordi liberi, è stato introdotto l'uso della formulazione esponenziale. La sua più grande incovenienza è la sua formulazione matematica che permette di applicarla solo a delle distribuzioni monotone e strettamente positive o negative. Un cambiamento di segno è frequente per gli effetti del bordo libero e dipende dal laminato considerato. Un'espansione della formulazione esponenziale con un terzo parametro può essere immaginata per prendere in considerazione questo tipo di distribuzione. Possono essere immaginati anche altri tipi di distribuzione, come una distribuzione in forma di onda, che appare nel  $[90, 0]_s$  cross-ply laminato. Un nuovo tipo di misura deve essere trattato a parte per questi tipi di distribuzione per tenere una comparabilità tra le formulazioni.

Fino ad adesso sono stati studiati solo dei laminati simmetrici. Per studiare in maggior dettaglio gli effetti ai bordi liberi tra trazione e flessione possono essere studiati anche altri laminati : non simmetrici e anche asimmetrici sono particolarmente interessanti perché hanno una connessione forte tra la deformazione delle membrane e flessione. Si attendono risposte diverse per i due tipi di carichi. A causa di queste connessioni delle concentrazioni appaiono sforzi addizionali.

Riguardando la applicazione della XVF, sono necessari ulteriori sviluppi per creare la connessione tra le formulazioni ESL e LW. Questo riguarda anche la connessione tra le formulazione PVD e RMVT. Grazie all'omogeneità delle dimensioni si attendono dei risultati simili. Al contrario rispetto al caso presentato della connessione solo tra elementi ESL, altri punti di campionamento sono necessari nello spessore per le formulazione LW. Qui la media integrale è allora applicata per ogni strato. Utilizzando  $\gamma = 1$  si applicano in ogni caso le condizioni basate sui modelli ESL che sono relativamente rilassate. Ci si aspetta che questi risultati siano più favorevoli.

## Appendix A

# Arlequin Method by Ben Dhia

### A.1 The Classical Arlequin Method with Overlap

The Arlequin method [16] was also formulated to locally improve the description of a sub-domain. The main difference to the Extended Variational Formulation is that the sub-domains do occupy completely separated spaces. Both have a common superposition zone in which the sub-domains are defined to be glued to each other. The three sub-domains are:  $\Omega_s$  with the displacement field  ${}^s\boldsymbol{u}$ ,  $\Omega_c$  with the displacement field  ${}^c\boldsymbol{u}$  and the superposition domain  $\Omega_a$  with the displacement field  ${}^a\boldsymbol{u}$ . Note Figure 4.8 which displays the sub-domains. Inside the superposition zone, meshes of the different sub-domains can be non-matching. The distribution of energy between this two sub-domains in the superposition domain has to be weighted to the different contributions.

Inside the corresponding sub-domain, there is no need for a distribution of the energy. Hence we can write the overall energy:

$$\underbrace{W_s}_{\Omega_s} + \underbrace{\alpha_s W_s + \alpha_c W_c}_{\Omega_a} + \underbrace{W_c}_{\Omega_c} = W_{ext} \quad (\text{A.1})$$

While  $\alpha_s + \alpha_c = 1$ . There are two interfaces at the outer boundaries of  $\Omega_a$  with the other non-overlaid parts of the sub-domains  $\Omega_s$  and  $\Omega_c$ .

As the information about the correlation of energies of the two sub-domains is provided, the link between the different displacement fields still needs to be done. Figure A.1 displays a different situation as used before for Hamilton's principle in Figure 4.7. The two interfaces,  $\Gamma_{as}$  and  $\Gamma_{ac}$ , at both extremes of the superposition zone are present. Inside the superposition zone  $\Omega_a$  the displacement-fields  ${}^s\boldsymbol{u}$  and  ${}^c\boldsymbol{u}$  have to be brought together to a unique field  ${}^a\boldsymbol{u}$ . Again Lagrange Multipliers will be used therefore. The Lagrange Multiplier fields is ranging from the Interface  $\Gamma_{as}$  to Interface  $\Gamma_{ac}$  inside  $\Omega_a$  minimizing the jump in-between the displacement fields. In contrast to the XVF only one Lagrange Multiplier field is present, like in the case of Hamilton's principle. In the Arlequin framework, two different coupling operators,

based on the Lagrange Multipliers, can be used. They are called  $H^1$  and  $L^2$  operator. The last one was presented in Equation 4.38. The  $H^1$  operator is defined as follows:

$$H^1 : \quad C(\lambda, u) = \int_{\Omega_a} \lambda \delta u + l^2 \epsilon_\lambda \delta \epsilon_u \, d\Omega_a \quad (\text{A.2})$$

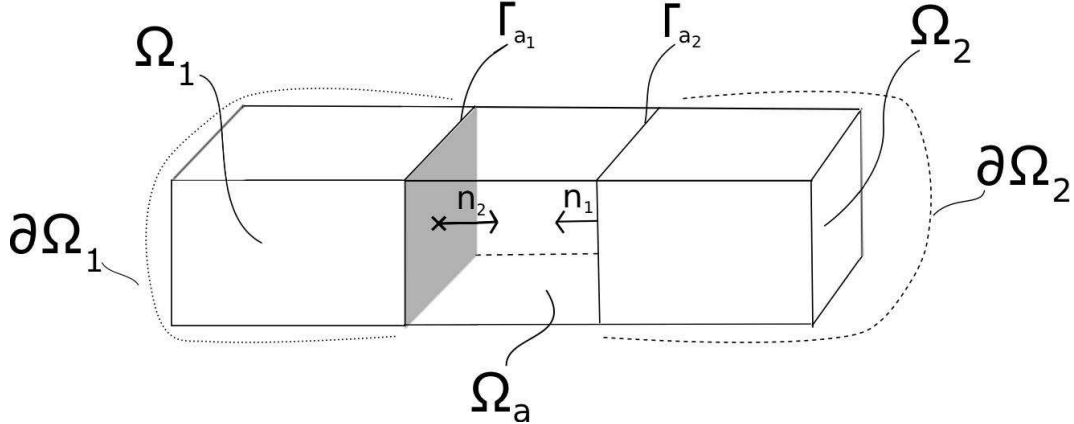


Figure A.1: Configuration with partial overlap for Arlequin Method

$l$  denotes the characteristic length of the coupling zone. As in the formulations before,  $\lambda$  denotes the Lagrange Multiplier field for the coupling. Regarding the difference between both coupling operators it is evident that the  $H^1$  Operator does include an additional formulation for the energy while the  $L^2$  is purely based on displacements. Having information about displacement and strain might be preferable but it might complicate the modelling effort. Therefore the use of the  $H^1$  Operator should not always be preferred. This is mainly due to the aim of achieving an overall less demanding model with a lower computational effort compared to a model made with only the complex kinematics.

Comparing the coupling operators with the one in XVF, which uses a combination of a single real parameter times a Lagrange Multiplier, to connect the different sub-domains, Arlequin has a very similar construction. In the Arlequin Method they are based on a single Lagrange Multiplier field, which has to be chosen before. The coupling operator  $H^1$  is used to minimize the difference in-between the two kinematics, while the factor  $\alpha$  is used for the partition of unity. The operator  $L^2$  can be handled as a special case of  $H^1$ .

Here the classical Principle of Virtual Displacements, see Equation (2.5), is used as basis, in order to keep the comparability. An adaption towards Reissner's Mixed Variation Theorem, stated in Equation (2.15) is possible. Regardless which coupling operator will be used, the energies from Equation (A.1) can be written identified into the following terms, accordingly to the initial definitions in Equation (2.11):

$$\begin{aligned}
 \delta\Pi_{int} &= \int_{\Omega_s/\Omega_a} {}^s\boldsymbol{\sigma} \delta^s \boldsymbol{\epsilon} d\Omega + \int_{\Omega_c/\Omega_a} {}^c\boldsymbol{\sigma} \delta^c \boldsymbol{\epsilon} d\Omega \\
 &\quad + \int_{\Omega_a} \alpha_s {}^s\boldsymbol{\sigma} \delta^s \boldsymbol{\epsilon} d\Omega + \int_{\Omega_a} (1 - \alpha_s) {}^c\boldsymbol{\sigma} \delta^c \boldsymbol{\epsilon} d\Omega \\
 \delta\Pi_{ext} &= \int_{\Omega_a/\Omega_a} \mathbf{f}_d \delta^s \mathbf{u} d\Omega + \int_{\Omega_c/\Omega_a} \mathbf{f}_d \delta^c \mathbf{u} d\Omega \\
 &\quad + \int_{\partial\Omega_s/\partial\Omega_a} \mathbf{f}_d \delta^s \mathbf{u} d\Omega + \int_{\partial\Omega_c/\partial\Omega_a} \mathbf{f}_d \delta^c \mathbf{u} d\Omega \quad (\text{A.3}) \\
 &\quad + \int_{\Omega_a} \alpha_s \mathbf{f}_d \delta^s \mathbf{u} d\Omega + \int_{\Omega_a} (1 - \alpha_s) \mathbf{f}_d \delta^c \mathbf{u} d\Omega \\
 &\quad + \int_{\partial\Omega_a} \alpha_c \mathbf{f}_d \delta^s \mathbf{u} d\Omega + \int_{\partial\Omega_a} (1 - \alpha_s) \mathbf{f}_d \delta^c \mathbf{u} d\Omega \\
 \delta\Pi_{couple} &= \int_{\Omega_a} \boldsymbol{\lambda} (\delta^s \mathbf{u} - \delta^c \mathbf{u}) + l^2 \boldsymbol{\epsilon}_\lambda (\delta^s \boldsymbol{\epsilon} - \delta^c \boldsymbol{\epsilon}) d\Omega
 \end{aligned}$$

For a given  $\alpha_s \in [0, 1]$  find  $(\mathbf{u}_s, \mathbf{u}_c, \boldsymbol{\lambda} \in \mathcal{U}_s \times \mathcal{U}_c \times \mathcal{L})$  such that:

$$\delta\Pi_{int}({}^s\mathbf{u}, {}^c\mathbf{u}, \delta^s \mathbf{u}, \delta^c \mathbf{u}) = \delta\Pi_{couple}({}^s\mathbf{u}, {}^c\mathbf{u}, \boldsymbol{\lambda}, \delta^s \mathbf{u}, \delta^c \mathbf{u}, \delta\boldsymbol{\lambda}) + \delta\Pi_{ext}(\delta^s \mathbf{u}, \delta^c \mathbf{u})$$

$$\forall (\delta^s \mathbf{u}, \delta^c \mathbf{u}, \delta\boldsymbol{\lambda} \in \delta\mathcal{U}_s \times \delta\mathcal{U}_c \times \delta\mathcal{L}) \quad (\text{A.4})$$

Within Equation (A.4) the difference in the displacement fields is vanishing in the integral sense rather over a volume than a surface. There is no possibility to weight the different Lagrange Multiplier constructions available.

As last step, it is important to define the Lagrange Multiplier field for the coupling operators. Belytschko [26] et al showed that using the Lagrange Multipliers with the coarser discretisation of the two sub-domains gives better and more robust results. They also showed the case of non-overlapping meshes, in the Arlequin method denoted as surface coupling. According to them, this can be achieved with simple linear depending Lagrange Multipliers along the principle directions of the coupling interface  $\Gamma_a$ . In the following section, the aspects of surface coupling are investigated

## A.2 Arlequin System in Finite Element Method

Brought into its matrix form for Finite Element solution, the Arlequin Method has a very similar form to the before mentioned XVF system. Matrices  $\mathbf{K}_{\Omega_s}$  and  $\mathbf{K}_{\Omega_c}$  are the ones from the simple and complex model far from the interface. Matrices  $\mathbf{K}_{\Omega_{s,\Omega_a}}$  and  $\mathbf{K}_{\Omega_{c,\Omega_a}}$  contain the stiffness terms of the superposition domain  $\Omega_a$ . The forces in the superposition domain  $\Omega_a$  are partitioned in the same manner as the stiffness. The displacements in the superposition domain are coupled through the entries of  $\mathbf{B}_s$ , respectively  $\mathbf{B}_c$  and the Lagrange Multipliers  $\boldsymbol{\lambda}_s$ . For the coupling of two sub-domains having one common superposition domain it gets:

$$\begin{pmatrix}
 K_{\Omega_s} & 0 & 0 & 0 & 0 \\
 0 & \alpha_s K_{\Omega_{s\Omega_a}} & 0 & 0 & B_s \\
 0 & 0 & (1 - \alpha_s) K_{\Omega_{c\Omega_a}} & 0 & -B_c \\
 0 & 0 & 0 & K_{\Omega_c} & 0 \\
 0 & B_s^T & -B_c^T & 0 & 0
 \end{pmatrix}
 \begin{pmatrix}
 {}^s q \\
 {}^s q_{\Omega_a} \\
 {}^c q_{\Omega_a} \\
 {}^c q \\
 {}^s \lambda
 \end{pmatrix}
 = \begin{pmatrix}
 {}^s f \\
 {}^s f_{\Omega_a} \\
 {}^c f_{\Omega_a} \\
 {}^c f \\
 0
 \end{pmatrix} \quad (A.5)$$

## Appendix B

# Coupling of Sinus $z^2$ with Timoshenko Theory

According to the examples given in the Chapter 4.3 here the according calculations for the projection and the coupling matrices are presented.

### B.1 Projection of Sinus $z^2$ into Timoshenko model

The displacements fields are given as follows:

$$\begin{aligned} u_1(x, z) &= v_0(x) + z \theta(x) \\ u_3(x, z) &= w_0(x) \end{aligned} \quad (\text{B.1})$$

$$\begin{cases} {}^c u_1(x, y, z) = v_0(x) - z v_1(x) + f(z) (v_1(x) + \theta(x)) \\ {}^c u_3(x, y, z) = w_0(x) + z w_1(x) + z^2 w_2(x) \end{cases} \quad (\text{B.2})$$

$$\begin{cases} {}^c u_{1\parallel}(x, y, z) = v_{0\parallel}(x) + z \theta_{\parallel}(x) \\ {}^c u_{3\parallel}(x, y, z) = w_{0\parallel}(x) \end{cases} \quad (\text{B.3})$$

While the Lagrange Multipliers are equal to Timoshenko kinematics:

$$\begin{cases} {}^s \lambda_1(x, y, z) = {}^s \lambda_{v_0} + z {}^s \lambda_{\theta} \\ {}^s \lambda_3(x, y, z) = {}^s \lambda_{w_0} \end{cases} \quad (\text{B.4})$$

The applied projection using Equations (4.14) and (4.15) reveals:

$$\begin{aligned} 0 &= \int_{\Gamma_a} \delta^s \boldsymbol{\lambda} \cdot ({}^c \mathbf{u} - {}^c \mathbf{u}_{\parallel}) d\Gamma = \\ &\int_{\Gamma} \delta^s \lambda_{v_0} \left[ ({}^c v_0 - {}^c v_{0\parallel}) + (f(z) - z) {}^c v_1 + f(z) {}^c \theta - z {}^c \theta_{\parallel} \right] \\ &+ z \delta^s \lambda_{\theta} \left[ ({}^c v_0 - {}^c v_{0\parallel}) + (f(z) - z) {}^c v_1 + f(z) {}^c \theta - z {}^c \theta_{\parallel} \right] \\ &+ \delta^s \lambda_{w_0} \left[ ({}^c w_0 + z {}^c w_1 + z^2 {}^c w_2 - {}^c w_{0\parallel}) \right] d\Gamma \end{aligned} \quad (\text{B.5})$$

From Equation (B.5) the following identities can be extracted:

$$\begin{aligned} \forall \delta^s \lambda_{v_0} : {}^c v_{0\parallel} &= \frac{1}{A} \int_{\Gamma_a} ({}^c v_0 + (f(z) - z) {}^c v_1 + f(z) {}^c \theta - z {}^c \theta_{\parallel}) d\Gamma \\ \forall \delta^s \lambda_{w_0} : {}^c w_{0\parallel} &= \frac{1}{A} \int_{\Gamma_a} ({}^c w_0 + z {}^c w_1 + z^2 {}^c w_2) d\Gamma \\ \forall \delta^s \lambda_{w'_0} : {}^c \theta_{\parallel} &= \frac{1}{I} \int_{\Gamma_a} (z ({}^c v_0 - {}^c v_{0\parallel}) + z (f(z) - z) {}^c v_1 + z f(z) {}^c \theta) d\Gamma \\ \text{with } \int_{\Gamma_a} 1 d\Gamma &= A \quad \text{and} \quad \int_{\Gamma_a} z^2 d\Gamma = I \end{aligned} \tag{B.6}$$

For a symmetric cross shape, Equation (B.6) gives the following relations between the parallel and the complex displacement field:

$$\begin{aligned} \forall \delta^s \lambda_{v_0} : {}^c v_{0\parallel} &= {}^c v_0 \\ \forall \delta^s \lambda_{w_0} : {}^c w_{0\parallel} &= {}^c w_0 + \frac{h^2}{12} {}^c w_2 \\ \forall \delta^s \lambda_{w'_0} : {}^c \theta_{\parallel} &= \frac{24}{\pi^3} {}^c \theta + \left( \frac{24}{\pi^3} - 1 \right) {}^c v_1 \end{aligned} \tag{B.7}$$

## B.2 Dual products of Sinus $z^2$ coupled with Timoshenko model

These Vectors, adapted to the simple and complex kinematical theory, are used to establish coupling matrices  $\mathbf{B}$ :

$$\begin{aligned} \int_{\Gamma_a} \delta^s \boldsymbol{\lambda} \cdot {}^s \mathbf{u} d\Gamma &= \int_{\Gamma} \delta^s \boldsymbol{\mathcal{E}}_{\lambda}^T {}^s \mathbf{F}^T {}^s \mathbf{F} {}^s \boldsymbol{\mathcal{E}}_u d\Gamma = \delta^s \boldsymbol{\mathcal{E}}_{\lambda}^T \mathbf{B}_{ss} {}^s \boldsymbol{\mathcal{E}}_u \\ \text{with } \mathbf{B}_{ss} &= \int_{-\frac{h}{2}}^{\frac{h}{2}} \begin{pmatrix} 1 & 0 & z \\ 0 & 1 & 0 \\ z & 0 & z^2 \end{pmatrix} dz \end{aligned} \tag{B.8}$$

Applying directly the dual product on the unprojected vector  ${}^c \mathbf{u}$  with the simple Lagrange Multipliers  ${}^s \boldsymbol{\lambda}$  delivers:

$$\begin{aligned} \int_{\Gamma_a} \delta^s \boldsymbol{\lambda} \cdot {}^c \mathbf{u} d\Gamma &= \delta^s \boldsymbol{\mathcal{E}}_{\lambda}^T \mathbf{B}_{sc} {}^c \boldsymbol{\mathcal{E}}_u \\ \text{with } \mathbf{B}_{sc} &= \int_{-\frac{h}{2}}^{\frac{h}{2}} \begin{pmatrix} 1 & 0 & -z \\ 0 & 1 & 0 \\ -\frac{24}{\pi^3} z & 0 & -\frac{24}{\pi^3} z^2 \\ \left(1 - \frac{24}{\pi^3}\right) z & 0 & -\left(1 - \frac{24}{\pi^3}\right) z^2 \\ 0 & z & 0 \\ 0 & z^2 & 0 \end{pmatrix} dz \end{aligned} \tag{B.9}$$


---

The dual product in Equation (B.8) with inserted identities from Equation (4.22) gives same result as the direct evaluation of  ${}^s\lambda$  with the unchanged complex displacement field  ${}^c\mathbf{u}$  in Equation (B.9). In the case of dimensional homogeneity, the same mathematical spaces are present due to same base kinematics. Therefore the space of the simple model is included in the complex model. The same is valid for the dual product of  ${}^s\mathbf{u}$  with  ${}^c\lambda$  in  $\mathcal{B}_{cs}$  which therefore is  $\mathcal{B}_{cs} = \mathcal{B}_{sc}^T$ .

Accordingly the same definition is made for  $\mathcal{B}_{cc}$ :

$$\int_{\Gamma_a} \delta^c \boldsymbol{\lambda} \cdot {}^c\mathbf{u} d\Gamma = \delta^c \boldsymbol{\mathcal{E}}_\lambda^T \mathcal{B}_{cc} {}^c\boldsymbol{\mathcal{E}}_u \quad (\text{B.10})$$

with  $\mathcal{B}_{cc} = \int_{-\frac{h}{2}}^{\frac{h}{2}} \begin{pmatrix} 1 & 0 & f(z) - z & f(z) & 0 & 0 \\ 0 & 1 & 0 & 0 & z & z^2 \\ f(z) - z & 0 & (f(z) - z)^2 & (f(z) - z)f(z) & 0 & 0 \\ f(z) & 0 & (f(z) - z)f(z) & (f(z))^2 & 0 & 0 \\ 0 & z & 0 & 0 & z^2 & z^3 \\ 0 & z^2 & 0 & 0 & z^3 & z^4 \end{pmatrix} dz$

The evaluation of the first half of the terms, with variation only of the Lagrange Multipliers gives:

$$\begin{aligned} & \delta^s \boldsymbol{\mathcal{E}}_\lambda^T \gamma \mathcal{B}_{ss} {}^s\boldsymbol{\mathcal{E}}_u - \delta^s \boldsymbol{\mathcal{E}}_\lambda^T \gamma \mathcal{B}_{sc} {}^c\boldsymbol{\mathcal{E}}_u + \delta^c \boldsymbol{\mathcal{E}}_\lambda^T (1 - \gamma) \mathcal{B}_{cs} {}^s\boldsymbol{\mathcal{E}}_u - \delta^c \boldsymbol{\mathcal{E}}_\lambda^T (1 - \gamma) \mathcal{B}_{cc} {}^c\boldsymbol{\mathcal{E}}_u = \\ & \gamma \delta^s \lambda_{v_0} [{}^s v_0 - {}^c v_0] h + (1 - \gamma) \delta^c \lambda_{v_0} [{}^s v_0 - {}^c v_0] h \\ & + \gamma \delta^s \lambda_{w_0} \left[ {}^s w_0 - {}^c w_0 - \frac{h^2}{12} {}^c w_2 \right] h + (1 - \gamma) \delta^c \lambda_{w_0} \left[ {}^s w_0 - {}^c w_0 - \frac{h^2}{12} {}^c w_2 \right] h \\ & + \underbrace{\gamma \delta^s \lambda_\theta \left[ \frac{h^3}{12} {}^s \theta - \frac{h^3(\pi^3 - 24)}{12\pi^3} {}^c v_1 - \frac{2h^3}{\pi^3} {}^c \theta \right]}_{I} \\ & + (1 - \gamma) \underbrace{\delta^c \lambda_\theta \left[ \frac{2h^3}{\pi^3} {}^s \theta - \frac{h^3(\pi - 4)}{2\pi^3} {}^c v_1 - \frac{h^3}{2\pi^2} {}^c \theta \right]}_{II} \\ & + (1 - \gamma) \underbrace{\delta^c \lambda_{v_1} \left[ \frac{h^3(\pi^3 - 24)}{12\pi^3} {}^s \theta - \frac{h^3(\pi^3 + 6\pi - 48)}{12\pi^3} {}^c v_1 - \frac{h^3(\pi - 4)}{2\pi^3} {}^c \theta \right]}_{III} \end{aligned} \quad (\text{B.11})$$

Applying factorization on the terms **I**, **II** and **III** gives:

$$\begin{aligned} \mathbf{I} : & \quad \delta^s \lambda_\theta \left[ ({}^s \theta - {}^c v_1) \frac{h^3}{12} + ({}^c \theta + {}^c v_1) \frac{2h^3}{\pi^3} \right] \\ \mathbf{II} : & \quad -\delta^c \lambda_\theta \left[ ({}^s \theta - {}^c v_1) \frac{2h^3}{\pi^3} + ({}^c \theta + {}^c v_1) \frac{h^3}{2\pi^2} \right] \\ \mathbf{III} : & \quad -\delta^c \lambda_{v_1} \left[ -({}^s \theta - {}^c v_1) \frac{h^3}{12} + ({}^s w'_0 - {}^c \theta - 2{}^c v_1) \frac{2h^3}{\pi^3} + ({}^c \theta + {}^c v_1) \frac{h^3}{2\pi^2} \right] \end{aligned} \quad (\text{B.12})$$

Therefore, we can identify the restrictions satisfying the conditions at the interface. The deduced sets of relations on the displacement components are now discussed. From Equation (B.12), two cases can be distinguished:

(i) For  $\gamma \in [0, 1[$

$$\begin{aligned} {}^s v_0 &= {}^c v_0 \\ {}^s w_0 &= {}^c w_0 + \frac{h^2}{12} {}^c w_2 \\ {}^c v_1 &= -{}^c \theta = {}^s \theta \end{aligned} \quad (\text{B.13})$$

For this case, the conditions show that the rotation of the cross-section and the unknown  $v_1$  of the complex model have the same value as the derivative of the deflection of the simple model at the interface. It seems to be a strong restriction, the additional variable of the complex model being reduced as only one unique variable of the simple one.

(ii) For  $\gamma = 1$

$$\begin{aligned} {}^s v_0 &= {}^c v_0 \\ {}^s w_0 &= {}^c w_0 + \frac{h^2}{12} {}^c w_2 \\ {}^s \theta &= \left(1 - \frac{24}{\pi^3}\right) {}^c v_1 - \frac{24}{\pi^3} {}^c \theta \end{aligned} \quad (\text{B.14})$$

## Appendix C

# FE Approximations for One Dimensional Structures

### C.1 Constitutive Law for One Dimensional Structures

Hooke's law in Equation (1.4) is valid for all kinds of material symmetries, also in the case of orthotropic materials. In the case of a local cartesian reference system {1, 2, 3} defined by the material orthotropy planes of the layer, Hooke's law for a general orthotropic material reads:

$$\left\{ \begin{array}{l} \sigma_{xx} \\ \sigma_{yy} \\ \sigma_{zz} \\ \sigma_{xz} \\ \sigma_{yz} \\ \sigma_{xy} \end{array} \right\} = \left[ \begin{array}{cccccc} C_{11} & C_{12} & C_{13} & 0 & 0 & C_{16} \\ C_{12} & C_{22} & C_{23} & 0 & 0 & C_{26} \\ 0 & 0 & 0 & 0 & 0 & C_{36} \\ 0 & 0 & 0 & C_{44} & C_{45} & 0 \\ 0 & 0 & 0 & C_{45} & C_{55} & 0 \\ C_{16} & C_{26} & C_{36} & 0 & 0 & C_{66} \end{array} \right] \left\{ \begin{array}{l} \varepsilon_{xx} \\ \varepsilon_{yy} \\ \varepsilon_{zz} \\ \varepsilon_{xz} \\ \varepsilon_{yz} \\ \varepsilon_{xy} \end{array} \right\} \quad (\text{C.1})$$

Figure 4.5 depicts a beam structure with its reference system. Here the principle axis is the  $x$ -axis, standing on the cross section, described by the  $y$  and  $z$ -axis. In Equation (2.12) the components were grouped into transverse and in-plane parts. For beam structures they are now composed as follows:

$$\mathbf{C}_{pp} = \begin{bmatrix} C_{22} & C_{23} & 0 \\ C_{23} & C_{33} & 0 \\ 0 & 0 & C_{44} \end{bmatrix}; \quad \mathbf{C}_{np} = \mathbf{C}_{pn}^T \begin{bmatrix} C_{12} & C_{13} & 0 \\ 0 & 0 & C_{45} \\ C_{26} & C_{36} & 0 \end{bmatrix}; \quad (\text{C.2})$$

$$\mathbf{C}_{nn} = \begin{bmatrix} C_{11} & 0 & C_{16} \\ 0 & C_{55} & 0 \\ C_{16} & 0 & C_{66} \end{bmatrix}$$

Only the mechanical behaviour into the  $x$  and  $z$  axis will be modelled for the beam structures inside this work. The behaviour into the width axis  $y$  is neglected. The same assumptions as for the thickness direction  $z$  are used normally. Through

this description of a representative section in the  $xz$ -plane, another simplification can be introduced, assuming plane stress. Therefore the Matrix  $\tilde{C}$  in the global system will be further reduced using only the effective modules for the plane stress and will be denoted  $\bar{C}$ .

## C.2 Geometric and Mechanical Relations for One Dimensional Structures

The displacement field of the desired kinematics is received by the thickness expansion functions from Equation (4.7) in order to adapt the general displacement field in Equation (4.6). This leads to the generalized displacement vector  $\boldsymbol{\varepsilon}_u$  in Equation (4.23) together with the thickness expansion vector  $\mathbf{F}_u$  given in (4.24). These vectors will be used to introduce the general approximations for the beam structures. Note therefore that entries for  $w_1$  and  $w_2$ ,  $z$  and  $z^2$  are set to zero for all kinematics except Sinus  $z^2$ .

Equally to the generalized displacement vector a generalized strain vector  $\boldsymbol{\varepsilon}$  is introduced:

$$\boldsymbol{\epsilon} = \mathbf{F}_\epsilon \boldsymbol{\varepsilon}_\epsilon \quad (C.3)$$

with  $\boldsymbol{\varepsilon}_\epsilon = [v'_0 \ w'_0 \ v'_1 \ \theta \ \theta' \ w_1 \ w_2]^T$

While expression (C.3) is introduced into Equation (2.11) in order to define the elementary stiffness Matrix:

$$\delta\Pi_{int}(\mathbf{u}, \delta\mathbf{u}) = \int_{\Omega} \delta\boldsymbol{\varepsilon}_\epsilon^T \mathbf{F}_\epsilon^T \mathbf{C} \mathbf{F}_\epsilon \boldsymbol{\varepsilon}_\epsilon d\Omega \quad (C.4)$$

were the integration on the cross section is separated:

$$k = \int \mathbf{F}_\epsilon^T \mathbf{C} \mathbf{F}_\epsilon dS \quad (C.5)$$

The terms for a single element are denoted by the subscript  $e$ . Through Equation (C.5) only the integration along the length is remaining, hence Equation (4.23) takes the final form:

$$\delta\Pi_{int_e}(\mathbf{u}, \delta\mathbf{u}) = \delta\mathbf{q}_e^T \mathbf{K}_e \mathbf{q}_e \quad \text{with } \mathbf{K}_e = \int_L d\mathbf{N}^T \mathbf{k}_e d\mathbf{N} dx \quad (C.6)$$

Matrices  $\mathbf{N}$  containing interpolation functions of the chosen FE approximation, were the application of the derivative operator  $\mathcal{D}$  to it is denoted as  $\mathcal{D}(\mathbf{N}) = d\mathbf{N}$ . The interpolation functions are linking FE DOFs  $\mathbf{q}_e$  with  $\mathbf{u}$  and  $\boldsymbol{\varepsilon}$ :

$$\begin{aligned} \boldsymbol{\varepsilon}_u &= \mathbf{N} \mathbf{q}_e \\ \boldsymbol{\varepsilon}_\epsilon &= d\mathbf{N} \mathbf{q}_e \end{aligned} \quad (C.7)$$


---

Generally, the interpolation functions are either a quadratic approximation via Lagrange Polynomials or a cubic approximation via Hermite polynomials. The quadratic Lagrange polynomials are only  $C^0$  continuous and will be using the two outer elements nodes and a centre node of the beam element. The  $C^1$  continuous Hermite polynomials are using only the two outer nodes of the beam element. At last a linear  $C^0$  continuous interpolation at 2 central Gauß Integration points of the Element is used for  $w_1$  and  $w_2$ . Those two DOFs will be condensed on elementary level.

### C.3 Interpolation for Euler Bernoulli Theory

From Equation (4.3) a need for a  $C^1$  continuos approximation of  $w_0$  can be identified. Hence the approximation is done via Hermite polynomials, while  $v_0$  is approximated via quadratic Lagrange polynomials. For the Euler Bernoulli Theory, the generalized vector of variables simplifies to  $\mathcal{E}_e = [v'_0, w''_0]^T$  and the vector of the finite element degrees of freedoms is  $\mathbf{q}_e = [v_0, w_0, w'_0]^T$ , which is shown in Figure C.1 (a).

With the effective modulus  $\bar{C}$ , gained from the reduced three dimensional elasticity law, the elementary matrix containing the kinematical behaviour integrated over the section for an element using the Euler Bernoulli Theory is:

$$\bar{k}_e = \int \begin{bmatrix} \bar{C}_{11} & -z \bar{C}_{11} \\ sym & z^2 \bar{C}_{11} \end{bmatrix} dS \quad (C.8)$$

### C.4 Interpolation for Timoshenko Theory

Equation (4.4) for Timoshenko Theory gives no more need for a  $C^1$  continuos  $w_0$ , hence all DOFs,  $v_0$ ,  $w_0$  and  $\theta$  are interpolated by quadratic Lagrange polynomials. The generalized vector of variables for Timoshenko, using  $\gamma^0 = (w'_0 + \theta)$ , is  $\mathcal{E}_e = [v_0, \theta, \theta', \gamma^0]^T$  and the vector of the finite element DOFs is  $\mathbf{q}_e = [v_0, w_0, \theta]^T$ , see figure C.1 (b) for an illustration.

For the Timoshenko Theory, the elementary matrix containing with the kinematical behaviour integrated over the section is:

$$\bar{k}_e = \int \begin{bmatrix} \bar{C}_{11} & 0 & z \bar{C}_{11} & 0 \\ & \bar{C}_{55} & 0 & \bar{C}_{55} \\ & & z^2 \bar{C}_{11} & 0 \\ & & & \bar{C}_{55} \\ sym & & & \bar{C}_{55} \end{bmatrix} dS \quad (C.9)$$

### C.5 Interpolation for Sinus $z^2$ Theory

For element using the Sinus  $z^2$  Theory from Equation (4.6), all active DOFs are interpolated via quadratic Lagrange polynomials. The two DOFs  $w_1$  and  $w_2$  are eliminated at elementary level through static condensation into  $w_0$ . Shear locking of this quadratic element for very thin beams is controlled via the field compatibility

approach as described in [58]. For an element based on this theory, the generalized vector of variables becomes  $\boldsymbol{\mathcal{E}}_\epsilon = [v_0, \theta, \theta', w_0, v'_1, \gamma^0, w_1, w_2]^T$ . The vector of the active finite element DOFs is  $\boldsymbol{q}_e = [v_0, w_0, \theta, v_1]^T$ , which can be seen in Figure C.1 (c).

The elementary matrix containing the kinematical behaviour integrated over the section for the Sinus  $z^2$  theory is:

$$\bar{k}_e = \int_{sym} \begin{bmatrix} \bar{C}_{11} & 0 & \bar{C}_{11} f(z) & 0 & \bar{C}_{11} (f(z) - z) & 0 & \bar{C}_{13} & 2\bar{C}_{13}z \\ \bar{C}_{55} f'(z)^2 & 0 & \bar{C}_{55} f'(z)^2 & 0 & \bar{C}_{55} f'(z) & 0 & 0 & 0 \\ \bar{C}_{11} f(z)^2 & \bar{C}_{11} f(z)^2 & 0 & \bar{C}_{11}(f(z) - z)f(z) & 0 & \bar{C}_{13} & 2\bar{C}_{13}f(z)z & 0 \\ \bar{C}_{55} f'(z)^2 & \bar{C}_{55} f'(z)^2 & 0 & \bar{C}_{55} f'(z) & 0 & 0 & 0 & 0 \\ & & \bar{C}_{11} (f(z) - z)^2 & 0 & \bar{C}_{13}(f(z) - z) & 2\bar{C}_{13}(f(z) - z)z & 0 & 0 \\ & & & \bar{C}_{55} & 0 & 0 & 0 & 0 \\ & & & & \bar{C}_{33} & 2\bar{C}_{33}z & 0 & 4\bar{C}_{33}z^2 \end{bmatrix} dS \quad (C.10)$$

---

### Appendix C. FE Approximations for One Dimensional Structures

---

An extensive study of the performance and convergence of this kinematical models with its different approximations can be found in [75], [76] and [77].

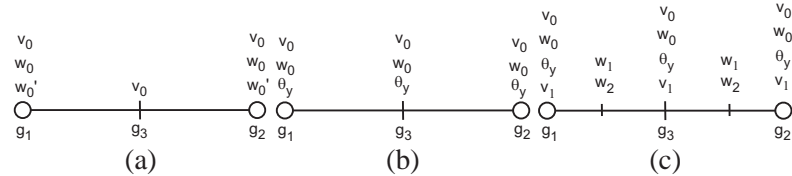


Figure C.1: (a): Euler Bernoulli - ; (b): Timoshenko - ; (c): Sinus  $z^2$  beam element

## Appendix D

# FE Code Implementation for One Dimensional Structures

In order to study one-dimensional structures, the laboratory own FE code EvalEF has been enriched with the XVF. Here a brief overview of the needed input is given. Four different main kinematics can be used: Euler-Bernoulli, Timoshenko, Sinus and Sinus-z2 models. Timoshenko and Sinus can be handled with different approximations, using either Lagrange or Hermite polynomials. Due to the poor conditioning of the XVF system, see Equation (4.37), a robust solver is needed in order to solve the system. Here a solver for a full matrix is used for the XVF applying a preconditioning and solving the overall system with a LU decomposition.

### D.1 The DATA file

---

<b>NOMELT NCLE(1:6)</b>	name of the element approximation types, each has to be given with its six specific keys
NOMELT	= PHER1D or PLAG1D or PLAG3D
	all element types used can be stated independently in any order
NCLE(1)	type of model
	= 4 : MultiModel
NCLE(2)	number of integration points (1-2-3)
<b>RConstElt(1:2)</b>	Real constants related to the used elements:
RConstElt (1)	width of the beam
RConstElt (2)	shear correction factor for Timoshenko model

---

<b>NOMANA</b>	Name of analysis = MECA
<b>TYPANA NANACLE(1:6)</b>	analysis type with its six specific keys
TYPANA	analysis type = STAT : static analysis = VALP : modal analysis ( $\lambda, \vec{v}_\lambda$ ) = BUCK : buckling analysis (critical load)
NANACLE(1)	algorithm for VALP or BUCK = 0 : <b>PI algorithm</b> = 1 : <b>QZ algorithm</b>
NANACLE(2)	eigenvalues indicator NBVALP : number of Eigenvalues if <b>PI algorithm</b>
NANACLE(3)	eigenmode indicator = 0 : VALP -> mass matrix = Identity ; rigid rang = 1 : VALP -> calculation of eigenvalues (modal analysis)
NANACLE(4)	model coupling indicateur = 0 : Common node assembly, using penalty value = 1 : XVF method with Lagrange Multiplier coupling
NANACLE(5)	model coupling indicateur = 0 : band assembly and solver = 1 : full assembly and solver
NANACLE(6)	post indicator = 1 : Post gives list of element energies = 2 : Post gives list format of stresses
<b>RconstAna(1)</b>	if algorithm VALP or BUCK = ValMax : PI algorithm = ValNul : QZ algorithm
<b>RconstAna(1)</b> used	if STAT and XVF algorithm is = value for $\gamma$

---

<b>NOMMATEMP</b>	name of MATerial/EMPilement
(stacking) file	
<b>NOMGEO</b>	name of GEOMETRY file
<b>NOMOUT</b>	name of result file
<b>Xmult Ymult</b>	scale for geometry $X$ and $Y$
<b>NBTYPECHG</b>	Load Type Number
loop on NBTYPECHG	
<b>NOMCHG NCHGL</b>	Load Name, Load Number
<i>if NOMCHG =’CC’: Concentrated Loads (Charges Concentrées)</i>	
<i>loop on NCHGL</i>	
	NUMCHG(1,.) = 1, NUMCHG(2,.) = 0
<b>NUMCHG(2:3,.) DCHG(.)</b>	node and DOF number (node,
DOF), load value	
<i>end of loop on NCHGL</i>	
<i>or if NOMCHG =’PL’: local pressure (Pression Locale)</i>	
	NUMCHG(1,.) = 2 , NUMCHG(2,.) = 0
<b>NUMCHG(3,.) DCHG(.)</b>	
NUMCHG(3,.) pressure direction	
= 1 : $X$	
= 2 : $Y$	
= 3 : $Z$	
DCHG(.)	pressure value
<i>or if NOMCHG =’PG’: global pressure (Pression Globale)</i>	
	NUMCHG(1,.) = 3, NUMCHG(2,.) = 0
<b>NUMCHG(3,.) DCHG(.)</b>	
NUMCHG(3,.) pressure direction	
= 1 : $x_1$	
= 2 : $x_2$	
= 3 : $z$	

---

NUMCHG(4,.)	pressure position
	= 0 : lower surface
	= 1 : upper surface
	= 2 : middle layer
DCHG(.)	pressure value

---

*or if NOMCHG =’PC’: contour pressure (Pression contour)*

*loop on NCHGL*

NUMCHG(1,.) = 4

**NUMCHG(2:3,.) DCHG(.)**

face, pressure direction, pressure  
value

NUMCHG(2,.)	face
	= 1 : $X = cste$
	= 2 : $Y = cste$
NUMCHG(3,.)	pressure direction
	= 1 : $X$
	= 2 : $Y$
	= 3 : $Z$

**DXYCHG(1 ou 2,.)**

coordinate value ( $X$  or  $Y$ )

*end of loop on NCHGL*

---

*or if NOMCHG =’PS’: sinus pressure (Pression Sinus)*

NUMCHG(1,) = 6

**NUMCHG(2:3,.) DCHG(.)**

NUMCHG(2,.)	along $x$
	= 0 : yes
	$\neq 0$ : no
NUMCHG(3,.)	along $y$
	= 0 : no
	$\neq 0$ : yes
DCHG(.)	pressure value

**DXYCHG(1,.) DXYCHG(2,.)** length along  $x$ , length along  $y$

---

or if NOMCHG = 'LC': kinematic relation (liaison cinématique)

NOMCHG(1,) = 8

**NUMCHG(2:3,.) DCHG(.)**

NUMCHG(2,.) concerned node

NUMCHG(3,.) first concerned DOF

NUMCHG(4,.) second concerned DOF

**DXYCHG(1,.) DXYCHG(2,.)** constrains first and second DOF

values to be equal via penalty method under the form of  $\alpha_1 u_1 + \alpha_2 u_2 = 0$ ,  
penalty value is fixed to  $10^{10}$

end if

end of loop on NBTYPECHG

---

**NXSub NYSub**

deformed mesh ; Subdivision along

$x$   $y$

## D.2 The Geometry file NOMGEO

**NND NEL**

NoDe Number, Element Num-

ber

loop on the number of nodes **NND**

**IVAR NBCDF(1:4,.) XYZ(1:3,.)**

IVAR, Num Boundary Condition NoDe, Node coord.

end of the loop on the number of nodes **NEL**

loop on the number of elements

**IVAR ICOEl(1) ICOEl(2) ICOEl(3) IVAR ICO(1:NNDEL,.)**

Num Elem, Typ Elem, Model Num, MatEmpil Num, Connect. Table

end of loop on the number of elements

According to Appendix C the general order of the DOFs is displayed in the following table, as well as the global availability in the different finite element models. This is due to the different FE approximations possible for certain models, which are either the  $C^1$ -continuous Hermite approximations (HER1D), the  $C^0$ -continuous Lagrange approximations (LAG1D) or the same Lagrange approximations with the

Model	$v_0$	$w_0$	$w'_0$	$\theta$	$v_1$
Her 1D					
EB	x	x	x	-	-
Timo	x	x	x	x	-
Sin	x	x	x	x	-
Lag 1D					
Timo	x	x	-	x	-
Sin	x	x	-	x	x
Lag 3D					
Timo	x	x	-	x	-
Sin-z2	x	x	-	x	x

Table D.1: DOF availability

transverse normal effect (LAG3D). Note that for the Sinus model with thickness effect, the additional DOFs  $w_1$  and  $w_2$  are condensed at elementary level:

In the EvaleEF code, a special convention for constraining the deflection  $w_0$  and its derivative  $w'_0$  was implemented for the models with the Hermite approximation. In the global DOF definition only the deflection  $w_0$  is common between the different approximations and therefore only this DOF is direct available. However all five DOFs can be constrained using this convention using only the four accessible DOFs. It is displayed in the table hereafter:

Input	Constraint on w	Constraint on w'	Constraint scheme	global constraint
0	0	0	0 0 0 0	0 0 0 0 0
1	1	0	0 1 0 0	0 1 0 0 0
2	1	1	0 2 0 0	0 1 1 0 0
3	0	1	0 3 0 0	0 0 1 0 0

 Table D.2: DOF constrainement for  $w_0$  in Hermite 1D

For all other DOFs in all models, a **zero** as constraint means that the concerned DOF is **free** and a **one** means that the concerned DOF is **constraint**. The order of the DOFs in the constraint table is:  $v_0 \ w_0 \ \theta \ v_1$

As all element types can be stated in any order , the user gets freedom. However one has to take care of the right position of Element type and model numbers in the mesh. They have to be according to the order in which the Element types are stated in the head of the DATA file.

Just as reference and for your orientation we will state here the internal variables used for identification of the element types used. They can be found in the subroutine CARELT:

While the kinematical models are always fixed to the following input values:

Table D.3: Element type numbers

Element Type	NUMELTVal
Hermite 1D	2
Lagrange 1D	1
Lagrange 3D	3

Table D.4: model type numbers

Model Type	Number
Sinus	1
Euler Bernoulli	2
Timoshenko	3

In the following table, the available combinations of Element types and kinematical models are given:

-	Her 1D	Lag 1D	Lag 3D
Sin	x	x	-
Sin-z2	-	-	x
Euler	x	-	-
Timo	x	x	x

Table D.5: available models for the three Element types

### D.3 The Material Stacking file MATEMP

```

NbMat                                     number of material
loop on the number of materials NbMat

PROPM(1:13,.)                         Material Properties
     $\rho \alpha_1 \alpha_2 \alpha_3 E_1 E_2 E_3 \nu_{23} \nu_{13} \nu_{12} G_{23} G_{13} G_{12}$ 
end of loop on the number of materials

NbEmpil                                    number of stacking
loop on the number of stackings NbEmpil

IVAR IEmpil(1,.) REmpil(1,1,.)
    IVAR, number of layers, distance of mid to outer layer basse
loop j on the number of layers IEmpil(1,.)

```

---

IEmpl(j+1,.) (REmpl(k,j+1,.),k=1,2)

number of material, orientation, thickness

*end of loop j on the number of layers*

*end of loop on the number of stackings*

## Appendix E

# ABAQUS Implementation of CUF Elements

For the study of the free edge problems, the CUF was implemented into the commercial FE code ABAQUS. It offers via the so-called subroutine USER ELEMENT, the possibility to create own elements. Scripting has to be done in FORTRAN using the provided interface structure, given in the ABAQUS documentation.

### E.1 The Problem Statement

In the first ABAQUS Plug-Inn, see Figure E.1, the mechanical problem is defined.

Therefore the following parameters are defined:

- Geometry:
  - rectangular plate
  - rectangular plate with central hole
  - skew angled plate
- Boundary Condition:
  - free
  - symmetry to  $x$ ,  $y$  or  $z$ -axis
  - simply supported
  - encasted
- Load:
  - uniform extension
  - uniform pressure load

- bi-sinusodial pressure load

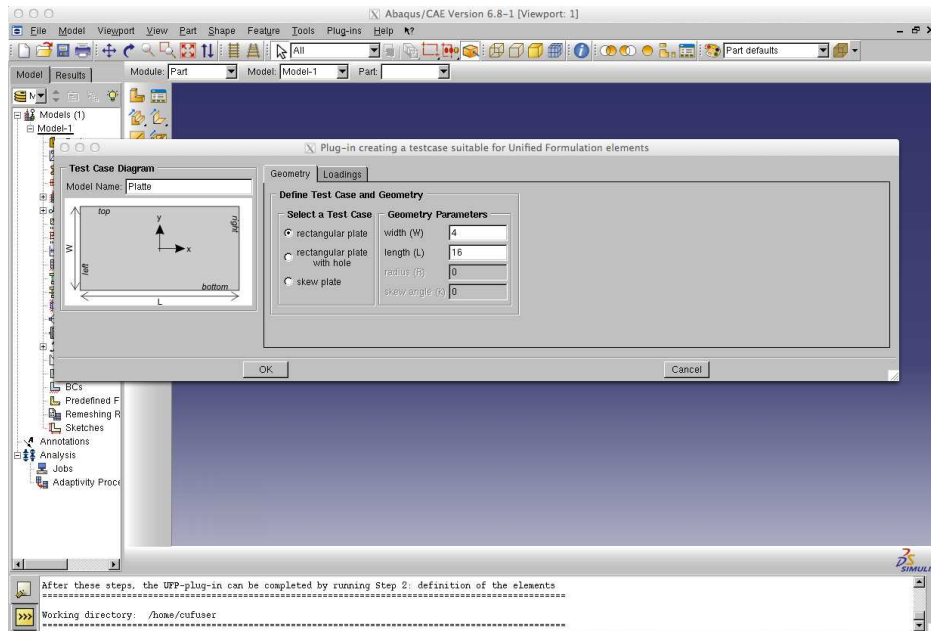


Figure E.1: Creating the mechanical problem via a Plug-Inn using pre-defined cases

The material model and its parameters have to be defined inside ABAQUS itself.

## E.2 The FE Approximation

In preparation of preparing the generation of the ABAQUS input file, only the element definition is missing. In order to do so, a mesh has to be generated before the definition of the CUF elements used. The standard ABAQUS tools for the mesh generations are used. Afterwards via a second ABAQUS Plug-Inn the CUF elements are defined, as indicated via Figure E.2. It is here, where the laminates lay-up is described. Afterwards the lay-up description for the element is defined, the variational statement and the expansion order, see Figure E.3. Further some advanced controls against shear locking, like reduced integration, and against thickness-locking, like reduced or simplified constitutive laws can be defined. For the test cases under consideration within this work neither of both have been used. After this definition has been done, the input file can be written and consequently solved.

## Appendix E. ABAQUS Implementation of CUF Elements

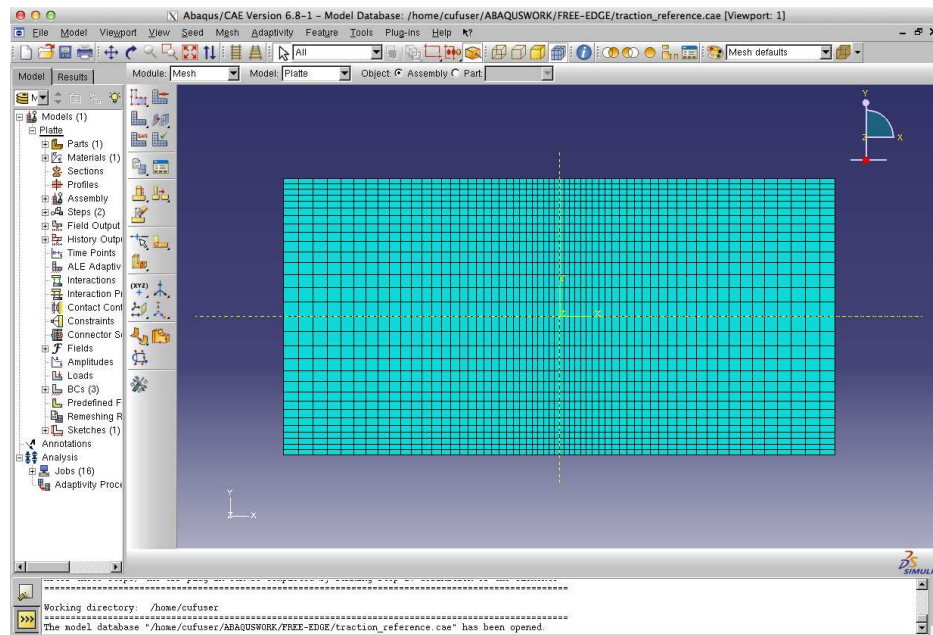


Figure E.2: The FE mesh is defined inside ABAQUS itself

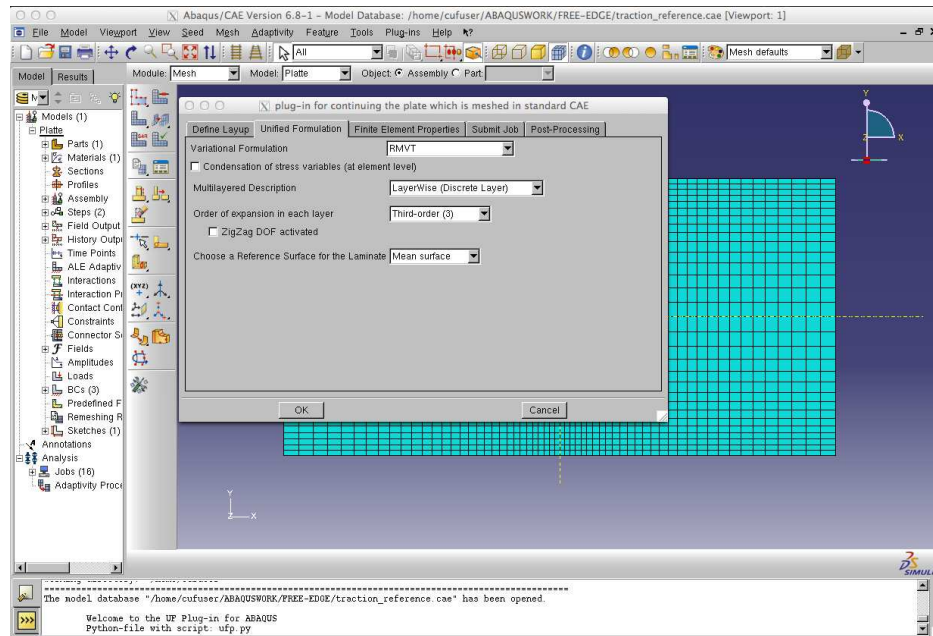


Figure E.3: The CUF elements are defined via a second Plug-In

### E.3 Post-Procesing

Via the subroutine, the results of the FE calculation are available in an output-file, containing the nodal values of each DOF. As this is not a very intuitive and comprehensive expression of the results a further output processing routine is written in FORTRAN. Its purpose is to provide the displacement field as well as stress and strain field, expressed in their components, based on the nodal DOFs. This results are provided via problem dependent files containing the results of each of the before mentioned fields. The numeric results presented within this work have been exported from the post-processor into MATLAB in order to provided the visualization of the results for the different CUF elements. From an implementation point of view, a functional post-processing with result visualization is still a missing feature.

# Bibliography

- [1] M. Aminpour, J. Ransom, and S. Mc Cleary. A coupled analysis method for structures with independently modeled finite element subdomains. *International Journal for Numerical Methods in Engineering*, 38:3695–3718, 1995.
- [2] S.N. Atluri. *On 'hybrid' finite-element models in solid mechanics*. Rutgers University, 1975.
- [3] P. Bar-Yoseph and J. Avrashi. On the nature of the free edge stress singularity in composite laminated plates. *International Journal for Numerical Methods in Engineering*, 26:1507–1523, 1988.
- [4] P. Bar-Yoseph and D. Ben-David. Free-edge effects in unsymmetrically laminated composite plates. *Composite Structures*, 30:13–23, 1995.
- [5] J.-L. Batoz and G. Dhatt. *Modélisation des structures pas éléments finis*. Hermès, 1990.
- [6] F. Biscani, G. Giunta, E. Carrera, and H. Hu. Variable kinematic plate elements coupled via arlequin method. *Composite Structures*, 91:1264–1290, 2012.
- [7] P.J. Blanco, R.A. Feijóo, and S.A. Urquiza. A variational approach for coupling kinematically incompatible structural models. *Computer methods in applied mechanics and engineering*, 197:1577–1602, 2008.
- [8] E. Carrera. Historical review of zig-zag theories for multilayered plates and shells. *Applied Mechanics Review*, 56(3), 2003.
- [9] E. Carrera. Theories and finite elements for multilayered plates and shells: A unified compact formulation with numerical assessment and benchmarking. *Archives of Computational Methods in Engineering*, 10(3):215–296, 2003.
- [10] E. Carrera and L. Demasi. Classical and advanced multilayered plate elements based upon pvd and rmvt. part 1: Derivation of finite element matrices. part 2: Numerical implementations. *International Journal for Numerical Methods in Engineering*, 55:191–231, 253–291, 2002.

---

## Bibliography

---

- [11] E. Carrera, M. Filippi, and E. Zappino. Laminated beam analysis by polynomial, trigonometric, exponential and zig-zag theories. *European Journal of Mechanics A/Solids*, 41:58–69, 2013.
  - [12] E. Carrera, A. Pagani, and M. Petrolo. Use of lagrange multipliers to combine 1d variable kinematic finite elements. *Composite and Structures*, 2013.
  - [13] M. Cho and H.S. Kim. Iterative free-edge stress analysis of composite laminates under extension, twisting and thermal loadings. *International Journal of Solids and Structures*, 37:435–459, 2000.
  - [14] G. Davì and A. Milazzo. Boundary element solution for free edge stresses in composite laminates. *Journal of Applied Mechanics*, 64:877–884, 1997.
  - [15] L. Demasi.  $\infty^3$  hierarchy plate theories for thick and thin composite plates: The generalized unified formulation. *Composite Structures*, 84(3):256–270, 2008.
  - [16] H. Ben Dhia and G Rateau. The arlequin method as a flexible engineering design tool. *International Journal for Numerical Methods in Engineering*, 62:1442–1462, 2005.
  - [17] M. D’Ottavio. *Advanced Hierarchical Model of Multilayered Plates and Shells Including Mechanical and Electrical Interfaces*. PhD thesis, Universität Stuttgart, 2008.
  - [18] M. D’Ottavio, P. Vidal, E. Valot, and O. Polit. Assessment of plate theories for free-edge effects. *Composites: Part B*, 48:111–121, 2013.
  - [19] C. Farhat and F-X. Roux. Implicit parallel processing in structural mechanics. *Computational Mechanics Advances*, 2:1–124, 1994.
  - [20] J. Fish. The s-version of the finite element method. *Computers & Structures*, 43(3):539–547, 1992.
  - [21] J. Fish and S. Markolefas. The s-version of the finite element method for multi-layer laminates. *International Journal for Numerical Methods in Engineering*, 33:1081–1105, 1992.
  - [22] L. Gendre, O. Allix, and P. Gosselet. A two-scale approximation of the schur complement and its use for non-intrusive coupling. *International Journal for Numerical Methods in Engineering*, 87(9):889–905, 2011.
  - [23] G.L. Ghiringhelli and G. Sala. Influence of stacking sequences and interlaminar layer in stress singularities at free edge of composite laminates. *Meccanica*, 25:32–39, 1990.
  - [24] G. Giunta and F. Biscani. Variable kinematic beam elements coupled via arlequin method. *Composite Structures*, 93:697–708, 2011.
-

---

## Bibliography

---

- [25] F. Gruttmann and W. Wagner. On the numerical analysis of local effects in composite structures. *Composite Structures*, 29, 1994.
  - [26] P.A. Guidault and T. Belytschko. On the l2 and the h1 couplings for an overlapping domain decomposition method using lagrange multipliers. *International Journal for Numerical Methods in Engineering*, 70:322–350, 2007.
  - [27] M. Haboussi. *Contribution à la modélisation de l'intercouche dans les stratifiés composites: application aux effets de bords libres*. PhD thesis, École Nationale Supérieure d'Arts et Métiers, 1998.
  - [28] M. Haboussi, H. Dumontet, and J.L. Billoët. On the modelling of interfacial transition behaviour in composite materials. *Computational Material Science*, 20:251–266, 2001.
  - [29] C.T. Herakovich. *Mechanics of Fibrous Composites*. Wiley, 1998.
  - [30] J. Hetherington, A. Rodríguez-Ferran, and H. Askes. The bipenalty method for arbitrary multipoint constraints. *International Journal for Numerical Methods in Engineering*, 93:465–574, 2013.
  - [31] I. Hirai, Y. Uchiyama, Y. Mizuta, and W.D. Pilkey. An exact zooming method. *Finite Elements in Analysis and Design*, pages 61–69, 1985.
  - [32] H. Hu. *Modélisation multi-échelle des structures sandwich*. PhD thesis, Université Paul Verlaine Metz, 2006.
  - [33] H. Hu, S. Belouettar, M. Potier-Ferry, and El M. Daya. Multi-scale modelling of sandwich structures using the arlequin method part i: Linear modelling. *Finite Elements in Analysis and Design*, 45:37–51, 2009.
  - [34] H. Hu, S. Belouettar, M. Potier-Ferry, E.M. Daya, and A. Makradi. Multi-scale nonlinear modelling of sandwich structures using the arlequin method. *Composite Structures*, 92:515–522, 2010.
  - [35] U. Icardi and A.M. Beretto. An evaluation of the influence of geometry and of material properties at free edges and at corners of composite laminates. *Composite and Structures*, 57(4):555–571, 1995.
  - [36] A. Idlibi, M. Karama, and M. Touratier. Comparison of various laminated plate theories. *Composite Structures*, 37:173–184, 1997.
  - [37] C. Kassapoglou. Determination of interlaminar stresses in composite laminates under combined loads. *Journal of Reinforced Plastics and Composites*, 9, 1990.
  - [38] C. Kassapoglou and P. A. Lagace. An efficient method for the calculation of interlaminar stresses in composite materials. *Journal of Applied Mechanics*, 53:744–750, 1986.
-

---

## Bibliography

---

- [39] C. Kassapoglou and P. A. Lagace. Closed form solutions for the interlaminar stress field in angle-ply and cross-ply laminates. *Journal of Composite Materials*, 21:292–308, 1987.
  - [40] H.-G. Kim. Interface element method (iem) for a partitioned system with non-matching interfaces. *Computer methods in applied mechanics and engineering*, 191:3165–3194, 2002.
  - [41] T. Kim and S.N. Atluri. Interlaminar stresses in composite laminates under out-of-plane shear/bending. *AIAA Journal*, 32(8), 1994.
  - [42] T. Kim and S.N. Atluri. Analysis of edge stresses in composite laminates under combined thermo-mechanical loading, using complementary energy approach. *Computational Mechanics*, 16:83–97, 1995.
  - [43] G. Kirchhoff. Über das gleichgewicht und die bewegungen einer elastischen scheibe. *Journal für die Reine und Angewandte Mathematik*, 40:51–88, 1850.
  - [44] G.M. Kulikov and S.V. Plotnikova. Exact 3d stress analysis of laminated composites by sampling surfaces method. *Composite Structures*, 94(12):3654–3663, 2013.
  - [45] C. Lacour and Y. Maday. Two different approaches for matching nonconforming grids: the mortar element method and the feti method. *BIT Numerical Mathematics*, 37:720–738, 1997.
  - [46] P. A. Lagace and K.J. Saeger. Approaches for preliminary design assessment of delamination potential in composite laminates. *First USSR-US Symposium on Composite Materials, Riga USSR*, 1989.
  - [47] S. Mistou and M. Karama. Edge effects on sandwich composite by analytical, finite element and experimental approach. *Journal of Sandwich Structures and Materials*, 6, 2004.
  - [48] C. Mittelstedt and W. Becker. Efficient computation of order and mode of three-dimensional stress singularities in linear elasticity by the boundary finite element method. *International Journal of Solids and Structures*, 43:2868–2903, 2006.
  - [49] C. Mittelstedt and W. Becker. Free-edge effects in composite laminates. *Applied Mechanics Review*, 60, 2007.
  - [50] H. Murakami. Laminated composite plate theory with improved in-plane response. *Journal of Applied Mechanics*, 53:661–666, 1986.
  - [51] P.L.N. Murthy and C.C. Chamis. Free-edge delamination: Laminate width and loading condition effects. Technical report, NASA Lewis Research Center, Cleveland, Ohio, 1987.
-

---

## Bibliography

---

- [52] V.-T. Nguyen and J.-F. Caron. A new finite element for free edge effect analysis in laminated composites. *Computers and Structures*, 84:1538–1546, 2006.
  - [53] N.J. Pagano. Exact solutions for rectangular bidirectional composites and sandwich plates. *Journal of Composite Materials*, 4:20–34, 1970.
  - [54] J. W. Park, J.W. Hwang, and Y. H. Kim. Efficient finite element analysis using mesh superposition technique. *Finite Elements in Analysis and Design*, 39:619–638, 2003.
  - [55] K.C. Park and C. A. Felippa. A variational principle for the formulation of partitioned structural systems. *International Journal for Numerical Methods in Engineering*, 47:395–418, 2000.
  - [56] L. Parussini. *Fictitious domain approach with spectral element approximation*. PhD thesis, Università degli studi di Udine, 2008.
  - [57] R.B. Pipes and N.J. Pagano. Interlaminar stresses in composite laminates under uniform axial extension. *Journal of Composite Materials*, 4, 1970.
  - [58] O. Polit, M. Touratier, and P. Lory. A new eight-node quadrilateral shear- a new eight-node quadrilateral shear-bending plate finite element. *International Journal for Numerical Methods in Engineering*, 37:387–411, 1994.
  - [59] W. Prager. In *Recent Progress in Applied Mechanics*, chapter Variational principles for linear elastostatics for discontinuous displacements, strains and stresses. Almquist and Wiksell, Stockholm, 1967.
  - [60] M. A. Puso. A 3d mortar method for solid mechanics. *International Journal for Numerical Methods in Engineering*, 59:315–336, 2004.
  - [61] I.S. Raju and J.H. Crews. Interlaminar stress singularities at a straight free edge in composite laminates. Technical memorandum 81876, NASA, Langley Research Center, 1980.
  - [62] J.B. Ransom. *On multifunctional collaborative methods in engineering science*. PhD thesis, Langley Research Center, September 2001.
  - [63] J.N. Reddy and D.H. Robbins. Theories and computational models for composite laminates. *Applied Mechanicis Review*, 47(6), 6 1994.
  - [64] E. Reissner. On a certain mixed variational theorem and a proposed application. *International Journal for Numerical Methods in Engineering*, 20:1366–1368, 1984.
  - [65] E. Reissner. On a mixed variational theorem and on a shear deformable plate theory. *International Journal for Numerical Methods in Engineering*, 23:193–198, 1986.
-

---

## Bibliography

---

- [66] R.I.Zwiers, T.C.T. Ting, and R.L. Spilker. On the logarithmic singularity of free-edge stress in laminated composites under uniform extension. *Journal of Applied Mechanics*, 49:561–569, 1982.
  - [67] D.H. Robbins and J.N. Reddy. Modelling of thick composites using a layerwise laminate theory. *International Journal for Numerical Methods in Engineering*, 36, 1993.
  - [68] D.H. Robbins and J.N. Reddy. Variable kinematic modelling of laminated composite plates. *International Journal for Numerical Methods in Engineering*, 39:2283–2317, 1996.
  - [69] N. Saeedi, K. Sab, and J.-F. Caron. Delaminated multilayered plates under uniaxial extension. part ii: Efficient layerwise mesh strategy for the prediction of delamination onset. *International Journal of Solids and Structures*, 49:3727–3740, 2012.
  - [70] H. Y. Sarvestani and M. Y. Sarvestani. Free-edge stress analysis of general composite laminates under extension, torsion and bending. *Applied Mathematical Modelling*, 36:1570–1588, 2012.
  - [71] R.L. Spilker and S.C. Chou. Edge effects in symmetric composite laminates: importance of satisfying the tractionfree edge condition. *Journal of Composite Materials*, 14:2–20, 1980.
  - [72] M. Tahani and A. Nosier. Edge effects of uniformly loaded cross-ply composite laminates. *Materials & Design*, 24:647–658, 2003.
  - [73] M. Tahani and A. Nosier. Three-dimensional interlaminar stress analysis at free edges of general cross-ply composite laminates. *Materials & Design*, 24:121–130, 2003.
  - [74] S.P. Timoshenko. *Theory of Elasticity*. McGraw-Hill, 1970.
  - [75] P. Vidal and O. Polit. A thermomechanical finite element for the analysis of rectangular laminated beams. *Finite Elements in Analysis and Design*, 42:868–883, 2006.
  - [76] P. Vidal and O. Polit. A family of sinus finite elements for the analysis of rectangular laminated beams. *Composite Structures*, 84:56–72, 2008.
  - [77] P. Vidal and O. Polit. Assessment of the refined sinus model for the non-linear analysis of composite beams. *Composite Structures*, 87:370–381, 2009.
  - [78] A.S.D. Wang and F.W. Crossman. Some new results on edge effect in symmetric composite laminates. *Journal of Composite Materials*, 11, 1977.
  - [79] J. Wissmann. *Finite Elemente in der Strukturmechanik*. Springer, 2005.
-

---

## Bibliography

---

- [80] L. Ye. Some characteristics of distributions of free-edge interlaminar stresses in composite laminates. *International Journal of Solids and Structures*, 26(3):331–351, 1990.
- [81] S. Yi. Finite element analysis of free edge stresses in non-linear viscoelastic composites under uniaxial extension, bending and twisting loadings. *International Journal for Numerical Methods in Engineering*, 40:4225–4238, 1997.
- [82] K. Yu, H. Hu, S. Chen, S. Belouettar, and M. Potier-Ferry. Multi-scale techniques to analyse instabilities in sandwich structures. *Composite Structures*, 96:751–762, 2013.